UNIVERSITY
OF TRENTO - Italy
Department of Materials Engineering
and Industrial Technologies

Doctoral School in Materials Engineering – XXII cycle

MICROSTRUCTURAL AND MECHANICAL PROPERTIES OF Co AND Ti ALLOYS FOR BIOMEDICAL APPLICATIONS PRODUCED BY METAL INJECTION MOLDING (MIM)

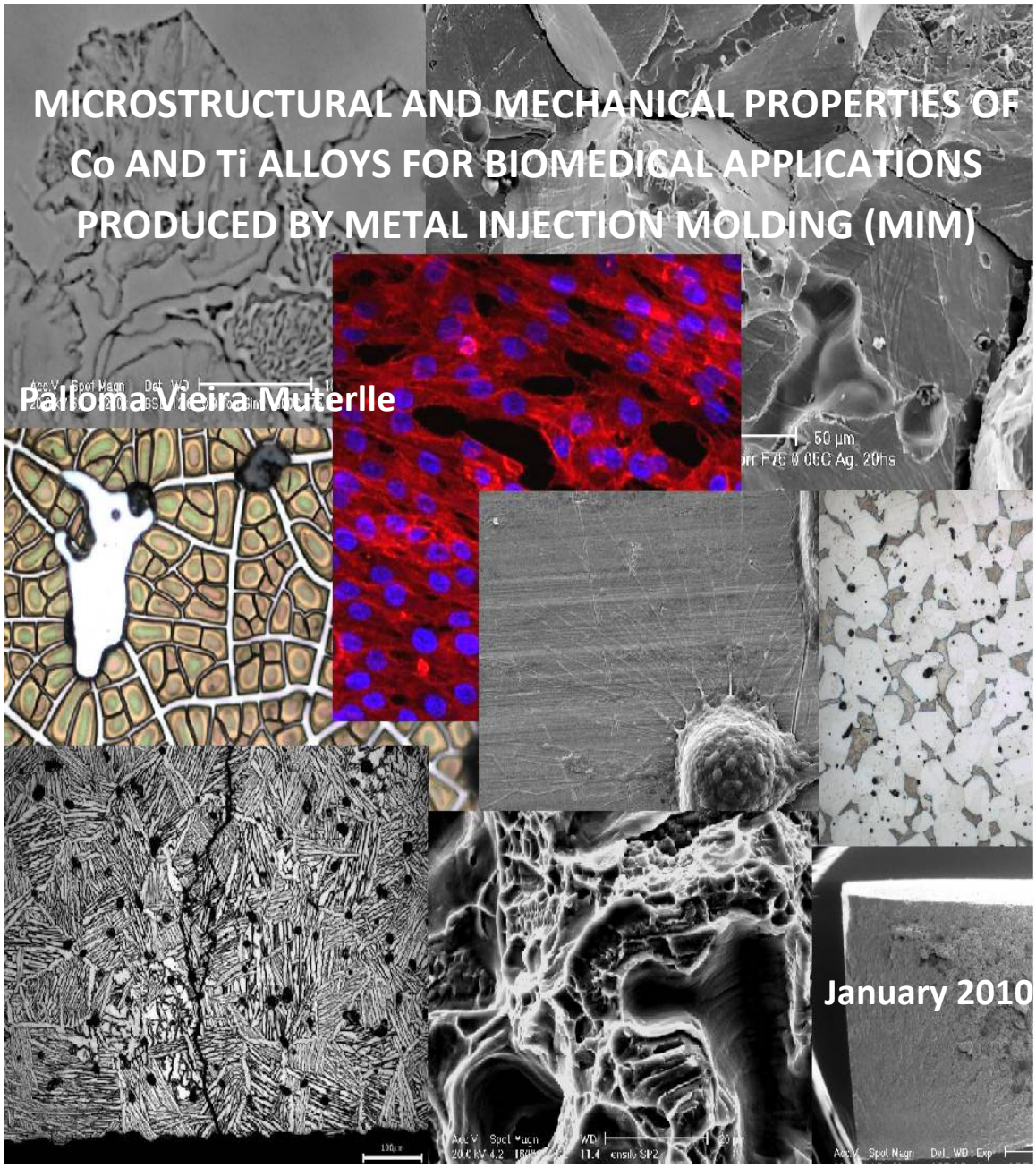

Palloma Vieira Muterlle

January 2010

INDEX

INTRODUCTION

The present work was carried out in the frame of a scientific cooperation between the Department of Materials Engineering and Industrial Technologies of Trento University and MIMEST spa (Pergine Valsugana, Trento), a small company specialized in the production of parts by metal injection molding (MIM) of powders.

The cooperation was established to develop the applications of MIM products in the biomedical fields, with the production of both prosthesis and external tutors and surgery tools. In this quite wide and promising area, four materials are of interest: cobalt alloys, titanium alloys, austenitic stainless steel and precipitation hardened stainless steels. The first three materials are biocompatible, thus they are used for the production of implantable devices. The latter is used for the production of tutors and tools.

The company has a well established know how in the specific process, and has developed a proprietary binder. At the beginning of the cooperation, the MIM process for the production of both near-full dense and full dense materials was already set up, and the interest of the company was mainly focused on the optimization of the properties. In particular, there were several open points concerning the effect of the as sintered microstructure on some of the properties which are requested for the specific applications.

Cobalt alloys can be produced with different carbon contents. The increase in the carbon content results in an increase in hardness but also in a corresponding decrease in ductility. It is thus important to find a proper combination of the carbon content and the processing route (sintering plus any post sintering treatments) to optimize mechanical properties. In addition, the role of carbides on both wear and corrosion resistance was unknown. Finally, since the biocompatibility of the cobalt alloys was assessed with reference to cast products, it seems very important to evaluate whether or not the specific microstructural features of the MIM alloy, which are different from the as cast one and can vary quite significantly on varying the carbon content, may influence the biocompatibility.

Concerning titanium alloys, the main problem is fatigue resistance. With reference to wrought products (hot working is the concurrent technology), the microstructure of MIM products is quite different, being not globular but lamellar. Since the fatigue resistance of titanium alloys is very sensitive to microstructure, the investigation was mainly dedicated to the study of fatigue resistance and to the possibility to increase it by shot-peening.

As far as stainless steels are concerned, both austenitic one and precipitation hardened varieties contain some residual delta ferrite in the as sintered microstructure. The concurrent products obtained by hot working do not contain such a constituent. The reason lies in the high sintering temperature. The main aim

of the work was, in this case, the study of the influence of delta ferrite on mechanical and corrosion properties.

The work has been carried out on all four materials described above. In all cases, the common approach was the study of the microstructural characteristics which are decisive in determining the properties, the possibility to modify them by either heat treatment or mechanical treatment, and the correlation with the specific properties. Most of the investigation has been dedicated to the cobalt alloys, since the range of open questions was quite large. Consequently, the cobalt alloys took most of the time dedicated to the project.

The thesis is organized in some chapters, and only the work on cobalt alloys and the titanium alloys is described in detail. However, for sake of completeness, the work done on stainless steel is reported as well; in the appendix two papers (one published in an international journal, another presented at an international congress) relevant to the austenitic and the precipitation hardened stainless steels are reported.

Most of the results presented here have already been published and presented at international conferences and national congresses. The full list of publications is reported at the end of this thesis.

CHAPTER 1

METAL INJECTION MOLDING (MIM)

1.1 Metal Injection Molding (MIM)

The MIM technique is a derivation of the injection molding of plastics. In MIM, metal powders are mixed with a polymer binder, injected into a mold and, after removal of the binder, sintered to produce very high density metal parts of almost any shape.

This technology was proposed for the first time on the industrial level 28 years ago. Thanks to the continuous development, MIM has been able to blossom into a mature commercial technique for the fabrication of small and complex shapes.

1.2 The Process

Figure 1 provides a schematic description of the MIM process [1].

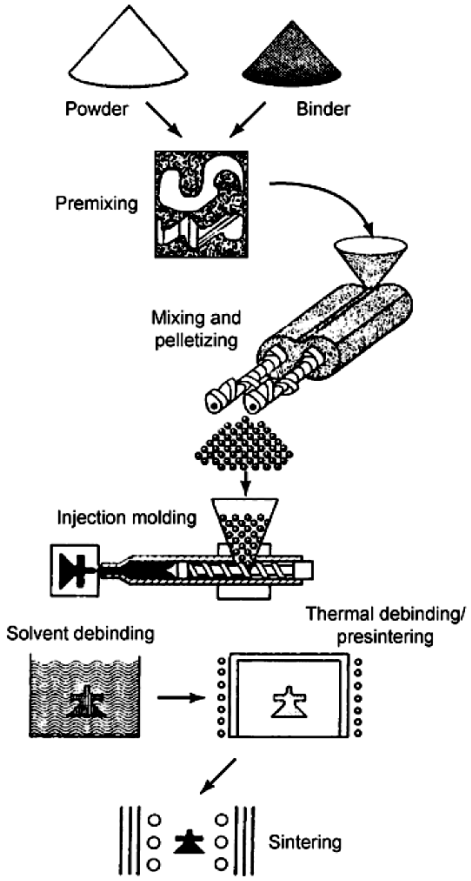

Figure 1: A schematic diagram of the MIM processing steps [1].

The powders are mixed with a binder which typically consists of waxes and polymers to produce a plastisol. This plastisol is granulated and forms a feedstock that can be molded by means of a commercial injection molding machine [2].

The MIM process can be divided in 4 steps:

- Mixing and pelletizing;
- Injection molding;
- Debinding;
- Sintering.

1.2.1 Mixing and pelletizing

Mixing of the feedstock is necessary to produce the plastisol suitable for injection molding. The goals in mixing are to coat the particles with the binder, to break up agglomerates, and to attain uniform distribution [3].

Mixing is carried out in either batch mixers, such as sigma-blade mixers, or in continuous mixers, such as twin screw extruders, at temperatures above the melting points of the binder components. Critical loading and mixing time are determined by torque measurements on a Brabender plasticorder [2].

The homogeneously mixed feedstock is cooled and formed into pellets for storage and transport [3]. This is necessary because in most cases the mixing station is separated from the molding machine and pelletization is used to prepare a uniformly sized material for the molding operation.

There are two objectives in granulating or pelletizing MIM feedstock. The first is to prepare easily transported clusters of feedstock which can be loaded automatically into the molding machine. The second is to incorporate recycled material back into the molding process. The recycled material comes from sprues, runners, and improperly molded parts (prior to debinding)[3].

Feedstock characteristics

In MIM, the powders used are much finer than those in conventional P/M technology. Particle size is usually <20 μm, and for metal powders, it has an average size of 5-10 μm. This is a good way to promote homogeneous dispersion of the particles in the mixed feedstock in such a way that it has the correct combination of flow and viscosity under injection molding conditions for uniformity of die filling. Moreover, since the sintering rate is inversely proportional to the fourth power of the particle size, sintering and densification of the part will occur more quickly [2].

A high loading volume of powders (approx. 60% for metals) with an acceptable flow will minimize the debinding schedules and also improve the dimensional control, so the sintering shrinkage can be controlled more easily. Therefore the use of high packing density systems made up of multi-size spherical particles [4]

is necessary. This means that powders with either a very narrow or a very wide particle size distribution are preferred.

Gas and water atomized and carbonyl powders are the three more commonly used powders. For this process, the particle morphology is very important. In particular, for improve rheological properties of the feedstock, rounded and smooth particles, as produced by gas atomization or the carbonyl process, are needed. Sometimes more irregular powders are required to enhance the green strength and shape retention during sintering [5]; in this case water atomized powders should be considered. As a result the size and the geometry are the limiting factors in whether a material can be injection molded or not.

The success of MIM is mainly determined by the right choice of binder. It has to act as a flow and carrier medium for the high volume loading of fine powders during mixing and injection molding. The binder should feature good wettability of the powder for easy mixing, high strength of the molded material (green strength) and should prevent segregation during injection molding [2]. After molding, the binder has to be removed without impairing the integrity of the part or introducing any adverse effect on the properties of the product. Decomposition of the binder should be progressive. This combination of characteristics can only be obtained using several components to form a multi-component binder. In a general classification, there are five types of binders used in PIM, most of which are polymers [3]:

- Thermoplastics compounds;
- Thermosetting compounds;
- Water-based systems;
- Gellation systems;
- Inorganics.

1.2.2 Injection molding

The MIM equipment is the same as used for conventional injection molding of plastics, with small modifications to reduce wear and assure homogeneity during the plasification. Fig. 2 shows an overview of an injection molding machine [1].

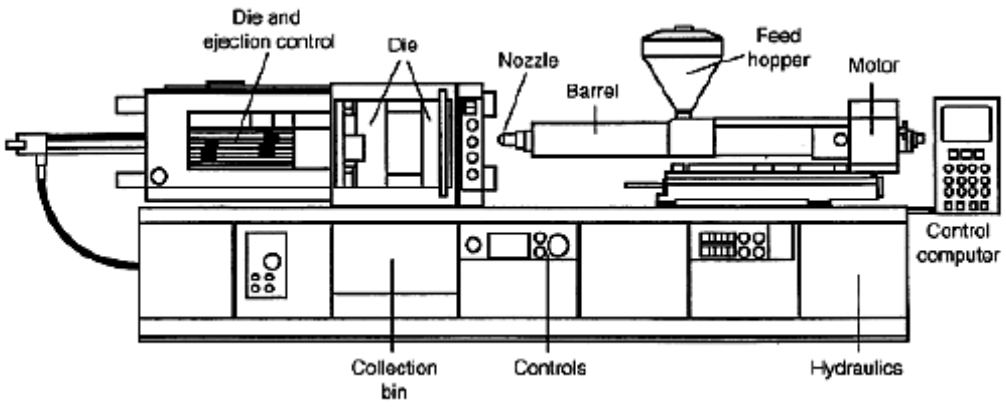

Figure 2: Overview of a horizontal injection molding machine and key components [1].

The time for molding depend on to cavity size, filling time, and cooling time. It can be as short as 5 s or as long as 1 min. First, in the classic molding cycle, the feedstock in the molding barrel is heated by a combination of external heaters and mechanical plasticization by the screw. Next, the mold is filled by moving the screw forward to inject the charge into the cavity at a rate that avoids jetting. With a high filling rate the feedstock shoots across the die. Combinations of high pressures, low viscosities, and rapid die filling rates that lead to jetting must be avoided [3]. However, if the speed is too low, it can result in incomplete filling due to premature feedstock freezing. So, a progressive mold filling is most desirable. In general the molded green parts are typically 17-22% larger (linear) than the final components [2].

Ejection and handling of the molded parts are complicated in the MIM process. Since the powder loading of the plastisol is very high, the injected material will be very brittle. This problem is less apparent for the polymer based binders than for the wax based ones. As a result, molding of complicatedly shaped and delicate parts with wax based binders requires proper location and sizing of the ejector and a high quality surface finish in the opening directions [6]. The molding machine should have the capacity to vary ejection speed in a few steps, so that the initial movement of the pins can be very slow in order to minimize changes of fracture [7].

In order to guarantee quality of the injection molded products and to be able to use statistical process control, closed-loop injection machines are essential [2].

The MIM process has some problems, and one of them is the packing inhomogeneities due to uneven die filling resulting in non-uniform dimensional changes. The defect population in the compact and the occurrence of distortions in sintering is highly dependent on the molding step. Therefore to have success when performing an analysis of the molding process, it is necessary to know the viscosity as a function of temperature, pressure, and shear rate. Likewise, to minimize residual stresses, it is important to do a thorough thermal characterization of the material [3].

1.2.3 Debinding

Debinding is the process where the binder is removed from the component prior to sintering. Compact cracking is a result of a failure in the step of debinding. Removal of the binder without have the particles disrupted is a delicate process that is best achieved in several steps. Initially the binder holds the particles together. When the binder is heated it softens and is unable to withstand shear stress from gravity, thermal gradients or internal vapor pockets. To retain compact shape an inherent particle-particle friction is needed. The binder must be extracted from the pores as a fluid (liquid or vapor) without distorting or contaminating the compact [3].

In figure 3, an idealized debinding process is depicted in a compact formed from monosized spheres.

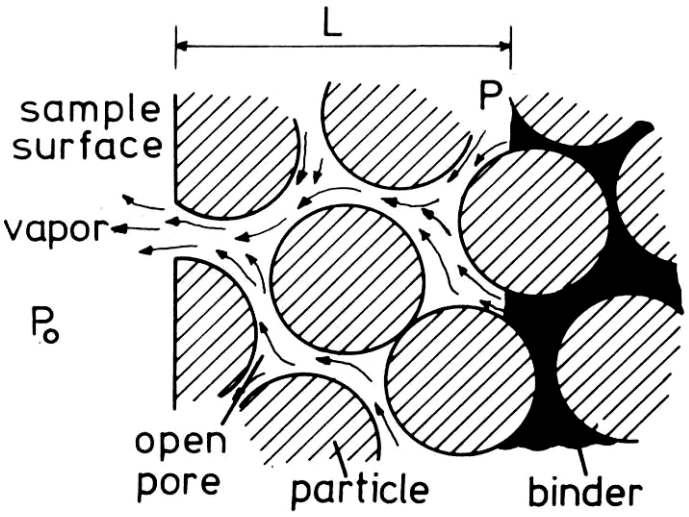

Figure 3: Debinding process for monosized spheres [3]

There are six debinding techniques, consisting of solvent and thermal processes, as listed below:

Thermal debinding:

- Diffusion (low pressure)
- Permeation (high pressure)
- Wicking (capillary flow)

Solvent debinding:

- Extraction (immersion)
- High pressure (supercritical)
- Thermally assisted (heat and solvent)

Thermal debinding is the easiest to envision. The component is slowly heated to decompose the binder.

One key to debinding is to use a multiple component binder system that decomposes progressively over a number of steps, so that removing a first binder constituent leaves a sufficient quantity of a second constituent to hold the particles in place.

The most popular approach is to immerse the component in a solvent that dissolves some binder, thereby leaving some polymer behind to hold the particles in place for subsequent handling and an open pore structure for subsequent debinding by evaporation. The remaining binder is thermally extracted in a further step before sintering. After complete debinding the compact material is called “brown”. For thermal debinding the binder can be removed in a gaseous form either by diffusion or permeation following thermal decomposition, or by chain scission or depolymerization.

Some binders are water soluble, so the debinding solvent is water. Major growth occurs in the use of catalytic phase erosion for debinding. Most of the binder is attacked by a catalytic vapor, and the residual

binder is removed during heating to the sintering temperature. This can now be performed as a continuous process at the beginning of sintering. Debinding is highly variable as to binder system, technique, and section thickness.

Solvent and catalytic debinding ensure the best dimensional control, because the binder is kept rigid during extraction. For these techniques penetration rates of 1 to 2 mm/h are common.

1.2.4 Sintering

Sintering is the final step in the MIM process, which can be incorporated directly into a thermal debinding cycle. Sintering bonds the powder particles together when heated to high temperatures, leading to densification. On a microstructural scale this bonding occurs as cohesive necks (weld bonds) grown at the points of contact between particles [3].

Figure 4a shows necks formed between sintered nickel spheres. Such a neck growth causes all of the important property changes associated with sintering. Figure 4b shows the microstructural changes when the necks between the particles grow (necks enlarge and merge).

The fact that the powders used are much finer in MIM than those used in PM means that sintering takes place more readily by reason of the higher surface energy of the particles [8]. Often sintering serves the dual role of densification and chemical homogenization, when elemental powders or masteralloys are used to produce an alloy.

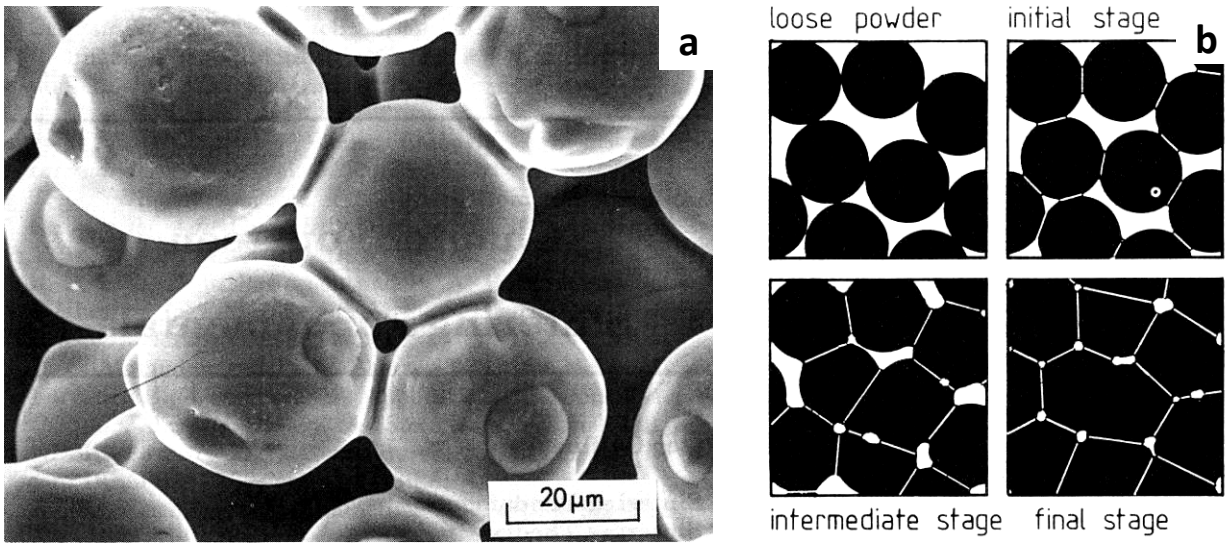

Figure 4: Neck formation (a) and microstructure changes when necks growth (b) [3]

As the “brown” part is extremely porous, a very large shrinkage occurs during sintering, as shown in figures 5a and b (the components shrink 17-22%, but tolerances are 0.3% on average and can be as low as 0.1% [2]), and the sintering temperature must be very closely controlled in order to retain the shape and prevent

'slumping'. Usually sintering shrinkage is uniform and isotropic, so the molded component is oversized to obtain the desired final dimensions.

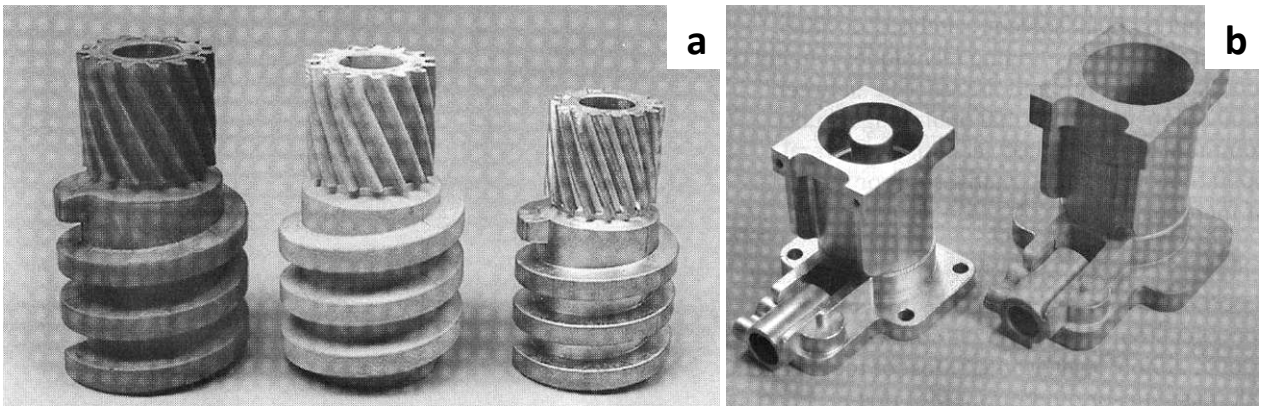

Figure 5: Examples of sintering shrinkage: (a) a demonstration steel automotive seat gear showing the shape after molding (left – green part), after thermal debinding (center – brown part) and after sintering (right); and (b) a solenoid valve body after molding (right – green part) and sintering (left – brown part) [9].

For the sintering process it is essential that all binder residuals are removed during the initial sintering stages. If binder residues, mainly graphite and tar, are left when the pores are closed, they will be incorporated in the final specimens [2].

Figure 6 shows the difference in the dimensional scatter between conventional PM and the MIM process. The MIM technology presents a very higher dimensional control than PM process after sintering.

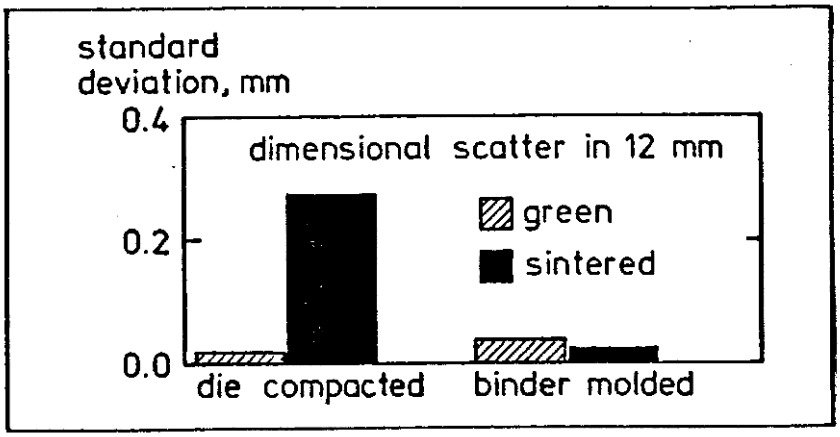

Figure 6: Comparison between die compacted and binder molded.

Using different gas atmospheres, the properties of the components can be modified. For metals, sintering is performed in a protective atmosphere or vacuum at a peak temperature that causes rapid elimination of the pores. Steels and stainless steels are sintered in the 1120 to 1350 °C range for 30 to 120 min, with

shrinkages of 12 to 18%. If the powder structure is formed homogeneously, then sintering is uniform and final dimensions can be held to close tolerances [1].

After sintering, the component has excellent strength, with properties near or even superior to those available from other processing routes. The density is close to the theoretical one, usually greater than 95%. Final densification can be assisted by both hot and cold deformation, including hot isostatic pressing.

Other post-sintering steps include coining, drilling, reaming, machining, plating, passivation, and heat treatment. Options in heat treatment include tempering, precipitation hardening, nitriding, and carburizing.

1.3 Advantages of MIM

The main benefits of this technique are [2]:

- Shape complexity: a wide range of geometry options, as in the plastic molding industry (see figures 7a and b) is available;
- Near net shape processing: complex parts consisting of a number of surfaces at different angles can be produced in one single step usually without machining (see figures 7a and b);
- Materials and properties: the materials are much denser (>95%) in comparison to conventional PM products, and the few remaining pores are small, isolated and spherical in shape. Compared with the as cast materials, this technique produces materials of excellent microstructural quality, characterized by finer grain sizes and absence of segregations;
- Cost efficiency: the near net shape capability of MIM reduces the machining cost to almost zero. For the production of large series (10000 or more) of small complex components (<100 grams) MIM offers the possibility to manufacture parts with cost savings up to 80%.

These features make MIM particularly suitable for complex, net shape components in many different areas where high demands are made upon material properties such as fatigue strength, toughness, magnetic properties and resistance against corrosion, wear and biocompatibility.

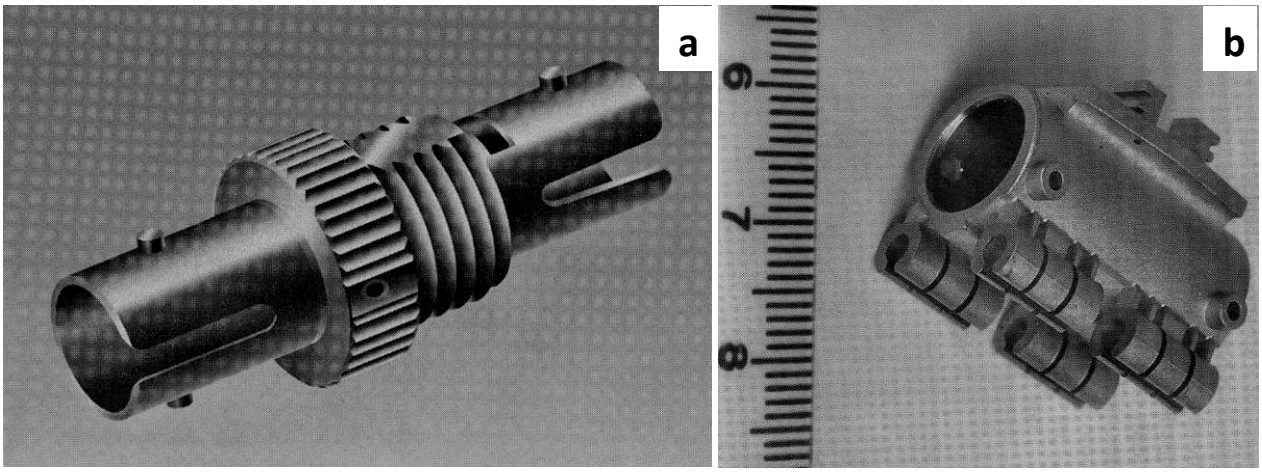

Figure 7: Examples of MIM parts: (a) A fiber optic connector and (b) Pivot hub for use in a computer hard disk drive, in both cases the parts are fabricated from stainless steel [9].

1.4 Process Limitations

MIM presents limitations in producing shapes with relatively simple or axial-symmetric geometries, this process is not cost-competitive with traditional die compaction and sintering. Also, the availability of suitable powders limits the current materials selection.

Other limitations relate to equipment size and equipment sophistication.

Because the time for binder removal depends on the square of the section thickness, formation of thick cross-sections remains a problem with MIM [3]. Uneven flow during mold filling can generate gradients of density. This is a problem when the feedstock sees a series of thickness variations during molding. These density gradients cause subsequent component warpage or cracking in sintering [10].

Finally there is a shortage of personnel able to solve the various problems associated with uneven mold filling, large compacts, powder selection, dimensional control, rapid debinding, process optimization and process control.

1.5 Applications and Markets

Applications for metal injection molded components are everywhere. Same examples are listed below:

- Metal and wood drills with replaceable cemented carbide tips;
- Alumina and stainless steel spraying nozzles for dispersion of paints and aerosols;
- Steel rocker arms for automobile engine variable valve timing mechanisms;
- Stainless steel orthodontic brackets for straightening teeth;
- Iron-nickel soft magnetic alloy actuators and latches for hand disk drives;
- Tool steel handheld wire cutting tools;
- Titanium surgical scalpel holders.

These products cover a diverse range of materials and applications. Almost all of the current production is based on the following material groupings in terms of their primary functional characteristic:

- Biocompatibility (stainless steels, cobalt-chromium, titanium);
- Corrosion resistance (stainless steels, cobalt-chromium, nickel, titanium alloys);
- Heat dissipation (aluminum, copper, tungsten-copper, aluminum nitride);
- High density, high inertia (tungsten heavy alloys);
- Magnetic response (iron, iron-nickel, iron-silicon);
- Structural (stainless steels, low alloy steels, tool steels);
- Wear resistance (tool steels, alumina, cemented carbides, silicon carbides).

Figure 8 shows the relative partitioning of current sales by market segments; note that the sectors automotive, casting, industrial, and watch applications are much larger than most of the other areas [9].

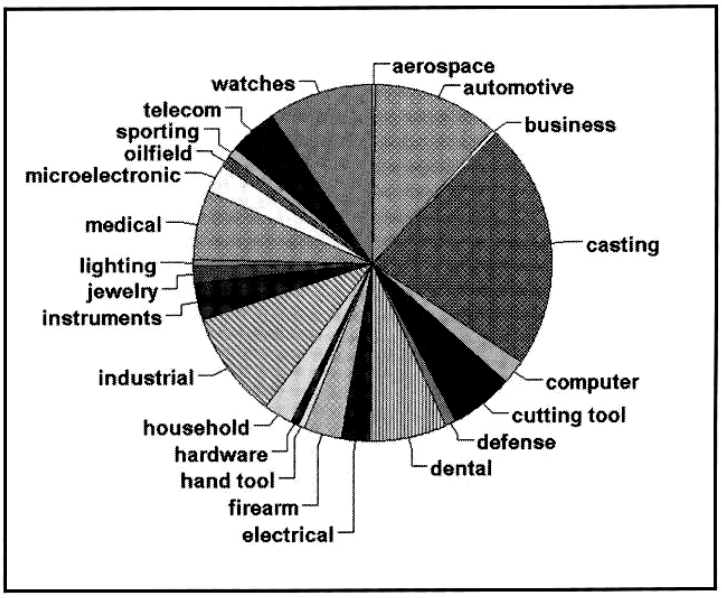

Figure 8: Relative partitioning of current sales by market segments [9]

Table 1 compares the materials parameters of MIM produced materials with others technologies. It can be seen that MIM products have a large number of "high" attributions than the others.

Table 1: Comparison between technologies.

Parameters	**MIM**	**Powder Metallurgy**	**Casting**	**Machining**	**Stamping**
Density	98%	86%	98%	100%	100%
Tensile strength	High	Low	High	High	High
Surface finish	High	Medium	Medium	High	High
Miniaturization	High	Medium	Low	Medium	High
Thin wall capability	High	Medium	Medium	Low	High
Complexity	High	Low	Medium	High	Low
Design flexibility	High	Medium	Medium	Medium	Low
Production quantity	High	High	Medium	Med-High	High
Range of materials	High	High	Med-High	High	Medium
Affordability	High	High	Medium	Low	High

Figure 9a is a plot of the sales expectations based on planned penetration into new markets such as sporting equipment, optical-electronic systems, sensors, instrumentation, and lighting. If the growth follows this pattern, MIM should easy exceed $2 billion in global sales by 2010 [9].

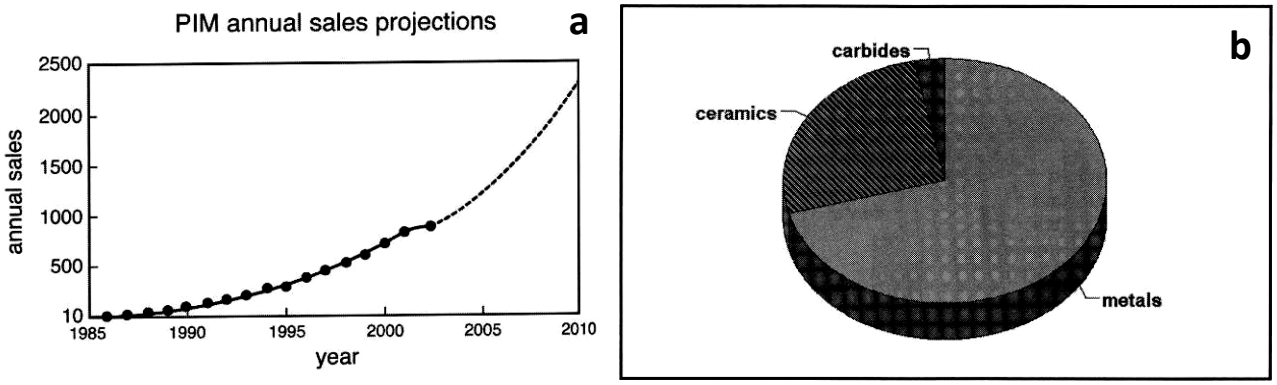

Figure 9: Linear plot of the past and future MIM sales extension up to 2010 (a), and partition of the sales activity over the three major classifications of MIM materials (b) [9].

With respect to the material, fig. 9b provides a similar pie chart, showing the values of the three main material classes. Metallic materials are dominant, followed by ceramics and carbides.

CHAPTER 2

COBALT AND ITS ALLOYS

2.1 Introduction

The metallic element cobalt appears as the middle member of the ferromagnetic trio, iron, cobalt, and nickel, which are from transition group VIII of the periodic table.

The Swedish chemist Brandt isolated the metal in 1735 and initiated the scientific study of the element, although its true element nature was not established until it had been extensively studied about 40 years later by Bergman [11].

Cobalt has a wide range of practical applications, but almost all of these involve its use as an alloying constituent or as a chemical compound; the pure metal has a few applications but is important as a metal for scientific study, being particularly characterized by its ferromagnetic properties with a uniquely high Curie point, its hexagonal crystal form at normal temperatures, transforming to cubic at higher temperature, and its low stacking-fault energy [11].

2.2 Properties of Cobalt

The physical and mechanical properties of metallic cobalt are particularly susceptible to variations due to the uncertain structure resulting from the sluggishness of the cubic-to-hexagonal transformation.

2.2.1 Atomic and nuclear properties

The atomic number of Co is 27 and the weight is 58,9332. The only naturally occurring isotope of Co, Co^{59}, is stable, but there are twelve other radioactive isotopes ranging in mass from 54 to 64. The isotope Co^{60}, by virtue of its reasonable half-life, is the most widely used source of radioactivity for such purposes as radiography, radiotherapy, food sterilization, etc.[11].

2.2.2 Crystal structure

Cobalt presents two allotropic modifications, a close-packed hexagonal form, ε (h.c.p. phase), stable at temperatures below about 400°C, and a face-centred-cubic form, α (f.c.c. phase), stable at higher temperatures. The temperature of the allotropic transformation depends critically on purity and on the rate of temperature change, but for the highest purity material (about 99,998%) and slow temperature change, the transformation temperature is 421.5°C [11].

The Gibbs energy change associated with the transformation is low, about 500 J mol^{-1} for $\varepsilon \rightarrow \alpha$ and about 360 J mol^{-1} for $\alpha \rightarrow \varepsilon$, and this accounts for the sluggishness of the transformation and its sensitivity to

experimental conditions. In particular the grain size affects the stability of the two allotropes, finer grain size favouring the cubic form; hence cobalt *powders* and sponge, or evaporated thin films or fibers, may retain the cubic structure at normal temperature. Even in normal solid cobalt subjected to some hot or cold deformation and subsequently annealed and slowly cooled to room temperature, the structure will not be entirely hexagonal. A fraction of metastable cubic phase may always be present [11].

The mechanism of the phase transformation is martensitic and proceeds by dislocation movements on the octahedral planes of the cubic lattice. These lead to the stacking sequence on these planes changing from *abcabc* characteristics of the cubic form, to *ababab* of the hexagonal form, so that the orientation relationship of the two phases is [11]:

$(111)\alpha \;//\; (0001)\varepsilon$

$(212)\alpha \;//\; (10\bar{1}0)\varepsilon$

The stacking fault energy of both allotropes is low.

The melting point of cobalt is 1495 ± 2°C.

2.2.3 Magnetic properties

Pure cobalt is distinguished by having the highest known Curie point, the temperature at which ferromagnetic materials lose this characteristic and become paramagnetic. For high-purity material with a cubic structure this temperature is 1121 ± 3°C compared with 770°C for iron. The hexagonal form of cobalt is ferromagnetic throughout the temperature range of its stability [11].

2.2.4 Hardness

The hardness at normal temperature of cobalt has been reported to be between 140 and 250 HV. For well-annealed samples of high-purity metal, the values are between 140 and 160 HV. The variation of hardness with temperature does not present an inflection at the transformation temperature. Microhardness measurements on zone-refined single crystals have given results critically dependent on crystal orientation, the values obtained varying from 81 to 250 HV. The low values are associated with deformation by slip on the basal planes of the hexagonal form, high values with twinning [11].

2.2.5 Tensile properties

For cobalt with a high purity and consolidated either by vacuum melting or powder metallurgy followed by hot working and annealing at temperatures of 800-1000°C, the tensile properties obtained are [11]:

0.2% proof stress	*Tensile strength*	*Elongation*
305-345 MNm^{-2}	800-875 MNm^{-2}	15-30%

Air-melted materials are much less ductile.

2.2.6 Frictional properties

In the restricted areas of true metallic contact, the structure of the metal can play a significant role. In these areas metals with hexagonal crystal structure can show lower values of friction and wear than cubic metals. Thus in measurements made in vacuum of the coefficients of friction between two samples of the same metal, all the face-centred-cubic metals had coefficients between 1.7 and 2.4, all the body-centred-cubic metals between 1.0 and 1.4, while for cobalt the coefficient was about 0.6. This low coefficient is due to easy slip on the basal plane, and is associated with the formation of a surface layer with the basal planes oriented parallel to the surface [11].

2.2.7 Chemical properties

In a massive form cobalt is resistant to many mild corrosive agents, but in a finely divided form it can be much more readily attacked. The rate of initial attack by any medium is very dependent on the form of the metal and the condition of the surface.

The corrosion rate of cobalt is found to be of the same order as that of nickel in many dilute media, but it is much less oxidation resistant than nickel over a wide temperature range.

Cobalt is vigorously corroded by concentrated nitric acid at room temperature but becomes passive at lower temperatures. Cobalt is more resistant than nickel in deaerated dilute hydrochloric acid.

Hydrogen is soluble in cobalt to an extent which increases with rising temperature from about 1 weight ppm at 700°C to about 8 weight ppm at the melting point. Oxygen is dissolved to a level of 60 weight ppm at 600°C, rising to 130 ppm at 1200°C but with an inflection at around 850°C. Nitrogen has been reported as being insoluble in solid cobalt but is soluble to the extent of 40 weight ppm at the melting point [11].

2.3 Constitution of Cobalt Alloys

A full understanding of the constitution and structure of the cobalt-containing alloys important in industry must be based on a study of the simpler binary and ternary systems from which more complex alloys were developed. Köster [12] was led to classify solute metals according to their influence on the transformation temperature; those solutes which raised the temperature being described as leading a restricted α-field and those lowering the temperature as giving an enlarged α-field. Köster's table of the effects of solute elements is given in table 2.

Table 2: Classification of solute elements in cobalt-rich binary alloys

Enlarged α-field	Restricted α-field	Combined
Al, B, Cu, Ti, Zr, **C**, Sn, Nb, Mn, Fe, Ni.	Si, Ge, As, Sb, **Cr**, **Mo**, W, Ta, Re, Ru, Os, Rh, Ir, Pt	Be, Pb, V, Pd, Ga, Au

The elements that have the greatest effect in raising the transformation temperature are silicon, **chromium**, arsenic, ruthenium, and osmium. On the other hand the elements that give maximum lowering of this transformation temperature are **carbon**, aluminium, iron and niobium.

2.3.1 Equilibrium diagram of cobalt-chromium

Figure 10 shows the equilibrium diagram for the cobalt-chromium system [11]. At the eutectic temperature of 1400°C α-cobalt dissolves about 38% of chromium, and the solubility remains almost constant with falling temperature, until at 960°C ε-cobalt starts to form. The solubility of chromium in cobalt then decreases, until at 700°C it is about 20%. At temperatures up to 1310°C the cobalt-rich solid solutions are in equilibrium with a **sigma phase** CoCr. Cobalt is soluble in chromium to about 38% at 1260°C, decreasing to about 10% at 800°C.

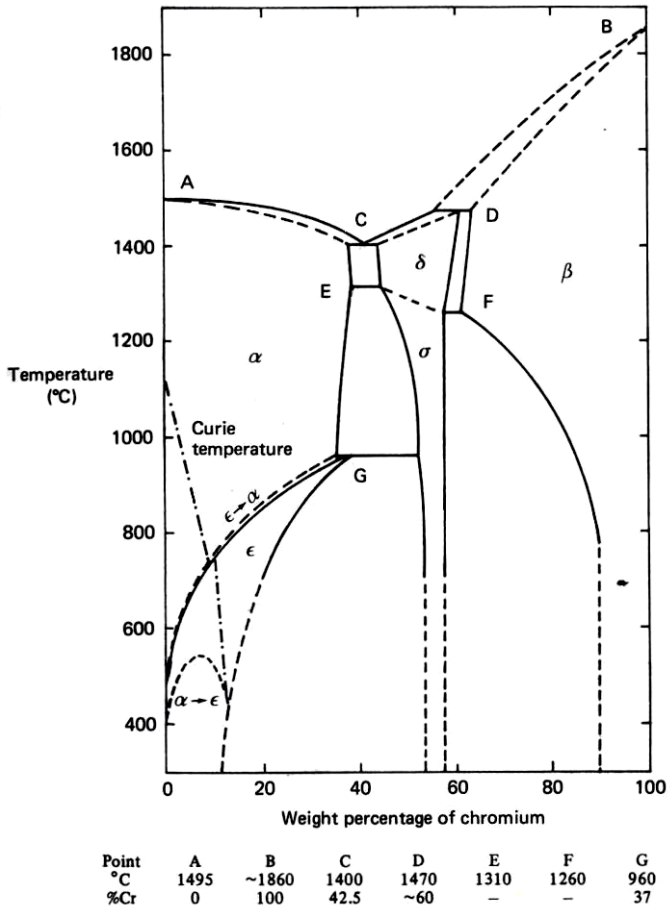

Point	A	B	C	D	E	F	G
°C	1495	~1860	1400	1470	1310	1260	960
%Cr	0	100	42.5	~60	–	–	37

Figure 10: Equilibrium diagram for cobalt-chromium system [11]

2.4 Cobalt-containing High-temperature Alloys

The major group of truly cobalt-base alloys is that consisting of the carbide-hardened cobalt-chromium high-temperature alloys in which the cobalt content lies within the range 40-70%. These alloys are mainly used in the cast form.

Alloys for use at elevated temperature require two main characteristics: first, adequate resistance to corrosion attack by the environment in which they have to operate, and second, sufficient mechanical strength to resist deformation or fracture under the stress imposed.

The earliest significant application of cobalt in high-temperature materials was the use in the late 1920s of cobalt-chromium-tungsten alloys termed 'Stellites' for the protective coating of the seats of aircraft piston-engine exhaust valves. These alloys present a high hot hardness and good wear resistance, coupled to the ease of deposition by gas welding [11].

Cobalt alloys were introduced to what is now termed the superalloy field largely on account of the well-established suitability of the **cobalt-chromium-molybdenum** alloy termed 'Vitallium' for the reproduction of complex shapes by precision lost-wax casting [11]. The alloy had been developed in the early 1930s for *dental prostheses* which were cast individually from wax models. After World War II, the lower-carbon Vitallium, HS21 (ASTM F75), was created for supercharger blades. Later, a similar alloy, HS31 (or X 40), was adopted in which the molybdenum content was replaced by tungsten and about 10% nickel added: it was adopted as the standard turbine blade material.

There are thus two main areas of interest to consider in relation to cobalt in superalloys – the cobalt-base carbide-hardened alloys mainly used in the cast form, but also as wrought sheet and as sintered; and the nickel-base γ'-hardened alloys used on both wrought and cast forms and containing 10-30% cobalt.

The cobalt-base carbide-hardened alloys have a cobalt-chromium matrix with about 20% chromium, which provides the major resistance to high-temperature corrosion. The carbon content lies in the range 0.25-1% for casting alloys, but is reduced to 0.05-0.4% for alloys to be hot worked in order to improve ductility [11].

2.5 Effect of Carbides in Cobalt-base Alloys

The strengthening of cobalt-base alloys is provided in part by solid-solution strengthening of the matrix, and in part by precipitation of carbides. The solid-solution strengthening is dependent on the amount of alloying elements not combined as carbides or, in a few instances, as intermetallic compounds, so that the two strengthening mechanisms are to some extent interdependent. Solid-solution strengthening is principally due to the content of *chromium*, tungsten, niobium, and tantalum, while nickel, when present, makes some contribution, but is mainly regarded as stabilizing the cubic structure and thus avoiding instability associated with the hexagonal transformation. The second-phase strengthening in cobalt-base is almost due to carbides or carbonitrides formed by **chromium**, which is primarily present to confer corrosion resistance, and other elements added as carbide formers – these may include tungsten, **molybdenum**, niobium, tantalum, zirconium, vanadium, and titanium. Carbides are usually mixed carbides in which the metal radical includes more than one of the elements listed above, and the forms reported include MC, **M_6C, M_7C_3, $M_{23}C_6$** and occasionally M_2C_3. The forms present in any alloy will depend on the

balance of metallic composition, on the carbon content, and on the thermal history of the alloy. Nitrogen may, in part, substitute for carbon in most of the above carbides [11].

The morphology and location of the carbide precipitates influence the strengthening effect and, for optimal improvement, precipitation both in grain boundaries and within the grains is required. At the grain boundaries the precipitates prevent gross sliding and migration of the boundaries, and when present in sufficient quantities may form a skeletal network which can support some of the imposed stress. Intragranular precipitation strengthens the matrix by providing obstacles to the movement of dislocations and thus inhibiting slip. The distribution of carbides is determined in any alloy by the solidification conditions [11].

A typical microstructure of such an alloy is shown in figure 11a. Additional carbide precipitation, both at grain boundaries and within the grains, occurs on heating to typical service temperatures for extended periods. This is shown in Fig. 11b for alloys HS 21 after 24 hours at 870°C.

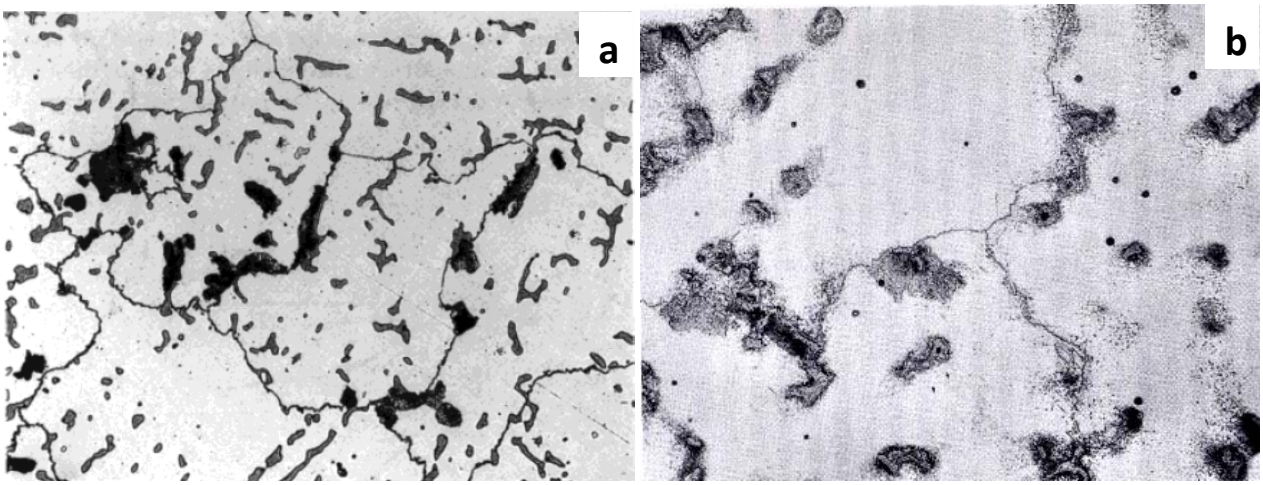

Figure 11: Typical as cast microstructure of HS 21 alloy, original magnification 100x [13] (a) and microstructure of HS 21 after 24 hours at 870°C, magnification 500x (b) [11]

Full solution of the primary carbides is not possible in most cobalt-base alloys since melting would occur before complete solution of the more stable carbides was achieved. The microstructure of a typical wrought cobalt-base superalloy in the solution-treated condition therefore normally shows the presence of undissolved primary carbides, largely at the grain boundaries, while after ageing or after a period of high-temperature service additional fine intergranular carbides precipitates are visible [11].

2.6 Cobalt-base Alloys for Biomedical Applications

Cobalt-base alloys were first used in the 1930s as said before. The Co-Cr-Mo alloy Vitallium was used as a cast dental alloy and then adopted to orthopedic applications starting in 1940s. The corrosion resistance of this alloy is more than an order of magnitude greater than that of stainless steel, and it possesses high mechanical property. The four main alloys used are [14]:

- *ASTM F75, a Co-28Cr-6Mo casting alloy*
- ASTM F90, a Co-20Cr-15W-10Ni wrought alloy
- ASTM F799, a Co-28Cr-6Mo thermomechanically processed alloy with a composition nearly identical to ASTM F 75
- ASTM F 562, a Co-35Ni-20Cr-10Mo wrought alloy

In order to produce wrought cobalt-chromium alloy, carbon must be reduced compared to the level in cast alloys (0.05% versus approximately 0.25% or higher). Low carbon contents mean that less strengthening is produced by carbides.

Alloys produced for structural applications such as hip prostheses can be forged if optimal properties are desired; this process results in maximum strength and toughness for cobalt-chromium alloys but may not produce uniform grain sizes. These alloys are difficult to machine, closed-die forging can minimize machining requirements, but wrought components still may require more machining than cast components. Consequently, investment casting often is used to produce cobalt-chromium implants at lower cost [14].

The preferred method to produce implants of cobalt-base alloy will be a function of the trade-off between cost and properties. Where the properties of casting are sufficient, casting will dominate, when maximum strength is required, hot pressing and/or forging will rule. Table 3 shows some mechanical properties of these alloys [14].

Table 3: Typical properties of cast and wrought cobalt-base alloys [14].

ASTM designation	**Condition**	**Young's modulus, GPa**	**Yield strength, MPa**	**Tensile strength, MPa**	**Fatigue endurance limit (at 10^7 cycles, R=-1)**
F75	As-cast/annealed	210	448-517	655-889	207-310
	PM HIP(a)	253	841	1277	725-950
F799	Hot forged	210	896-1200	1399-1586	600-896
F90	Annealed	210	448-648	951-1220	Not available
	44% cold worked	210	1606	1896	586
F562	Hot forged	232	965-1000	1206	500
	Cold worked, aged	232	1500	1795	689-793(b)
(a) PM: HIP, hot isostatic pressing. (b) Axial tension, R=0,05, 30 Hz.					

MIM is another technology used to produce this alloys. The main attributes that make MIM a competitive technology versus investment casting and machining is cost. Applications such as femoral components, tibial trays, and cable crimps, represent a challenge in terms of their size, material performance, and biocompatibility issues [15].

2.6.1 ASTM F75

Commonly used commercial/proprietary names to describe this alloy include Vitallium and Haynes 21 (HS21). Cobalt-chromium-molybdenum-carbon alloys are used in aircraft engines and surgical implants. These alloys are known for high strength and good wear resistance, but their main attribute is the corrosion resistance in chloride environments, which is related to their bulk composition (principally the high chromium content) and the surface oxide (nominally Cr_2O_3).

When F75 is cast into shapes by investment casting, the alloy is melted at 1350 to 1450°C and then poured into ceramic molds [16].

In the case of the F75 produced by MIM, the sintering behavior of this alloy is of critical importance to obtain a high performance product. Some of the variables affecting the sintering response of this alloy are the starting particle size, chemistry, and the sintering atmosphere [15].

The high sintering temperature in a MIM process is needed to obtain a high sintered density (more than 95%) and a homogeneous microstructure.

Within the relatively broad ASTM F75 chemistry specification it is important to note that minor variations in levels of carbon can lead to significantly different sintering response and, hence, can affect density and mechanical properties. From a sintering standpoint, process control is much easier for a material containing little or no carbon, versus one requiring carbon within a tight tolerance. However, it is known that carbon is required to impart strength in F75, hence, process control is expected to be a challenge with respect to the sintering atmosphere [15]. A higher carbon content (0.3-0.35% C) promotes the formation of eutectic liquids which activate sintering; therefore sintering temperature is lower than in the case of a low carbon alloy [17].

As-cast F75 alloy typically has a fcc matrix (cubic phase), while as sintered F75 is usually hexagonal. The microstructure presents interdendritic and grain- boundary carbides (primarily $M_{23}C_6$, where M represents chromium or molybdenum). There can also be interdendritic cobalt and molybdenum-rich sigma intermetallic and cobalt-base gamma phases [14].

If nonequilibrium cooling occurs during solidification, a cored microstructure can arise. In this situation, the interdendritic regions result solute (chromium, molybdenum, carbon) enriched and contain carbides, while dendrites become chromium depleted and richer in cobalt. This is an unfavorable electrochemical situation, with the chromium-depleted regions being anodic with respect to the rest of the microstructure. Coring also results in small differences in the mechanical properties between the cobalt-rich dendrites and the chromium-rich interdendritic regions. Subsequent solution annealing heat treatments at 1225°C (2235°F) for 1 to 3 h can help alleviate the problems associated with coring [14].

A further feature of cast cobalt implant alloys is the extremely large grain size observed in the original castings. This problem is particularly severe in castings having a large cross section, because here any

chilling effect from the mold wall is quickly lost, and the remaining liquid solidifies slowly, resulting in coarse grain size [18]. The large grain size is a feature of MIM parts too.

Examples of microstructures of as cast, as sintered and wrought materials are shown in figure 12.

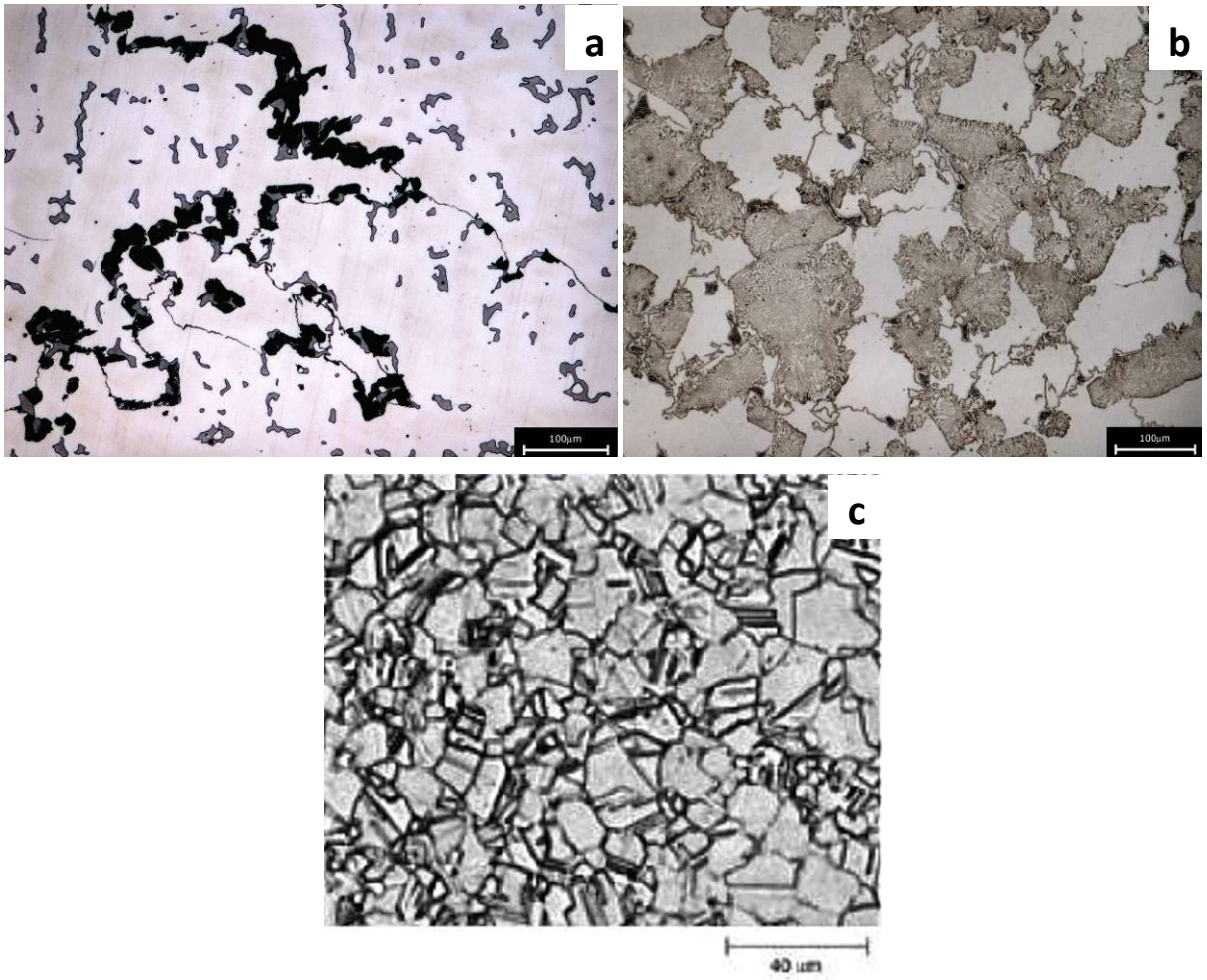

Figure 12: Microstructure of as cast (a) and as sintered (b) F75 alloys with 0.35%C. Microstructure of forged high-strength Co-Cr-Mo alloy (c) [19].

The influence of metal additions and carbide formation on strengthening was already discussed in section 2.4.

More details about the sintering temperature, carbon content, microstructures, heat treatments and mechanical properties of MIM F75 are described in the chapter of results.

2.6.2 Examples of biomedical applications

The Co-Cr-Mo alloys have their principal applications in bone and joint replacement, dental implants, dental restorations and heart valves. This alloy is popular primarily because of its ability to bear significant loads, withstand fatigue loading, and undergo plastic deformation prior to failure.

Total hip replacement (THR)

Femoral components (figure 13), usually are manufactured from Co-Cr-Mo or Co-Ni-Cr-Mo alloys or titanium alloys (see chapter 3). The ball is made either of highly polished Co-Cr alloys or of a ceramic. Modular designs, where the stem and ball are made of two different materials, are common. For example, hip replacement implants featuring a Ti alloy femoral stem will have a Co-Cr femoral head. Similarly, the UHMWPE (ultra high molecular weight polyethylene) socket of the common acetabulum replacement [14].

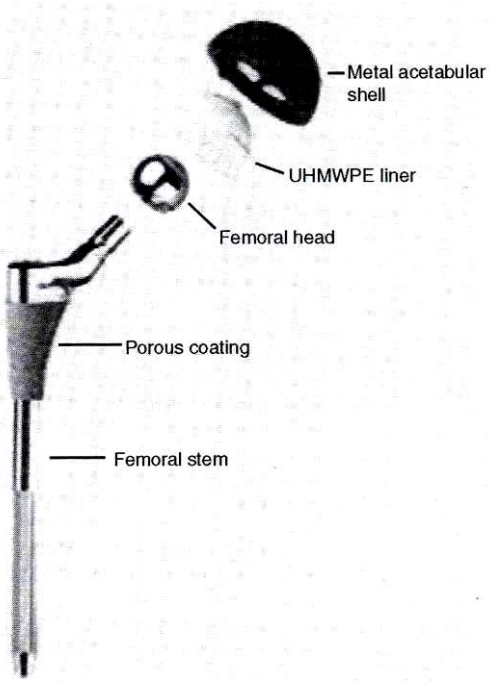

Figure 13: Unassembled THR implant.[14]

Table 4 lists some of femoral head-to-socket combinations that have been used for total hip replacement arthroplasty [14]. Cobalt-base alloys are the most commonly used alloys for current metal-on-polymer implants.

Table 4: Materials combinations in total hip replacement prostheses [20]

Femoral component	Socket component	Results
Co-Cr-Mo	Co-Cr-Mo	Early high loosening rate and limited use: new developments show lowest wear rate (THR only-in clinical use in Europe)
Co-Cr-Mo	UHMWPE	Widely employed: low wear
Alumina/zirconia	UHMWPE	Very low wear rate: zirconia more impact resistant
Alumina	Alumina	Minimum wear rate (components matched): pain-not in clinical use in the United States
Ti-6Al-4V	UHMWPE	Reports of high UHMWPE wear due to breakdown of titanium surface
Surface-coated Ti-6Al-4V	UHMWPE	Enhanced wear resistance to abrasion: only thin treated layer achieved

Total knee arthroplasty (TKA)

In the TKA the diseased cartilage surfaces of the lower femur (thighbone), the tibia (shinbone), and patella (kneecap) are replaced by a prosthesis made of metal alloys and polymeric materials, see figure 14 [14].

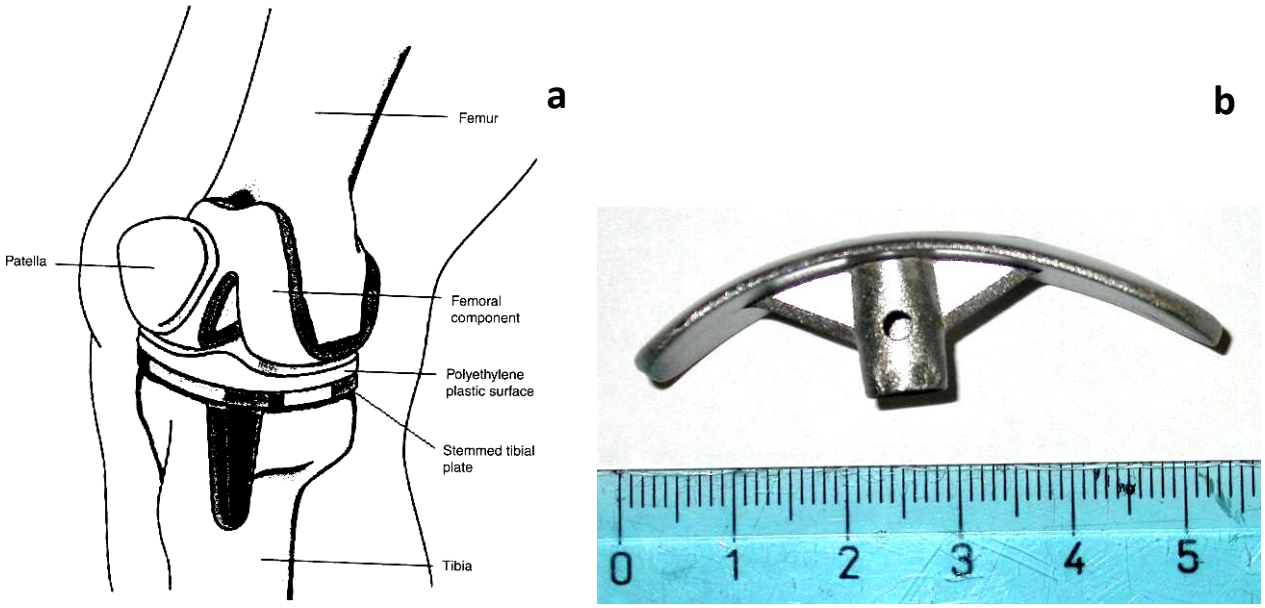

Figure 14: Components of a total replacement arthroplasty (a) [14] and the MIM femoral prostheses (b).

The metals parts of the implant are made of titanium alloys (Ti-6Al-4V) or cobalt-chromium alloys. The plastic parts are made of UHMWPE [14].

The principal requirements for each alloy in the biomedical device industry are the corrosion resistance when inserted in the body and optimal mechanical properties. The biocompatibility of pure metals and some metallic biomedical alloys are compared in figure 15, and it is seen that the Co-Cr alloys present a higher corrosion resistance and biocompatibility.

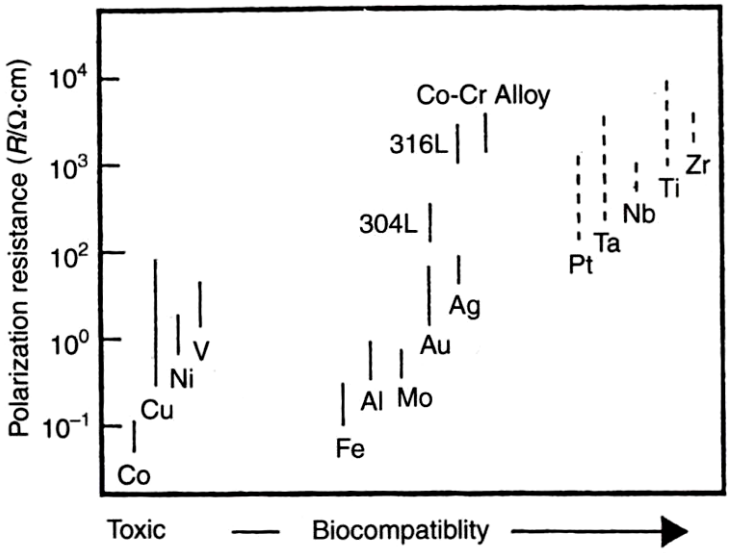

Figure 15: The relationship between polarization resistance and biocompatibility of same materials [21].

CHAPTER 3

TITANIUM ALLOYS

3.1 Introduction

Titanium is present in the earth's crust at a level of about 0.6% and is therefore the fourth most abundant metallic element after aluminum, iron, and magnesium. The most important mineral sources are ilmenite ($FeTiO_3$) and rutile (TiO_2) [22].

The first suspicion of a new, unknown element present in a dark, magnetic iron-sand (ilmenite) in Cornwall (UK) was expressed in 1791 by Gregor, a clergyman and amateur mineralogist. In 1795, Klaproth, a German chemist, named the element titanium after the Titans, the powerful sons of the earth in Greek mythology.

Many attempts were made to isolate the metal from the titanium ore introducing titanium tetrachloride ($TiCl_4$) as an intermittent step. The production of ductile, high purity titanium still proved to be difficult, because of the strong tendency of this metal to react with oxygen and nitrogen. Early demonstrations of the reduction of $TiCl_4$ using either Na or Mg produced small quantities of brittle titanium metal. It was not until well into the 20^{th} century (1937-1940) that a commercially attractive process was developed by Kroll in Luxembourg. This process involved the reduction of titanium tetrachloride with magnesium in an inert gas atmosphere. The resulting titanium is called "titanium sponge" because of its porous and spongy appearance. This famous Kroll process remained essentially unchanged and is the dominant process for titanium production today. Only 5% of the $TiCl_4$ production is used to produce titanium metal [22].

3.2 Properties of Titanium

Some of the basic characteristics of titanium and its alloys are listed in table 5 and compared with those of other structural metallic materials. Although titanium has the highest strength to density ratio, it is the material of choice only for certain niche application areas because of its high price. This high price is mainly a result of the high reactivity of titanium with oxygen. The use of inert atmosphere or vacuum is required during the production process of titanium sponge from titanium tetrachloride as well as during the melting process. The high reactivity with oxygen leads to the immediate formation of a stable and adherent oxide surface layer when exposed to air, resulting in the superior corrosion resistance of titanium in various kinds of aggressive environments, especially in aqueous acid environments. The high reactivity of titanium with oxygen limits the maximum use temperature of titanium alloys to about 600°C. Above this temperature the diffusion of oxygen through the oxide surface layer becomes too fast resulting in excessive growth of the oxide layer and embrittlement of the adjacent oxygen rich layer of the titanium alloy [22].

Table 5: Some important characteristics of Ti compared with those of other structural metallic materials [22].

	Ti	**Fe**	**Ni**	**Al**
Melting Temperature, °C	1670	1538	1455	660
Allotropic Transformation, °C	$\beta \xrightarrow{882} \alpha$	$\gamma \xrightarrow{912} \alpha$	-	-
Crystal Structure	bcc → hex	fcc → bcc	Fcc	Fcc
Room Temperature E, GPa	115	215	200	72
Yield Stress Level, MPa	1000	1000	1000	500
Density, g/cm^3	4.5	7.9	8.9	2.7
Comparative corrosion resistance	Very high	Low	Medium	High
Comparative reactivity with oxygen	Very high	Low	Low	High
Comparative price of metal	Very high	Low	High	Medium

3.2.1 Crystal structure

Pure titanium exhibits an allotropic phase transformation at 882°C, changing from the body-centred cubic crystal structure (β phase) at higher temperatures to the hexagonal close-packed crystal structure (α phase) at lower temperatures. The transformation temperature is strongly influenced by interstitial and substitutional elements and therefore depends on the purity of the metal. Figure 16a shows the hexagonal unit cell of the α phase indicating also the room temperature values of the lattice parameters a (0.295 nm) and c (0.468 nm). The three most densely packed lattice planes are indicated in figure 16a, too. [22].

The unit cell of the body-centred cubic (bcc) β phase is illustrated in figure 16b indicating also one variation of the six most densely packed lattice planes and the lattice parameter value of pure β titanium at 900°C (a_0 = 0.332 nm). [22]

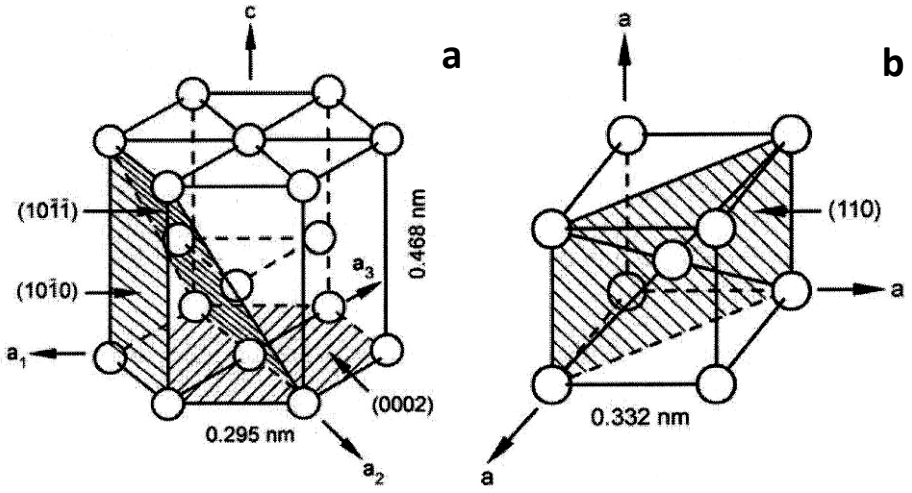

Figure 16: Unit cell of α phase (a) and β phase (b) [22]

3.2.2 Elastic properties

The intrinsically anisotropic character of the hexagonal crystal structure of the α phase has important consequences for the elastic properties of titanium and its alloys. The modulus of elasticity E of pure α titanium single crystals at room temperature is a function of the angle γ between the c-axis of the unit cell and the stress axis. The modulus of elasticity E varies between 145 GPa (stress axis parallel to the c-axis) and 100 GPa (stress axis perpendicular to the c-axis). Similar strong variations are observed for the shear modulus G of single crystals varying between 46 GPa and 34 GPa for shear stresses applied in $<11\bar{2}0>$ direction and in (0002) or $\{10\bar{1}0\}$ planes, respectively [22].

With increasing temperature, the modulus of elasticity (E) and the shear modulus (G) decrease almost linearly for polycrystalline texture-free α titanium [23]. It can be seen that E drops from about 115 GPa at room temperature to about 58 GPa at the β transus temperature, while G decreases from about 42 to 20 GPa over the same temperature range.

In general, commercial β titanium alloys have lower E values than α and α+β alloys. Typical values are 70-90 GPa for the as-quenched condition and 100-105 GPa for the annealed condition of commercial β alloys, 105 GPa for CP (commercially pure) titanium, and about 115 GPa for commercial α+β alloys [24].

3.2.3 Deformation modes

The ductile behavior of hexagonal α titanium, especially at low temperatures, results from the activation of twinning deformation modes in addition to conventional slip by dislocations. These twinning modes are important for the deformation behavior of CP titanium and some α titanium alloys. Although twinning is suppressed nearly completely in two-phase α+β alloys by the small phase dimensions, high solute content, and presence of Ti_3Al precipitates, these alloys are quite ductile at low temperatures due to their small grain size [22].

3.2.4 Phase diagrams

Alloying elements in titanium are usually classified into α or β stabilizing depending on whether they increase or decrease the α/β transformation temperature of 882°C of pure titanium.

The substitutional element Al and the interstitial elements O, N and C are all strong α stabilizers and increase the transus temperature with increasing solute content, as can be seen from the schematic phase diagram in fig. 17. Aluminum is the most widely used alloying element in titanium alloys, because it is the only common metal raising the transition temperature and having large solubility in both the α and β phases. Among the interstitial elements, oxygen can be considered as an alloying element in titanium in those cases where the oxygen content is used to obtain the desired strength level (for example different CP-Ti grades) [22].

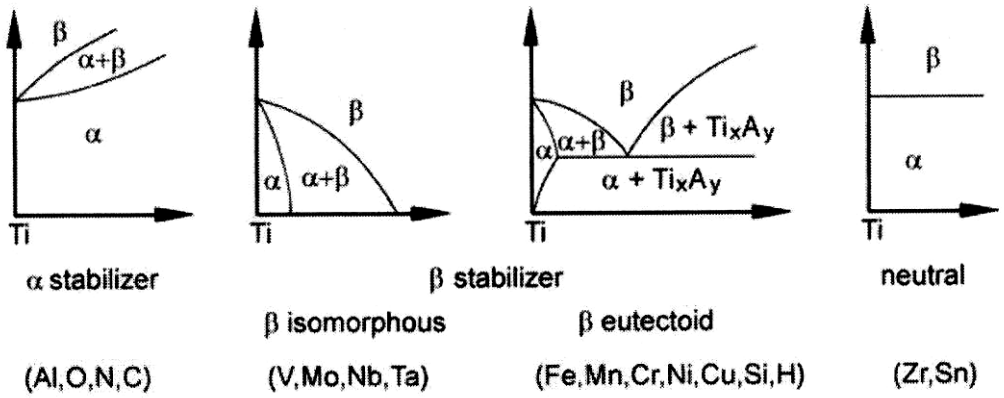

Figure 17: Schematically effect of alloying elements on phase diagrams of Ti alloys [22].

The β stabilizing elements are divided into β isomorphous elements and β eutectoid forming elements, depending on the resulting binary phase diagram. Both types of phase diagrams are shown schematically in figure 17. The most frequently used β isomorphous elements in titanium alloys are V, Mo, and Nb. Sufficient concentrations of these elements make it possible to stabilize the β phase at room temperature. From the β eutectoid forming elements, Cr, Fe, and Si are used in many titanium alloys. Hydrogen belongs to these β eutectoid forming elements and the low eutectoid temperature of 300°C in combination with the high diffusivity of hydrogen led to a special process of microstructure refinement, the so-called hydrogenation/dehydrogenation (HDH) process. Generally, the maximum hydrogen content in CP titanium and titanium alloys is strictly limited to about 125-150 ppm because of hydrogen embrittlement [22].

Zr and Hf are isomorphous with titanium and, therefore, both exhibit the same β to α allotropic phase transformation. These elements have complete solubilities in the α and β phases of titanium.

The binary Ti-Al phase diagram (figure 18) shows that with increasing aluminum content the Ti_3Al (α_2) phase will form and the two phase region (α + Ti_3Al) starts at about 5% Al for a temperature of about 500°C. To avoid any appreciable amount of coherent Ti_3Al precipitates in the α phase, the aluminum content in most titanium alloys is limited to about 6%. From figure 18 it can be seen that for an aluminum content of about 6% the α/β transformation temperature of 882°C for pure titanium is increased to about 1000°C for the two phase region (α+β). In addition to conventional titanium alloys, the Ti-Al phase diagram is also the basis for the so-called titanium-aluminides, which are recently developed alloys based on the two intermetallic compounds Ti_3Al (alpha-2 alloys and the orthorhombic variant, Ti_2AlNb alloys) and TiAl (Gamma alloys) [22].

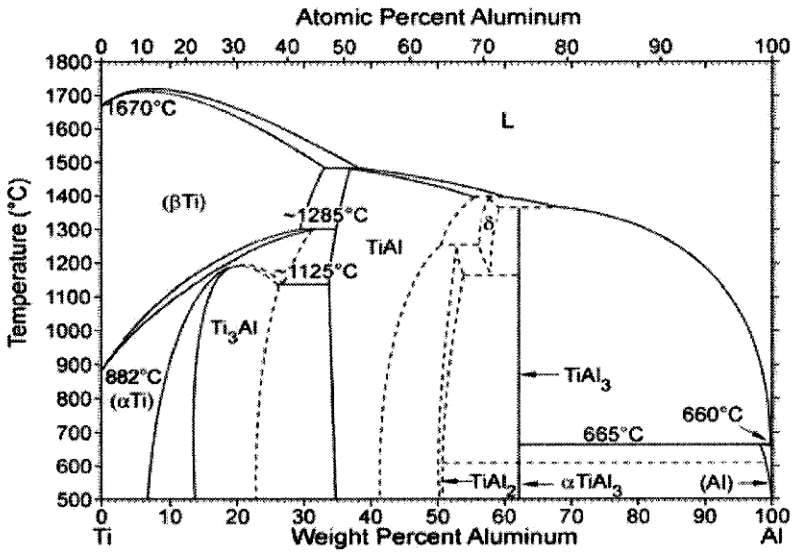

Figure 18: Ti-Al phase diagram [25].

Most commercial titanium alloys are multicomponent alloys. The equilibrium states of Ti-6Al-4V alloy at different temperatures are indicated by special points in figure 19. The addition of V decreases the (α + β)/α transus.

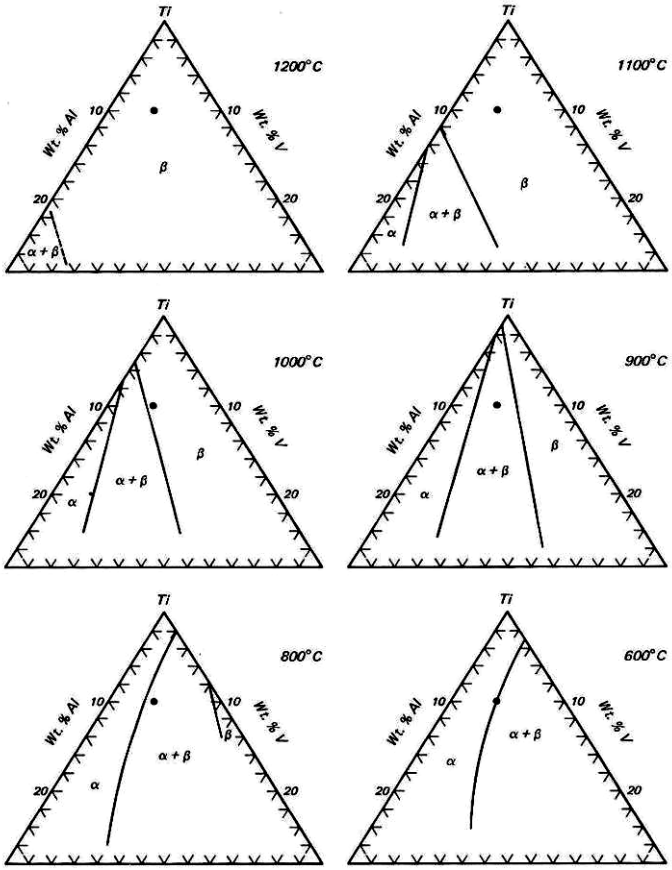

Figure 19: Isothermal sections of the Ti-Al-V versus T equilibrium-phase prism. The solid circle represents the alloy Ti-6Al-4V [26].

3.2.5 Phase transformations

The transformation of the bcc β phase to the hexagonal α phase in CP titanium and titanium alloys can either occur martensitically or by a diffusion controlled nucleation and growth process depending on cooling rate and alloy composition.

The crystallographic orientation relationship between α and β is named the Burgers relationship [22]:

$$(110)_\beta \,||\, (0002)_\alpha$$

$$[1\bar{1}1]_\beta \,||\, [11\bar{2}0]_\alpha$$

Martensitic transformation

The martensitic transformation involves the cooperative movement of atoms by a shear type process resulting in a microscopically homogeneous transformation of the bcc into the hexagonal crystal lattice over a given volume. The transformed volume is usually plate shaped or better described geometrically as disk shaped for most titanium alloys. This hexagonal martensite is designated as α' and is observed in two morphologies: massive martensite (other names: lath or packet martensite) and "acicular" martensite [27].

Massive martensite occurs only in pure titanium, very dilute alloys, and in alloys with a high martensitic transformation temperature. Figure 20a shows an example of "massive martensite", showing large colonies by optical microscopy (a) and individual plates within this colonies by electron microscopy (b).

"Acicular" martensite occurs in alloy with higher solute content (lower martensitic transformation temperature). Figure 20b shows the "acicular martensite", by optical microscopy (a) and the lenticular-shaped plates, some of which are internally twinned by electron microscopy (b).

Generally, the martensitic plates contain a high dislocation density and sometimes twins. The hexagonal α' martensite is supersaturated in β stabilizers and, upon annealing in the (α+ β) phase field, decomposes to α+ β by precipitating incoherent β particles at dislocations or β phase layers at plate boundaries [22].

With increasing solute content the hexagonal structure of the martensite becomes distorted and, from a crystallographic viewpoint, the crystal structure loses its hexagonal symmetry and must be described as orthorhombic [27]. This orthorhombic martensite is designated α".

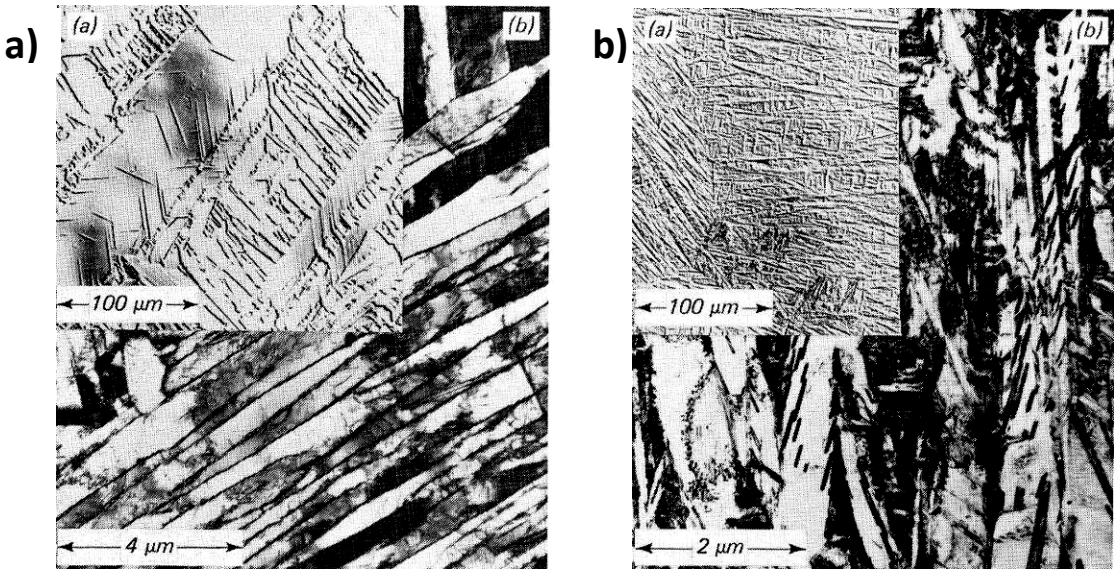

Figure 20: An example of "massive martensite" (a) and "acicular martensite" (b) [26].

Nucleation and Diffusional Growth

When titanium alloys are cooled at sufficiently low rates from the β phase field into the (α+β) phase field, the α phase, which is incoherent with respect to the β phase, first nucleates preferentially at β grain boundaries leading to a more or less continuous α layer along β grains boundaries. During continued cooling α plates nucleate either at the interface of the continuous α layer or at the β grain boundary itself and grow into the β grains as parallel plates [28] belonging to the same variant of the Burgers relationship (so-called α colony). They continue to grow into the β grain interior until they meet other α colonies nucleated at other grain boundary areas of the β grain and belonging to other variants of the Burgers relationship. This process is often called sympathetic nucleation and growth. The individual α plates are separated within the α colonies by the retained β matrix, which are commonly, but incorrectly, called β plates.

An example of such a microstructure which was obtained by slow cooling from the β phase field is show in figure 21 for the Ti-6Al-4V alloy.

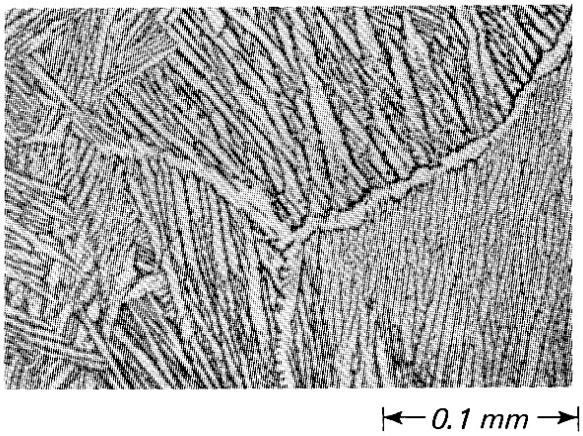

Figure 21: Lamellar α+β microstructure in Ti-6Al-4V slowly cooled from the β phase field [26].

With increasing cooling rate the size of the α colonies as well as the thickness of the individual α plates become smaller.

3.2.6 Alloy classification

Commercial titanium alloys are classified conventionally into three different categories (α, α+ β, and β alloys) according to their position in a pseudo-binary section through a β isomorphous phase diagram, schematically shown in figure 22.

The group of α alloys consists of the various grades of CP titanium and α alloys which upon annealing well below the β transus contain only small amounts of β phase (2-5 vol%) stabilized by iron. The β phase is helpful in controlling the recrystallized α grain size and improves the hydrogen tolerance of these alloys. The four different grades of CP titanium differ with respect to their oxygen content from 0.18% (grade 1) to 0.40% (grade 4) in order to increase the yield stress. The two alloys Ti-0.2Pd and Ti-0.3Mo-0.8Ni offer better corrosion resistance than CP titanium [22].

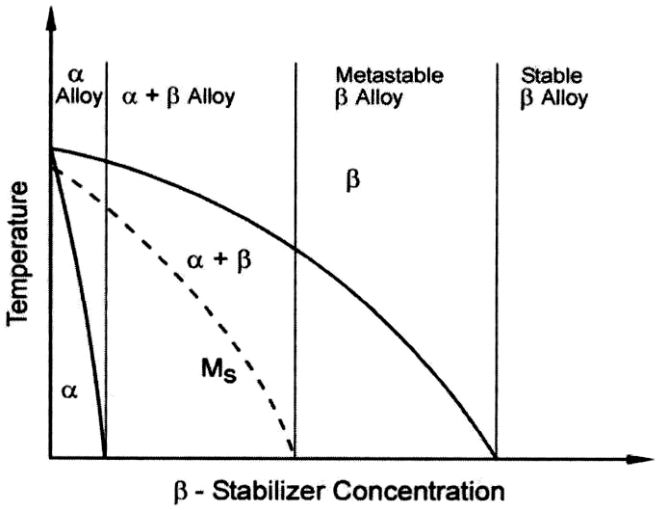

Figure 22: Pseudo-binary section through a β isomorphous phase diagram (schematically) [22].

The group of α+ β alloys has a range in the phase diagram (figure 22) from the α/α+ β phase boundary up to the intersection of the Ms-line with room temperature, thus α+ β alloys transform martensitically upon fast cooling from the β phase field to room temperature. Alloys which contain in equilibrium only a small volume fraction of β phase (less than about 10 vol%) are also often called “near α” alloys and their main usage is at high service temperatures [22]. The Ti-6Al-4V alloy contains in equilibrium at 800°C about 15 vol% β phase (see figure 19). This alloy has an exceptionally good balance of strength, ductility, fatigue, and fracture properties but can be used only up to temperatures of about 300°C. Alfa-beta alloys can be strengthened by solution treating and aging.

All alloys in the group of β alloys are actually metastable β alloys because they all are located in the equilibrium (α+ β) phase region of the phase diagram (figure 22). Since stable β alloys located in the β single

phase field (figure 22) do not exist as commercial materials, the expression β alloys is commonly used for the metastable β alloys.

The feature of the β alloys is that they do not transform martensitically upon fast cooling from the β phase field.

3.2.7 Hardening mechanisms

Two hardening mechanisms are active in all commercial titanium alloys: solid solution and precipitation hardening. These mechanisms are different for α and β phases.

Grain boundary hardening plays a significant role in $\alpha+\beta$ alloys cooled at high rates from the β phase field reducing the α-colony size to a few α plates or causing martensitic transformation. In both cases, a high dislocation density is created which also contributes to hardening [22].

3.2.8 Corrosion behavior

In the galvanic series of metals, titanium has a standard potential of -1.63 V which is close to aluminum. Therefore, titanium cannot be considered as being intrinsically noble. The excellent resistance of titanium to general corrosion in most environments is well-known. This is the result of a stable protective surface film, which consists basically of TiO_2. This thin oxide film passivates titanium as long as the integrity of the film is maintained. In general, this is the case in most oxidizing environments, for example in salt solutions, including chlorides, hypochlorites, sulfates, and sulfites, or in nitric and chromic acid solutions. On the other hand, titanium is not corrosion resistant under reducing conditions, where the protective nature of the oxide film breaks down. Consequently, the corrosion resistance of titanium in reducing environments, such as sulfuric, hydrochloric, and phosphoric acids, is not good [29].

Passivated titanium is highly corrosion resistant in flowing seawater at room temperature having a potential close to that of Hastelloy, Inconel, Monel, and passive austenitic stainless steels [30]. Therefore, titanium has a much greater resistance to pitting corrosion than the materials just mentioned. The resistance to pitting corrosion of titanium is generally very high because of its protective oxide film and the virtual absence of inclusions. The CP titanium exhibits higher resistance to pitting corrosion than other titanium alloys and this resistance is better in some β alloys, including Beta C and Beta 21S, than the $\alpha+\beta$ Ti-6Al-4V alloy.

The good general corrosion resistance of unalloyed titanium is also observed for α+ β and β alloys. From an economic standpoint (cost, formability, weldability) CP titanium grades are preferred in applications that do not require higher strength levels [22].

The resistance to general corrosion of the higher strength α+ β and β titanium alloys has been evaluated in a reducing acid environment by Schutz [31]. These results show that alloy contents of more than 3% Mo and 8% Zr are exceptionally beneficial, vanadium is of minor importance, but Al levels above 3% are increasingly detrimental.

The resistance to crevice corrosion of Ti-6Al-4V is similar to that of CP titanium grade 2, whereas the β titanium alloys Beta C and Beta 21S show a better resistance to crevice corrosion in most aggressive environments [31].

The combination of corrosive environment and applied stress can cause the degradation of some important mechanical properties. The tensile ductility can be reduced if crack nucleation is shifted to the specimen surface, cracks connected to the surface can propagate under constant load conditions (stress corrosion cracking), and in fatigue loading surface cracks can nucleate and propagate at lower stress amplitudes as than in inert environment (corrosion fatigue).

3.3 Fabrication Aspects

3.3.1 Melting

Melting technology is used to produce ingots which are the starting materials for both mill products and remelt stock for titanium casting. Resolidification of the molten metal is the key to obtain homogeneous, high quality ingots for conversion to mill products [22].

Titanium and its alloys are melted either in a vacuum arc remelting (VAR) furnace or in a cold hearth melting (CHM) furnace.

The principal melted defects known in titanium are: type I (“hard alpha”) also called high interstitial defect (HID), high density inclusions (HDIs), beta flecks, type II (alpha stabilized) and voids.

After the melting process and before hot working, the ingot undergoes conditioning. This process creates a smoother ingot surface that is free from stress concentrators.

Once the ingot is melted and conditioned, it is normally given a homogenization anneal in the β phase field prior to working. Time and temperature for homogenization are alloy dependent, but they are typically 200-450°C above the beta transus for 20-30 hours.

3.3.2 Shaping

Shaping of titanium mill products into actual components is accomplished by mechanical deformation operations such as forging or ring rolling to create rough shapes with the desired properties. These shapes are finished by mechanical metal removal (milling, turning, and drilling) to improve feature definition and reduce weight of the final component.

3.3.3 Near net shape process

One approach to realize a high raw material utilization uses the net shape technologies (casting, powder metallurgy, laser forming, conventional sheet forming, and superplastic forming and diffusion bonding).

Powder Metallurgy and MIM:

The powder cost limits the range of potential applications for Ti parts. This is because the reactivity of Ti with oxygen essentially precludes production of gas atomized powder. Direct gas atomization of molten titanium is not possible on a large scale using an atomization process analogous to that currently being used for Fe, Ni and Cu base alloys. The powder particles are small, spherical and exhibit smaller secondary spheres, called satellites, which are attached to the larger powder particles during atomization, see figure 23a.

Other kinds of powders used are Al6-V4 master alloy and TiH_2 (HDH titanium), which morphology are shown in figure 23.

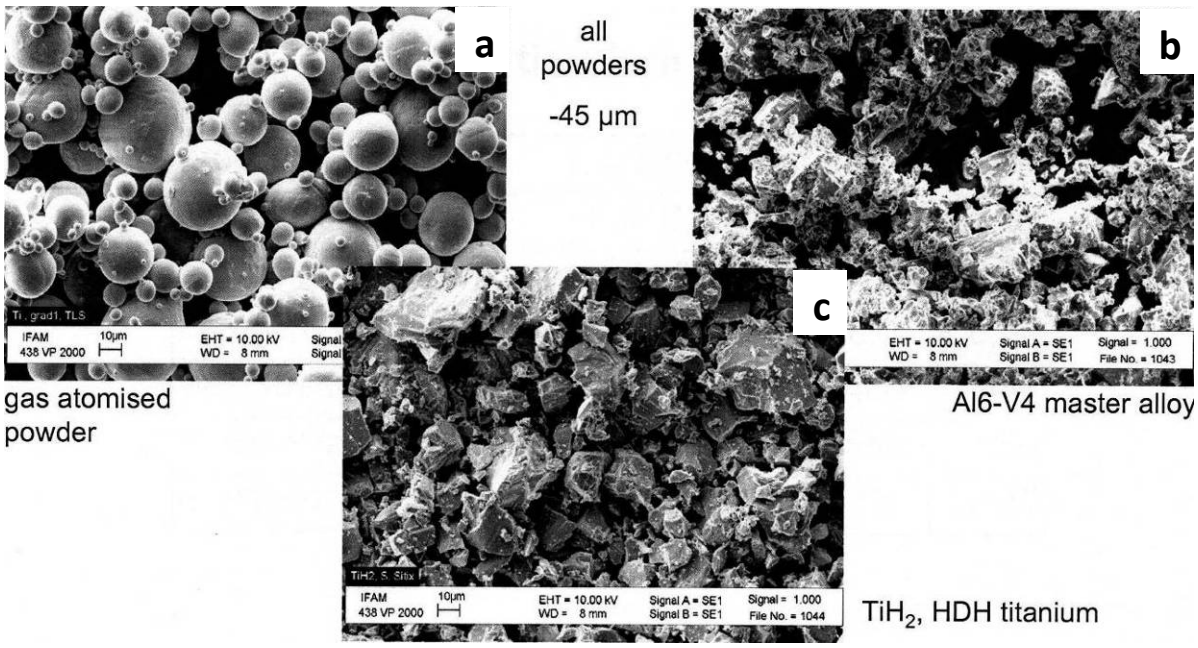

Figure 23: Pre-alloyed Ti6Al4V powders [32].

The utilisation of titanium-based implants is limited by the costly, multi-step process of fabrication and associated geometry design constraints. MIM is a technique that can provide minimization of such problems because it combines the material flexibility of powder metallurgy and the design flexibility of plastic moulding. MIM of titanium is different from established MIM-processing of e.g. special steel powders owing to the high susceptibility of the material to interstitials. Therefore it is crucial to shelter this alloy from the atmosphere throughout the entire manufacturing process, starting with production of the powder right up to the sintering process.

Titanium is very highly reactive with atmosphere components like oxygen, nitrogen and carbon. The quantity of these elements in the alloy is problematic and strongly influences its mechanical properties. A too high content of these elements in particular causes a non-tolerable brittleness of MIM parts.

Other problems in MIM of Ti are the choice of the powder, adequate protection of the Ti during sintering and a suitable binder. Usually atomized powders are used and sintering is made in high vacuum furnaces.
One of the principal problems to obtain titanium by MIM is the oxygen level. Oxygen is the major contributor to the mechanical properties, thus, the aerospace oxygen specification for CP titanium is 0.4 w/o, whereas for Ti-6Al-4V it is 0.2 w/o [33].
So, the factors which affect the strength-ductility are the oxygen content (strength up, ductility down), relative density (strength and ductility up) and the beta grain size (smaller grain size for increased strength and ductility). An additional effect is powder size, with a smaller size likely to give increased oxygen content and a finer beta grain size [33].

3.3.4 Surface treatment

The use and proper execution of surface treatments such as shot peening and chemical milling are individually or jointly critical to the technological success of titanium and its alloys, because in many cases , particularly in fatigue, cracks initiate at the surface of components. The main surface treatments for titanium alloys are: shot peening, laser shock processing, chemical milling, and electrochemical machining.
Shot peening is used to create a state of compressive residual stresses at the surface enhancing the resistance to fatigue crack initiation. Quite recently, the use of a laser to create also a surface compressive stress has been proposed.
Chemical milling is an important means of selectively removing material from the surface of Ti parts. It is an important method to remove material that has become contaminated, for example by oxygen, during processing. In this case, removal of a brittle surface layer intrinsically improves the resistance to crack initiation and fracture. Chemically milled surfaces are often shot peened to create or restore surface residual compressive stress [22].

<u>Shot Peening:</u>

The resistance of Ti specimens with stress-free surfaces to fatigue failure is quite low. Expressed as a fraction of the yield strength, the fatigue strength at 10^7 cycles to failure is typically 0.4-0.5 [22].
This technique introduces a compressive stress in the near surface region of the material by local plastic deformation. A plot of local stress as a function of distance below the shot peened surface is shown in the figure 24.

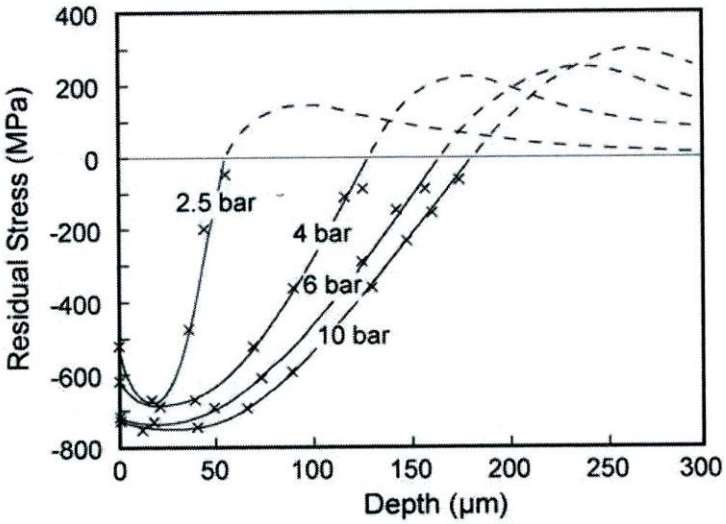

Figure 24: Residual stress distributions after shot peening Ti6Al4V for 4 min at different peening pressures [34]

The shot peened fatigue specimens exhibit subsurface crack initiation sites, figure 25; this confirms that compressive stress due to shot peening reduces the sensitivity in the material to surface crack initiation.

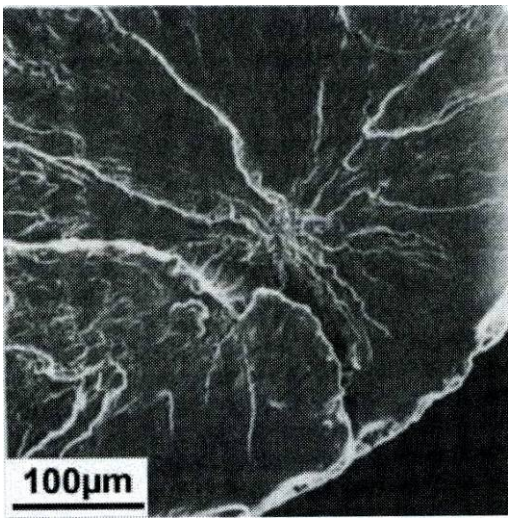

Figure 25: Fractograph showing a subsurface fatigue crack initiation in a shot peened Ti6Al4V [34].

The benefits of shot peening on fatigue performance depend on the alternating stress level and on the service temperature. At low stress amplitudes ($N_F \geq 10^6$ cycles) and room temperature, peening can extend the life by 30-50%. This improvement decreases at higher stresses and essentially disappears at $N_F=10^3$ cycles to failure [22].

There are several external parameters that affect the magnitude of the shot peening effect: type, hardness and size of shot, shot velocity and peening time.

Figure 26 shows the beneficial effects of shot peening and the effect of overpeening. From this figure it is possible to observe that the shot peening is beneficial for improving the fatigue capability of Ti alloys, but it is clear that overpeening should be avoided.

Peening intensity is typically measured by peening metallic coupons called Almen strips and measuring the bowing or deflection due to the residual stress on one side of the strip [22].

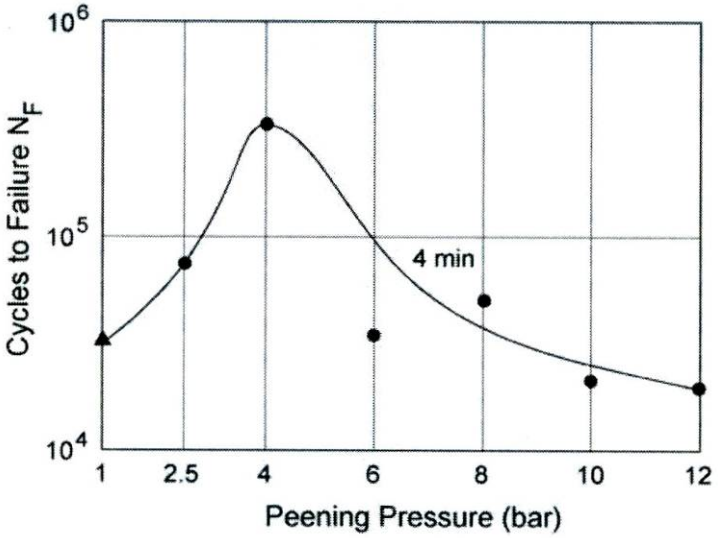

Figure 26: Fatigue life vs. peening pressure [34].

3.4 Ti-6Al-4V Alloy

Ti6Al4V is an $\alpha+\beta$ alloy. It presents three different types of microstructures, which can be obtained by changing the thermo-mechanical processing route: fully lamellar structures (figure 27a), fully equiaxed structures (figure 27b), and so-called bi-modal (duplex) microstructures containing equiaxed primary α (α_p) in a lamellar $\alpha+\beta$ matrix (Figure 27c).

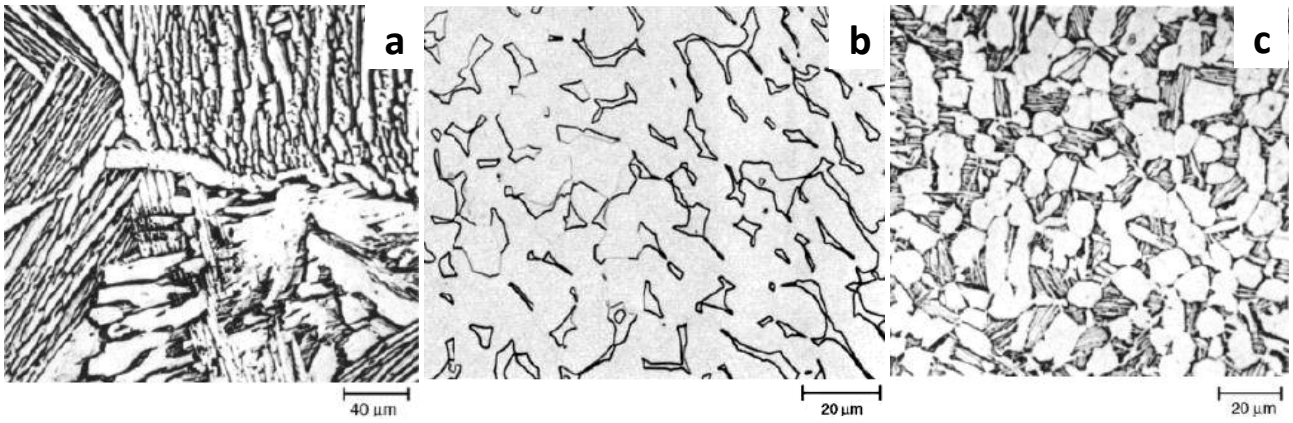

Figure 27: Ti-6Al-4V bar, held for 1 h at 1065 °C, above the beta transus and furnace cooled (a), Ti-6Al-4V plate, recrystallize annealed at 925 °C 1 h, cooled to 760 °C at 50 to 55 °C/h and air cooled (b), and Ti-6Al-4V forging, solution treated 1 h at 955 °C, air cooled, and annealed 2 h at 705 °C (c) [35].

Ti-6Al-4V is the most widely used titanium alloy, accounting for about 45% of total titanium production. One major application area of this alloy is aircraft structural parts. For such applications this alloy is selected over other competing metallic materials, such as high strength aluminum alloys, because of higher yield stress and fatigue strength (even on a density normalized basis), better corrosion resistance, higher modulus of elasticity, and higher resistance to thermal softening [22].

The most influential microstructural parameter on the mechanical properties of lamellar microstructures is the α colony size, which is controlled by the cooling rate from the β heat treatment temperature, because the α colony size determines the effective slip length in lamellar microstructures. Although the two phases, the α plates and the β matrix, have to deform independently, slip can be fairly easily transferred across the incoherent α/β interface, because the two slip systems in each phase are exactly parallel and two others are off by only 10 degrees [22].

The general effect of slip length (α colony size) on mechanical properties is shown in figure 28.

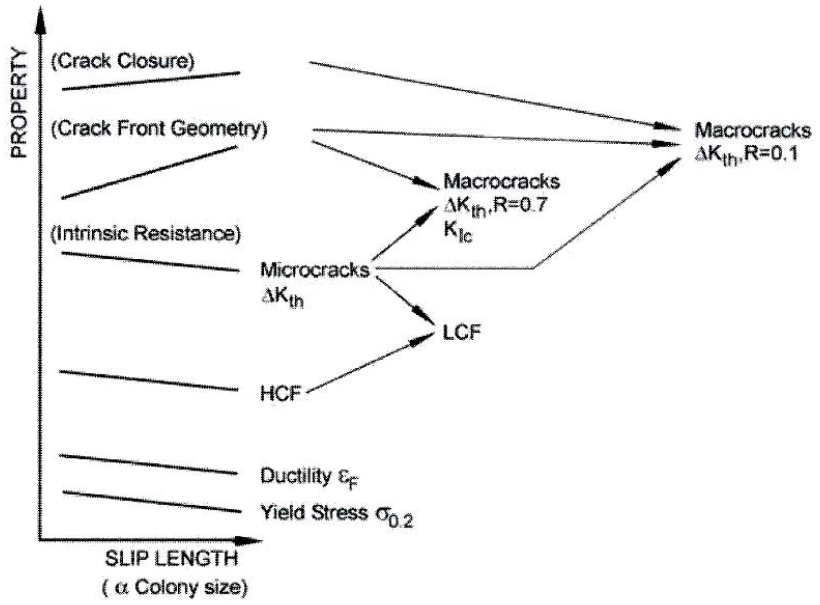

Figure 28: Influence of slip length on mechanical properties for lamellar structures [22].

With increasing cooling rate the α colony size decreases with a commensurate reduction in effective slip length and a corresponding increase in yield stress. This is illustrated in figure 29. This figure shows a variation in ductility in terms of tensile elongation. The maximum in ductility corresponds to a change in fracture behavior. At low cooling rates a ductile transgranular dimple type of fracture is observed, whereas at high cooling rates a ductile intergranular dimple type of fracture occurs along the continuous α layers at β grain boundaries [36].

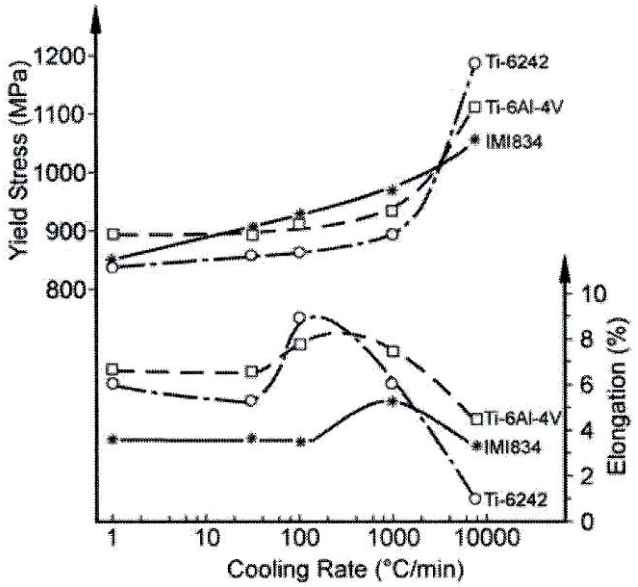

Figure 29:Effect of cooling rate from the β phase field on yield stress and elongation of lamellar structures [22].

The effect of the continuous α layers on ductility is related to the preferential plastic deformation and concomitant premature crack nucleation in these areas. The magnitude of the ductility decline depends primarily on the strength difference between these areas and the matrix and in addition on the grain boundary length (β grain size). A large increase in tensile elongation can be achieved by reducing the β grain size from 600 μm to 100 μm by rapid cooling. The bi-modal structure has much higher ductility values in the fast cooling regime than fully lamellar structures [22].

For such large structural parts, the most important mechanical property is the fatigue crack propagation of macrocracks resulting in a requirement for setting the service time between inspections. The mill-annealed structure exhibits much faster fatigue crack propagation rates of macrocracks than a fully lamellar microstructure [22].

The HCF strength (resistance to crack nucleation) depends primarily on the resistance to dislocation motion. Consequently, the HCF strength dependence on slip length and α colony size is qualitatively similar to that of the yield stress. Increased cooling rates in the slow to medium cooling rate regime results in a moderate HCF strength increase, but much larger increases are seen at faster cooling rates. This is illustrated for lamellar microstructures of the Ti-6Al-4V alloy in figure 30 where the HCF strength at 10^7 cycles is plotted as a function of cooling rate from the β phase field. The ratio of HCF strength (R = -1) to yield stress, which is typically about 0.5 for α+β alloys, can be as low as 0.45 for very coarse microstructures (for example for a cooling rate of 1 K/min) and as high as 0.60 for very fine mi-

crostructures. It should be pointed out that for fully lamellar microstructures the absolute values for both the HCF strength and the yield stress depend on the cooling rate effect [22].

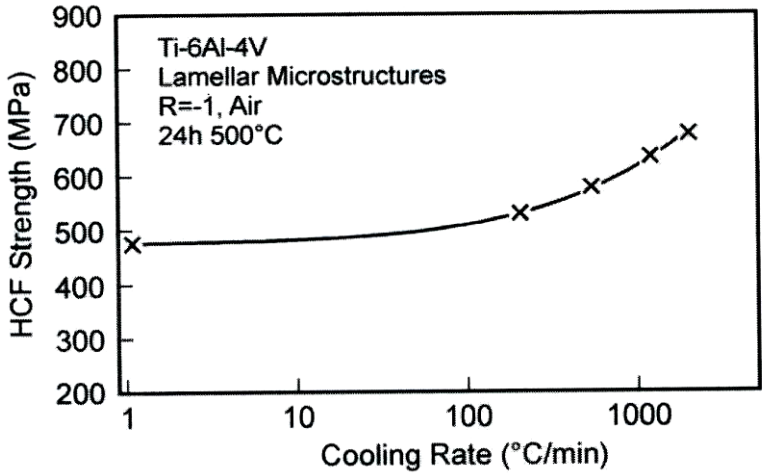

Figure 30: HCF strength (R=-1) of lamellar microstructures on cooling rate from the β phase field for Ti6Al4V [22].

The fatigue cracks nucleate in the colony type of microstructures, formed at low to medium cooling rates, either within pronounced slip bands which extend over almost the whole colony width, or at the intersection of these slip bands with the adjacent α colony boundary. In microstructures composed more of individual α plates, characteristic of faster cooling rates, the fatigue cracks usually nucleate at the longest and widest α plates. Ivasishim et al. [37] suggested that cracks nucleate upon preferred slip band activity within these coarse α plates. Fatigue cracks are only occasionally nucleated at the continuous α layers at β grain boundaries in these fast cooled microstructures of α+β alloys. This is a surprising result considering the observed fracture along the continuous α layers at β grain boundaries in tensile specimens and the concomitant decrease in tensile ductility [22].

3.4.1 Ti-6Al-4V alloy for biomedical applications

Titanium fulfills the property requirements for biomedical applications better than any competing material (stainless steels, CoCr-alloys, CP niobium, and CP tantalum). The properties which are of interest are corrosion resistance, biocompatibility, bioadhesion (bone ingrowth), modulus of elasticity (should be as close as possible to the modulus of bone which is in the range of 10-30 GPa), fatigue strength, and good processibility including joining and casting. Especially the excellent corrosion resistance and biocompatibility make titanium the material of choice. Even the price of titanium, which is normally the drawback for its application, is only slightly higher than that of CoCr alloys or of the types of stainless steel used [22].

In terms of biomedical applications, Ti-6Al-4V and its extra-low interstitial variant (Ti-6Al-4V ELI) and CP-Ti grades are the most widely used. Table 6 compares some of the characteristics of orthopedic metallic implant materials.

Table 6: Comparison of some of the characteristics of orthopedic metallic implant materials [20]

	Cobalt-base alloys	**Ti and Ti-base alloys**
Designation	ASTM F75 ASTM F799 ASTM F562 (cast and wrought)	ASTM F67 ASTMF136 (Ti6Al4V) ASTM F1295 (cast and wrought)
Principal alloying elements	Co (bal), Cr (19-30%), Mo (0-10%), Ni (0-37%)	Ti (bal), Al (6), V (4), Nb (7)
Advantages	Wear and corrosion resistance, fatigue strength	Biocompatibility, corrosion resistance, minimum modulus and fatigue strength
Disadvantages	Biocompatibility, high modulus	Lower wear resistance, low shear strength
Primary uses	Dentistry casting, prostheses stems, load-bearing components in total joint replacement (TJR) (wrought alloys)	Total hip replacements (THR) with modular (CoCrMo or ceramic) femoral heads; long-term, permanent devices (nails, pacemakers)

The alloys Ti-6Al-4V and Ti-6Al-4V ELI are most commonly and are widely used for total joint replacement arthroplasty, primarily hips and knees as described in chapter 2 (section 2.6.2).

The most demanding application for biomedical implants requiring high fatigue strength is the stem of a hip joint implant. A schematic of a complete artificial hip joint is shown in figure 13 (chapter 2). The stem blanks are usually Ti-6Al-4V $\alpha+\beta$ forged and stress relieved, therefore the microstructure is either mill-annealed or fully equiaxed depending on the details of the processing route. Typical HCF strength values at R = -1 for these microstructures in the stress relieved condition are around 400 MPa [22].

To facilitate better bioadhesion (bone ingrowth) the surface of the finished stem is very important. In general, the bone ingrowth behavior improves with increasing roughness of the stem surface. One very popular surface treatment is plasma spraying of hydroxyapatite (main component of bone tissue) as bioactive coating on the titanium implant. The desired surface roughness of the stem can be also directly obtained by designing it into the casting [22]. Such a cast hip stem is shown in the figure 31.

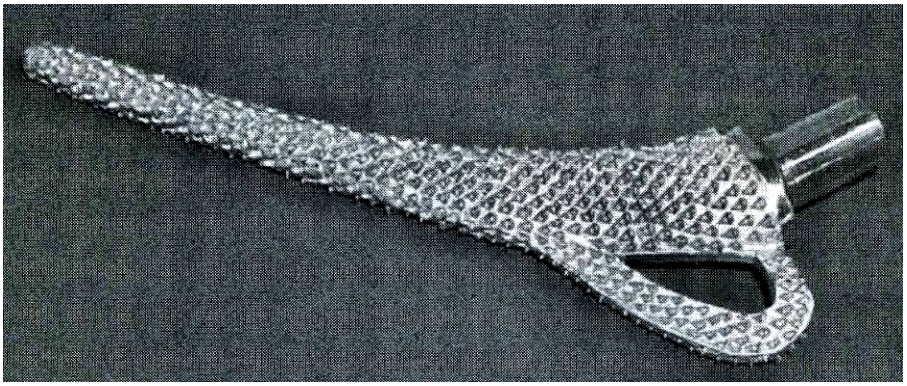

Figure 31: Investment cast hip joint stem, Ti64 [38].

The main disadvantage is that the fatigue strength of investment cast parts of $\alpha+\beta$ titanium alloys is usually lower than that of forged parts because of the fairly coarse fully lamellar microstructure typical of castings. The increase in HCF strength is mainly associated with the microstructure characteristics of the Ti6Al4V alloy, as mentioned before. The S-N curves of forged and cast hip stems are compared in figure 32, the forged hip stem has a higher HCF strength than the cast hip stem with the fully lamellar micro-structure whereas the cast hip stem with the bi-lamellar microstructure even has a higher HCF strength than the forged material [22].

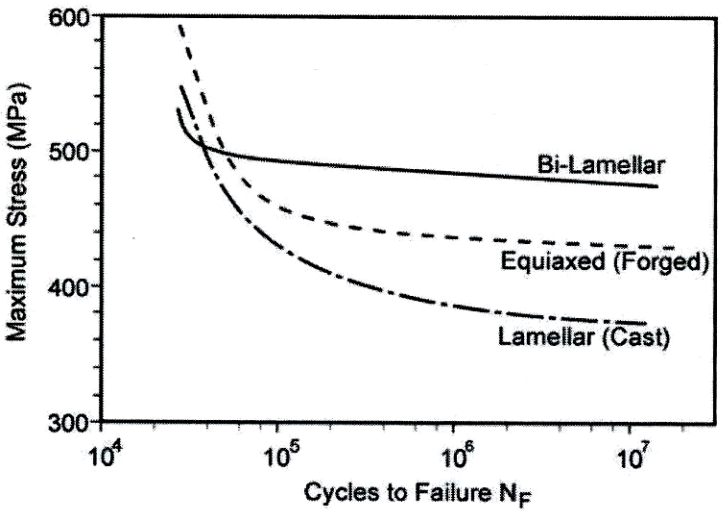

Figure 32: S-N curves (R=-1) of specimens taken from forged and investment cast hip joint stems [22].

Titanium alloys have high notch sensitivity in fatigue. For biomedical applications this sensitivity is a critical factor in the performance of porous coated implants and porous coated hip stems show a large reduction in the fatigue limit in comparison with those of surface smooth conditions. So, for orthopedic applications the notch fatigue behavior is more closely associated with strain-controlled fatigue, and may be more representative of in vivo conditions [14].

The friction and mechanical properties of titanium are quite different from those of most other metals. This is due to its tenacious oxide (passive) film that remains intact under low loads and slow sliding speeds in articulating conditions. However, if the film is worn away and not regenerated quickly, galling will cause metal-on-metal contact and cold welding. This leads to very high friction and wear rates; consequently Ti-to-Ti (or to other metal) articulating joints are not used [14]. This happens when titanium is used for components of modular construction where a titanium femoral stem will be used with a Co-Cr alloy or a ceramic ball to articulate against a UHMWPE liner (THR, section 2.6.2).

To improve wear, ion implantation (N^+) has been the most common treatment employed.

Hip simulator testing has shown that wear rates for UHMWPE mated against Ti64 are 35% greater than that for CoCrMo alloy. The high wear rates of the polymer associated with a titanium alloy counterpart were related to the mechanical instability of the metal oxide layer [20]. If a breakdown of the surface passive layer is induced, the exposed metal surface may then either reform a passive layer or adhesively bond (cold weld) to the polymer surface. The breakdown of the oxide layer creates the potential for abrasive wear, where the hard oxide debris acts as third-body abrasive component.

Wear of joint prostheses materials represents a long-term limitation to the life-time of a THR, because the accumulation of polymer and, to a lesser extent, metal or ceramic wear debris was associated with incidence of nonspecific pain (adverse tissue reaction) and prosthesis loosening (adverse reaction of wear debris of the implant/bone fixation) [20].

CHAPTER 4

MATERIALS AND EXPERIMENTAL PROCEDURES

4.1 Co-Cr-Mo alloys

4.1.1 Production of the specimens

The specimens were produced by pre-alloyed Co-29Cr-6Mo (F75) powders with different carbon contents, produced by gas-atomization, (80% of particle sizes below 22µm). The powders were blended with a proprietary binder (polyolefin based), to produce the feedstock.

Test bars, according to ASTM E 8M-03 – Standard Flat Unmachined Tension Test Specimen for Powder Metallurgy (P/M) Products - were injection molded and debinded by a two steps process (80% of the total binder content was dissolved in water, while the remaining 20% was removed by thermal debinding in Ar/10%H_2 atmosphere). The brown parts were sintered in a graphitic vacuum furnace (at 10^{-2} bar) (manufactured by TAV Spa, Caravaggio, Italy) under the following conditions: 1 hour holding time, N_2 backfilling, free cooling at 1 bar of nitrogen flux (approximately 15 K/min). The sintered density is higher than 95% of the theoretical one. The materials investigated are listed in table 7.

Table 7: Materials and sintering conditions.

Materials	**Temperature of Sintering**
*F75 with **0.35%C***	*Sintering at **1300°C***
F75 with **0.23%C**	Sintering at **1300°C**
*F75 with **0.23%C***	*Sintering at **1350°C***
F75 with **0.05%C**	Sintering at **1380°C**

4.1.2 Heat treatments

The sintered materials were solution annealed at different temperatures (1200°C, 1220°C and 1250°C) with 4 hours of isothermal holding, in the same vacuum furnace used for sintering under argon backfilling and then gas quenched in 8 bar of nitrogen flux. After solution annealing, the samples were aged in a tubular furnace at 750°C in argon atmosphere for 3 and 20 hours and then air quenched.

4.1.3 Chemical analysis

The carbon content was measured by LECO CS125.

4.1.4 Porosity and density

Density was measured by Archimedes' method, according to standard ASTM B 328-96. Measurements were carried out with a precision balance (AdventurerSL - OHAUS) with a sensibility of 0.0001g.

4.1.5 Thermal analysis

Thermal analyses were carried out by differential scanning calorimetry (DSC - Netzsch STA 409PC - Luxx) to study the transformation on heating of the sintered materials. The analyses were carried out in Ar with a heating rate of 0.33 K/sec and a cooling rate of 0.83 K/sec.

4.1.6 Metallography

Metallographic characterization was carried out by a LOM microscopy (Leica DC300) and by environmental scanning electron microscopy (ESEM, Philips XL 30) before and after electrolytic etching with 94 ml distilled water, 4.5 ml HNO_3 and 1.5 ml H_2O_2 solution for 3V and 4sec. The Staining method, a chemical color etching with 1 part (20% $KMnO_4$ + 80% water) + 1 part (8% NaOH + 92% water), was carried out after electrolytic etching to distinguish the different types of carbides ($Cr_{27}C_6$ brown, Cr_7C_3 pale yellow to light tan, M_6C red, green, yellow, blue) [39].

Microanalysis was carried out by energy dispersive X-ray spectroscopy (EDXS).

4.1.7 X-Ray analyses

X-ray diffractometry (XRD) was used to investigate the cobalt matrix constitution (f.c.c./h.c.p. phases) and the type and amount of carbides. The diffraction patterns were collected using a Cu-Kα source and the experimental data were elaborated with the Rietveld method using the MAUD software ("Materials Analysis Using Diffraction") [40,41].

4.1.8 Hardness and microhardness

The microhardness was measured by the Vickers methods, according to ASTM384, with a MHT-4 machine (Anton Paar), on etched metallographic specimens, with a load of 0.5N (HV0.05).

The hardness was measured by the Vickers method, according to ASTM 18, with an Emco test machine, on etched metallographic specimens, with a load of 300N (HV30).

4.1.9 Tensile tests

Tensile tests were carried out in an Instron 8516 SH 100 kN machine, at a strain rate of 0.1 s^{-1} and measuring strain with an axial extensometer with a gauge length of 12.5 mm. The morphology of the fracture surfaces was examined by ESEM.

4.1.10 Corrosion tests

Two kinds of corrosion tests were carried out:

- the measurement of open-circuit potential according to *ISO 16429 – Implants for surgery*
- the potentiodynamic polarization.

The OCP measurements were carried out in a thermostatically controlled cell at 37°C. The electrolyte solutions employed consisted of 0.9% NaCl and as reference electrode a silver/silver chloride electrode (Ag/AgCl 3M) was used. The inert Argon gas was continuously flushed during 72 hours test.

The polarization test were carried out in the same environment and temperature, but no gas was flushed in this case. The electrochemical cell was a three electrode cell using platinum as counter and Ag/AgCl 3M as reference. Since the open circuit potential was very instable at the beginning of immersion, all the samples were immersed for 30 min before starting the potentiodynamic measurements. The potential range was from -0.25 mV vs OCP to 1 V with a scan rate of 0.1 mV/s. Two measurements were performed for each samples and representative curves will be reported.

For both tests the samples were first mechanically polished using SiC grinding paper and polished with 1µm diamond solution to a mirror finish and then cleaned in alcohol and dried.

4.1.11 Wear tests

The tests were performed in a block on disc configuration using an AMSLER A135 testing machine, see figure 33.

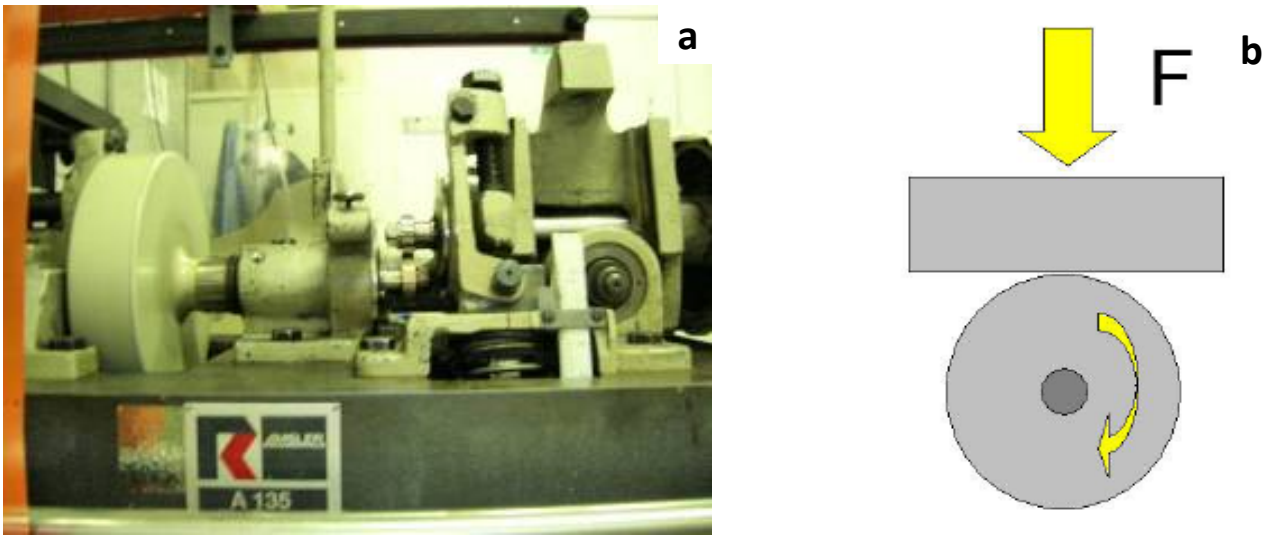

Figure 33: AMSLER A135 testing machine (a) and the block on disc configuration (b).

Co-29Cr-6Mo alloy and ultrahigh molecular weight polyethylene (UHMWPE) were used as block and disc materials, respectively. Tests were carried out with a sliding speed of 0.105m/s (50 rpm) and 300N applied load, corresponding to 24MPa nominal contact stress, this value is in accord to the range of conformity in total knees replacements and it varies from 10 to 45 MPa [42]. Water was used as lubricant. The total

sliding distance was 3 km and the weight loss was measured after each test. The surface roughness of the samples was measured before and after wear tests using a Hommelwerke T8000 machine and the results analyzed with a Turbo Roughness V 2.86" program.

4.1.12 Preliminary in vitro tests

Biocompatibility refers to the interaction between a medical device and the tissues and physiological systems of the patient treated with the device. The clinical success and safety of a medical device largely depend on its safe interaction with body tissue. Preliminary *in vitro* tests were carried out for the 0.23%C materials sintered at 1350°C in both conditions: as sintered (CS) and solution annealed (C), in order to evaluate cytotoxicity, and cell behavior in terms of proliferation, adhesion , distribution and cell adhesion morphology. All tests were conducted using an osteoblast-like MG63 cell line, the microscopic image (Microscope ZEISS AXIOVERT 25) of these cells before culture is shown in figure 34.

Figure 34: Microscopic image of osteoblast-like MG63 cell before culture.

Cytotoxicity:

Cytotoxicity is usually due to the release of toxins, which causes the device to be "not compatible". In order to monitor the biocompatibility and to ensure the safety under normal physiological conditions of a medical device, the device itself or its extract prepared in exaggerated conditions is often used. The ISO 10993 set entails a series of standards from Part 1 to 20 for evaluating the biocompatibility of a medical device.

One of the methods to determine biocompatibility is to study the cytotoxic effect of the extracts on a well-established cell line (in vitro study) according to ISO 10993 Part 5. The cost of 'in vitro study' is generally lower, and easier to be accepted in region against using animal for laboratory testing.The first test carried out was the cytotoxicity to evaluate the potential cytotoxicity of samples when in contact with cells. Compounds that have cytotoxic effects often compromise cell membrane integrity, so assessing cell membrane integrity is one of the most common ways to measure cell viability and cytotoxic effects.

The test used to measure the cytotoxicity was the lactate dehydrogenase (LDH) test (kit TOX7 Sigma Aldrich). It is a cytoplasmic enzyme which is released in the culture medium if the cellular membrane of a cell is damaged. Before starting the culture, the samples were sterilized in 70% ethanol at 4°C for 12 hours, after this they were immersed in a PBS (phosphate-buffered saline) solution for 72hours at 37°C (in order to extract degradation substances). The cytotoxicity test was carried out in this extracted solution. MG63 cells were seeded with a concentration of 10^5 cells/ml in a well plates. After 24 hours of culture, the extracted solutions were mixed with the medium and used to replace the medium in the cell culture. After 24 hours, a LDH test was carried out.

Procedure to measure the cytotoxicity:

- Remove culture from incubator;
- Centrifuge surnatant at 300g for 4 minutes to pellet debris;
- Transfer aliquot to a clean plate (put in each well 1/2 of the original volume of medium per well);
- Proceed with enzymatic analysis.

Procedure to enzymatic analysis:

- Prepare assay mixture mixing equal amounts of
    - LDH assay substrate
    - LDH assay cofactors
    - LDH assay dye
- Add assay mixture in each well in an amount equal to 2X the volume of the culture medium;
- Cover the plate with an opaque material to protect from light and incubate at room temperature for 20-30 minutes;
- Terminate the reaction adding 1/10 volume of 1M HCl to each well;
- Put 100 µl of each sample in a 96-well plate;
- Read the absorbance at a wavelength of 490 nm. Measure the background absorbance at 690 nm and subtract from the previous measurement.

The spectrophotometer tests were carried out on a Thermo Labsystems Multiskan EX, Thermo Labsystems 2004 machine.

<u>In vitro cell culture:</u>

The proliferation, activation and adhesion morphology of the MG63 cells on the CoCrMo alloys were evaluated. Before seeding cells, the samples (24 samples for each condition with 1x4,9x3,5 mm of dimension) were sterilized in 70% ethanol at 4°C for 12 hours, washed several times with sterile distilled water, conditioned in culture medium and finally a $1x10^4$ cell/ml cell suspension was used per well. The culturing times were 3, 7 and 14 days.

After each experimental time, cells were characterized as follows:

- Alamar blue and ALP (alkaline phosphatase): to asses cell proliferation and activation;
- Confocal microscopy (DAPI, rodamina-phalloidina) and SEM observations: to evaluate the cell adhesion morphology.

Figure 35 shows the distribution of the samples in the tissue culture plate wells, 0,23CS is the as sintered sample while the 0.23 C is the solution annealed sample

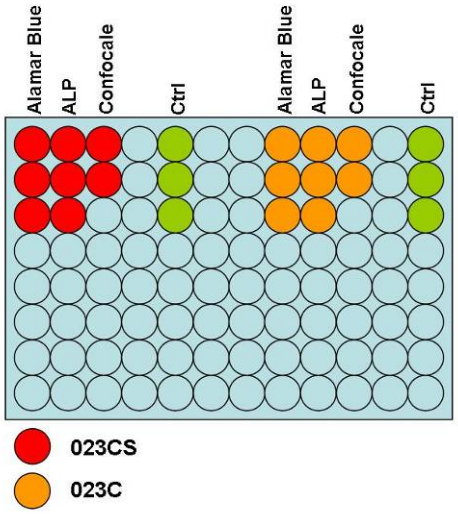

Figure 35: Schematic distribution per well of the samples.

Alamar blue test

This test indicates the cell's health by using the reducing power of live cells to quantitatively measure the proliferation of various human and animal cell lines. Resazurin (7-hydroxy-3*H*-phenoxazin-3-one 10-oxide) is a blue dye used mainly as an oxidation-reduction indicator in the resazurin test, it is used as an indicator for cell viability. Blue colored Resazurin is reduced to pink colored, fluorescent compound Resorufin in the presence of live cells.

Test procedure:

- After each culturing time the culture medium was removed and 1ml of Alamar blue solution was added;
- Incubate at 37°C for 3-4 hours;
- 4x100µl was transferred from each well to 96 well plate;
- The samples were washed with PBS (these samples were used for SEM analyses);
- The absorbance at 570 nm and 630 nm (as reference) were measured.

ALP (alkaline phosphatase) test

ALP is a hydrolyse enzyme responsible for removing phosphate groups from many types of molecules, including nucleotides, proteins, and alkaloids; this process is called dephosphorylation. Elevated ALP indicates that there could be active bone deposition occurring as ALP is a byproduct of osteoblast activity.

Test procedure:

- Make up phosphatase substrate – 4mg/ml solution using diethanolamine buffer;
- Make up p-nitrophenol - dilute 1:50 with 0.02M NaOH (light sensitive);
- Make up diethanolamine buffer – 97ml diethanolamine, 100mg $MgCl_2$, 200mg sodium azide, 800ml H_2O. pH 9.2 with HCl;
- Make up triton X buffer – 50mM tris HCl, 0.1% triton X, 0.9% NaCl. pH 7.6;
- Wash cell layer off well with PBS and add 200µl triton X buffer to samples;
- Scrape cells off well, or cut scaffold up, if in well transfer solution (and scaffold) to an eppendorf, and vortex well;
- Freeze the samples then thaw 3 times;
- Centrifuge for 5 minutes at 1000 rpm;
- Warm alkaline buffer, samples and phosphate substrate to 37^{o}C;
- Add 50µl alkaline buffer to each eppendorf;
- Add 10µl sample (in duplicate) to 8;
- Add 50 µl phosphatase substrate to 8. and vortex immediately;
- Incubate for 15 minutes at 37^{o}C;
- Add 100 µl 3M NaOH to each eppendorf (this stops the reaction);
- Make standards as follows: (during incubation)

Standard concentration (µmol)	Vol 200µmol pnp (µl)	Vol 0.02M NaOH (µl)
Blank	0	1000
1	5	995
5	25	975
10	50	950
20	100	900
50	250	750
100	500	500
200	1000	0

- Transfer 100µl from each eppendorf into a 96 well plate;
- Read on plate reader 405nm

Confocal microscopy

Confocal microscopy is a technique for obtaining high-resolution optical images with depth selectivity.

The confocal analyses were carried out by a Nikon eclipse Ti confocal microscope A1. To observe the cells in the microscope they need to be fixated and stained.

Fixation:

- The medium was removed at the end of the culture;
- Samples were washed 1x with pre-warmed PBS ;
- In the solution of 4% paraformaldehyde in PBS were added for 48-wells, 800 µl/well;
- The samples were incubated at room temperature RT for 20-30 minutes.

Permeabilization:

- The solution with paraformaldehyde was removed;
- The samples were washed once with PBS at RT;
- A solution of 7% paraformaldehyde + 0.2% Triton X -100 in PBS was added for 48-wells, 300 µl/well (or at least to cover the sample);
- Waited for 15 minutes;
- The samples were washed again for 2x with PBS for 5 minutes;

Cell acting filament staining: phalloidin-rhodamine (R 415 – invitrogen):

- Solution for the staining: for 25 ml of staining solution, add 100 µl of stain in 25 ml of 1% BSA in PBS (protect from light)
- Add the staining solution: for 48-wells, 300 µl/well (or at least to cover the sample) PBS (protect from light)
- Wait for 1 hour
- Wash samples 2x with PBS for 5 minutes under shaking (protect from light)

Cell nuclei staining: DAPI (D3571 – invitrogen):

- Prepare the solution for the staining: for 25 ml of staining solution, add 54 µl of stain (DAPI at 0,5 mg/ml) in 25 ml di PBS (protect from light)
- Add the staining solution: for 48-wells, 300 µl/well (or at least to cover the sample) (protect from light)
- Wait for 40-50 minutes
- Wash samples 2x with PBS for 5 minutes under shaking (protect from light)

SEM (scanning electron microscope)

The samples of the alamar blue test were chemically stabilized and examined by SEM using a Supra 40 ZEISS, GEMINI column.

Fixative procedure:

- The samples were immersed in Fixative 1 (Glutaraldehyde 25% in cacodylic buffer 0.1M (100 ml)) for 30 minutes at + 4°C;
- The Fixative 1 was removed and the samples were washed in Fixative 2 (Cacodylic buffer 0.1 M (100 ml)) for 3 times;
- The fixative 2 was removed and the samples were immersed in ethanol/water solution: 30% - 50% - 70% - 90% - 100% - 100%, 10 minutes each step;
- The ethanol was removed and the samples were left to dry in the hood.

After fixation the samples were metalized before SEM observation.

Another in vitro biocompatibility test was carried out on the samples with 0.35%C and 0.23%C sintered at 1350°C, both in the as sintered conditions. In this case only two samples of each material were investigated. The samples were polished before the tests.
The culturing time was 7 days and only analyzes of adhesion morphology by SEM was carried out.

4.2 Ti6Al4V alloys

4.2.1 Production of the specimens

The specimens were produced by a commercial feedstock of pre-alloyed gas atomized Ti-6Al-4V powders.
Test bars, according to ASTM E 8M-03 – "Standard Flat Unmachined Tension Test Specimen for Powder Metallurgy (P/M) Products" - were injection molded and debinded by a two steps process (80% of the total binder content was dissolved in water, while the remaining 20% was removed by thermal debinding at 500°C in argon backfilling). The brown parts were sintered in a metallic vacuum furnace (at 10^{-3} bar) (manufactured by TAV Spa, Caravaggio, Italy) under the following conditions: sintering at 1315°C, 100 min holding time at 100 mbar argon backfilling, free cooling until 600°C (approximately 15K/min) and then under 1 bar of nitrogen flux. The materials investigated are listed in table 8.

Table 8: Materials investigated.

Materials
Ti64 as sintered **(AS)**
Ti64 shot peening at 14Almen with steel shot **(SP1)**
Ti64 shot peening at 18Almen with steel shot **(SP2)**
Ti64 shot peening at 12Almen with s Zirshot Z210 **(SP3)**

4.2.2 Shot peening conditions

Three different shot peening treatments were carried out (table 8):

SP1:

This shot peening was conducted using steel ASH230 shots with a diameter of 0.6mm and 55-62 HRC of hardness. The air pressure and peening intensity was 4.5-5.0 bar and 14 Almen, respectively. The work distance applied was 80-100mm and the inclination with respect to the surface was 80°. The coverage was >100%. The shot peening was conducted in a pression machine.

SP2:

In the SP2 samples almost the same conditions of shot peening were applied changing only the air pressure and intensity. The samples were shot peened at 6.5-7.0 bar and 18 Almen intensity.

SP3:

The third shot peening condition was totally different from the others. It was conducted using ceramic shot Zirshot Z210 shots with a diameter of 0.2-0.3mm. The air pressure and peening intensity was 4.5-5.0 bar and 12 Almen, respectively. The work distance, coverage and inclination applied were the same as in the two cases explained before. The shot peening was conducted in a depression machine.

4.2.3 Chemical analysis

The carbon and oxygen contents were measured by LECO CS125 and LECO TC400, respectively, after sintering.

4.2.4 Porosity and density

Density was measured by Archimedes' method, according to standard ASTM B 328-96. Measurements were carried out with a precision balance (AdventurerSL - OHAUS) with a sensitivity of 0.0001g.

4.2.5 Roughness

The surface roughness was measured along a length of 10mm in the center of the samples using a DEKTAK3 machine version 1.05.

4.2.6 Metallography

Metallographic characterization was carried out by optical microscopy (Leica DC300) before and after electrolytic etching with Kroll solution.

4.2.7 Hardness and microhardness

The microhardness was measured by the Vickers method, according to ASTM384, with a MHT-4 machine (Anton Paar), on etched metallographic specimens, with a load of 0.5N (HV0.05).

The hardness was measured by the Vickers method, according to ASTM 18, on an Emco test machine, on etched metallographic specimens, with a load of 100N (HV10).

4.2.8 Tensile tests

Tensile tests were carried out in an Instron 8516 SH 100 kN machine, at a strain rate of 0.1 s^{-1} and measuring strain with an axial extensometer with a gauge length of 12.5 mm. The morphology of the fracture surfaces was observed by SEM.

4.2.9 High cycle fatigue (HCF) tests

High cycle fatigue tests were carried out in a push-pull (axial) configuration using a Rumul Mikrotron 20kN machine with a frequency of 150Hz and a load ratio of 0.02 (R=0.02). A run-out test of $2x10^6$ cycles was assumed.

To determine the mean endurance limit, the statistical staircase method was applied, suggested by the MPIF 56 standard. For each condition, 15 specimens were tested and the stress step was 15 MPa.

The fracture surfaces were investigated by SEM.

CHAPTER 5

RESULTS AND DISCUSSION

5.1 Co-Cr-Mo Alloys

The mechanical and wear properties of the biocompatible Co-Cr-Mo alloys are strongly influenced by the microstructure, and in particular by carbides precipitated in the metallic matrix.

To modify the microstructure with the aim to increase ductility, a solution annealing treatment is carried out, which dissolves the carbide particles almost completely. The improved ductility is, however, accomplished by a decrease of strength. The constitution of the metallic matrix evolves with heat treatment, as well, but the major effect on properties is attributed to the change in the number of carbide particles and their distribution.

MIM produces an as sintered microstructure largely different from that of cast alloys of similar composition. In particular, the as cast microstructure is quite coarse, with both dendritic and interdendritic carbides resulting from micro-segregation on solidification (coring). The as sintered microstructure, instead, contains large eutectic cells, and carbides are less finely segregated. Even in the case of a similar chemical composition, the transformations during heat treatment could be influenced by the different distribution and composition of carbides.

As a preliminary work, the effect of the solution annealing temperature, in the range from 1200°C to 1250°C, on the microstructure, microhardness and hardness of a 0.35%C Co-Cr-Mo alloy produced by MIM of prealloyed powders was investigated. The high carbon material was chosen because it presents the higher quantity of carbides.

5.1 .1 Study of solution annealing temperature

Figure 36a shows the as sintered microstructure of the Co alloy. It contains a large amount of eutectic cells, as well as grain boundary precipitates. Three types of carbides were revealed by the color metallographic etching:

- $M_{23}C_6$ is the main constituent of the eutectic cells (pearlite like);
- M_6C and M_7C_3 are present in the eutectic cells and along grain boundaries.

The ESEM image (figure 36b) shows details of the morphology of these carbides ($M_{23}C_6$ in the centre, M_6C and M_7C_3 on the right).

In addition, the small and fragmented precipitates at the grain boundary are sigma phase.

The microstructure is quite coarse, the grain size is 115±12 μm, because of the high sintering temperature.

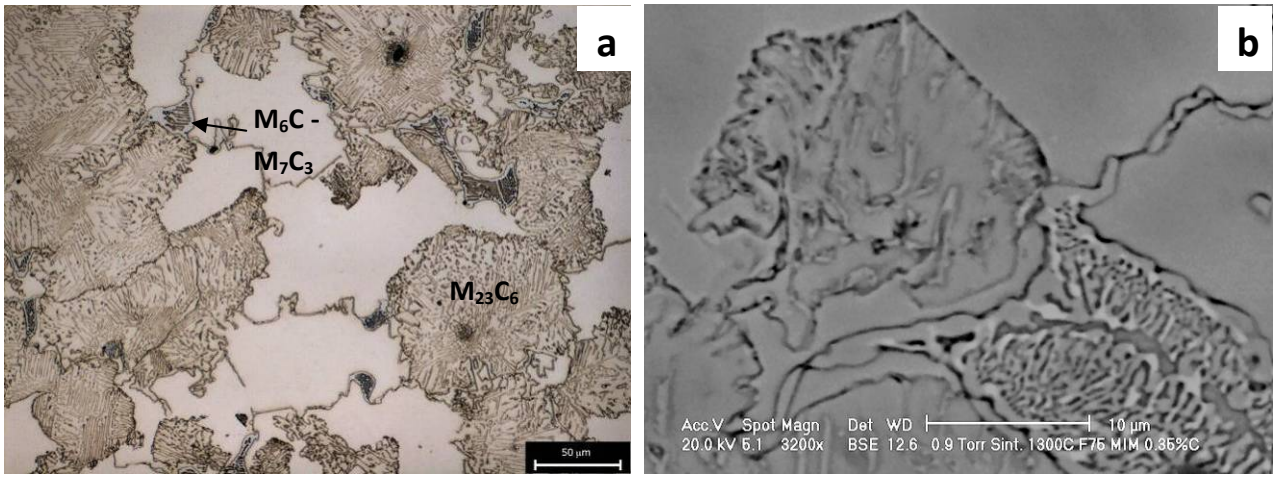

Figure 36: As sintered 0.35%C Co-Cr-Mo alloy: optical (a) and ESEM (b) micrographs.

DSC analysis was carried out with the purpose to individuate the eutectic transformations leading to the formation of the liquid phase. Figure 37 shows the DSC curve. Two endothermic peaks are well evident, with the maximum around 1245 °C and 1265 °C, respectively. They correspond to two eutectic reactions involving the eutectic cells containing $M_{23}C_6$ (1245°C) and M_7C_3 carbide (1265°C). M_6C can both precipitate directly from the f.c.c. solid solution and form as a product of the transformation on heating of $M_{23}C_6$ [39,43].

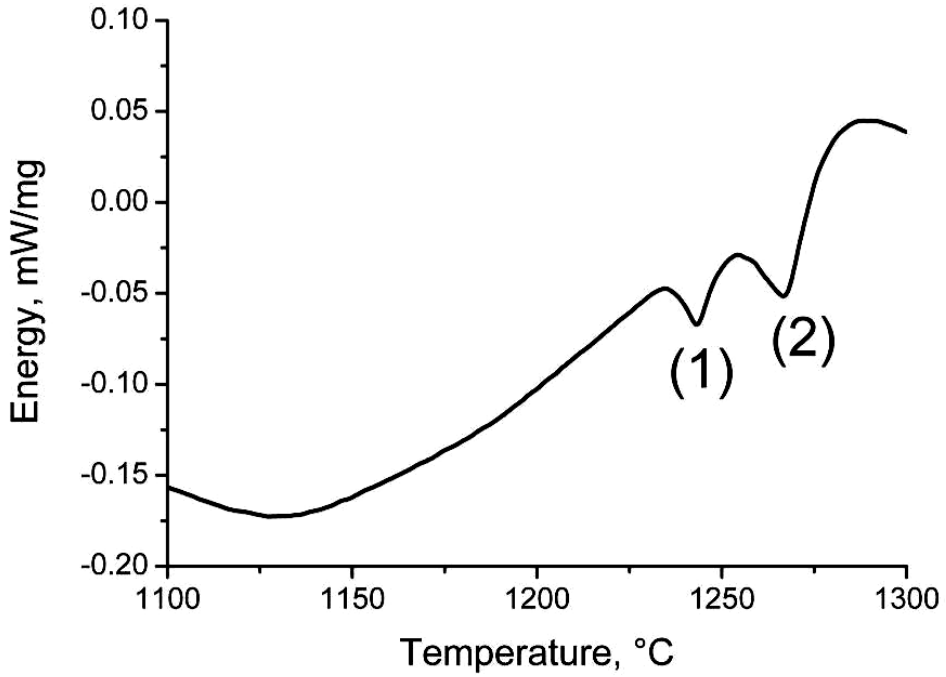

Figure 37: DSC curve of the 0.35%C as sintered alloy.

Three temperatures were selected for the solution annealing treatment: 1200°C, 1220°C e 1250°C. The first two temperatures are lower than the eutectic ones, the third is just in between.

The results of the microstructural characterization of the material, after solution annealing at the three temperatures are presented in the following.

Solution annealing at 1200°C

Figure 38 shows the microstructure of the material solution annealed at 1200°C.

Solution annealing at 1200°C causes the partial solubilisation of the eutectic cells and the fragmentation of the grain boundary precipitates. The grain size of the metallic matrix does not change with heat treatment.

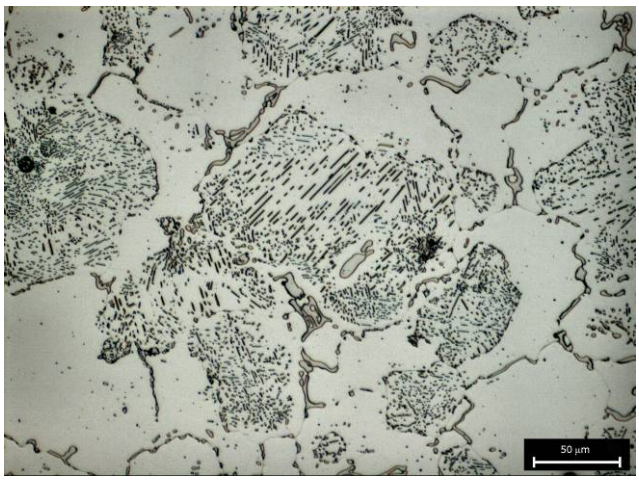

Figure 38: Microstructure of 1200°C solution annealed 0.35%C material.

Solution annealing at 1220°C

Figure 39 shows the microstructure of the material solution annealed at 1220°C.

The treatment at 1220°C causes the complete solubilisation of the eutectic cell. $M_{23}C_6$ e M_7C_3 particles are still present at the grain boundary. Sigma phase is also still present, and the grain size of the metallic matrix does not change with the treatment. Kilner [44] found that the heat treatment at temperatures close to but below the melting point of the interdendritic constituent results in the appearance of $M_{23}C_6$ as the only interdendritic phase. Prolonged heat treatment (more than 24 hours) eventually dissolves this carbide resulting in a homogeneous alloy.

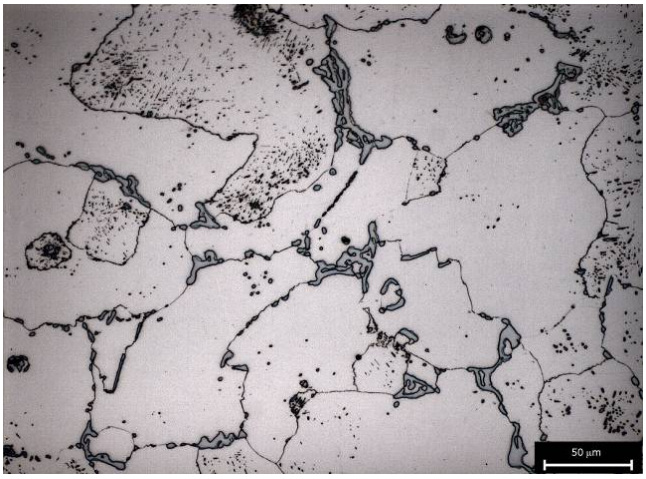

Figure 39: Microstructure of 1220°C solution annealed 0.35%C material.

Solution annealing at 1250°C

Figure 40a shows the microstructure of the material solution annealed at 1250°C. The eutectic cells are completely solubilised, as well as most of the other carbides. Only a few $M_{23}C_6$, M_6C e M_7C_3 with a modified morphology are visible. In particular, SEM analysis (figure 40b) highlights globular particles of $M_{23}C_6/M_7C_3$ and eutectic M_6C with a very low dihedral angle. The grain size of the metallic matrix is slightly increased to 140±23 µm, because of the carbide solubilisation.

The heat treatment above the eutectic reaction was studied by Kilner [44]. He found a strikingly serrated appearance of the boundary between the interdendritic constituent and the matrix. This has been described as “starlike” phase. In addition to this phase, the grain boundary melting takes place, as in the present study, as demonstrated by the change of morphology of residual eutectic carbides.

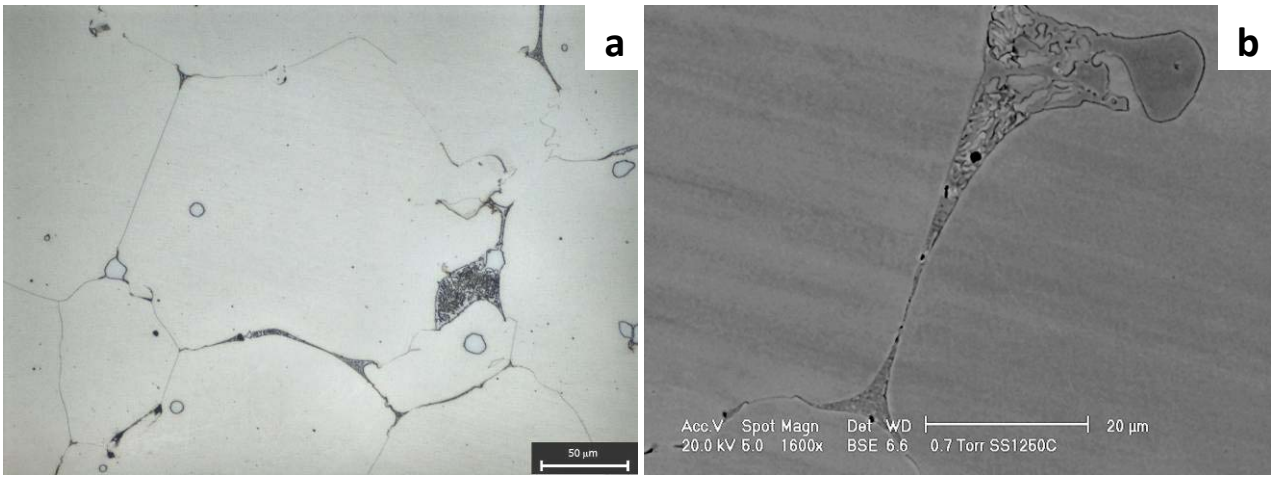

Figure 40: Optical (a) and SEM (b) microstructure after solution annealing 0.35%C material at 1250°C.

Table 9 lists the matrix microhardness, and the hardness of materials investigated. Solution annealing causes an increase in microhardness (because of solution hardening by carbon and alloying elements), that

does not show any significant influence of temperature. Hardness decreases after solution annealing, since it is influenced by carbides and by the grain size; this justifies the decrease with the solution annealing temperature, as well.

Table 9: Matrix microhardness and hardness

Material	**HV0.05**	**HV30**
0.35%C alloy – As Sintered	366 ± 13	347 ± 7
0.35%C alloy – SA at 1200°C	*421 ± 21*	*349 ± 5*
0.35%C alloy - SA at 1220°C	395 ± 12	313 ± 5
0.35%C alloy - SA at 1250°C	*400 ± 15*	*294 ± 5*

On the basis of the results of the microstructural and of microhardness and hardness tests, the solution annealing temperature for the Co-Cr-Mo materials was selected at 1220°C. The lower temperature (1200°C), does not significantly reduce the amount of carbides. The higher temperature (1250°C) results in an effective solubilisation of carbides but causes a decrease of hardness and grain growth. The material solution annealed at 1220°C is expected to have a much lower brittleness than that treated at 1200°C, and a greater strength than that treated at 1250°C.

5.1.2 Microstructures of Co-Cr-Mo alloys

0.35%C Alloy:

The density is 99% of the theoretical one.

Figures 41 a and c show the microstructure of the as sintered and heat treated 0.35%C alloy sintered at 1300°C. The as sintered alloy, as described at the previous 5.1.1 section, contains both lamellar carbides ($Cr_{23}C_6$) within large eutectic cells and grain boundary carbides (Cr_7C_3 and M_6C), as confirmed by the colour metallographic etching, figure 41b, as well as fine grain boundary precipitates of sigma phase.

The $Cr_{23}C_6$ carbides are the product of the slow eutectic solidification of a liquid phase [45]. M_6C can both precipitate directly from the f.c.c. solid solution and form as a product of the transformation on heating of $M_{23}C_6$ [39, 46]. The formation of sigma phase was detected by Signorelli, in conjunction with, or subsequent to, $M_{23}C_6$ precipitation [39]. According to Shortsleeve [47], the precipitation of carbides promotes the formation of sigma phase, then a large quantity of carbides enhances the probability of the precipitation of sigma phase.

Most of the cellular carbides of the 0.35%C alloy are effectively dissolved by solution annealing, see figure 41b, and only a discontinuous network of grain boundary carbides ($Cr_{23}C_6$ and Cr_7C_3) is still present.

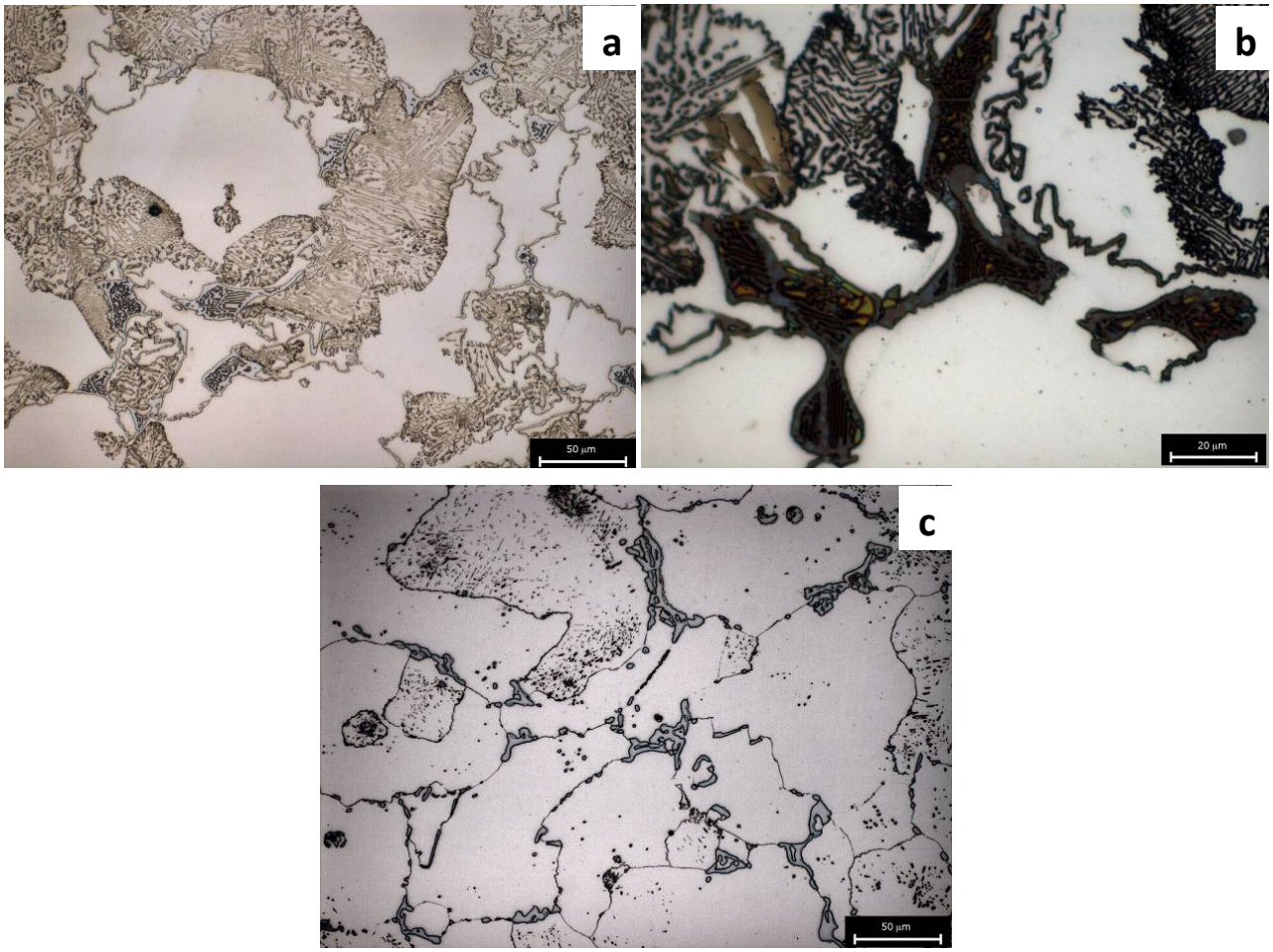

Figure 41: Optical micrographs of as sintered (a and b) and solution annealed (c) 0,35%C material

The ESEM images of the aged 0.35%C alloy at 750°C for 3 and 20 hours are shown in figures 42a and 42b, respectively. Aging promotes an intragranular star-shape (Widmanstätten type) precipitation and the formation of a fine constituent (very closely packed lamellae) which nucleates at the grain boundary and grows inside grains. The amount of these precipitates increases with the aging time.

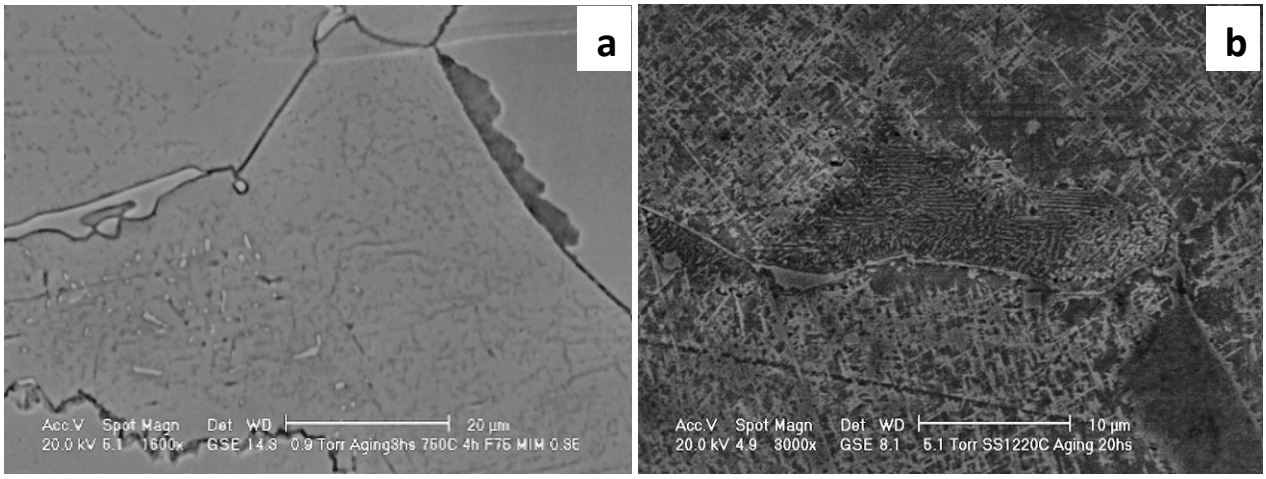

Figure 42: ESEM images of aged 3hours (a) and 20hours (b) 0,35%C material.

The Widmanstätten precipitates are $M_{23}C_6$ particles [39, 48, 49, 50]. This demonstrates that solution annealing and aging are effective in promoting the formation of a homogeneous dispersion of carbides in the metallic matrix from the highly segregated microstructure of the as sintered materials. The fine lamellar constituent is described by K. Rajan [49, 50]. For short aging time, the f.c.c. phase transforms to a highly faulted h.c.p. phase with a martensitic mechanism involving interstitial diffusion. This hcp phase contains some carbides nucleated at the grain boundary (hcp_1). On increasing aging time, it evolves to hcp_2 which differs from hcp_1 for the lack of any crystallographic relationships with the parent phases and for the lower fault density. This evolution is coupled to an abundant precipitation of carbides.

<u>0.23%C Alloy sintered at 1300°C:</u>

Density of this material is 7.55 g/cm^3, 91.1% of the theoretical value.

The microstructure of the as sintered and of the heat treated 0.23%C alloy sintered at 1300°C are reported in the figures 43a and 44a, respectively. This material contains only lamellar eutectic carbides of the $Cr_{23}C_6$ type, as confirmed by the colour metallographic etching.

The ESEM image, figure 43b, shows the grain boundary precipitates of sigma phase.

After solution annealing all the carbides and sigma phase are fully solubilised in the metallic matrix, figure 44a. The grain size increases from 75±16 μm to 90±13 μm after annealing.

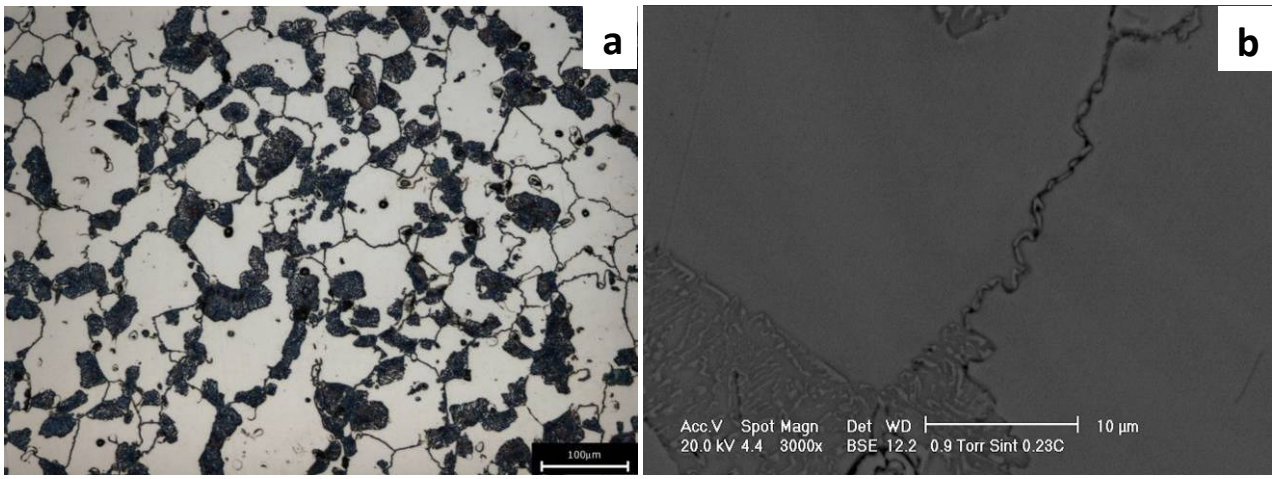

Figure 43: Optical and ESEM images of as sintered 0,23%C material sintered at 1300°C.

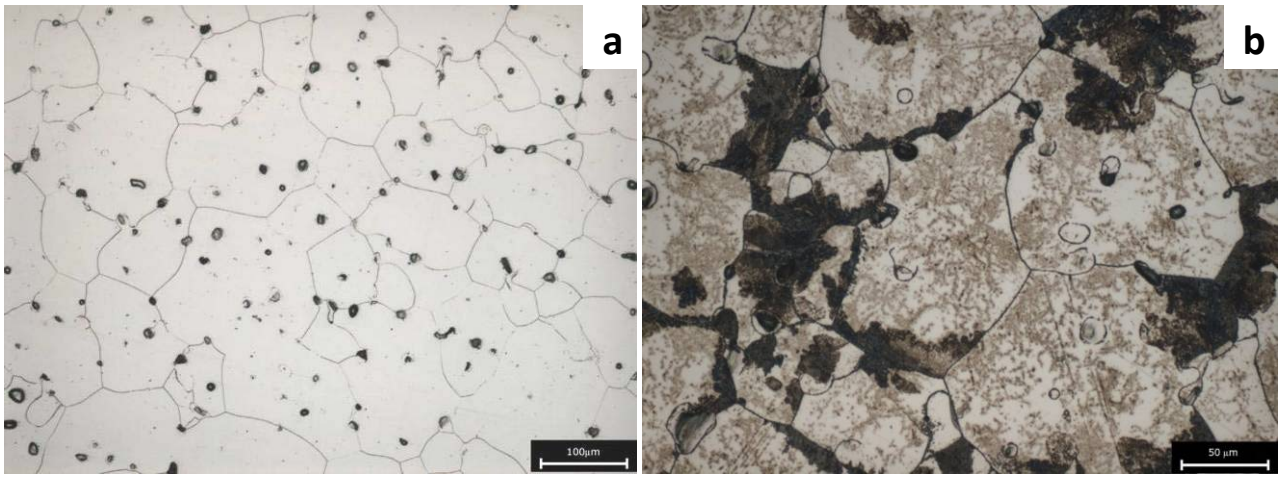

Figure 44: Optical micrographs of sol. annealed (a) and aged for 20hours (b) 0.23%C material sintered at 1300°C.

On aging, the same transformations described previously occur, involving the intragranular Widmanstätten precipitation and the grain boundary precipitation of the hexagonal constituents. A detail of the microstructure after 20 hours of aging is shown in figure 44b.

<u>0.23%C Alloy sintered at 1350°C:</u>

The 0.23%C alloy sintered at 1350°C presents a higher density (98.7% of the theoretical one) than the same material sintered at 1300°C. The matrix grain size increases from 75±16 μm up to 193±25 μm.

Figure 45 shows the microstructures of the as sintered and of the solution annealed 0.23%C alloy (sintered at 1350°C). This sintered material contains again both lamellar $Cr_{23}C_6$ carbides and grain boundary M_6C carbides and sigma phase. After solution annealing, some small spheroidized $M_{23}C_6$ particles and a very low fraction of sigma phase are still present at the grain boundary, figure 46a. The spheroidised particles are the product of breaking-up and spheroidisation of the lamellar “pearlite-like” eutectic carbides [39].

Grain size remains almost unchanged after solution annealing, because of the grain boundary pinning exerted by the residual carbides.

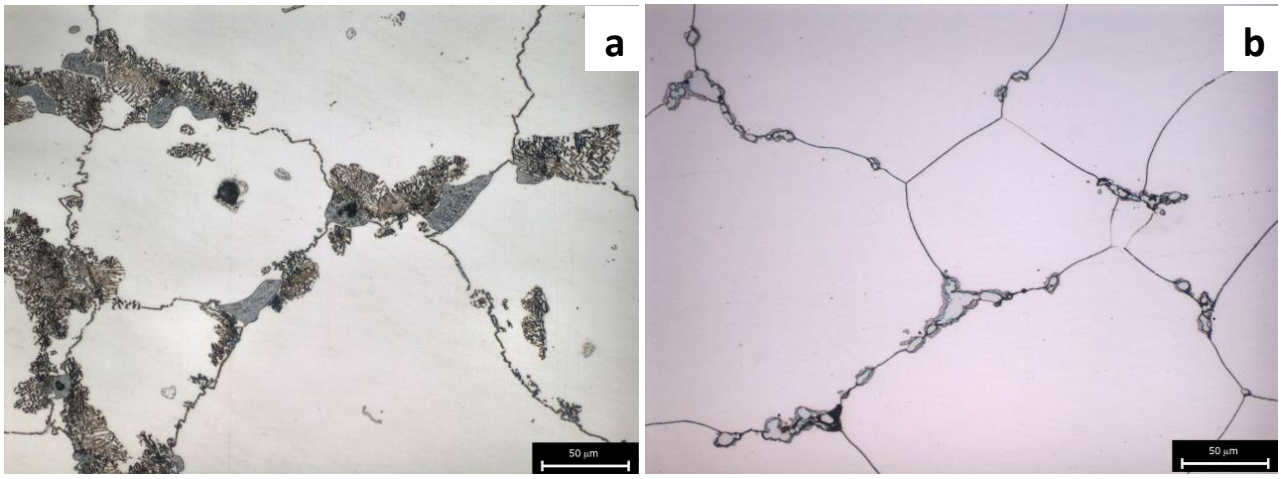

Figure 45: Optical micrographs of as sintered (a) and solution annealed (b) 0.23%C material sintered at 1350°C

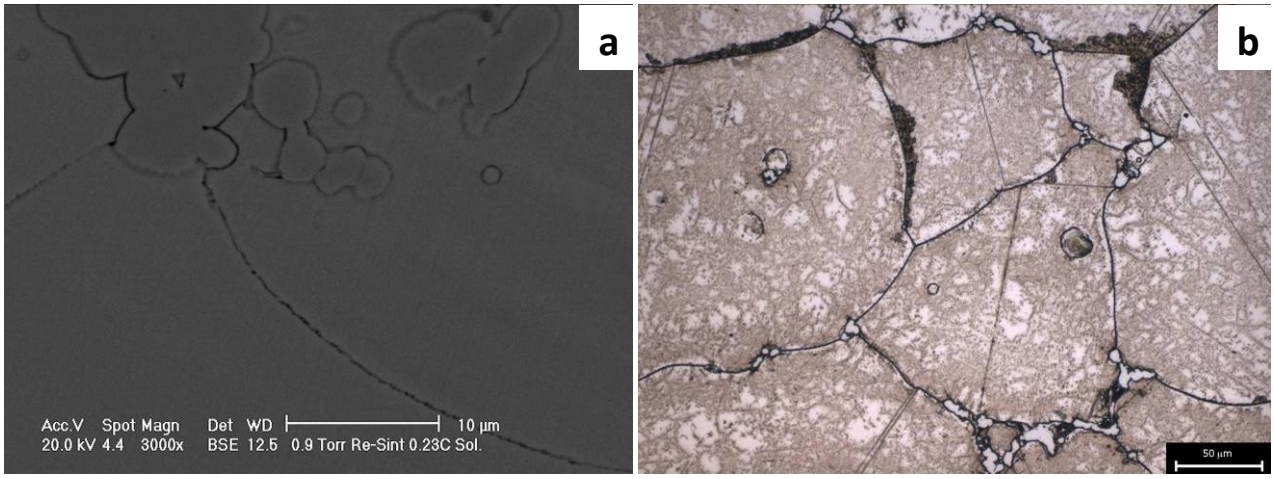

Figure 46: Optical and ESEM images of sol. annealed (a) and aged for 20hours (b) 0.23%C material sintered at 1350°C.

After aging (figure 46b), both the intragranular Widmanstätten precipitates and the grain boundary precipitates of the hexagonal constituents are visible. The material sintered at 1300°C contains a higher fraction of hcp phases than the present material, likely because of the smaller grain size (larger grain boundary surface area which enhances nucleation) and the uncompleted solubilization of the as sintered carbides. It also shows a lower amount of Widmanstätten carbides, because of the concurrent carbide precipitation coupled to hcp phase formation. Grain size does not change with aging.

<u>0.05%C Alloy:</u>

Figure 47 shows the microstructure of the as sintered and of the solution annealed 0.05%C alloy. This as sintered alloy contains a less quantity of carbides than the others, showing only discontinuous precipitates of $Cr_{23}C_6$ particles on the original particles boundaries. The sigma phase is absent, as expected, due to the

low quantity of carbides. Solution annealing is very effective on this material; only a few $Cr_{23}C_6$ particles are visible in the microstructure after heat treatment.

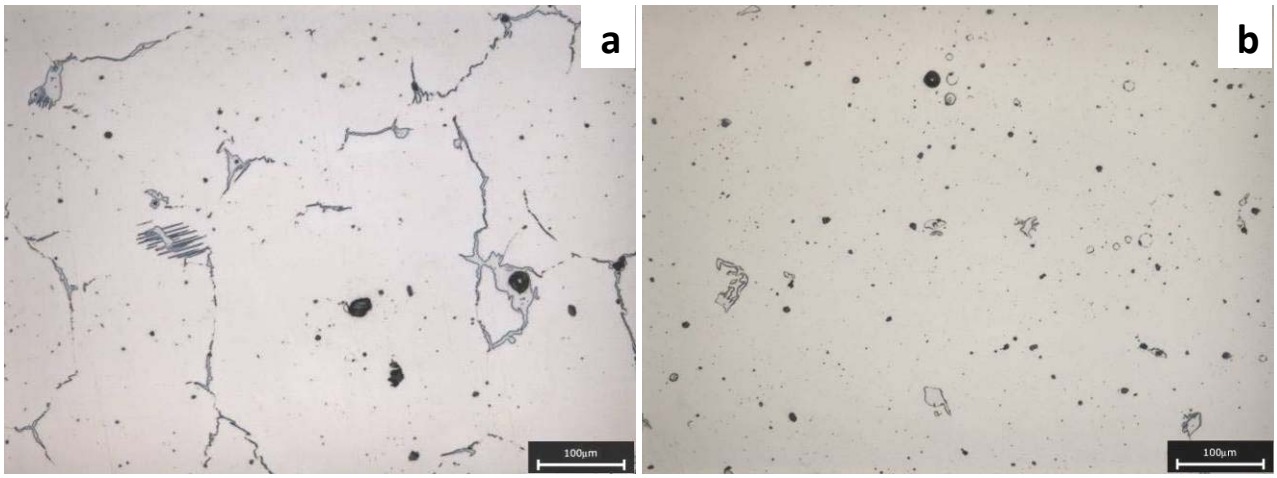

Figure 47: Optical micrographs of as sintered (a) and solution annealed (b) 0.05%C material

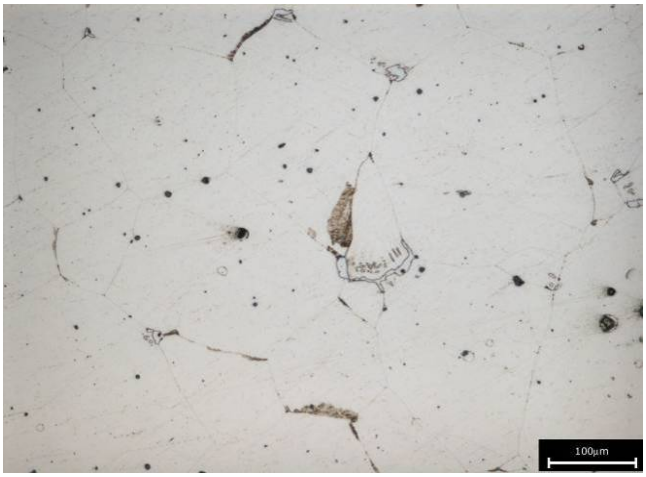

Figure 48: Optical micrograph of 0.05%C material aged for 20hours.

On aging, the same transformations described previously occur, but these transformations are quite less pronounced. Figure 48, relevant to the 20 hours aged specimen, shows only a slight amount of grain boundary martensite.

5.1.3 Constitution of the metallic matrix

Figure 49 shows, as an example, the XRD pattern of 0.23%C alloy, both in the sintered at 1300°C and solution annealed conditions. It is possible to identify the h.c.p. and f.c.c. peaks in the patterns. Carbides are not detected by XRD because their mean peaks are in the same positions of those of the f.c.c. and h.c.p. phases.

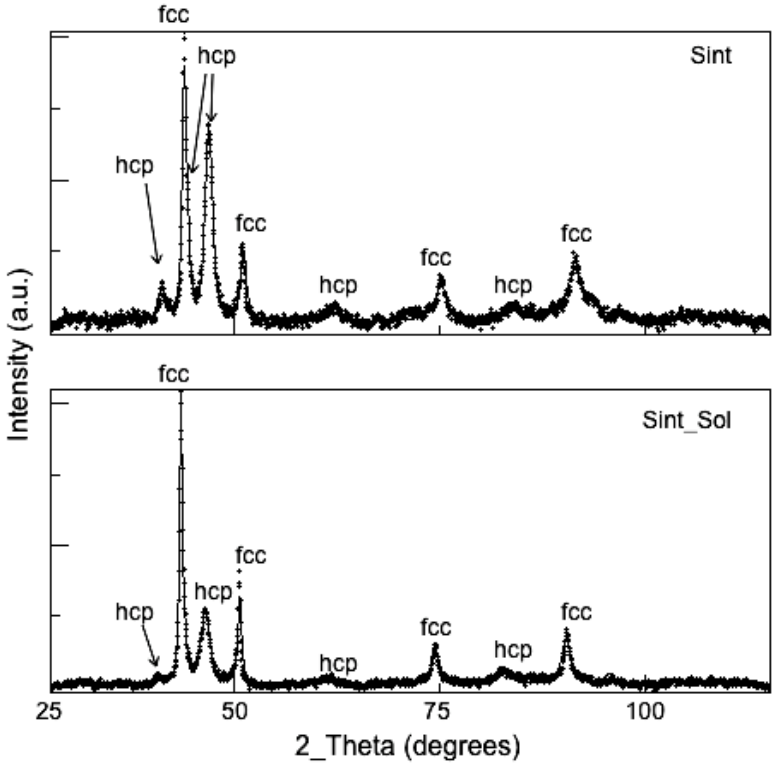

Figure 49: XRD patterns for 0.23%C alloy sintered at 1300°C and sintered + solution annealed.

Table 10 reports the results of the quantitative XRD analyses on the as sintered and the solution annealed materials. The as atomized powder is fully f.c.c. in all cases, since the carbide precipitation is suppressed by the large solidification undercooling on atomization.

Table 10: XRD analyses.

Materials	**Constitution of the metallic matrix**	
	% fcc	***% hcp***
0.35%C alloy as sintered	-	*100*
0.35%C alloy + SA	*62±1.3*	*38±1.3*
0.23%C alloy - S1300°C	42±1.2	58±1.2
0.23%C alloy - S1300°C + SA	61±1.2	39±1.2
0.23%C alloy - S1350°C	*43±1.5*	*57±1.5*
0.23%C alloy - S1350°C + SA	*33±1.5*	*67±1.5*
0.05%C alloy as sintered	-	100
0.05%C alloy + SA	-	100

The 0.05%C alloy is fully h.c.p. in the as sintered condition since the low C content allows the $\alpha \rightarrow \varepsilon$ transformation to go to completion on slow cooling. The as sintered 0.35%C material is fully h.c.p.

too, since carbon is almost completely bounded to carbides and the behavior on cooling is very similar to the previous material.

The 0.23%C as sintered alloys contains both f.c.c. and h.c.p. phases in the same relative proportions, despite the different microstructures. In the 1300°C materials, f.c.c. phase is stabilized by the residual interstitial carbon in solid solution and by the fine grain size. The main difference between the two materials is the presence of the Mo-rich M_6C carbides and a significantly larger grain sizes than those found after sintering at higher temperature. Whilst the carbon in solution tends to stabilize the f.c.c. phase, smaller grain size is favorable to the $\alpha \rightarrow \varepsilon$ transformation [11]. The two effects are then balanced, and the fraction of h.c.p. in the as sintered materials does not change with the sintering temperature

Solution annealing does not influence the matrix constitution in 0.05%C alloy, since there is no significant modification of the composition of the matrix. The extensive dissolution of carbides in 0.35%C is responsible for the stabilization of some f.c.c. phase in the final microstructure.

In the 0.23%C material sintered at 1300°C, solution annealing dissolves most of carbides which increases the concentration of interstitial carbon, therefore the f.c.c. fraction increases after heat treatment. The f.c.c. phase is then stabilized against the transformation in h.c.p. on quenching.

In 0.23%C material sintered at 1350°C, solution annealing dissolves preferentially the M_6C carbides, leading to an increase in the Mo content of the f.c.c. phase. Consequently, the transformation to h.c.p. upon quenching is enhanced, and the amount of f.c.c. phase decreases with heat treatment.

XRD analyses were not carried out on aged materials, because of the lower interest they present for mechanical properties as described in the next section.

5.1.4 Hardness and microhardness

Microhardness and hardness are reported in figures 50 to 53.

Both microhardness and hardness do not change with heat treatment in 0.05%C material, since microstructural characteristics are very similar because of the very low C content.

Solution annealing causes a slight increase in microhardness (because of solution hardening by carbon and alloying elements) in all the other materials. On aging, microhardness increases, in particular after 20 hours, because of the intragranular precipitation.

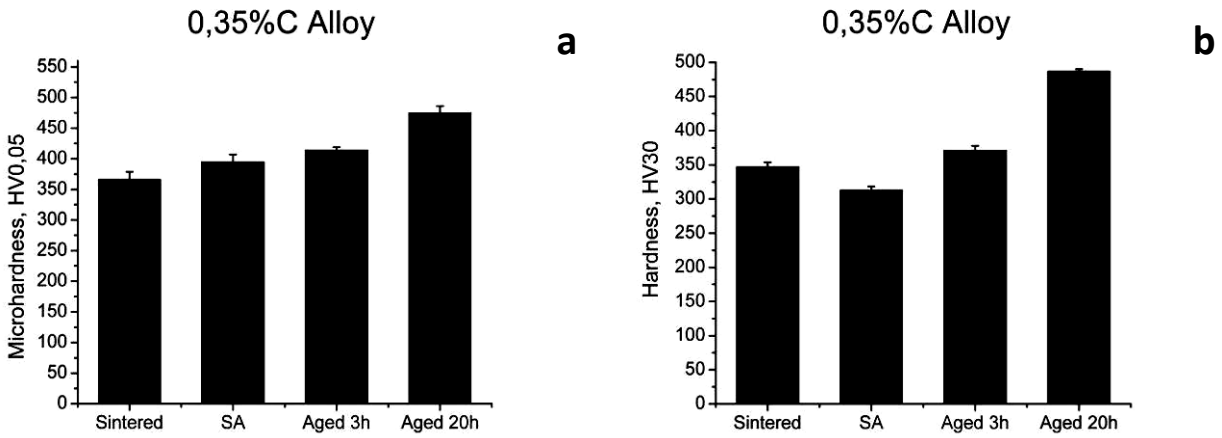

Figure 50: Microhardness (a) and hardness (b) of 0.35%C alloy sintered at 1300°C.

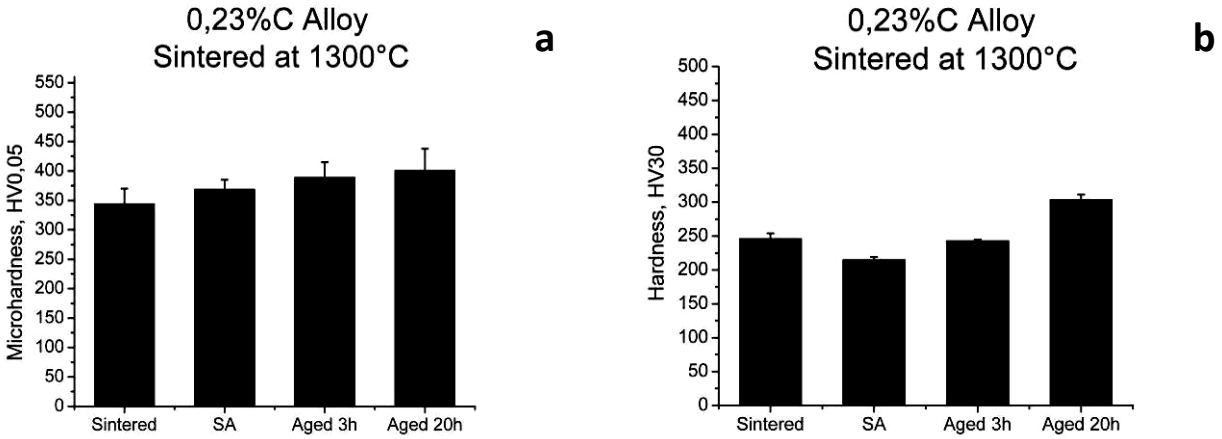

Figure 51: Microhardness (a) and hardness (b) of 0.23%C alloy sintered at 1300°C.

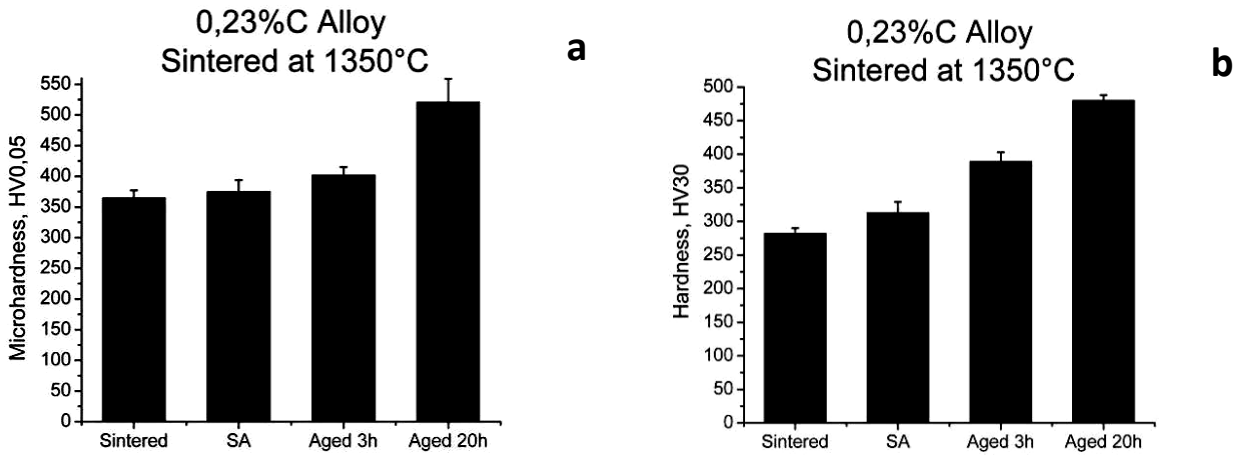

Figure 52: Microhardness (a) and hardness (b) of 0.23%C alloy sintered at 1350°C.

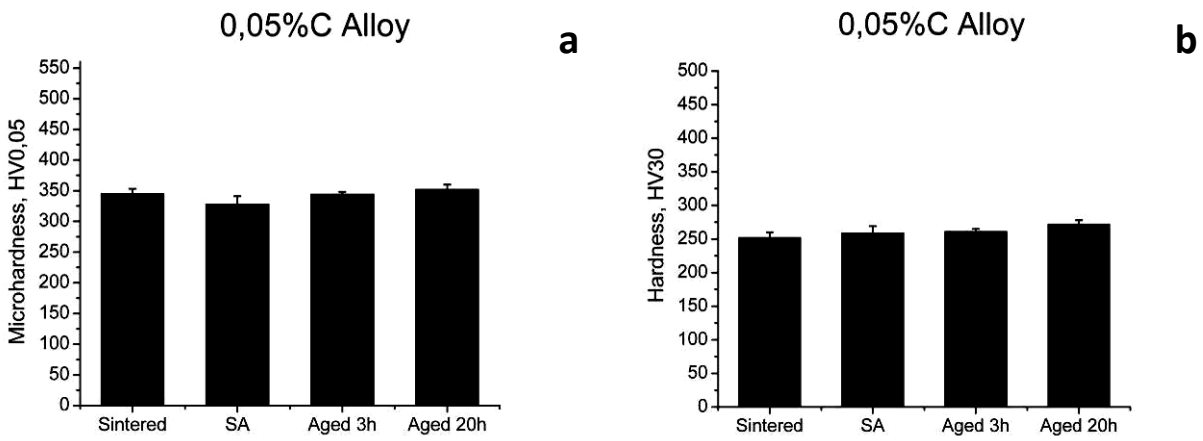

Figure 53: Microhardness (a) and hardness (b) of 0.05%C alloy sintered at 1380°C.

Hardness values of the 0.35%C (figure 50b) and 1300°C sintered 0.23%C (figure 51b) materials decrease with solution annealing because of grain growth and dissolution of carbides. These two effects prevail on the solution hardening of the metallic matrix provided by the enrichment in alloy elements. Contrarily, solution hardening of the matrix causes a slight increase in hardness of the material 0.23%C sintered at 1350°C (figure 52b) since solution annealing does not eliminate all carbides and does not cause grain growth.

Figure 54 shows hardness versus aging time.

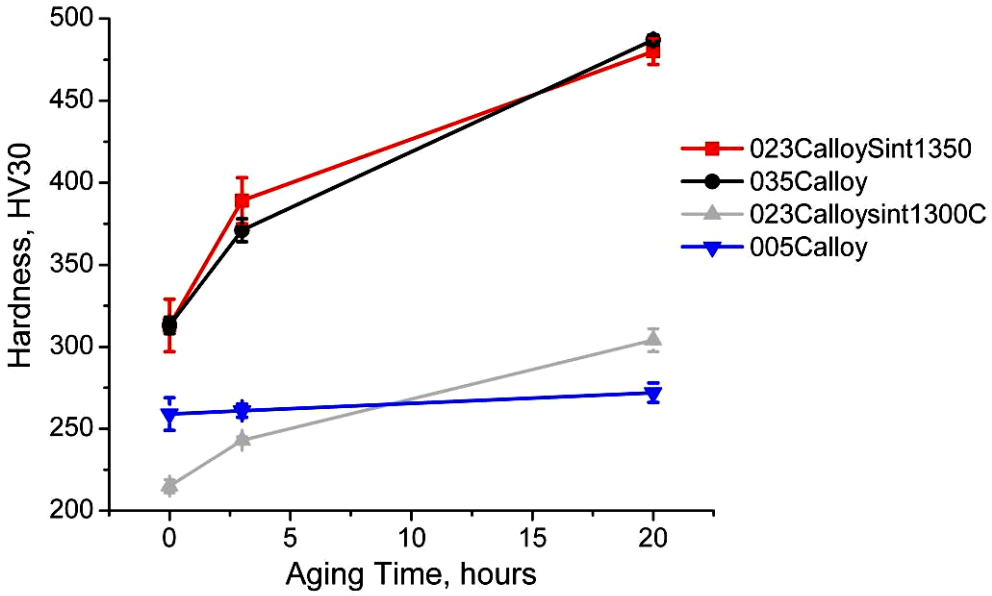

Figure 54: Hardness versus aging time profile.

The increase in hardness during aging is due to the intragranular precipitation of the Widmanstätten carbides and of the grain boundary lamellar constituent. The trend is less pronounced for the 0.05%C

material because of the less precipitation during aging. The lower density of the material 0.23%C sintered at 1300°C accounts for the lower hardness, with respect to that other materials.

5.1.5 Tensile tests

The results of tensile tests are summarized in figures 55 to 58, and compared with the prescriptions of the ISO 5832-4 standard for orthopaedic implants.

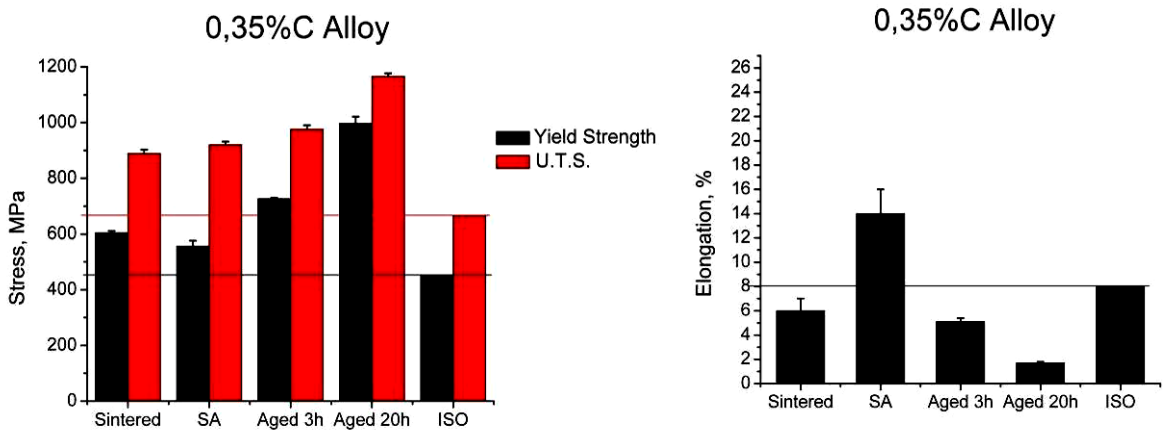

Figure 55: Tensile properties of 0.35%C alloy sintered at 1300°C.

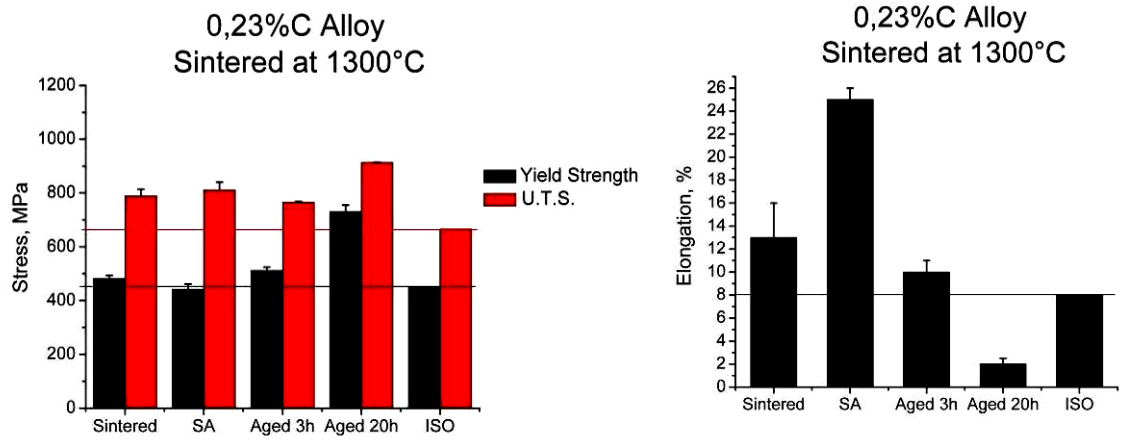

Figure 56: Tensile properties of 0.23%C alloy sintered at 1300°C.

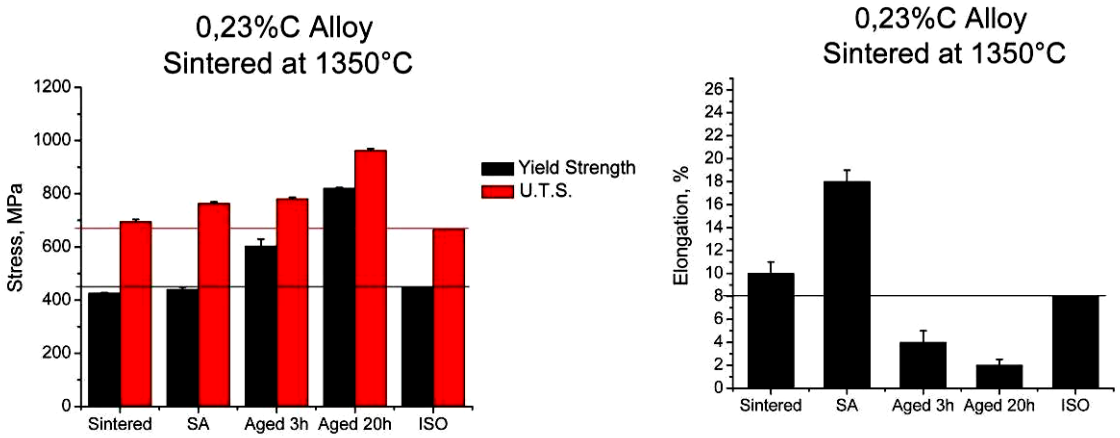

Figure 57: Tensile properties of 0.23%C alloy sintered at 1350°C.

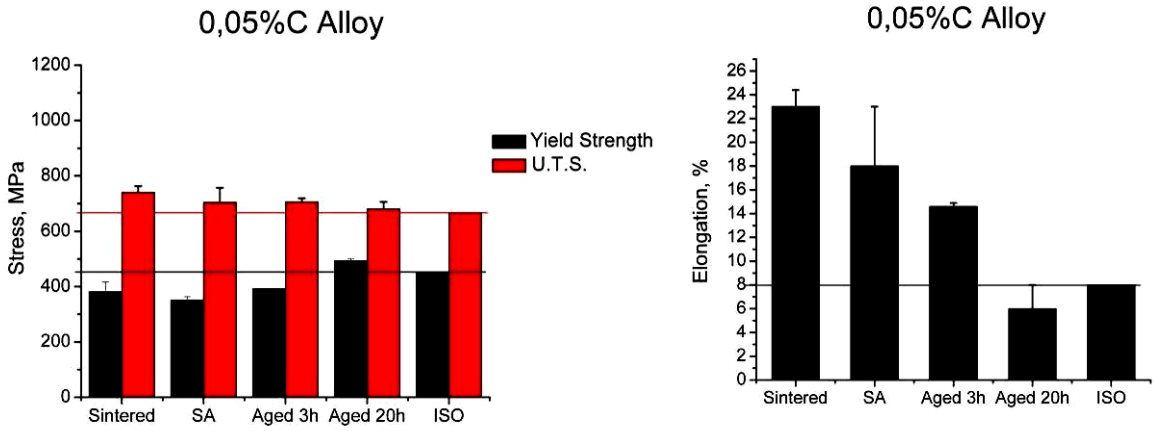

Figure 58: Tensile properties of 0.05%C alloy sintered at 1380°C.

Solubilisation modifies the mechanical properties of the 0.23%C and the 0.35%C materials significantly; yield strength is decreased since the strengthening effect of carbides is stronger than that of the dissolved carbon and alloying elements in the matrix, and ductility and UTS are correspondingly increased because of the improved plasticity of the material. The 0.05%C material has both better strength and ductility in the as sintered condition, likely because the microstructure remains martensitic.

The 0.23%C material sintered at lower temperature presents both strength and ductility surprisingly better than those of that sintered at the higher one, despite the lower density. The higher yield stress may be correlated to the smaller grain size, according to the Hall-Petch relation. Even after solution annealing, the material sintered at lower temperature has better mechanical properties than the high temperature one. The different grain size and the residual grain boundary carbides are responsible for this difference.

After aging, strength still increases but ductility strongly decreases for all materials, because of the slip restrictions exerted by faults in h.c.p. martensite and by the Widmanstätten precipitates [48], but mainly of the grain boundary precipitates of the h.c.p_2. phase.

Figure 59 shows the effect of the carbon content on the yield strength and elongation of the as sintered materials. In principle, on increasing the carbon content the strength of the alloy increases, whilst ductility decreases, because of the effect of carbides on the deformation and fracture behavior [17, 51, 52], which promote an intergranular fracture [52].

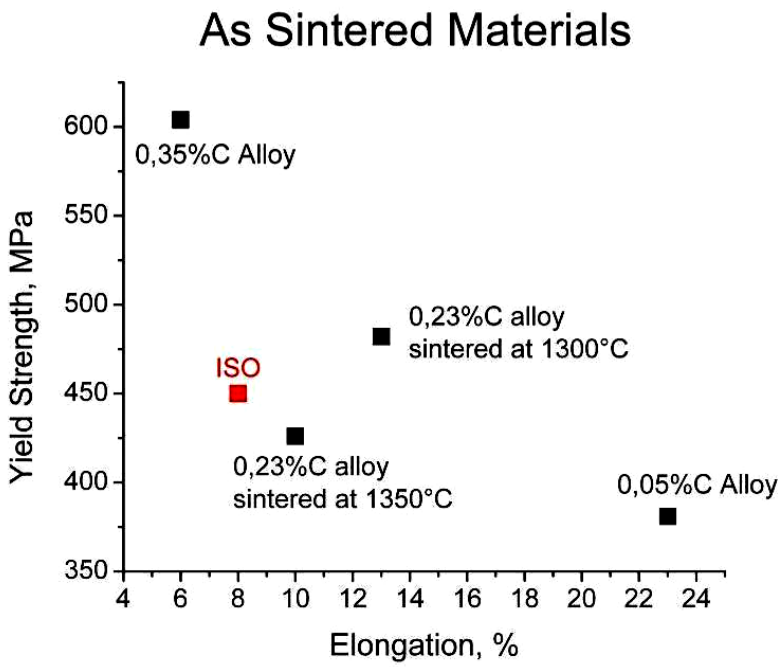

Figure 59: Graphic of yield strength vs. elongation for as sintered materials.

With reference to the ISO standard, the solution annealed 0.35%C material matches all the specifications. The material with 0.23%C sintered at 1300°C and solution annealed shows good mechanical properties too, but due to its high porosity cannot be considered for the specific applications. The same material, when sintered at 1350°C and solution annealed matches UTS and ε% of the ISO standard, whilst yield strength is slightly lower. The 0.05%C alloy has a yield strength much lower than that required by ISO specifications. Figure 60 shows the summarized results of tensile tests of the 0.35%C material in a "yield strength – percent elongation" map.

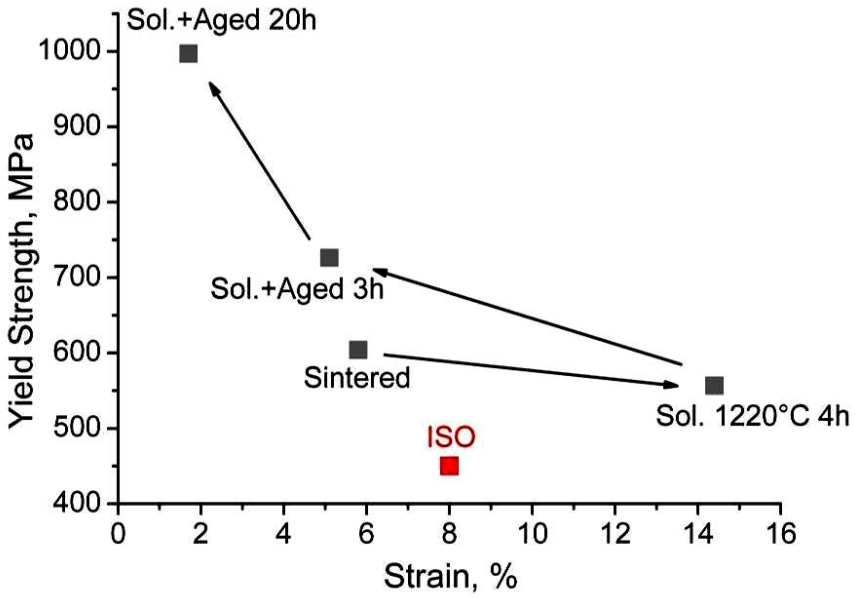

Figure 60: Yield strength and percent elongation at fracture for 0.35%C as sintered material, solution annealed and then aged.

So, solution annealing increases ductility, with a slight decrease of yield strength. On aging strength further increases, but the decrease in ductility is very pronounced because of the negative effect of the grain boundary hexagonal constituent [51].

Fracture surfaces:

In figure 61, the fracture surfaces for 0.35%C material are showed. In the as sintered material, figure 61a, cracks propagate along grain boundaries by cracking of grain boundary carbides and separation at the carbide/matrix interface. After solution annealing, figure 61b, the failure mode is still intergranular, but ductility of the alloy is increased due to the increased ability of the material to deform by localized shear in the regions near grain boundaries.

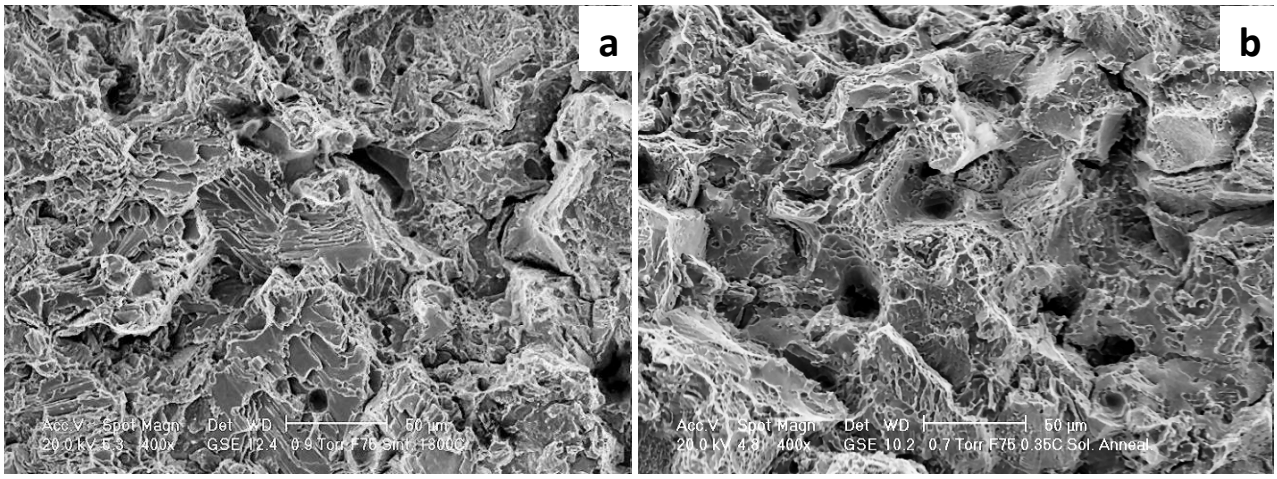

Figure 61:Fracture surface for 0.35%C material as sintered (a) and after solution annealing (b).

The different ductility for 0.23%C materials finds an explanation in the fracture behaviour. Figure 62 shows the fracture surfaces of the two as sintered materials.

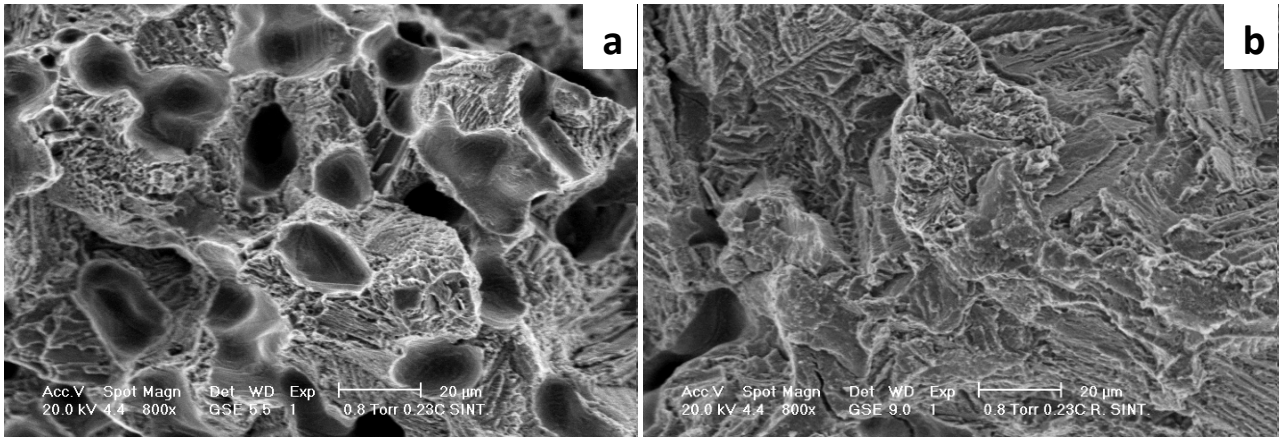

Figure 62: Fracture surface for as sintered 0.23%C material, sintered at 1300°C (a) and 1350°C (b).

Fracture is fully intergranular and associated with the presence of carbides and sigma phase which cause strain localization and favour the nucleation and propagation of cracks [43].

The fracture surface of the solution annealed 0.23%C material gives evidence of the improved ductility with respect to the as sintered ones (figure 63). Fracture involves the cobalt matrix, which shows striations similar to deformation bands in the regions between the zones of intense shear. Only in the material sintered at the higher temperature (figure 63b), a brittle morphology is visible, attributable to grain boundary carbides. The low amount of carbides, and their absence in the 1300°C sintered material, allows deformation to propagate through the metallic matrix by stacking fault formation and twining [43].

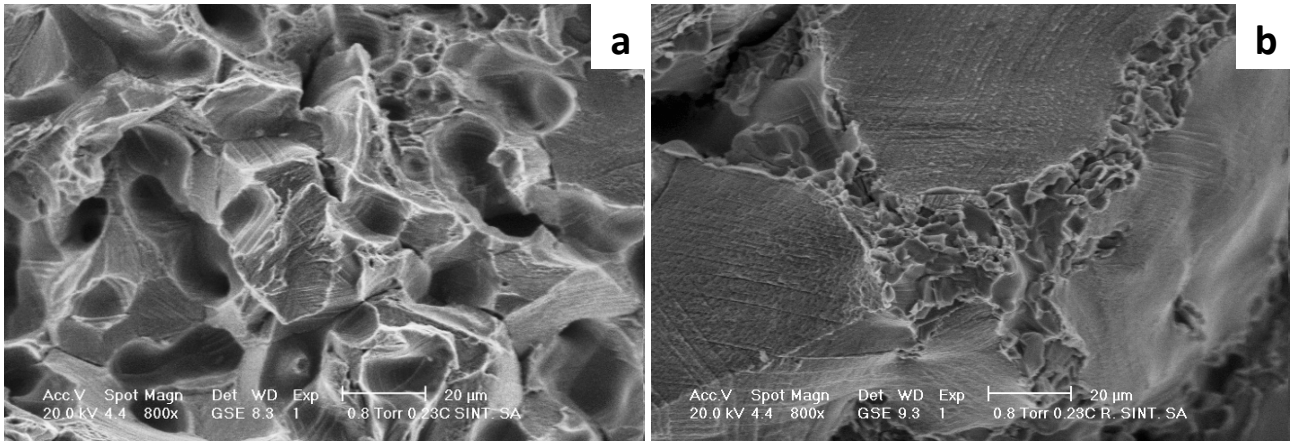

Figure 63: Fracture surface for the solution annealed 0.23%C material, sintered at 1300°C (a) and 1350°C (b)

In aged specimens, the grain boundary precipitation of hcp_2 causes intergranular fracture, clearly visible on the fracture surfaces shown in figure 64.

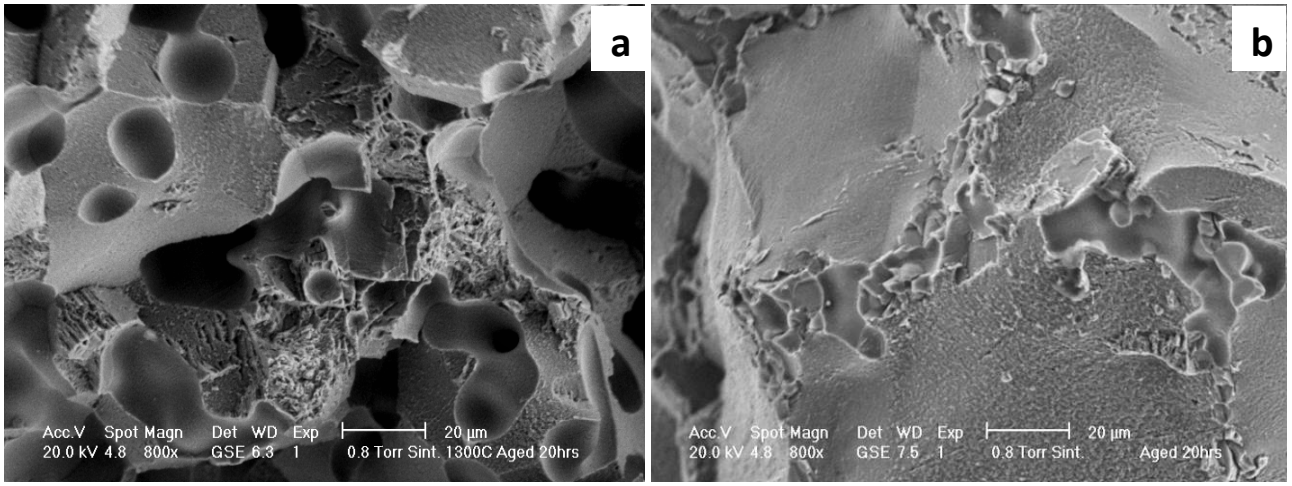

Figure 64: Fracture surface for the aged 0.23%C material, sintered at 1300°C (a) and 1350°C (b)

The fracture surface of the 0.05%C as sintered material, figure 65a, is still intergranular with dimples, which accounts for the large ductility. The large decrease of ductility on aging is clearly demonstrated by the fracture surfaces of the as sintered and 20 hours aged materials, shown in figure 65.

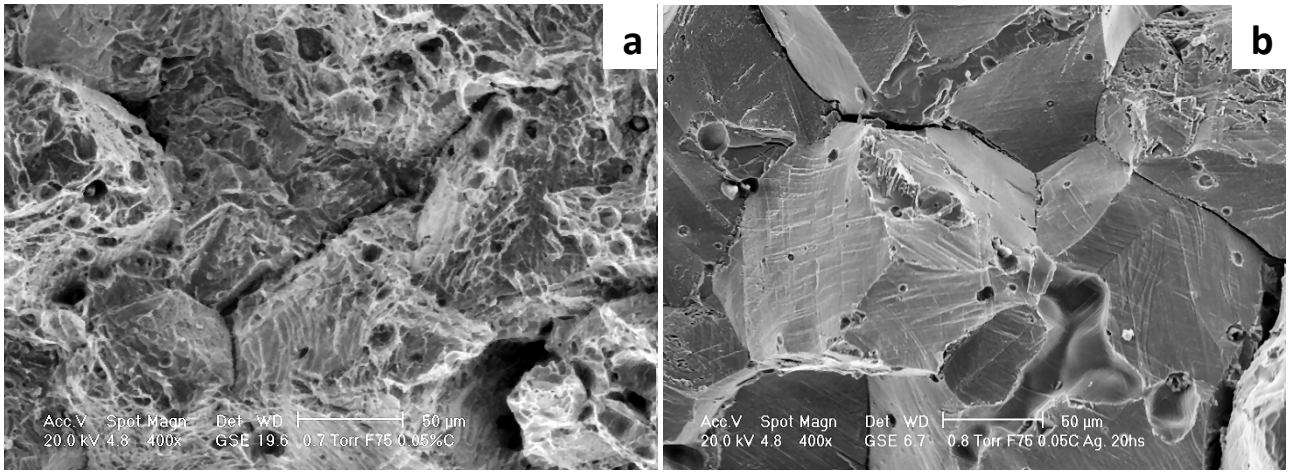

Figure 65: Fracture surface of 0.05%C material as sintered (a) and aged for 20hs (b).

For all materials the fracture is intergranular and the best combination of mechanical properties is obtained by solubilization, which minimizes the amount of grain boundary phases, responsible of brittleness irrespective on their nature.

Strain hardenability:

An interesting feature of these materials is the large difference between yield strength and UTS, which is representative of a high strain hardenability. Figure 66 shows the stress-strain curves for the materials that present the best mechanical properties of this study; the increase in the proof stress along the plastic field is pronounced, significant of a great resistance to plastic deformation [43]. This property is of great importance to resist overloading.

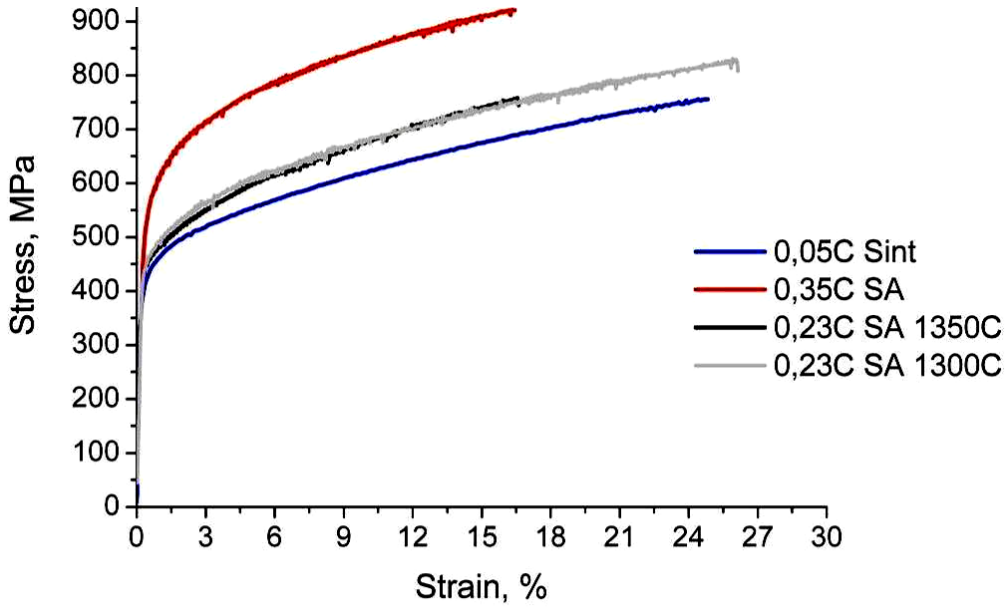

Figure 66: Tensile stress - strain curves for the materials.

The microstructure of the solution annealed material is mainly austenitic (Table 10), but the amount of austenite close to the fracture surface after tensile tests is almost negligible, as shown by XRD analysis. Strain hardenability is therefore due to the strain induced transformation of austenite into martensite. The strain hardening coefficient cannot be calculated with the classical Ludwick-Hollomon model [53], since the log-log diagram of true stress versus true strain does not depict a linear correlation but it shows a continuous increase in the slope, as figure 67 demonstrates. The upward curvature is significant of the increasing strain hardenability with plastic strain [17].

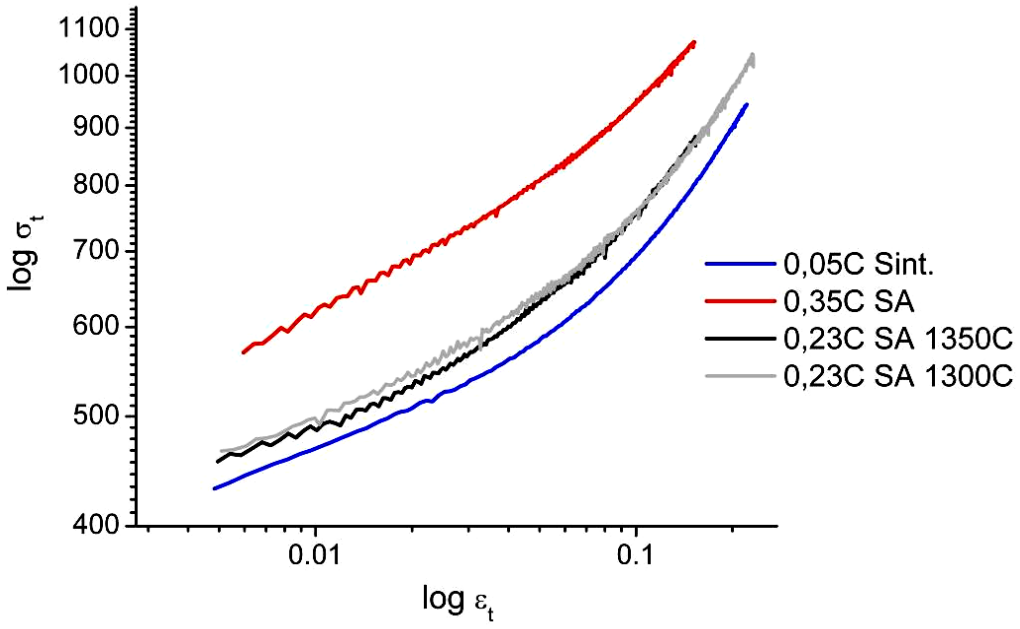

Figure 67: True stress – true strain plot of the as sintered 0.05%C material and solution annealed 0.35%C and 0.23%C materials.

The cobalt alloy has a low stacking fault energy, which promotes stacking faults formation and twinning [43, 48-50]. Interaction of dislocations of limited mobility with other sessile dislocations, and with stacking faults and twins, can lead to very high strain hardening rates that produce intensive localized stresses which need to be relieved in order to allow the material to resist higher loads [43]. Moreover, the f.c.c. phase transforms into h.c.p. martensite on straining, providing an additional contribution to strain hardenability by the well known transformation induced plasticity - TRIP – phenomenon [17, 54].

Kim and Lin [55] proposed a three parameters model to determine the strain hardening coefficient for a metastable austenite in steel. The correlation between true stress and true strain, assumed to be quadratic, is:

$$ln\sigma_t = a(ln\varepsilon_t)^2 + b(ln\varepsilon_t) + c \quad (1)$$

where a, b and c are constants to be determined by interpolation of experimental data. Experimental data show that a linear relationship can be assumed between strain hardening coefficient n and true strain, then the following equation is proposed by Kim and Lim [55]:

$$n = d\ln\sigma_t / d\ln\varepsilon_t = M\varepsilon_t + N \quad (2)$$

where M and N are temperature dependent constants. Upon integration of equation 2, the following flow equation is obtained:

$$\sigma_t = K\varepsilon_t^{N} exp(M\varepsilon_t) \quad (3)$$

K is a constant depending on the material, whilst M describes how the flow stress increases with the plastic strain because of the strain induced transformation of austenite.
Figure 68 shows the results of fitting of equation (2) and Table 11 lists K, M and N parameters. The correlation parameter is included, as well, to evaluate the goodness of the model.

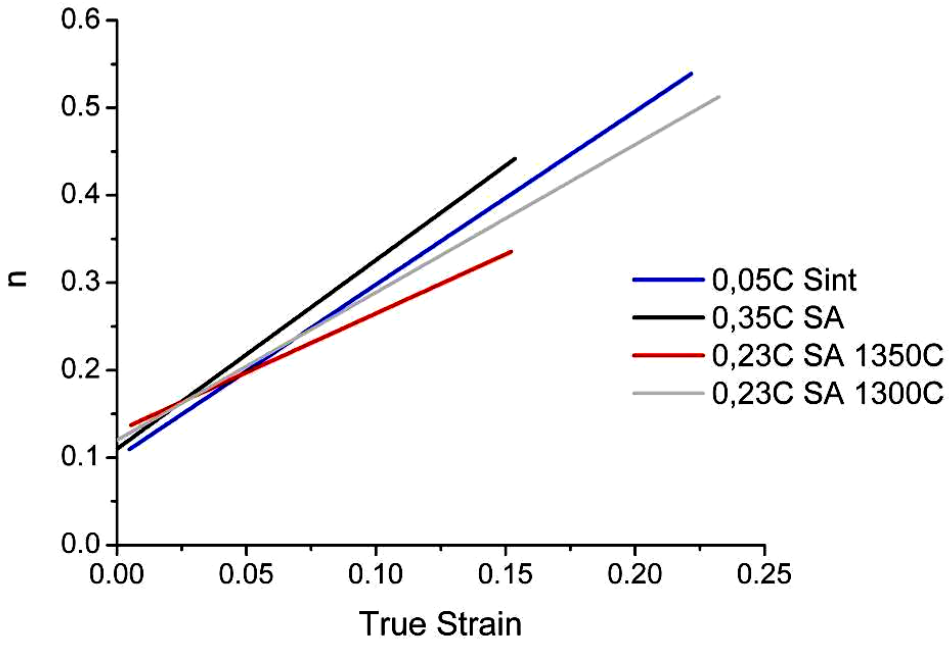

Figure 68: strain hardening coefficient versus plastic strain for as sintered 0.05%C material and solution annealed 0.35%C and 0.23%C materials.

Table 11: Parameters of the fitting of plastic field

Materials	K	M	N	R^2
***0.35%C** alloy – SA*	*1120*	*1.35*	*0.13*	*0.9992*
0.23%C alloy – S1300°C + SA	839.43	1.69	0.12	0.9992
***0.23%C** alloy – S1350°C + SA*	*775.29*	*2.16*	*0.11*	*0.9992*
0.05%C alloy – as sintered	706.50	1.98	0.10	0.9997

N, which represents the initial work hardening coefficient, is quite low in all the materials. The increase in strain hardening with strain is represented by M. It is higher in the 0.23%C material sintered at 1350°C and in the 0.05%C as sintered material, which contains the higher fraction of martensite having a great tendency to strain hardening, because of the large density of stacking faults which accompany its formation on heat treatment [56].

The high strain hardening can be the explanation for the good ductility of the solution annealing materials also in presence of the intergranular fracture, because the material has a great capacity to resist localized loads by deformation.

5.1.6 Wear resistance

The influence on the wear resistance of MIM products is not yet established, so lubricated wear tests are carried out on all as sintered and solution annealing materials. On aged materials the tests are not made because of their less favorable mechanical properties.

As far as wear resistance is concerned, a study on a cast alloy concludes that carbides may cause abrasive wear of the counterface polymeric material, which could release debris at the metal-polyethylene interface [42]. The UHMWPE wear debris is mainly responsible for periprosthetic tissue reaction, osteolysis, and eventually, late aseptic loosening. In a metal-on-metal wear test, the effect of the constitution of the metallic matrix on wear was investigated, concluding that a fully h.c.p. martensitic material has a lower wear resistance than a fully austenitic, because of the more favourable friction coefficient [57].

In figure 69 the friction coefficient tracks for the 0.35%C materials are reported, as representative of the results obtained for the other materials, too. A gradual decrease of the friction coefficient towards a steady value occurs. The steady value is typical of a mixed lubricant condition, and is slightly but significantly lower for the solution annealed material.

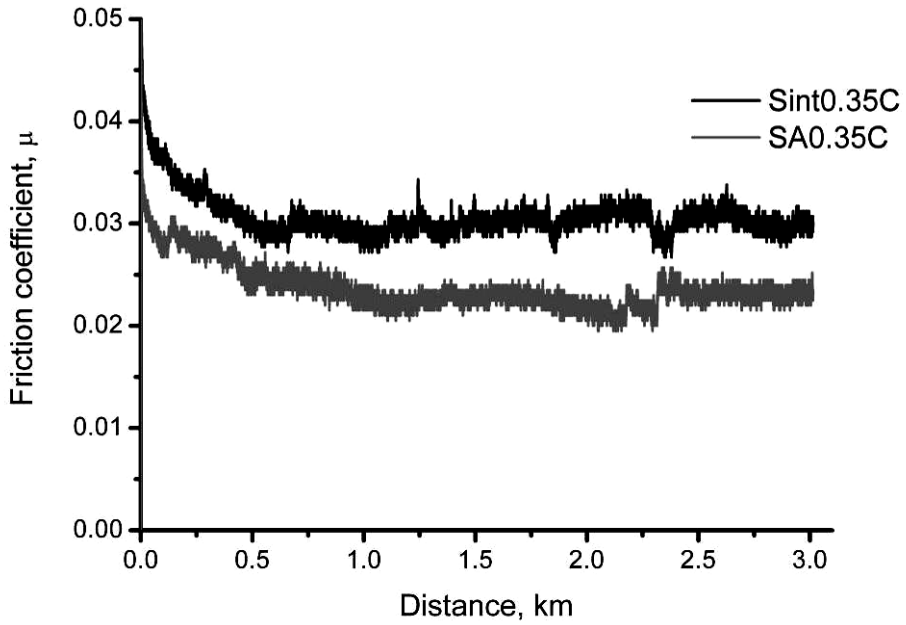

Figure 69: Friction coefficient vs. distance curve.

As expected from the different hardness of the two counteracting materials, no mass loss of the Co alloys was measured, whilst some debris of UHMWPE are transferred to its surface, as figure 70 shows. This phenomenon was described by Walker [42] on a cast cobalt alloy. A slight but measurable mass loss of the polymer is then induced, comparable to literature data [58]. A higher quantity of transferred polymer in the solution annealed materials is found for all materials.

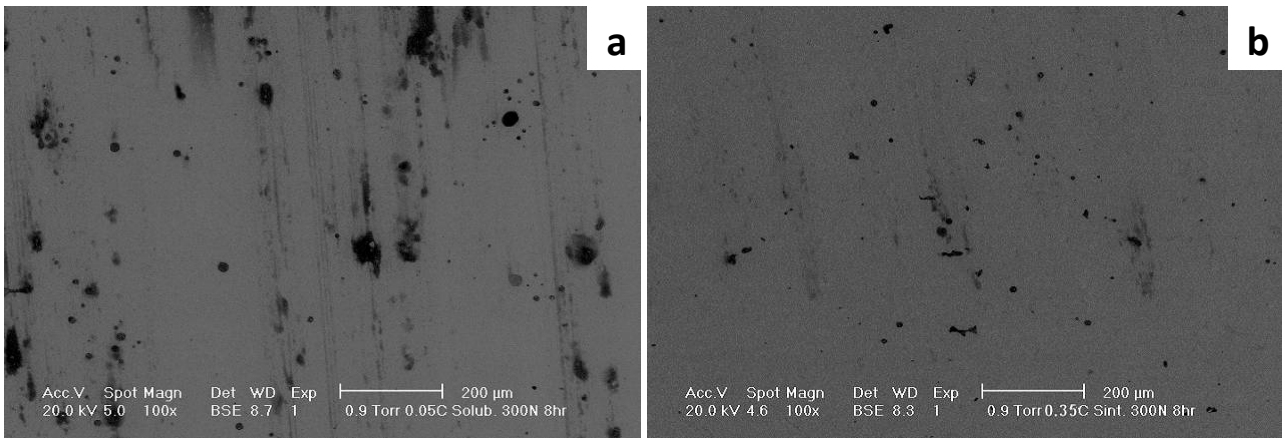

Figure 70: Wear traces for 0,05%C SA material (a) and 0,35%C sintered material (b)

To quantify the wear phenomenon, the mass loss of UHMWPE and the increase in the surface roughness of the Co alloys, which is significant of the material transfer, are considered and reported in table 12. It has to be considered that the measure of the mass loss of the polymer, even with the use of a precision balance, is quite a hard task; therefore data must be considered as indicative.

Table 12: Mass loss of UHMWPE versus surface roughness of the Co alloys.

Materials	ΔRa cobalt alloy (μm)	Δm UHMWPE (mg)
***0.35%C** alloy – as Sintered*	*0.028*	*0*
***0.35%C** alloy – SA*	*0.031*	*-0.4*
0.23%C alloy - S1300°C	0.055	-1
0.23%C alloy - S1300°C + SA	0.087	-0.5
***0.23%C** alloy - S1350°C*	*0.076*	*-0.9*
***0.23%C** alloy - S1350°C + SA*	*0.100*	*-0.6*
0.05%C alloy – as sintered	0.061	-0.4
0.05%C alloy – SA	0.076	0

The solution annealed materials cause a lower mass loss on the UHMWPE. They also evolve towards a higher surface roughness than the as sintered ones which, in combination with the lower steady value of the friction coefficient, could suggest that the transferred layer may give an additional contribution to lubrication. The 0.35%C material is the exception, because the polymer did not present a mass loss.
The data of table 12 are reported in figure 71 to compare the eight materials for a global evaluation.

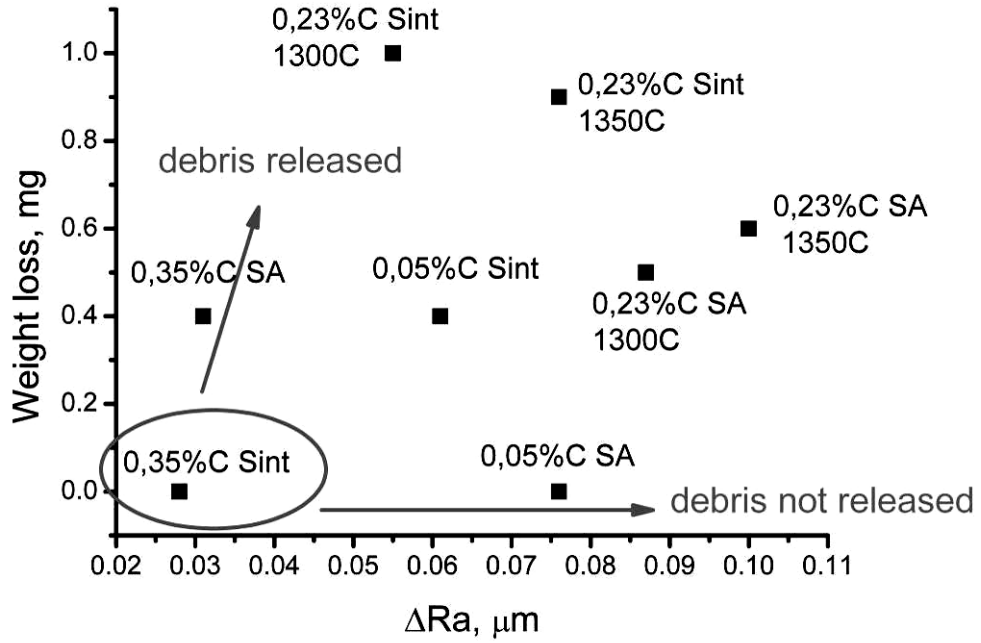

Figure 71: Weight loss and ΔRa of the investigated materials

The best wear behavior is displayed by the 0.35%C material, in the as sintered condition. It does not cause a measurable wear of the polymer and the surface roughness worsens very slightly. In presence of a

lubricant, the abrasive effect of carbides is then almost completely avoided. All the other materials have a worse behavior. Among them, solution annealed 0.35%C and solution annealed 0.05%C represent two opposite situations. The former causes a measurable wear of the polymer, but roughness of the cobalt alloy does not worsen significantly; the latter does not cause a measurable mass loss of the polymer, but its surface roughness worsens significantly. This different behavior could be interpreted considering that debris of the polymer can either adhere on the metal surface (increasing roughness) or be removed by the lubricant (in this case the surface roughness does not change). Which of the two options might be preferred in application is a matter of discussion; in principle, the former could be preferred, which does not release debris from the tribological system and, at the same time, does not worsen the contact conditions, as the decrease of the steady friction coefficient indicates.

The role of carbides, which are suspected to abrade the counterface polymer, is minimized by the lubricant. However, the comparison between as sintered and solution annealed 0.35%C seems to indicate that the localized particles after heat treatment are more abrasive than the more homogeneously distributed carbides in the as sintered material.

So, wear tests show that the wear rate of the counterface UHMWPE (0,05÷0,4 mm/year) is comparable to that reported for a real prosthesis (0.1÷0.3 mm/year [58]), and is influenced by the Co alloy microstructure.

5.1.7 Corrosion tests

Co-base alloys are known to possess a high resistance to corrosion in physical media, imparted by a passive oxide film that forms spontaneously on the alloy surface, and to their excellent mechanical properties. According to Georgette and Davidson [59], a more stable, uniform oxide layer would be expected with a more homogeneous matrix (annealed alloy) than with a highly dendritic as cast structure. Placko et al. [60] found a progressive dissolution of the matrix with preferential attack of the grain boundaries and regions adjacent to carbides due to sensitization. According to Montero-Ocampo and Rodriguez [61], the low C content ASTM-F75 as cast alloys resulted in lower release rates of corrosion products. Heat treatments may change the biocompatibility of the alloys through the modification of the electrochemical properties [62].

The influence on the corrosion resistance of MIM products is not yet established, so the corrosion tests are carried out for the as sintered and solution annealed materials.

<u>Open circuit potential test</u>

As shown in figures 72a, b, c and d, all the materials reach a similar OCP value just after immersion that was about -0.3 and -0.2 V, except the 0.23%C material sintered at 1300°C, but the behavior and the stabilization of the potential during time is quite different: the 0.35%C and 0.23%C sintered at 1300°C materials become much nobler during the first 10-15 hours of the immersion, showing an increase of about 0.3 and 0.5 V compared with the starting value and monitoring a change in the surface equilibrium due to the exposure

environment. The 0.23%C material sintered at 1350°C, SA material sintered at 1300°C, and 0.5%C material on the contrary do not show big changes in the potential during immersion. After this initial transient two different behaviors are visible:

- a stabilization of the potential on a steady value, (0.05%C SA, 0.23%C Sint at 1350°C and SA, and 0.23%C SA sintered at 1300°C).
- a slight but continuous increase in the potential, towards more noble values (0.05%C Sint., 0.35%C Sint., 0.35%C SA and 0.23%C sintered at 1300°C).

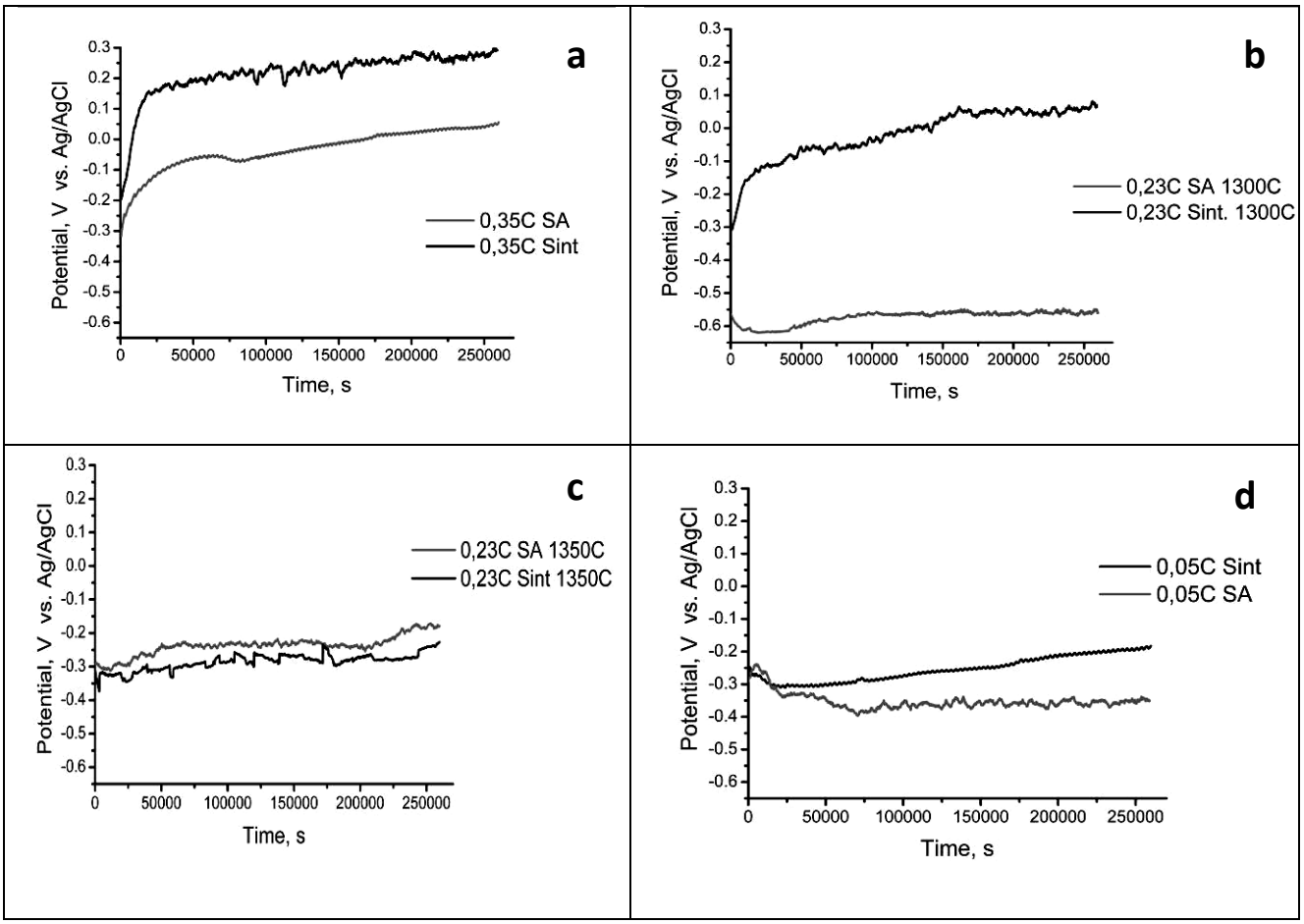

Figure 72: Open circuit curves for 0.35%C (a), 0.23%C (b and c) and 0.05%C (d) materials.

The influence of the presence of carbides can be appreciated comparing the same material in the as sintered and solution annealed conditions, figure 72, even if they have a different matrix constitution. When the carbide content increases, the potential increases too.

In order to consider the effect of the matrix constitution on the OCP evolution, the 0.05%C SA, 0.023%C SA sintered at 1350°C and 0.35%C SA materials containing a decreasing amount of h.c.p. phase and almost no carbides are compared, figure 73. The difference in OCP values is quite evident and the more h.c.p. fraction (0.05%C SA > 0.23%C SA sint. at 1350°C > 0.35%C SA), the less noble is the electrochemical behavior.

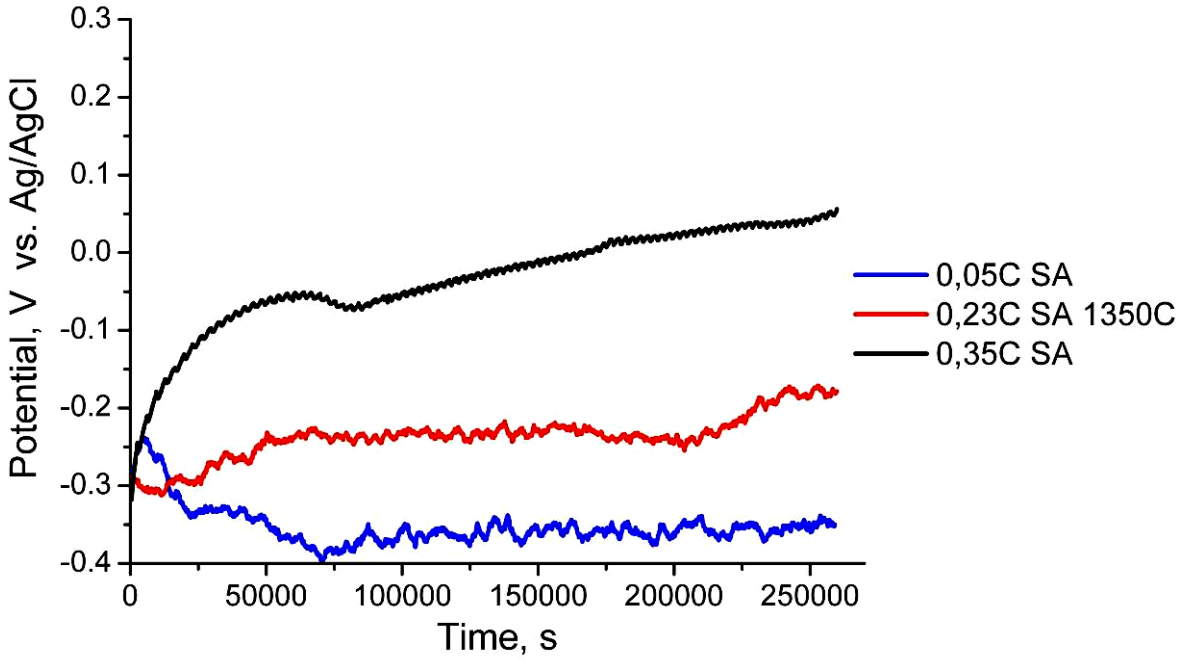

Figure 73: Effect of the matrix constitution on the OCP evolution.

Considering samples with the same matrix phase, figure 74, the comparison between 0.05%C sintered and solution annealed materials and 0.35%C sintered confirms that the higher quantity of carbides tends to enhance nobility.

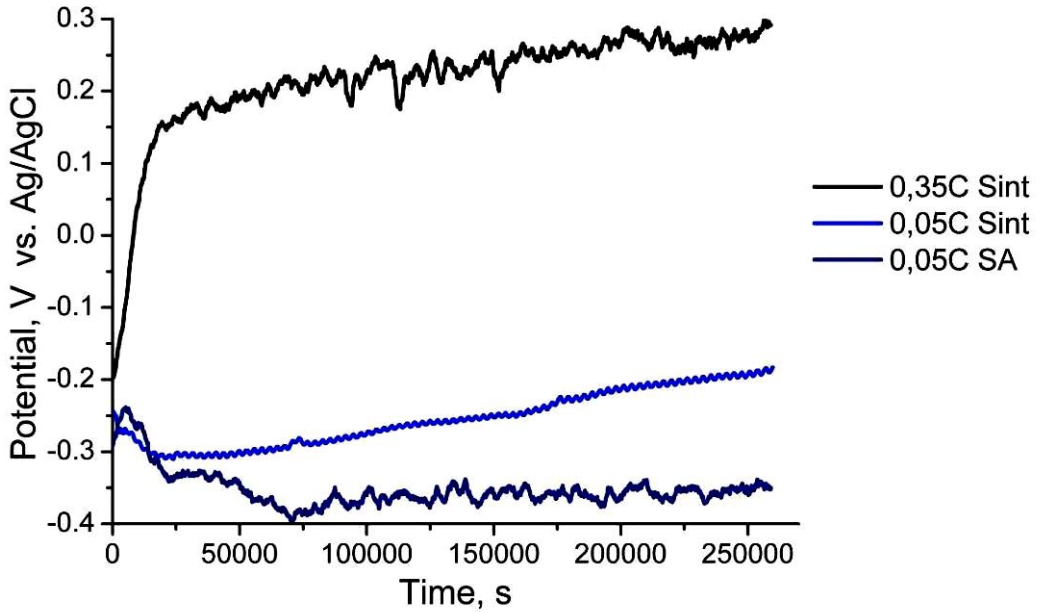

Figure 74: Effect of carbides on the OCP evolution.

Potentiodynamic curves

In order to better evaluate the stability of the passivity and the electrochemical behavior of the samples potentodynamic curves were analyzed.

Some representative potentiodynamic curves are reported in figure 75.

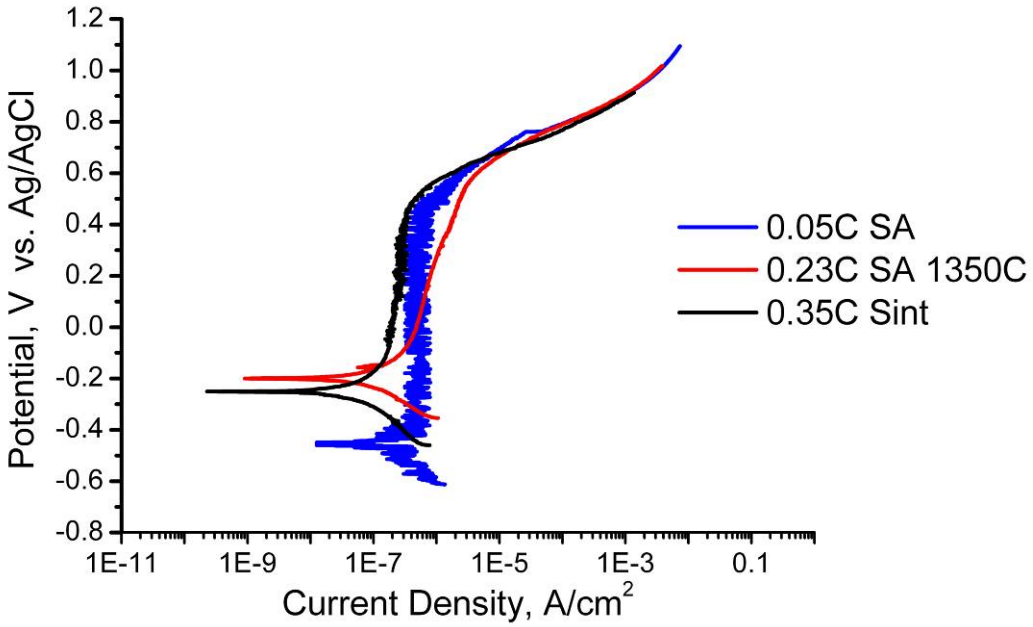

Figure 75: Potentiodynamic curves.

All the materials show passive behavior in this environment and the main electrochemical parameters are summarized in table 13.

Table 13: Electrochemical parameters.

Materials	**E_{corr} [V]**	**i_{pass} [A/cm^2]**	**E_b [V]**
***0.35%C** alloy – as Sintered*	*-0.24*	*$3x10^{-7}$*	*0.6*
0.23%C alloy - S1350°C + SA	-0.2	10^{-6}	0.6
***0.05%C alloy** – SA*	*-0.48*	*$5x10^{-7}$*	*0.6*

The sintered 0.35%C and 1350°C sintered and solution annealed 0.23%C materials present a nobler free corrosion potential than 0.05%C, as found in open circuit curves.

Regarding the passive corrosion density, the material with 0.23%C presents higher values than 0.35%C and 0.05%C, but the potential of breakdown is the same for all specimens.

To understand the morphology of the corrosion process, the specimens have been examined by optical microscopy just after breakdown and after the evolution of the corrosion process (figures 76 to 78). Based on the micrographs we can appraise:

- Carbides do not oxidize;
- The metal matrix oxidizes, the breakdown is due to the transpassivity and no pits are present;
- The corrosive attack is localized at the carbides-matrix interface and leads to the complete removal of the carbide particles/eutectic cells.

The composition of the layer is predominantly Cr_2O_3 oxide with some minor contribution of other oxides (Co and Mo oxides) [63]. According to Hodgson et al. [64], the passive behavior of Co-Cr-Mo is due to the formation of an oxide layer with high content of Cr (mainly as Cr III) and a smaller amount of $Cr(OH)_3$.

Moreover it may be appreciated that the corrosion of the 0.05%C occurs by localized attacks, while the 0.23%C samples show an intergranular corrosion morphology. The 0.35%C material shows a large corroded area corresponding to carbide/eutectic phase.

Therefore, although carbides enhance the electrochemical nobility, the presence of the carbide/eutectic phase leads to a different corrosion morphology when the traspassivity state is reached.

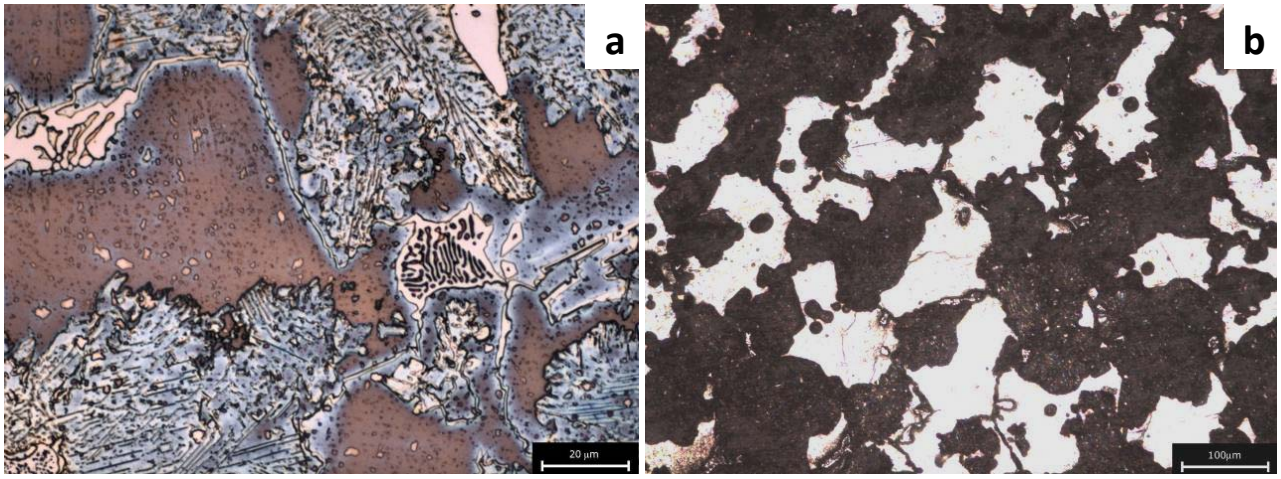

Figure 76: Corrosion micrographs of 0.35%C after breakdown (a) and the evolution of corrosion process (b).

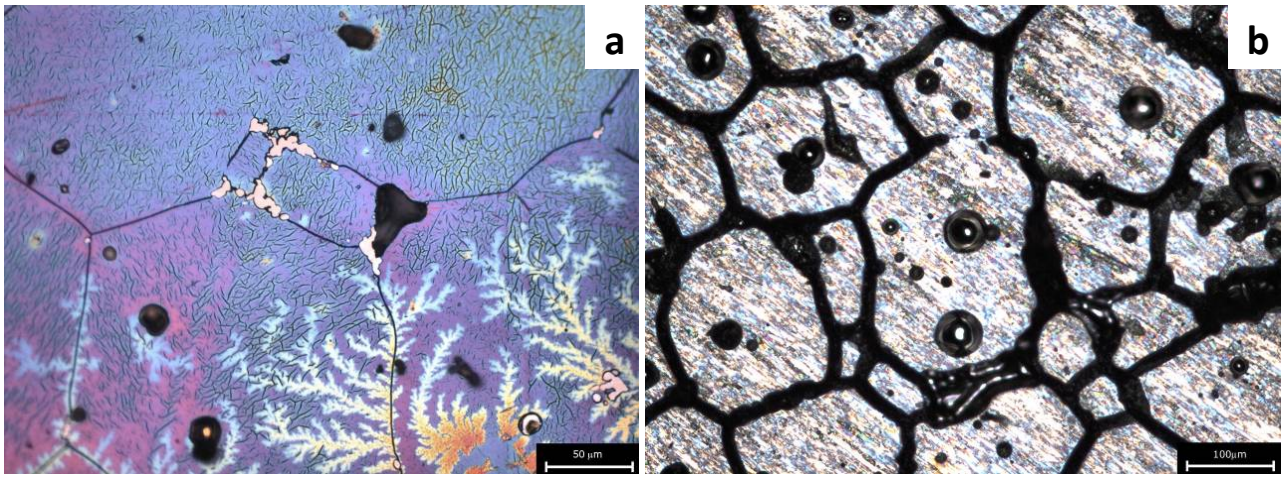

Figure 77: Corrosion micrographs of 0.23%C after breakdown (a) and the evolution of corrosion process (b).

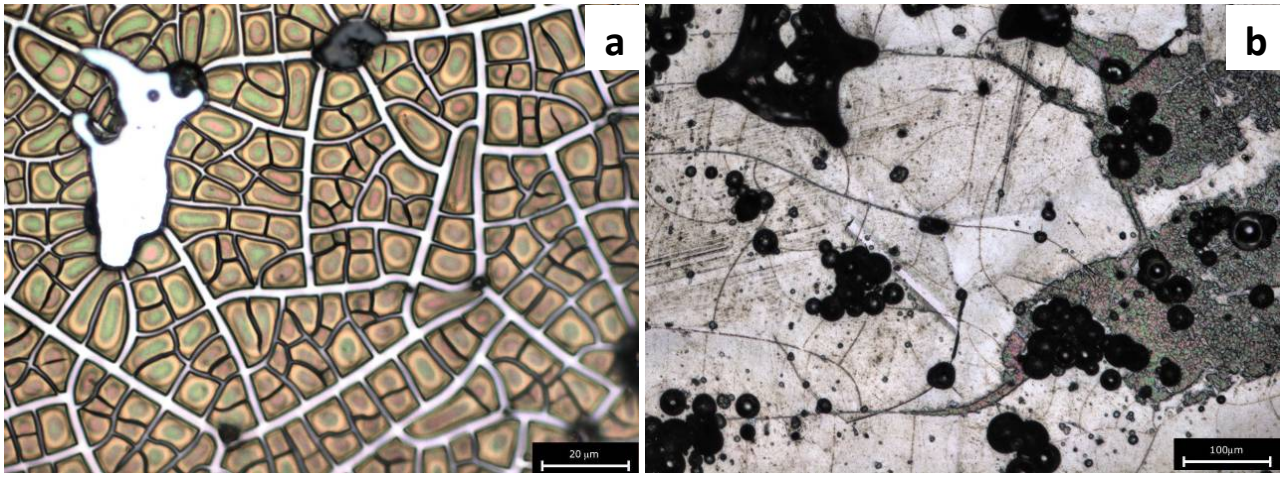

Figure 78: Corrosion micrographs of 0.05%C after breakdown (a) and the evolution of corrosion process (b).

5.1.8 Preliminary in vitro tests

Cytotoxicity (LDH):

The amount of LDH (cytoplasmic enzyme) released in the culture medium is proportional to the number of dead cells during culture. Therefore, the cytotoxicity of a given substance is measured by the concentration of this enzyme.

This analysis is based on the ability of LDH to reduce NAD to NADH. Then, NADH is used to convert a tetrazolium dye (absorbance wavelength 490 nm). So, as more LDH is present in a culture medium, more NADH is reduced, and more dye is produced.

The absorbance values of CS, C and the control are reported in figure 79. The LDH values of the samples and of the control are the same, so the Co-Cr-Mo alloy is not toxic for the cells.

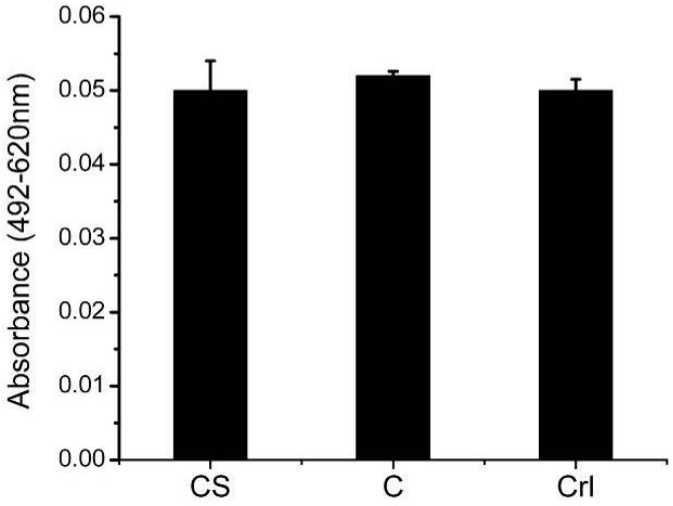

Figure 79: Cytotoxicity (LDH) measurements.

In vitro tests:

Alamar blue and alp (alkaline phosphatase) tests:

These tests indicate the cells' health and activation. The results of the alamar blue measurements are reported in the table 14. The values found for the samples investigated are lower than those of control, and only after 15 days the CS sample presented a significant value.

For the ALP tests the results obtained are lower than the machine sensibility and are not reported.

These problems with the alamar blue and ALP tests were due to the low quantity of the seeded cells, but that small amount of cells was needed to observe the growth and the adhesion morphology of the cells, as it will be reported in the following.

Table 14: Results of alamar blue measurements.

	Sample CS	*Sample C*	*Control*
After 3 days	0.029451	0.036278	0.143011
After 7 days	0.035656	0.060053	1.594985
After 15 days	0.083461	0.504773	3.502434

Confocal microscopy and sem:

Culturing time of 3 days:

In figures 80a and b, the morphologies of the osteoblast cells are shown for CS (a) and C (b) samples. The blue areas are the nuclei and the red parts are the cytoplasm in the confocal images. In this case the morphologies of the cells for the two samples are quite similar, and the proliferation is in agreement with the culturing time.

After the observation by SEM, figures 80c and d, a strong difference in distribution and growth of the cells is found. The solution annealed samples present a higher quantity and more developed cells than as sintered ones. In both materials the cells present a good adhesion with the sample surface, as clearly confirmed in figure 81 by the adhesion of the cells phyllopods.

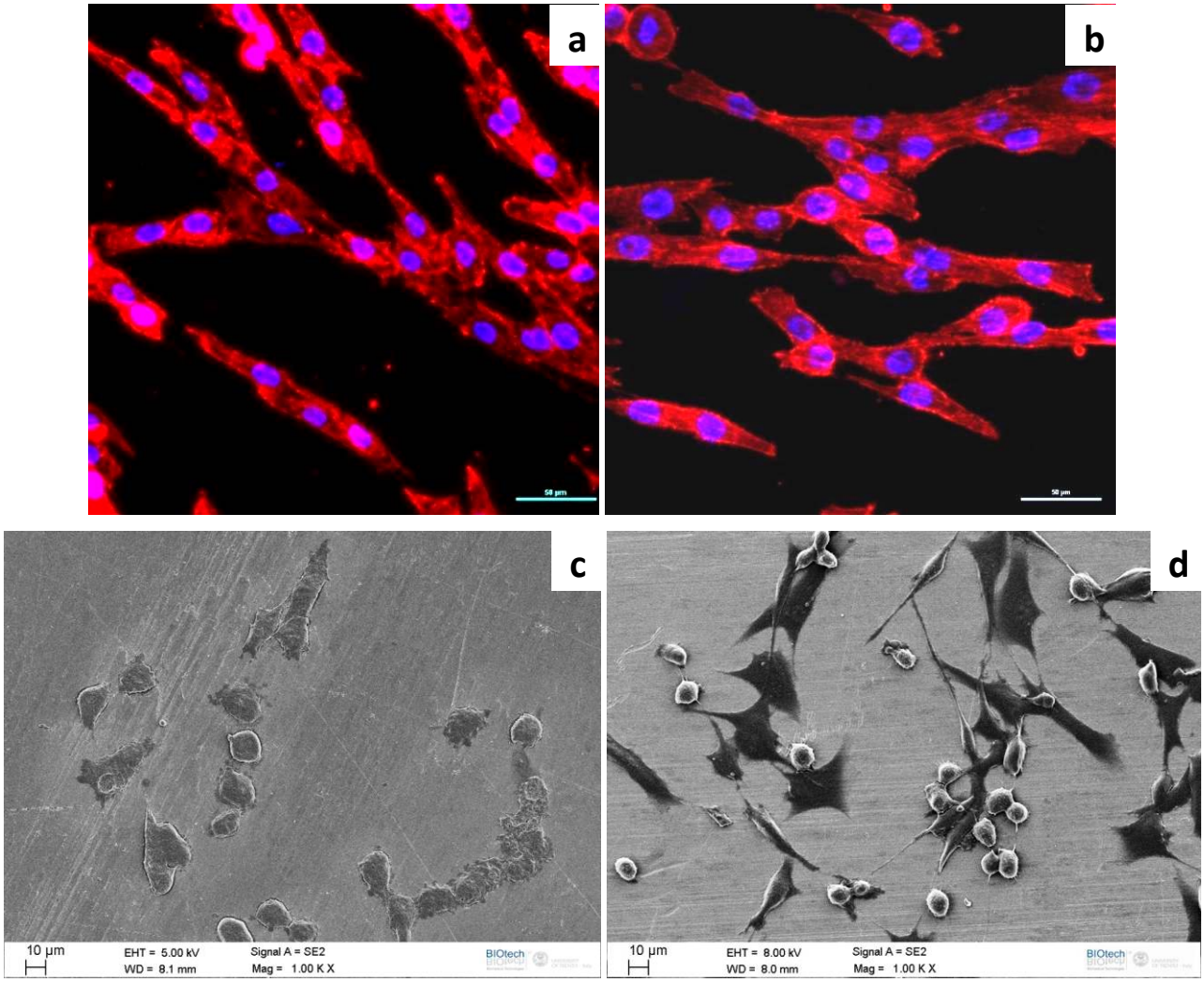

Figure 80: Cells morphology of CS (a and c) and C (b and d) samples after 3 days of culturing time.

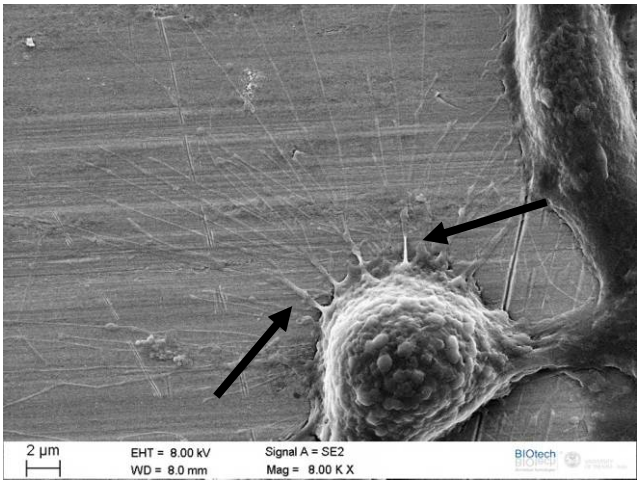

Figure 81: Cells with longer phyllopods adhered in the sample surface (SEM).

Culturing time of 7 days:

In figures 82a and b, the cell morphology for as sintered material imaged by confocal microscopy is shown. As the confocal analyses for the two materials do not present a significant difference only the image of the as sintered one is reported. So, after 7 days of culturing time the cells proliferation and growth increase and the cytoplasm presents a connection as seen in figure 82b.

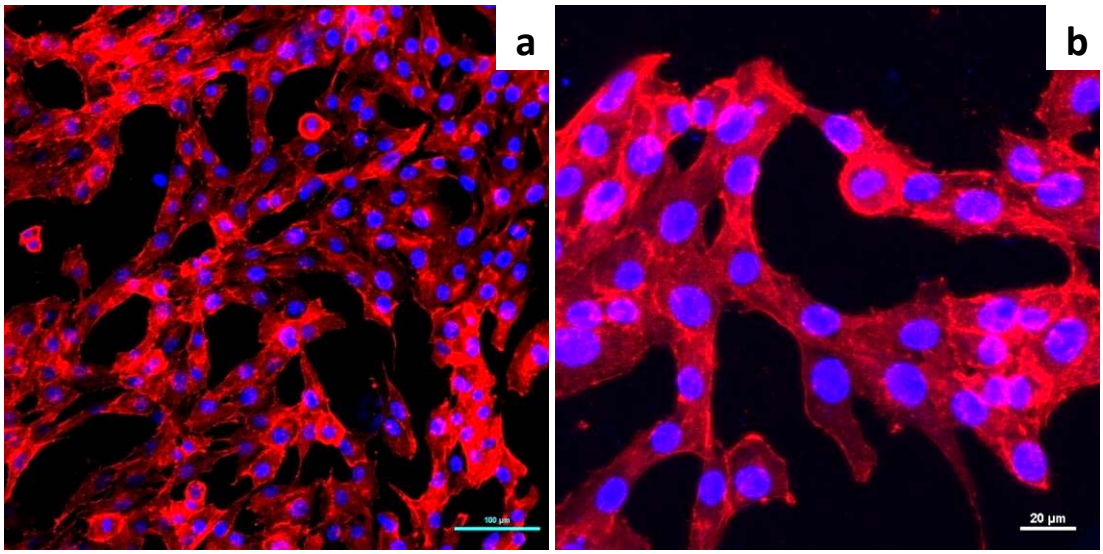

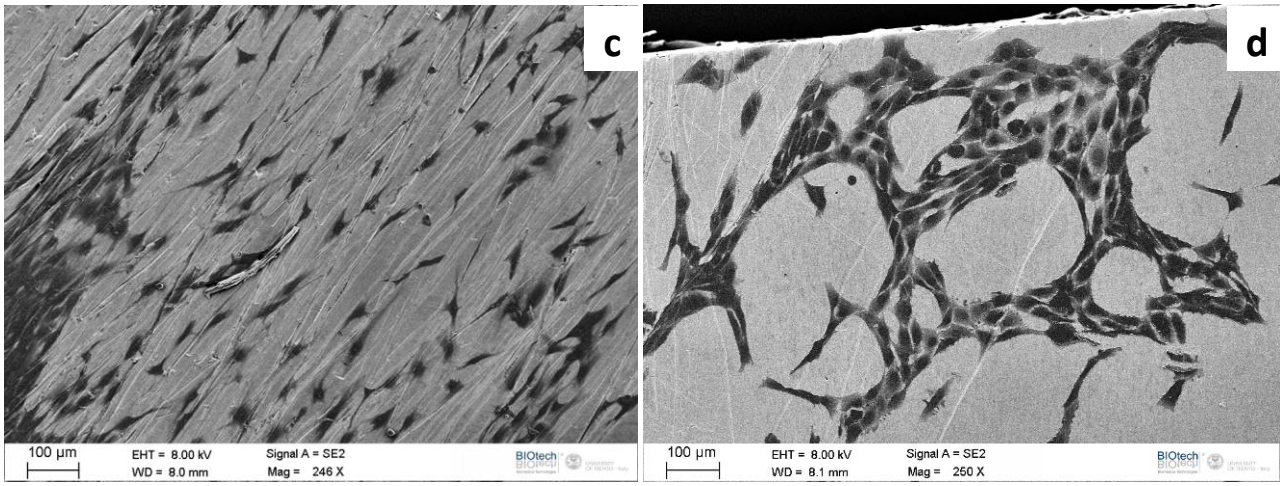

Figure 82: Cells morphology of CS (a,b and c) and C (d) samples after 7 days of culturing time.

SEM analyses showed again a difference in cells proliferation and growth for the two investigated samples, see figure 82c and d. For CS material, the cells grow in the same direction of the sample surface scratches, while for the C material the cells do not follow the scratches but grow in circle-like form. This circle form is shown at higher magnification in figure 83b.

The circle-like morphology can be associated with the grain sizes of the sample. An example of the etched microstructure of C sample is shown in figure 83a. The possible growth of the cells at the grain boundary will be discussed in detail in the following.

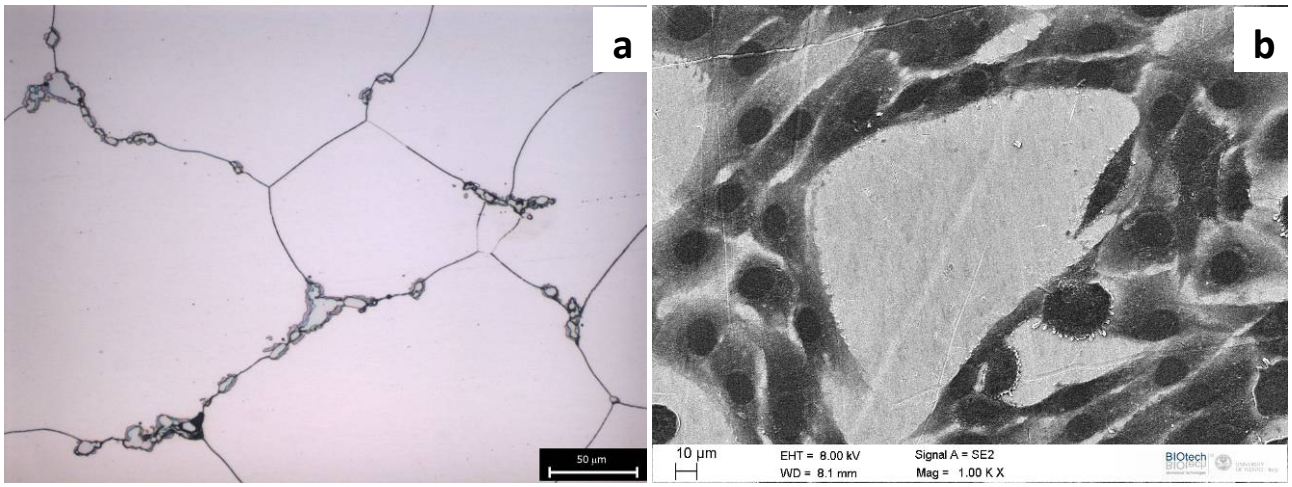

Figure 83: Optical microstructure (a) and SEM cells morphology (b) of C sample.

Culturing time of 14 days:

In figure 84a and b, the cell morphology after 14 days of culturing time for as sintered material imaged by confocal microscopy is shown. Even in this case only the image of as sintered condition is reported. After 14

days of culturing time the cells present a high proliferation and growth, and almost no places without cells are observed.

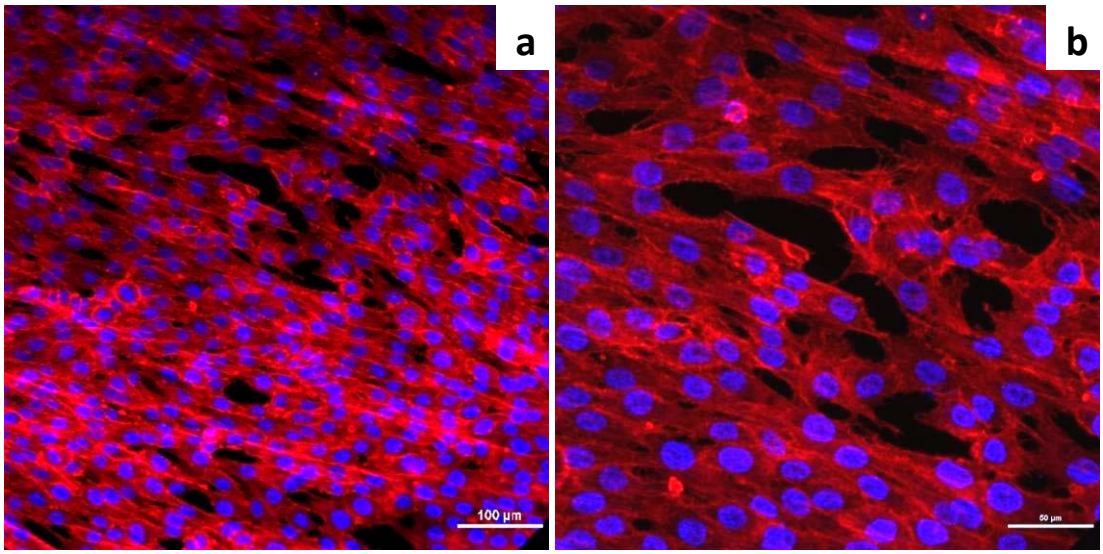

Figure 84: Confocal cells morphology of CS sample after 14 days of culturing time.

SEM analyses showed again a difference in cells proliferation and growth for the two investigated samples, see figures 85 and 86. In both cases the quantity of cells is higher than before.

For the CS material, figures 85a and b, the cells grow again in the direction of the scratches and seem to prefer to grow one above the other instead of on the sample surface, as is shown in the figure 85b. For C material, see figures 86a and b, the cells proliferate on the whole sample surface and fill the circle-like areas.

In both cases the cells present a good adhesion on the surface.

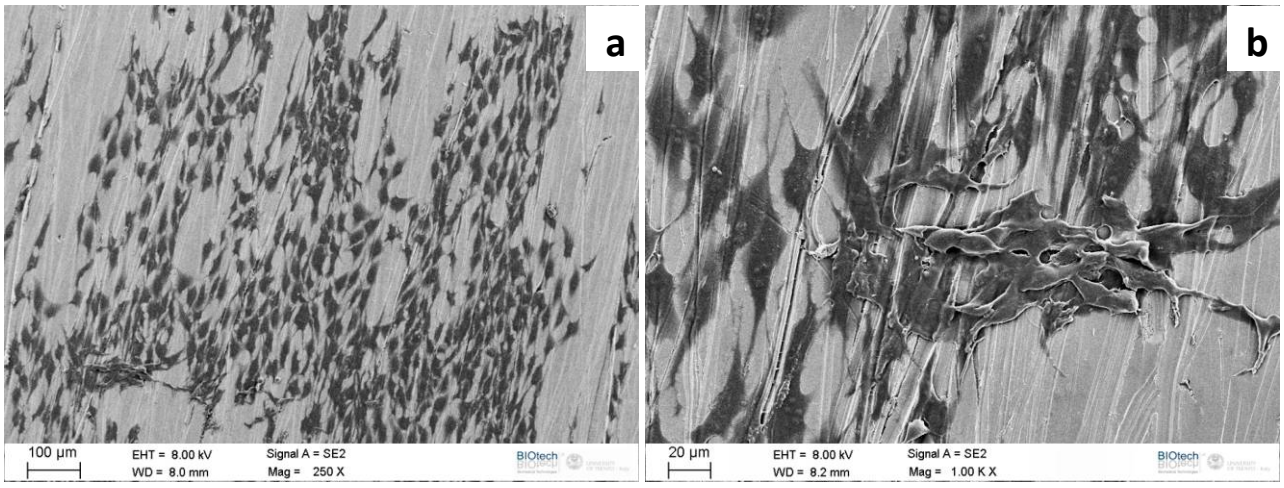

Figure 85: SEM cells morphology of CS sample after 14 days of culturing time.

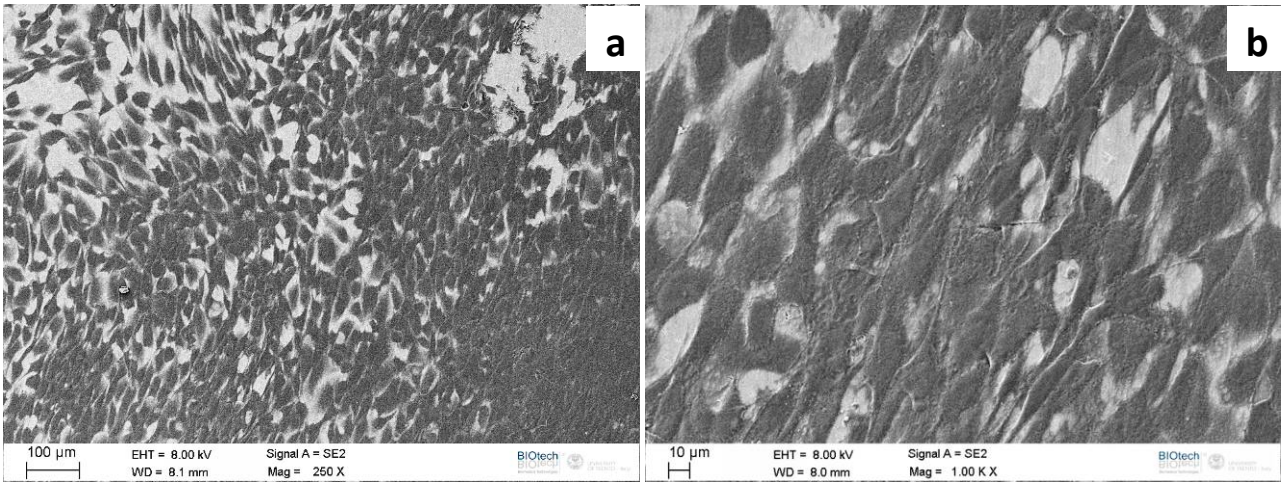

Figure 86: SEM cells morphology of C sample after 14 days of culturing time.

By analyzing the results of in vitro biocompatibility tests for 0.23%C material sintered at 1350°C, in as sintered and solution annealed conditions, it is evident that the Co-Cr-Mo alloys are biocompatible. This can be concluded because they are not toxic and present a good adhesion and proliferation in the sample surface. A different behavior in growing and proliferation of the cells was found between the different sample conditions. To understand better the behavior of the cell growth, biocompatibility tests for the 0.35%C and 0.23%C materials in as sintered conditions were carried out. These two materials were chosen because they present a larger difference in the carbides distribution. For this test, the samples were polished to obtain low roughness and no scratches in the surface.

The cells were seeded for 7 days and the results of SEM analyses are shown in the following. In figure 87 the cell distributions are shown. In the 0.23%C material the cells are uniformly distributed on the surface, whilst for the 0.35%C the cells are concentrated in the center of the surface.

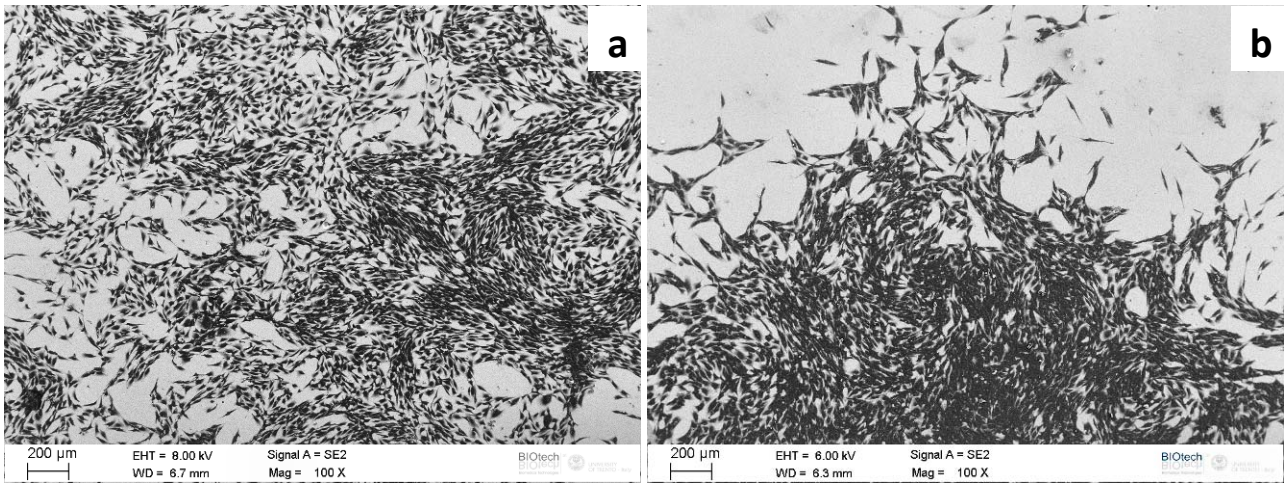

Figure 87: Cells distribution on the as sintered surface of the as sintered materials: 0.23%C (a) and 0.35%C (b).

If the magnification is increased, the same growth behavior is observed for the two materials, see figure 88. This means, that the cells start to grow at circle-like form, but on 0.35%C material, they prefer to fill the void space and then grow to another direction.

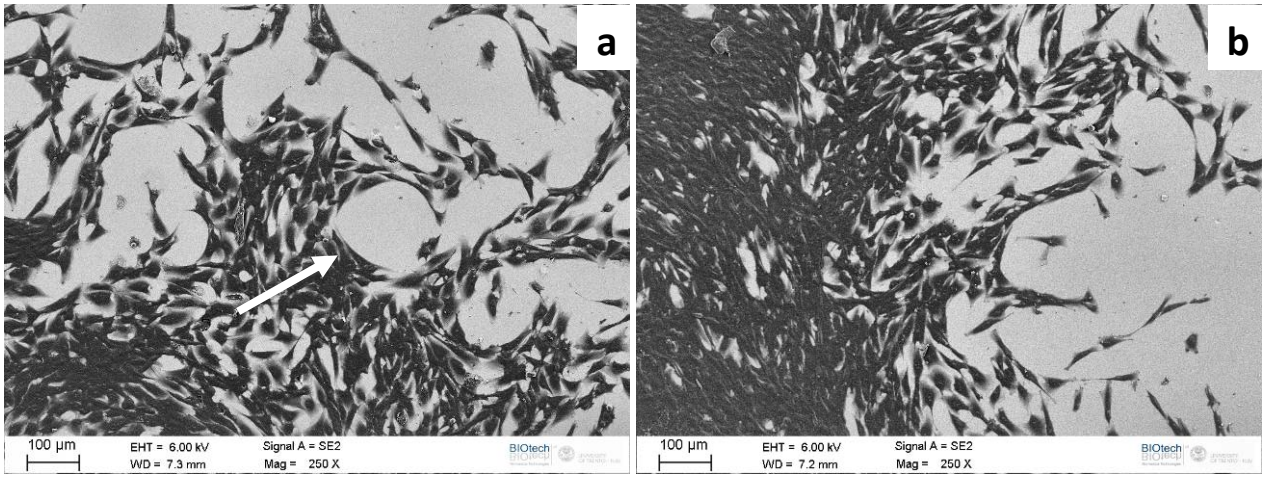

Figure 88: Cells distribution (II) on the as sintered surface of the as sintered materials: 0.23%C (a) and 0.35%C (b)

Details of the upper and the lower parts of the circle indicated by the arrow in figure 88a are shown in figures 89a and b. The cells have grown in the carbides, so it is possible that the circle-like morphology follows the grain boundary of the material.

Figure 89c shows the adhesion of cell cytoplasm on the carbide surface. The optical microstructure of the 0.23%C material with the adhered cells is shown in figure 89d. From the optical image it is possible to identify the grain boundary and the precipitated carbides, and to confirm that the cells have preference to grow in the regions of the carbides.

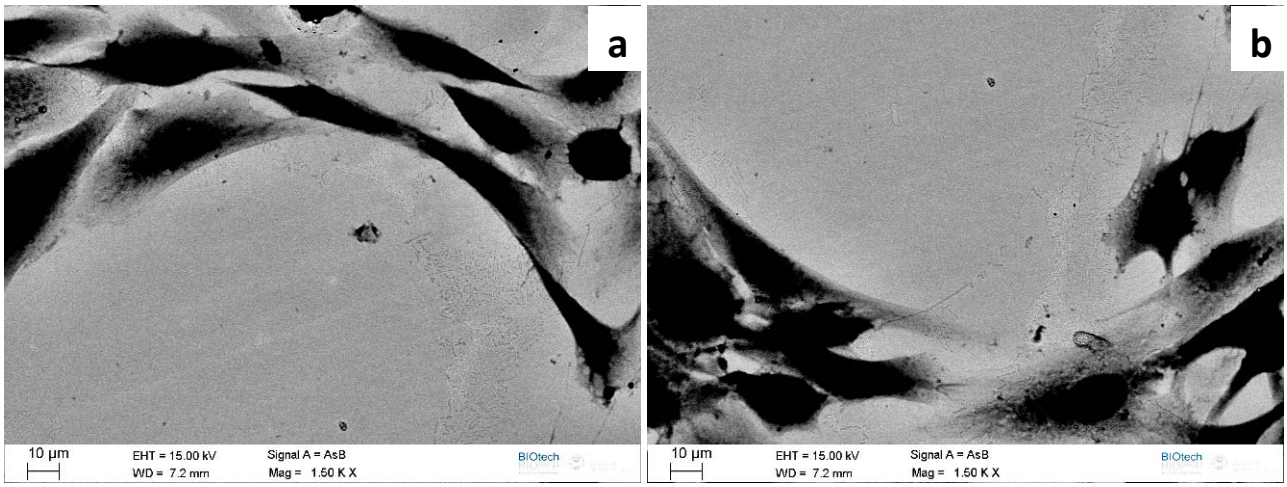

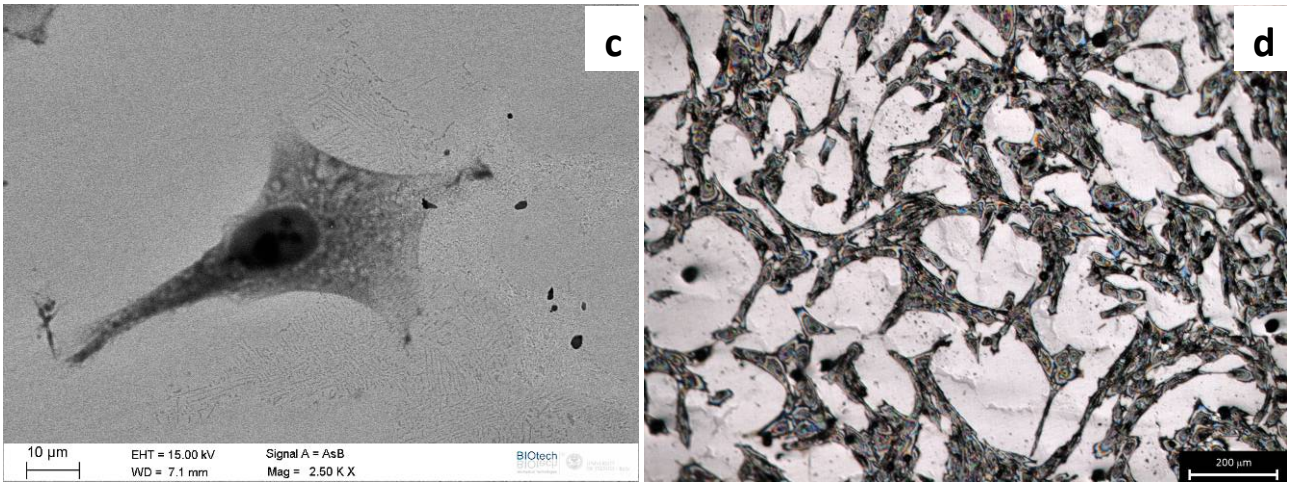

Figure 89: Up and down parts of the circle-like cell morphology (a and b), cytoplasm adhesion on the carbides (c) and optical microstructure (d) for as sintered 0.23%C material.

Figures 90a and b show the cells morphology in the 0.35%C material. The adhesion of cell cytoplasm on the carbide surface is confirmed.

The optical microstructures with the adhered cells are shown in figures 90c and d. Also in the case of the 0.35%C materials the cells have preference to grow in the carbide regions.

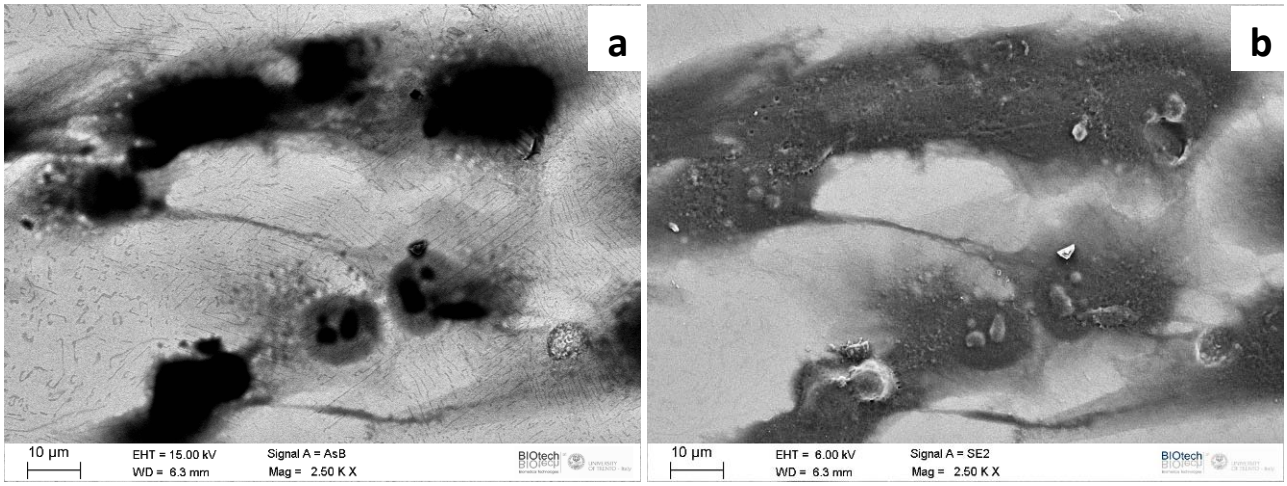

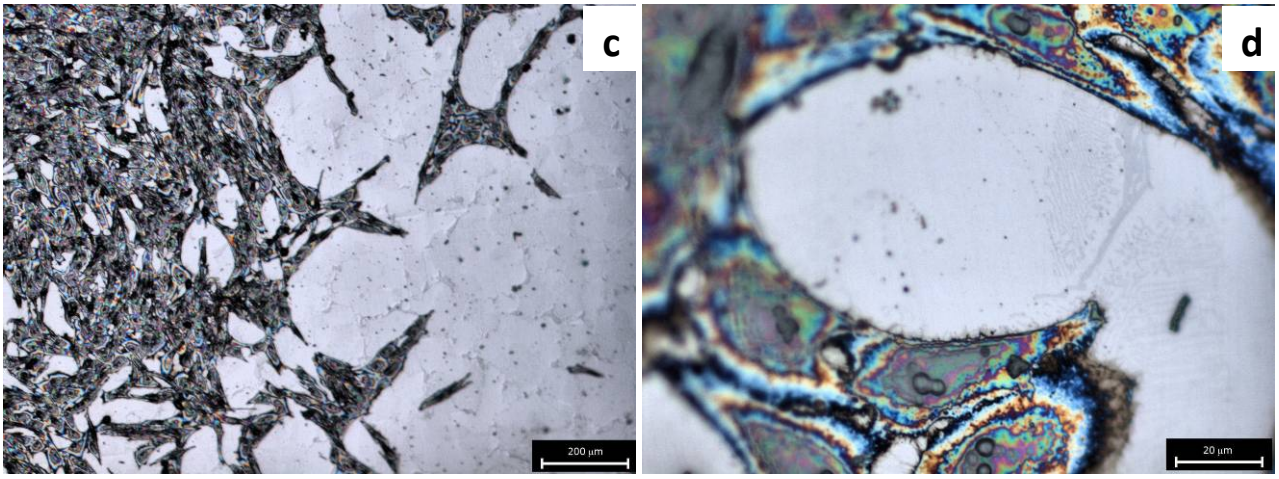

Figure 90: ESEM cell morphology (a and b), and optical microstructure (c and d) for as sintered 0.35%C material.

The differences in cell growth, proliferation, and distribution on the as sintered 0.23%C and 0.35%C can be explained by the preference to grow and adhere at the carbide zones. On one hand we have the 0.35%C material containing a microstructure with higher content of carbides and small zones without carbides, so the cells are able to fill all void spaces and then this expands to another region.

On the other hand, the 0.23%C material has lower carbide content, and inside the grain there is more space without carbides, so the cells tend to grow at all the grain boundaries and afterword they start to fill the free spaces.

In the case of the previous investigated materials, as sintered (CS) and solution annealed (C) 0.23%C, the differences found are due to the presence of scratches, probably for the proliferation on Co-Cr-Mo alloys the cells prefer a less roughness surface.

Therefore, carbide seems to be a suitable substrate for cells adhesion.

5.1.9 Summary and concluding remarks

Near-full dense Co-Cr-Mo alloys with different carbon contents were obtained by MIM and sintering at temperature increasing from 1300°C up to 1380°C on decreasing the C content.

The mechanical properties are strongly influenced by the microstructural characteristics and in particular by carbides.

The content of carbides increases from 0.05%C to 0.23%C and to 0.35%C. After solution annealing the amount of carbides decreases significantly but grain size tends to increase.

Aging causes the re-precipitation of carbides within grains and of h.c.p.$_1$ and h.c.p.$_2$ at the grain boundaries.

Heat treatment changes the phase constitution of the matrix.

As far as mechanical properties are concerned:

- Microhardness is affected by the matrix constitution, so after solution annealing, when C, Cr and Mo are in solid solution and after aging, when re-precipitation of the carbides takes place within the grain, microhardness increases for all materials.
- Hardness is influenced by carbides, after solution annealing it decreases and after aging it increases. The hardness of the 0.05%C material does not change with heat treatments.
- Tensile strength: The yield strength is strongly correlated with the quantity of carbon content in the alloy, the higher the carbon content, the higher σ_y. After solution annealing the strength of the materials slightly decreases, but on aging it increases due to the precipitates.
- Ductility is inversely proportional to the carbon content, the lower the C content, the more ductile is the alloy. After solution annealing ductility increases for almost all materials and after aging it decreases again.

The best mechanical properties are obtained on the SA 0.35%C alloy, which match all the ISO requirements. The 0.23%C material presents good mechanical properties too, but due to its high porosity, it cannot be considered for orthopedics applications. When sintered at high temperature, it matches requirements although yield strength is very slightly lower than that requested.

Wear tests were carried out against a UHMWPE under lubricated conditions. The wear mechanism is characterized by the transfer of wear debris from the polymer to the metallic alloy, and is quantified by the mass loss of the former and the increase in the roughness of the latter. The material with the best wear properties is as sintered 0.35%C alloy, which does not cause a measurable mass loss of the polymer and displays only a very slight increase in the surface roughness.

Corrosion tests were carried out by measuring the Open Circuit Potential. All the materials have a fast transition to a noble behavior, with an effect of both the matrix constitution and the carbide amount. In particular, the higher the hcp fraction, the less noble is the electrochemical behavior, and a higher incidence of carbides tends to enhance nobility. On forcing corrosion by potentiodynamic tests, carbides tend to localize the attack responsible for transpassivation.

Wear and corrosion would suggest the use of the as sintered 0.35%C material, which is too brittle. The 0.35%C SA alloy presents the best mechanical properties while the corrosion behavior remains quite good, and the mass loss of the polymer is very low, and compatible with the application. This material could then represent the best solution for the production of the orthopedic prostheses by MIM of prealloyed powders.

To summarize, the materials investigated are compared in table 15:

Table 15: Comparing the properties for the investigated materials.

Materials	Strength	Ductility	Wear	Corrosion
0.35%C alloy as sintered	☺	☹	☺	☺
0.35%C alloy + SA	☺	☺	☺	☺
0.23%C alloy - S1300°C	☺	☺	☹	☺
0.23%C alloy - S1300°C + SA	☹	☺	☹	☹
0.23%C alloy - S1350°C	☹	☺	☹	☺
0.23%C alloy - S1350°C + SA	☹	☺	☹	☺
0.05%C alloy as sintered	☹	☺	☺	☺
0.05%C alloy + SA	☹	☺	☹	☺

5.2 Ti6Al4V Alloy

5.2.1 Microstructures of Ti6Al4V alloy

Figure 91a shows the typical rounded pore morphology in the as sintered Ti6Al4V alloys. The density measured in these samples after sintering is almost 96% of the theoretical one. The oxygen and carbon contents are 0.227 % and 0.0302%, respectively.

Figure 91b shows the microstructure of the Ti6Al4V alloy after etching with Kroll reagent. The microstructure consists of a fully lamellar structure, typical of MIM Ti6Al4V samples due to slow cooling (section 3.4), with alpha colony size around 100μm and alternating coarse alpha and beta plates with the same orientation.

After shot peening the microstructure doesn't change.

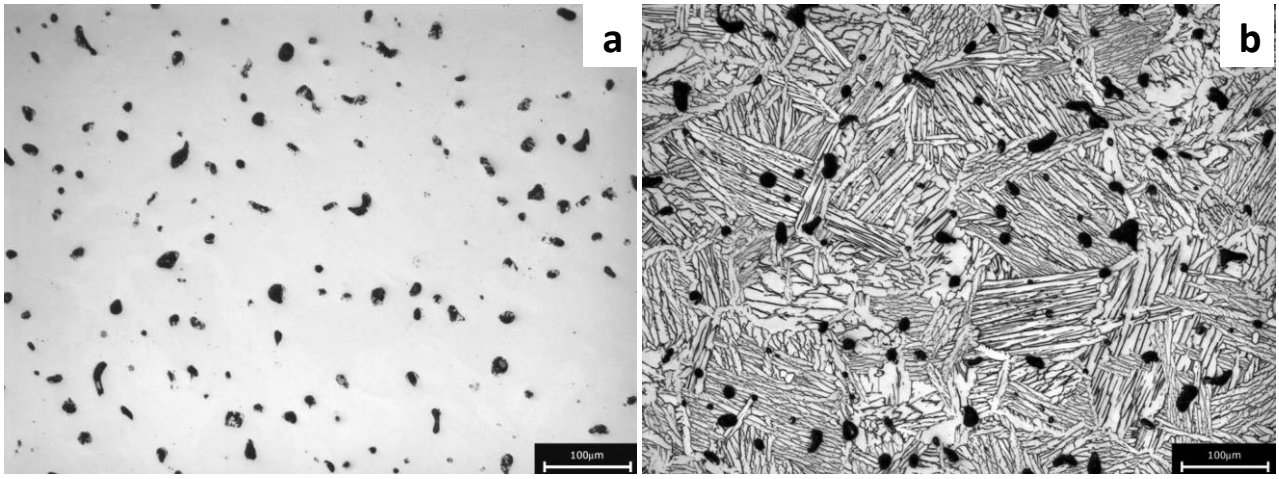

Figure 91: Microstructure of as sintered materials before and after etching with Kroll reagent.

5.2.2 Surface quality of Ti6Al4V as sintered and shot peened

Figure 92 shows a general overview of the surface quality for the as sintered and shot peened tensile test bars. The samples peened with steel shots (SP1 and SP2) present an opaque surface, due to an increase in roughness. The specimen peened with ceramic (SP3) shots presents a mirror like surface.

Figure 92: Surfaces appearance of the tested samples.

The average (Ra) and quadratic (Rq) roughness were measured and the results are reported in table 16.
The specimens shot peened with steel shots show a greater roughness than the other two conditions (AS and SP3), mainly in the case of the strong shot peened conditions (SP2). The specimens shot peened with ceramic shots present the best roughness.

Table 16: Values of average and quadratic roughness of the investigated materials.

Samples	Ra [µm]	Rq [µm]
AS	1.93	2.43
SP1	2.30	2.90
SP2	2.62	3.39
SP3	1.22	1.54

The surface of the AS, SP1 and SP2 is suitable for contact to bone tissue which is supposed to adhere to the implant. Its typical Ra value is 2 to 5 µm [65]. Shot peening is used in many cases when a roughness increase is desidered.

Surface quality:

Figures 93a to d ilustrate the surface profile and morphology of MIM specimens after sintering (a and c) and after SP1 (b and d). The AS samples show cavities on the surface due to injection and debinding steps of MIM processing.
In the as sintered specimens during injection, their surfaces are exposed to a higher shear stress than the interior regions due to the turbulence effect promoted by the fluid (hot feedstock) and mould wall interaction. Such shear stress could promote local separation of binder/powder mixture. This separation leads to regions where only binder is present. Therefore, the notches are formed during thermal debinding and sintering in these specific surface regions due to missing particle powder contact. Another possibility of

separation could be due to the fact that the powder particles, on some specific surface regions after injection, could be surrounded by only one binder component (e.g. paraffin) of the binder system. Therefore, during chemical debinding these particles will be removed together with the paraffin which leads to a local empty space [66].

These notches are a potential fatigue crack nucleation sites on the samples surface. Consequently, the high cycle fatigue behavior will be affected by the presence of such cracks.

After the application of shot peening these notches are almost completely removed by local plastic deformation as shown in figures 93b and d.

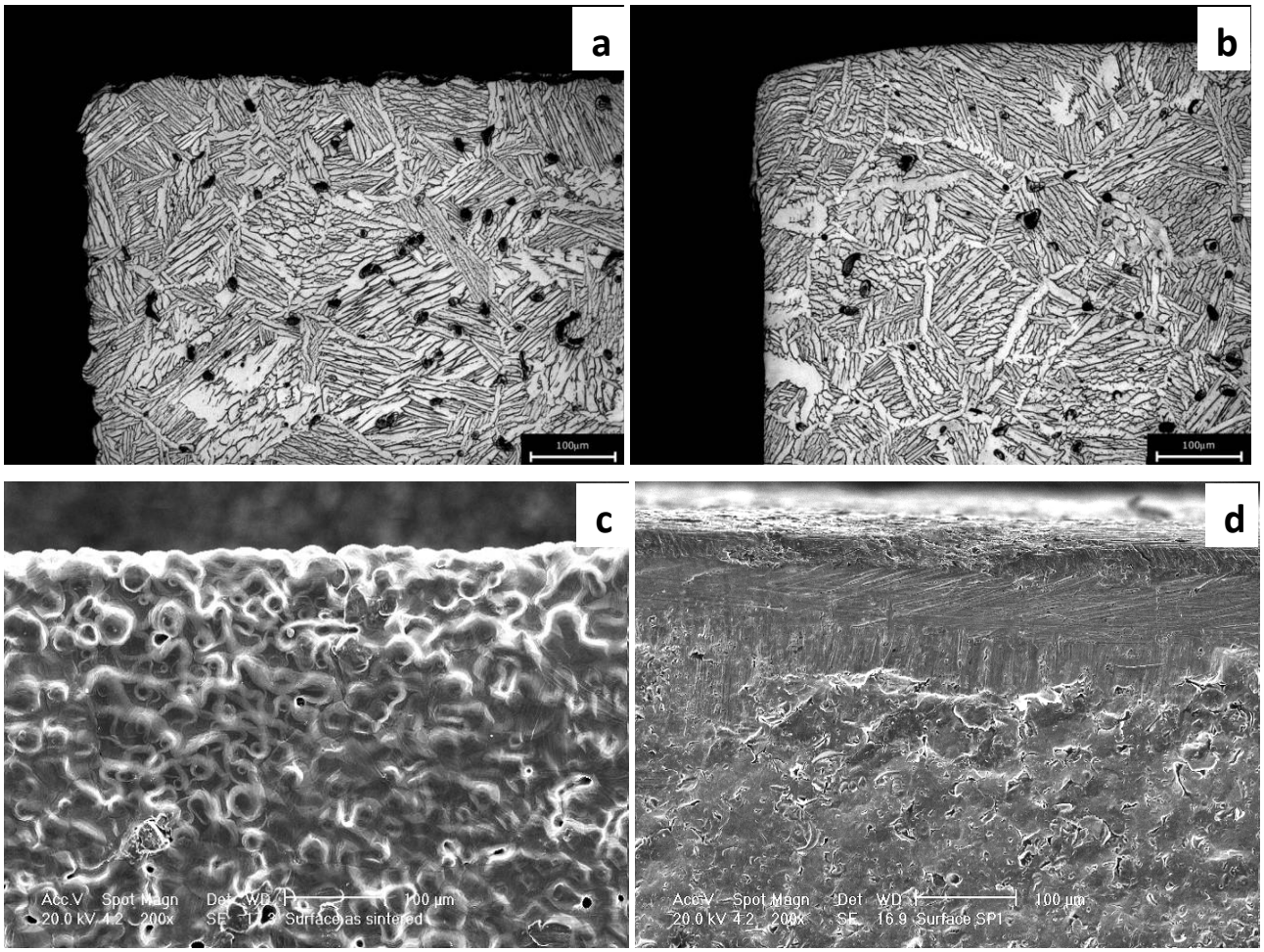

Figure 93: Surface profile and morphology of AS (a and c) and SP 1 (b and d) specimens.

Figure 94a to d illustrate the surface profile and morphology of MIM specimens after SP2 (a and c) and SP3 (b and d). The specimens shot peened at strong conditions (SP2), show a strong surface plastic deformation, which can be deleterious for the fatigue strength.

For the specimens peened with ceramic shots (SP3), a slight plastic deformation was observed. The SP conditions were sufficient to close the notches without an excessive local plastic deformation.

In all shot peening conditions the notches present in the as sintered samples were removed and the higher plastic deformation was localized in the edge of the samples (see SEM images).

So, the higher is the plastic deformation after SP on the surface, the higher is the surface roughness (table 16).

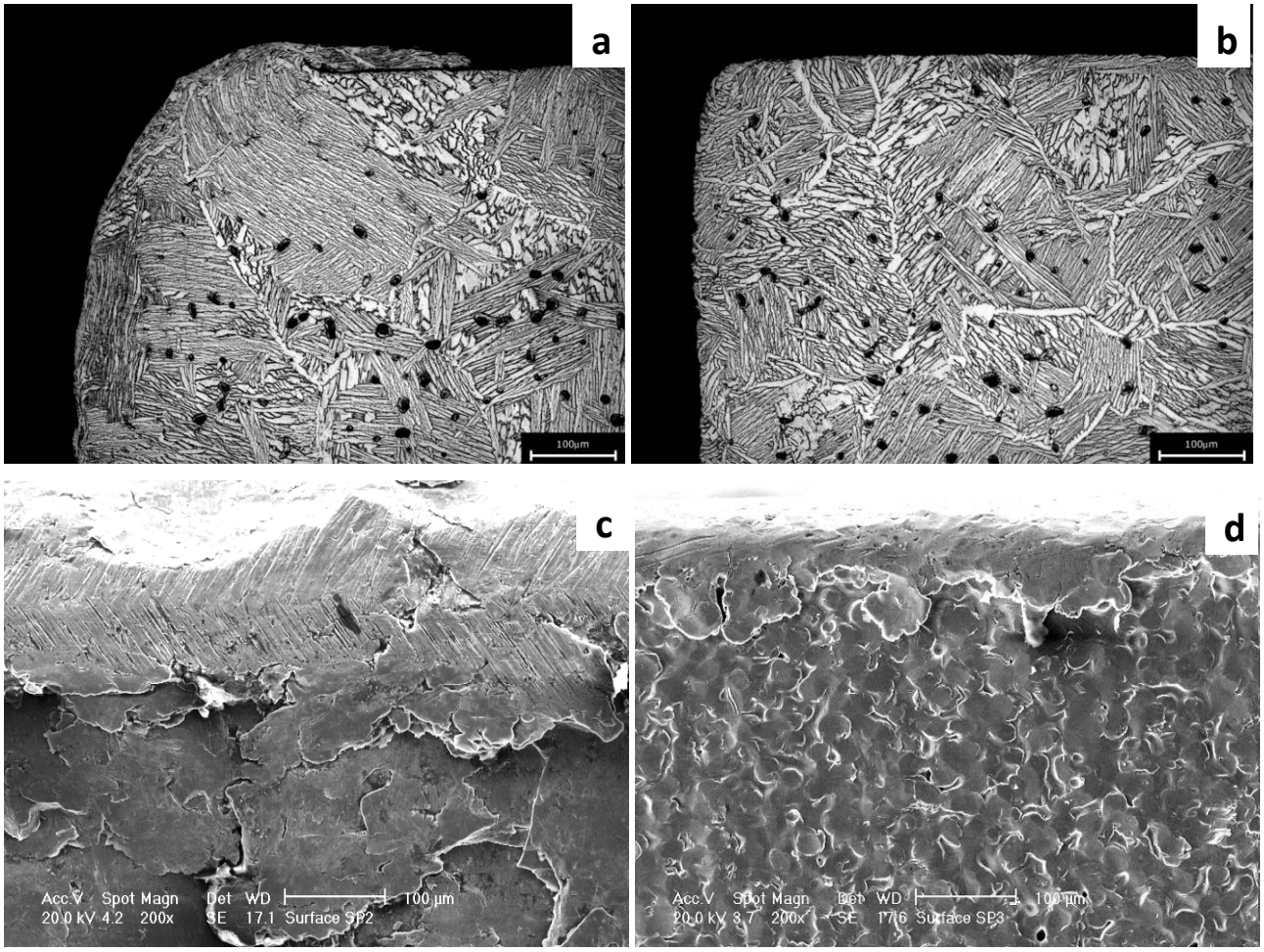

Figure 94: Surface profile and morphology of SP 2 (a and c) and SP 3 (b and d) specimens.

5.2.3 Microhardness

The microhardness of the samples was measured in the bulk and near the surface and is reported in figure 95. The microhardness for the AS samples is the same in the two areas, as expected.

The surface microhardness increase after SP is larger for SP2 than for SP1 and SP3 conditions. The increase in microhardness is due to plastic deformation of the surface layers.

For the SP Ti6Al4V, the compressive residual stress is confined to a shallow surface layer, within ± 250µm in depth and is dependent of the peening pressure, see section 3.3.4.

The microhardness in the bulk region is almost the same for all conditions.

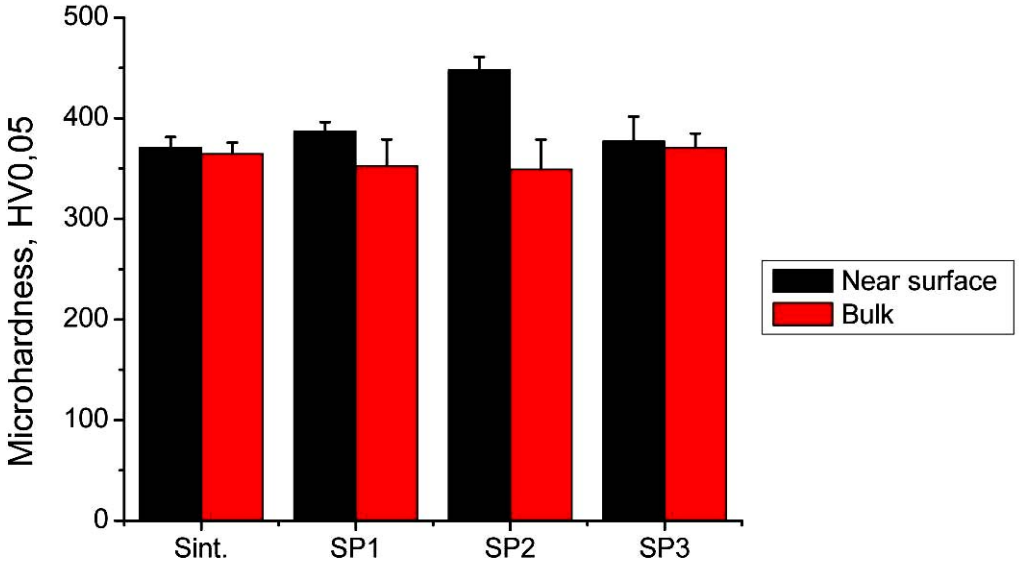

Figure 95: Microhardness for AS and SP samples.

5.2.4 Tensile tests

Tensile tests were carried out for all materials conditions to know the effect of the shot peening intensity on the strength and elongation. The results are summarized in figures 96a and b, and compared with the prescriptions of the ISO 5832-3 standard for orthopaedic implants (horizontal lines).

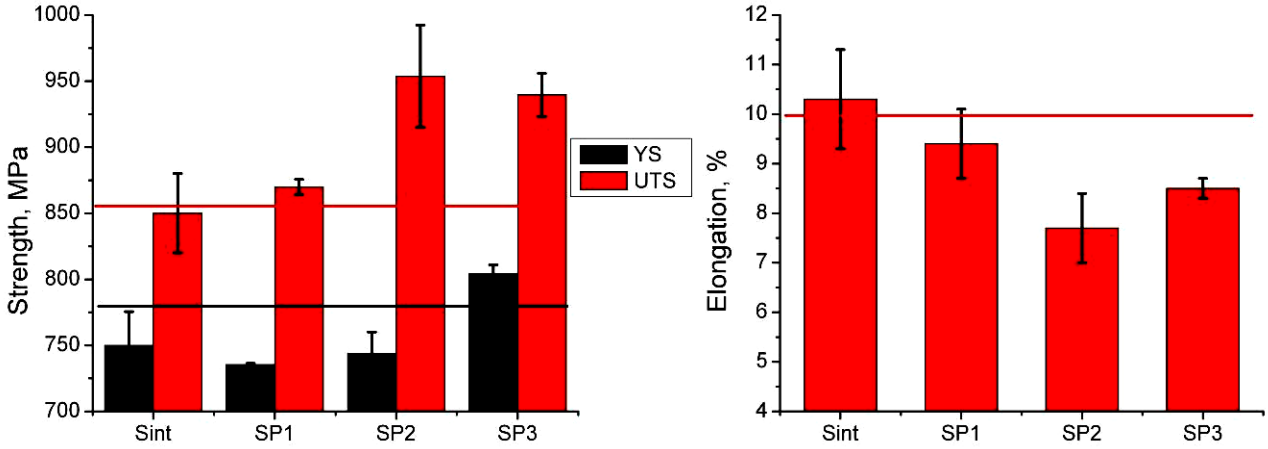

Figure 96: Tensile properties for the four materials investigated.

The AS samples present a lower UTS and higher elongation than the shot peened ones. This is due to the compressive stress and strain hardening on the surface. It is known that stress promotes an increase in tensile strength and a decrease in ductility [67]. This is confirmed by the results, because the stronger are the shot peening conditions, the deeper is the residual compressive stress profile and the larger are the residual tensile stresses in the bulk (section 3.3.4); this results in a higher tensile strength and a lower ductility.

All the materials do not match the ASTM specifications.

For MIM Ti6Al4V alloys the typical tensile properties are 700 MPa of YS, 800MPa of UTS and 10-15% of elongation [65], so the tensile properties of the as sintered specimens match the typical MIM results.

Figure 97 shows the stress-strain tensile curves for the tested materials. They display the typical behavior of Ti-6Al-4V, characterized by a low-strain hardening (low difference between yield strength and UTS).

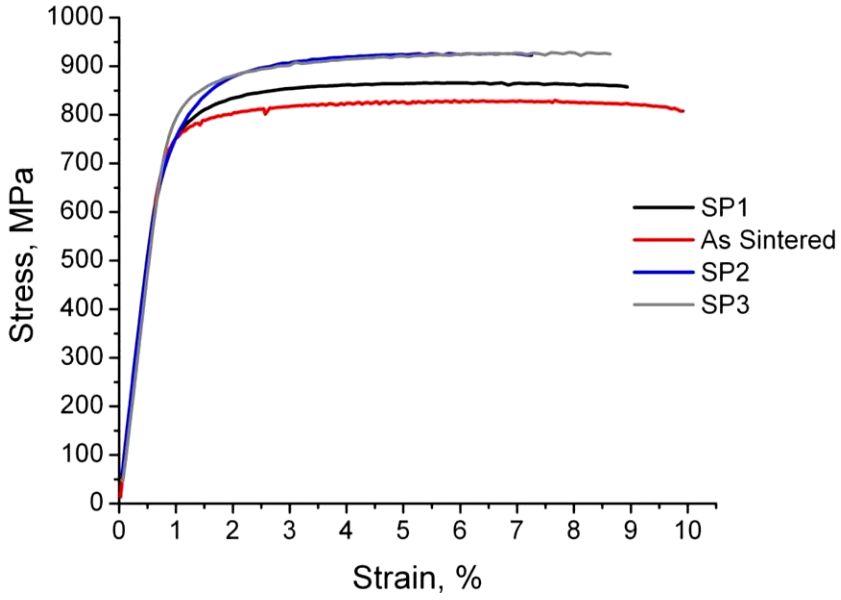

Figure 97: Curves stress vs. strain for the four investigated specimens.

Fracture surface of tensile specimens:

In figures 98 to 100 the fracture surfaces for the four samples investigated are presented.

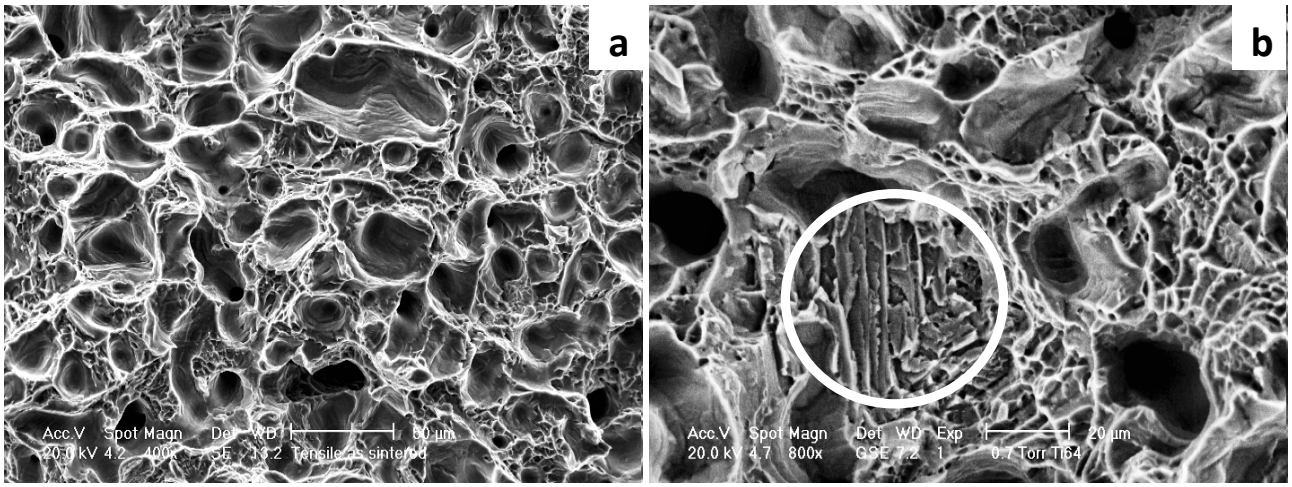

Figure 98: Fracture surfaces of AS specimen (a and b).

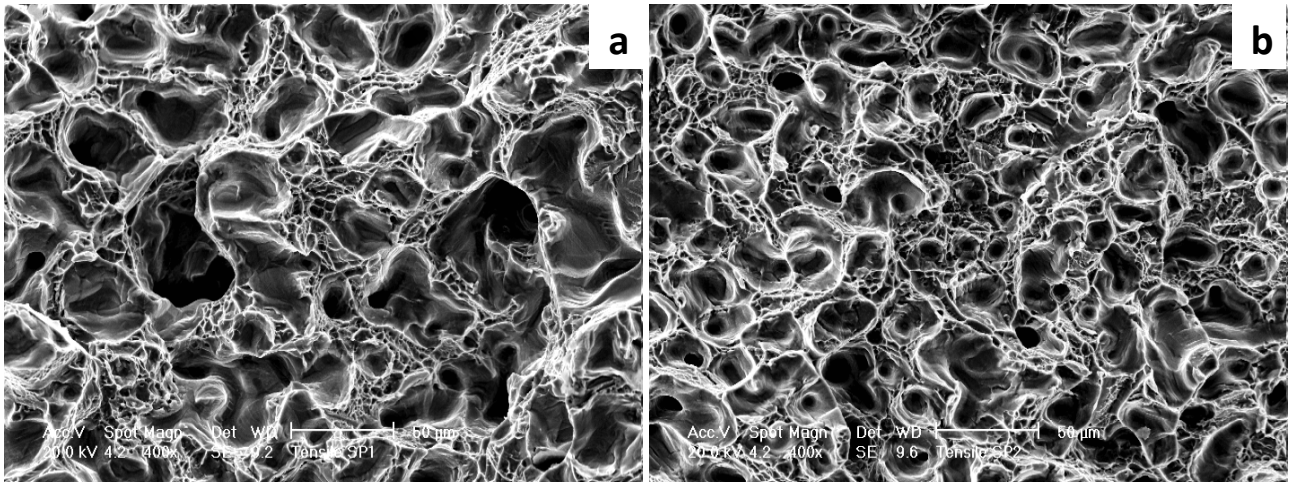

Figure 99: Fracture surfaces of SP 1 (a) and SP 2 (b) specimens.

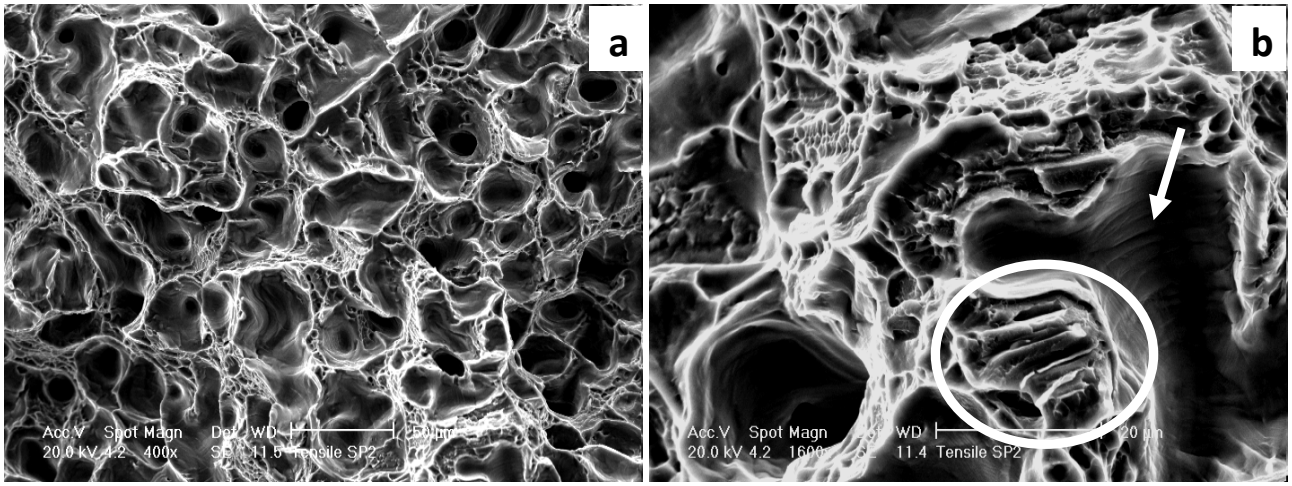

Figure 100: Fracture surfaces of SP 3 (a and b) specimen.

The fracture surfaces present coarse and fine transgranular dimples. In some regions, see figures 98b and 100b, a transcrystalline fracture along the colony boundaries, indicated by white circle areas, was identified. At higher magnification, serpentine glide zones in coarse dimples (white arrow zone) were observed.

The fracture surface of SP2 specimen (figure 99b) shows less pronounced quantity of coarse dimples due to less ductility.

5.2.5 High cycle fatigue (HCF) tests

The staircase method applied to a set of 15 specimens for each condition, provided the mean endurance limit at 50% of fracture probability, as reported in table 17. The fatigue limit for a cast Ti6Al4V for biomedical implants is given, as well [14]. Since the fatigue conditions are similar to those used in the present investigation, HCF resistance of the reference material is close to the values obtained for shot peened specimens in this study.

The shot peened MIM samples show a significantly higher endurance limit than the as sintered material, see table 17. This is explained by the effect of residual stresses which influence the crack initiation mechanisms. The worse surface roughness induced by shot peening (table 16) does not have a significant effect on the fatigue performance of the shot peened samples.

Table 17: Mechanical properties of the materials investigated.

Samples	**Yield Strength (MPa)**	**HCF 50% (MPa)**	**HCF/YS**
AS	750±25	178±30	0.24
SP1	735±1	306±14	0.42
SP2	744±16	289±5	0.39
SP3	804±7	323±1	0.40
Ti6Al4V*	-	330	0.40

* For orthopedic implant - Axial fatigue (R=0.1/292Hz) [20]

According to Telesman et al. [68] the effect on fatigue crack initiation and growth increases with the magnitude and the depth of compressive residual stresses. This is not the case in the present work, since overpeening is found in the SP2 samples. The best increase in fatigue limit was found in the samples peened at 4.5 bar of air pressure.

The fatigue endurance limit cannot be compared directly with literature data since the test conditions are different.

Ferri et al. [66], in a four-point bending fatigue using a cyclic frequency of 95Hz and R=0.2, found an endurance limit of 450MPa. Since the endurance limit of the push pull configuration is around 0.7 of the value found in four point bending fatigue tests, so the value found by Ferri corresponds to 370 MPa for the push pull configuration. If it is considered that higher R-values cause a greater value of the maximum stress [69], the values obtained in this study are comparable with those found by Ferri.

<u>Crack propagation:</u>

The fatigue crack propagation was analyzed for each specimens after fatigue failure. Figure 101 shows a crack for the as sintered material.

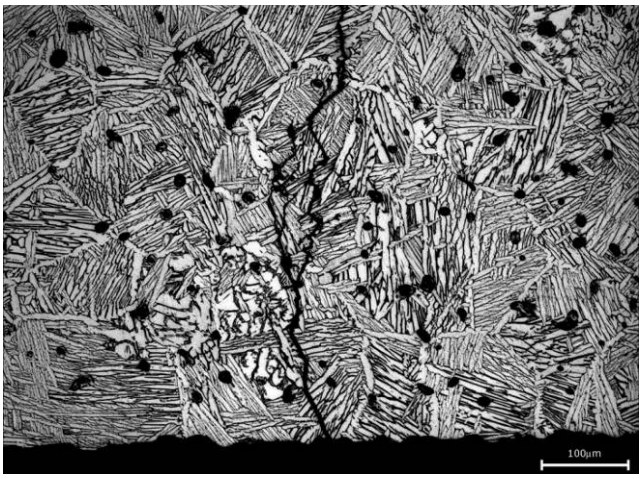

Figure 101: Fatigue crack propagation of AS material.

The fatigue crack crosses the lamellar colonies and the pores. It crosses the lamellar colonies due to preferred slip band activity (which extends over almost the whole colony width) within the coarse α plates [37]. The cracks can propagate at the intersection of these slip bands with the adjacent α colony boundary, too [22]. The increased crack path deflection is a major contributor to the higher toughness of the lamellar microstructure [70].

Branching of the cracks is visible too, see figure 101; branches extend mainly in the pore and also cross the lamellar colonies.

Fracture surface of fatigue specimens:

Fracture surface of the as sintered sample is shown in figure 102.

The white arrow shows the region where the fracture crack nucleated. Crack nucleation in the as sintered specimens occurred at the edge surface. Two distinct regions are visible: region 1 shows a brittle fracture surface and region 2 shows a crack closure. This is a typical feature when dimples are formed and an R value near to zero is applied.

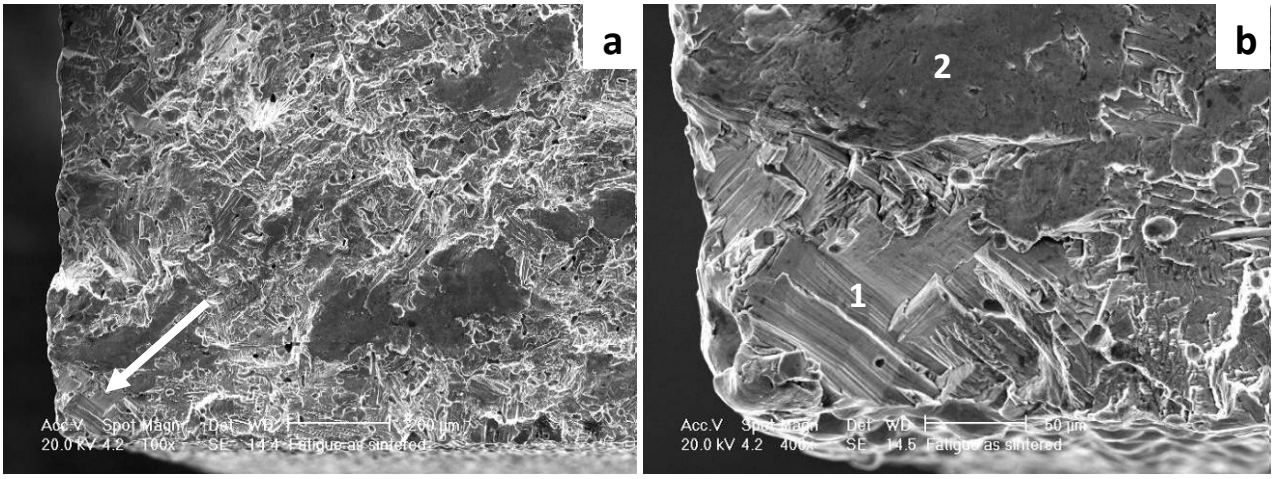

Figure 102: Fracture surface of crack propagation for AS samples (a and b).

In figures 103 to 105, fracture surfaces of shot peened samples are shown. The crack nucleation sites in the shot peened specimens are in the subsurface regions, because of the residual stresses and the improved surface morphology and profile. In shot-peened specimens, fatigue failure tends to initiate in the subsurface where the residual stress profile changes from compression to tension.

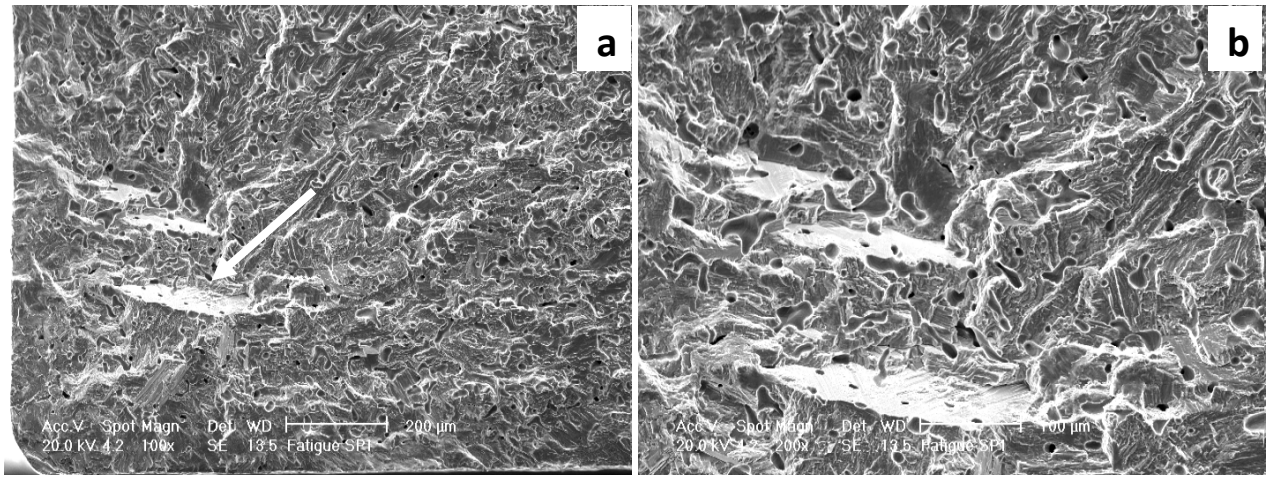

Figure 103: Fracture surface of crack propagation for SP1 (a and b).

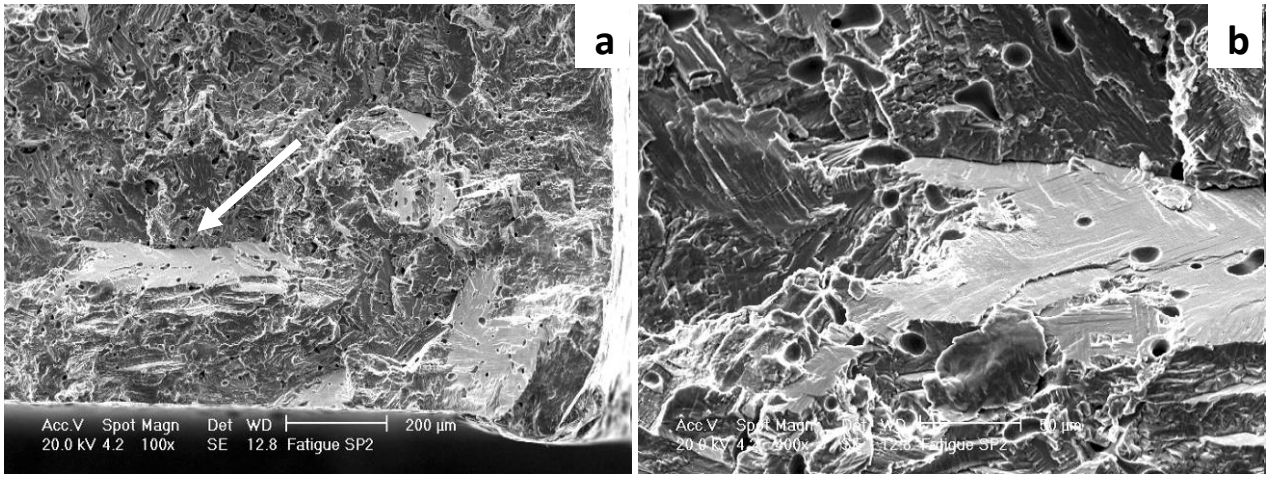

Figure 104: Fracture surface of crack propagation for SP2 (a and b).

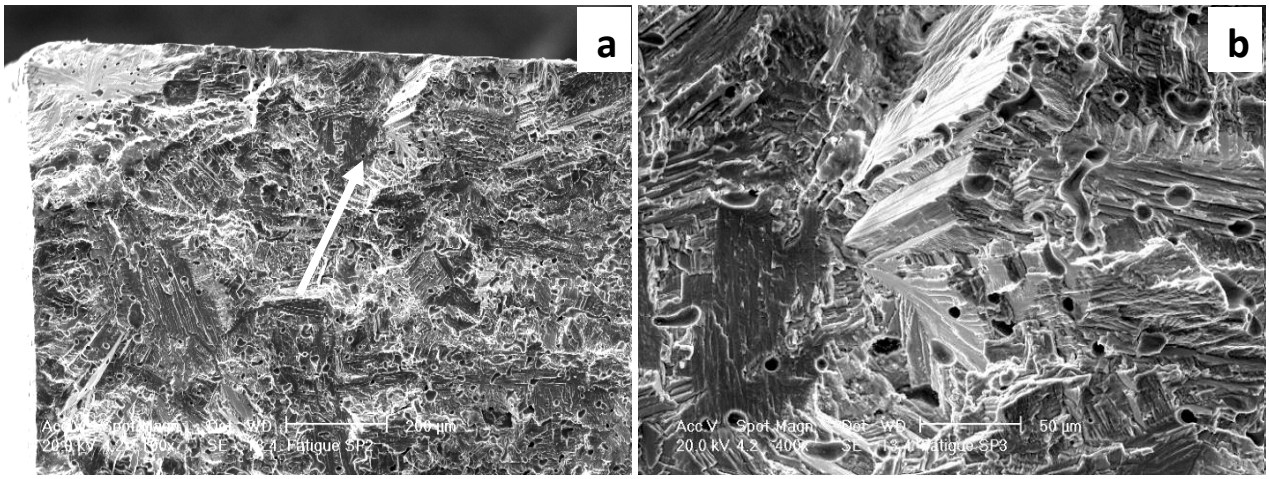

Figure 105: Fracture surface of crack propagation for SP3 (a and b).

Crack initiation in alpha/beta titanium alloys is invariably associated with the formation of quasi-cleavage facets [71]. The formation of such facets is related to the fact that a weak grain, favorably orientated for slip, generates a dislocation pileup at the boundary with a neighboring strong grain. The pile-up leads to the required combination of shear and tensile stresses on the unfavorably plane which induces facet formation [66]. In the facet zones the lamellae boundaries structures are observed. The crack is supposed to nucleate at the intersection of two slip bands.

Subsurface crack initiation sites in fully lamellar Ti6Al4V alloy were related to cross-colony slip-band fracture [70], as observed in the crack propagation.

After the brittle fatigue crack nucleation the propagation of the crack is ductile for all samples. Figure 106a shows the change in fracture behavior (white arrow) and figure 106b shows the dimples in the ductile zone.

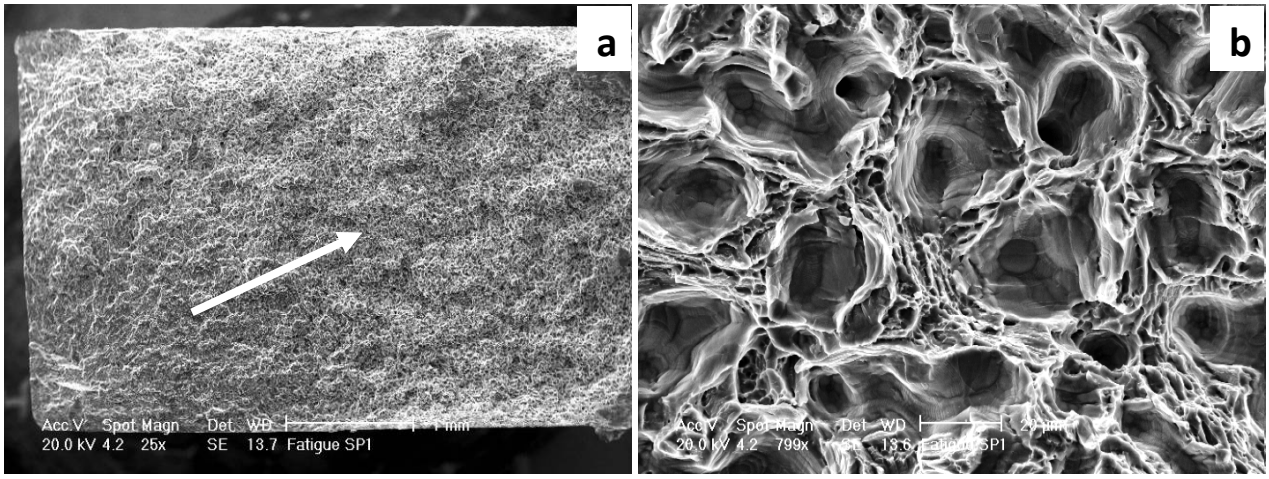

Figure 106: Fracture surface of ductile zone for SP1 (a and b).

5.2.6 Conclusions

The existences of pores together with a coarse microstructure are the main factors responsible for the significant lower HCF strength of MIM samples in comparison with the wrought materials. Nevertheless, the fatigue strength of MIM alloy is comparable to that of a cast material. Shot peening increases the fatigue resistance of the MIM Ti6Al4V alloy but, at the same time, it decreases ductility below the threshold of the standards. The decrease of ductility should be evaluated with reference to the mechanical behavior expected in applications. This point remains open for discussion. Anyway it seems very important to reduce the residual porosity in the as sintered microstructure, since shot peening does not give any bulk improvement of this characteristic.

CONCLUSIONS

This PhD thesis work was carried out in the frame of a scientific cooperation between the Department of Materials Engineering and Industrial Technologies of Trento University and MIMEST Spa (Pergine Valsugana, Trento). The aim of the research was the study of the influence of the microstructure of materials produced by MIM on some specific properties related to the application in the biomedical field.

Four materials were investigated: cobalt alloys with different carbon contents, Ti6Al4V alloy, AISI 316 austenitic stainless steel and 17-4 PH (Precipitation Hardening) stainless steels.

The MIM process has been previously optimized to obtain near-full dense materials.

The thesis was mainly focused on cobalt and titanium alloys. However, for sake of completeness, the work done on stainless steel was reported as well (in an appendix, two papers relevant to the austenitic and the precipitation hardening stainless steels are included).

The results can be summarized as follows.

Cobalt alloys (CoCrMo) from 0.05%C up to 0.35%C

- The decrease in carbon content requires an increase in the sintering temperature, from 1300°C up to 1380°C.
- The mechanical properties are strongly influenced by carbides, whose amount increases with the increase in C content. In the as sintered condition, the carbon containing materials tend to be brittle.
- Solution annealing promotes the carbide solubilization, but grain size tends to increase.
- Aging causes the re-precipitation of carbides within grains and of h.c.p.$_1$ and h.c.p.$_2$ constituents at the grain boundaries.
- Both heat treatments change the constitution of the matrix (fcc to hcp ratio).
- The matrix microhardness increases after solution annealing and aging.
- Hardness decreases after solution annealing, and increases after aging. The hardness of the 0.05%C material does not change with heat treatments.
- After solution annealing, the strength of the materials slightly decreases, but on aging it increases due to the extensive precipitation of carbides and grain boundary constituents.
- After solution annealing, ductility increases for almost all materials but after aging it decreases again due to precipitation.
- The best mechanical properties are obtained for the solution annealed 0.35%C alloy, which matches all the ISO requirements.

- The best wear properties against a polymeric material are found for the as sintered 0.35%C alloy, which does not cause a measurable mass loss of the polymer and displays only a very slight increase in the surface roughness (transfer of polymer).
- In the corrosion tests all the materials have a fast transition to a noble behavior. The higher the hcp fraction, the less noble is the electrochemical behavior. Carbides tend to enhance nobility.
- In the potentiodynamic tests, carbides tend to localize the attack responsible for transpassivation.
- In the in vitro tests the CoCrMo alloy is not toxic for the cells irrespective to microstructure.
- The cells prefer to grow and to proliferate in the carbide zones; consequently, in the 0.35%C material the cells are able to fill all void spaces.
- Carbides seem to be a suitable substrate for biological cells adhesion.

Wear, corrosion and in vitro tests suggest the use of the as sintered 0.35%C material for biomedical applications. However, this material is too brittle. The 0.35%C solution annealed alloy presents the best mechanical properties while the corrosion behavior remains quite good, and the mass loss of the polymer is very low. This material could then represent the best solution for the production of an orthopedic prostheses.

Titanium alloys (Ti6Al4V)

- The as sintered density is around 96% of the theoretical one.
- The oxygen and carbon contents are in accordance with the specifications.
- The microstructure consists of a fully lamellar structure, typical of MIM Ti6Al4V.
- The as sintered material does not match the ASTM specifications since yield strength is quite low. Moreover, the fatigue resistance is rather poor.
- After shot peening the microstructure doesn't change significantly, but the micronotches present on the surface of the as sintered material are almost completely removed by local plastic deformation.
- The specimens shot peened with ceramic shots present the best surface roughness.
- The surface microhardness increases after shot peening mainly for the SP2 condition.
- Shot peening increases UTS and decreases ductility. This effect increases with the intensity of shot peening. Consequently, these materials do not match the ASTM specifications for the tensile tests.
- The shot peened material shows a higher fatigue resistance than the as sintered material.
- The results found for the HCF tests are comparable with literature values for cast and MIM conditions;

- The existence of pores together with a coarse microstructure are the main factors responsible for the significant lower HCF strength of MIM samples in comparison with the wrought materials.

Shot peening increases the fatigue resistance of the MIM Ti6Al4V alloy but, at the same time, it decreases ductility below the threshold of the standards.It seems very important to reduce the residual porosity in the as sintered microstructure. One alternative solution to improve the mechanical properties of MIM samples maintaining the same sintering process and changing only the post treatment is hot isostatic pressing (HIP) possibly followed by shot peening.

Stainless steel (316L and 17-4PH)

- Density is influenced by the presence of delta ferrite at high temperature; the higher the content of this constituent, the higher the as sintered density.
- The content of delta ferrite depends on the carbon content; increasing carbon content, decreases the fraction of delta ferrite.
- In the case of the 17-4 PH stainless steel, ferrite causes a decrease of tensile strength, without a corresponding increase in ductility. In presence of large amounts of delta ferrite, ductility tends to decrease significantly.
- For the austenitic stainless steel, delta ferrite increases hardness and both yield strength and ultimate tensile strength, correspondingly. On the other side ductility decreases.
- The fatigue strength is correlated to tensile ductility; it decreases with the increase in the delta ferrite content at a constant density.

Most of the results of this work have been subject of the following publications and presentations:

1. P. Vieira Muterlle, M. Perina, M. Mantovani, A. Molinari. “Dissolution the ‘the key’ to make carbide more friendly”, *Metal Powder Report*, v.64, p.30 - 33, 2009.

2. P. Vieira Muterlle, M. Zendron, M. Perina, R. Bardini, A. Molinari. “Influence of carbon content on microstructure and tensile properties of the 17-4PH stainless steel produced by MIM”, *Powder Injection Moulding International* (2008), vol. 2, n°4, pg. 56-59. (See appendix 2)

3. Muterlle P. V., D’Incau M., Perina M., Bardini R., Molinari A.. “Effect of Heat Treatment on Microstructure and Properties of Co-Cr-Mo Alloy Produced by MIM” (2008) *Advances in Powder Metallurgy & Particulate Materials* 4:183-190. Presented at World Congress PM2008, Washington, USA.

4. P. Vieira Muterlle, M. Zendron, C. Zanella, M. Perina, R. Bardini, A. Molinari, “Effect of Microstructure on the Properties of a Biomedical Co-Cr-Mo Alloy Produced by MIM”. *Advances in Powder Metallurgy & Particulate Materials*, Metal Powder Industries Federation, Princeton, NJ, 2009, vol. 4, pp. 60-69. Presented at the PowderMet 2009, Las Vegas, USA.

5. P. V. Muterlle, M. Zendron, M. Perina, R. Bardini, A. Molinari, “Microstructure and tensile properties of metal injection molding Co-29Cr-6Mo-0,23C alloy”, *Journal of Materials Science*, published online 03 December 2009.

6. Palloma Vieira Muterlle, Ivan Lonardelli, Matteo Perina, Marianna Zendron, Rudj Bardini, Alberto Molinari, “Solution annealing and aging of CoCrMo alloy produced by MIM”, was *accepted in 24 November 2009 to be published in the International Journal of Powder Metallurgy.*

7. P. Vieira Muterlle, M. Perina, M. Mantovani, L. Girardini, A. Molinari. “Microstructure and mechanical properties of Co alloyed Co-Cr-Mo produced by MIM”, *Proceedings EURO PM2007*, Tolouse, 2007, ed. EPMA, Shrewsbury (UK), vol. 2, p. 215-220.

8. P. Vieira Muterlle, M. Zendron*,* M. Perina*,* R. Bardini, A. Molinari. “Influenza del tenore di carbonio sulla microstruttura e sulle proprieta’ meccaniche di acciaio inossidabile 17-4PH prodotto per MIM”. *Presented at 32°Convegno Nazionale AIM*, 2008, Ferrara, Italy.

9. P. V. Muterlle, M. Perina, M. Zendron, R. Bardini, A. Molinari. “Studio della solubilizzazione e dell’invecchiamento della lega Co-Cr-Mo prodotta per MIM di polveri”. *Presented at 22° Convegno Nazionale Trattamenti Termici*, 2009, Salsomaggiore, Italy.

10. P. V. Muterlle, M. Zendron, M. Perina, A. Molinari. “Influence of delta ferrite on mechanical properties of 316L stainless steel produced by MIM”, *Presented at COBEM2009*, 15-10 November 2009, Gramado, Brazil. (See appendix 1)

ACKNOWLEDGEMENTS

Vorrei ringraziare MIMEST spa che mi ha dato l'opportunità di realizzare il mio dottorato preso l'Università di Trento ed alla Marianna per l'aiuto di sempre.

Ringrazio anche tutti quelli che mi hanno aiutato e mi sono stati vicini in questi anni, principalmente vorrei ringraziare ancora Marianna, Giusy, Luca F., Cinzia, Lorena, Giovanna, Ivan, Massimo, Straffelini, Vigilio, Matteo Benedetti, Emilio, Elena, Denis, Stefano, Mario, Luca G., Francesco C. e Francesco Endrici.

Ringrazio anche Caterina, Michele, Veronica e Luca Benedetti del laboratorio di corrosione ed anche Fabrizio, Angela, Vilma e Mirco, per l'aiuto di sempre. A Gianpaolo ed alla dottoressa Antonella Motta per l'aiuto e pazienza nella realizzazione delle prove di biocompatibilità

Ad Anna, Aylin, Lorenzo e Vincenzo per l'amicizia, mi siete sempre stati vicini.

Vorrei ovviamente ringraziare ai miei amici brasiliani, che si non fosse stato per loro non sarei stata capace di finire il mio dottorato, lontana della mia famiglia e di tutto, loro sono stati la mia famiglia e lo so che saranno per sempre, per questo ringrazio: Nerio, Camila, Prette, Tati, Ketner, Ana Paula, Izabel, Patricia, Stefano, Debora, Fabio, Thiago, "Gianluca, Gianpiero e Davide" (amici italiani però con spirito brasiliano).

Al mio ragazzo Gustavo, per il suo amore e compagnia in quest'ultimo anno di dottorato, lui è stato un regalo di dio per chiudere con chiave di oro questi anni. Mi sei sempre stato vicino, mi aiutando, dando amore e mi facendo ridere, e hai sempre avuto molta pazienza con me, pure adesso che sono in vacanza a casa sua ed invece di andare in giro sto finendo di scrivere la mia tesi ☺. Grazie di tutto vita, ti amo.

Vorrei fare un ringraziamento speciale ad Alberto Molinari, mio tutor ed amico, una persona che è sempre stata al mio lato e che mi ha sempre aiutato, alzando la mia morale quando ero demotivata, insegnandomi molte cose e appoggiandomi nei momenti di difficoltà. Grazie di tutto, ho imparato molto con te, spero che adesso che sarò in Brasile possiamo continuare a lavorare insiemi e che l'amicizia non finisca.

E per ultimo ringrazio molto alla mia famiglia che amo molto e che mi è mancata troppo in questi 4 anni, al mio padre Erineu, alla mia madre Zilda, alle miei sorelle Carolle e Carmella, al mio cognato Romeu, ai miei zii, alle miei nonne Zilda e Maria e al mio nonnino Silvo che purtroppo non potrà vedermi diventare una PhD in Ingegneria dei Materiale.

Grazie a tutti voi ed arrivederci, mi mancherete tutti. Un bacione

BIBLIOGRAPHIC REFERENCES

[1] German R.M., Powder injection molding, ASM Handbook, v. 7, 1998;

[2] P.J. Vervoort, R. Vetter and J. Duszczyk, Overview of Powder Injection Molding, A*dvanced Performance Materials,* 3 (1996) 121-151;

[3] Randall M. German, Powder Injection molding, Princeton, N.J.: Metal powder industries federation, 1990;

[4] Riedel H., Zipse H., and Svoboda J.: Acta Metall. Mater., 42(2):445-52, 1994

[5] German R.M.: Reviews in Particulate Materials, v. 1, 1993, MPIF, Princeton, New Jersey, pp. 109-160

[6] Dalskov N.P.: In Proc. of the Int. Conf. on Powder Injection Molding, november 10, 1994, The Netherlands, Microcentrum Nederland

[7] Steger R.: in Proc. of the PM Word Conference'94, Paris, June 6-9, pp. 1197-1200, 1994

[8] European powder metallurgy association, EPMA, A Manufacturing Process for Precision Engineering Components: Metal Injection Molding, Shrewsbury, UK

[9] German M. Randall, Powder injection molding: design and applications, State college, Pa.: Innovative material solutions, 2003

[10] M. Peltsman, "Low Pressure Injection moulding and mould design", Metal Powder Report, 1986, vol. 41, pp. 367-369

[11] Betteridge W.: *Cobalt and Its Alloys*, Ellis Horwood Limited, UK, 1982

[12] Köster W., On the influence of the elements on the polymorphic transformation of cobalt, *Z. Metallkunde,* 43, 297-303, 1952

[13] M. Go´mez, H. Mancha,* A. Salinas, J. L. Rodrı´guez, J. Escobedo, M. Castro, and M. Me´ndez "Relationship between microstructure and ductility of investment cast ASTM F-75 implant alloy", J Biomed Mater Res. 1997;34:157–163

[14] Davis J.R.: *Handbook of Materials for Medical Devices,* ASM International, USA, (2006)

[15] R. Tandon, in Cobalt-Base Alloys for Biomedical Applications, ASTM STP 1365, J.A. Disegi, R.L. Kennedy, R. Pilliar eds., West Conshohocken, PA, ASTM, 1999, p. 3-10

[16] J.B. Brunski, Metals, *Biomaterials science: An Introductrion to Materials in Medicine*, B.D. Ratner, A.S. Hoffman, F.J. Schoen, and J.E. Lemons, Ed., Academic press, 1996, p 37-50

[17] Muterlle P. V., D'Incau M., Perina M., Bardini R., Molinari A. (2008) *Advances* in Powder Metallurgy & Particulate Materials 4:183-190

[18] A.M. Weinstein and A.J.T. Clemow, Cobalt-Based Alloys, *Concise Encyclopedia of Medical & Dental Materials*, D. Williams, Ed., Pergamon Press and The MIT Press, 1990, p. 106-112

[19] Revised by D. Klarstrom, P. Crook, and J. Wu, Metallography and Microstructures of Cobalt and Cobalt Alloys, *Metallography and Microstructures,* Vol 9, *ASM Handbook*, ASM International, 2004, p. 762–774

[20] M. Long and H.J. Rack, Titanium Alloys in Total Joint Replacement - A Materials Science Perspective, *Biomaterials,* vol. 19, 1998, p. 1621-1639

[21] N. Niinomi, Recent Titanium R&D for Biological Applications in Japan, *JOM,* June 1999, p. 32-34

[22] Lütjering G., Williams J.C.: *Titanium, Engineering Materials and Process*, Spring, Berlin, Germany, (2003)

[23] Conrad H., Doner M., de Meester B.: Titanium Science and Technology, Plenum Press, New York, USA, (1973) P. 969

[24] Boyer R., Welsch G., Collings E. W., eds.: Materials Properties Handbook: Titanium Alloys, ASM, Materials Park, USA, (1994)

[25] Baker H., ed.: Alloy Phase Diagrams, ASM Handbook, Vol. 3, ASM, Materials Park, USA, (1992)

[26] Collings E.W., The physical metallurgy of Titanium Alloys, ASM, USA, 1984

[27] Williams J. C.: Titanium Science and Technology, Plenum Press, New York, USA, (1973) p. 1433

[28] Peters M., Lutjering G., Ziegler G.: Z. Metallke. 74, (1983) p. 274

[29] Schutz R. W., Thomas D. E.: Corrosion, Metals Handbook, 9th edn, Vol. 13, ASM, Metals Park, USA, (1987) p. 669

[30] Davis J. R., ed.: Stainless Steels, ASM, Materials Park, USA, (1994) p. 139

[31] Schutz R. W.: Metallurgy and Technology of Practical Titanium Alloys, TMS, Warrendale, USA, (1994) p. 295

[32] Hartwig T., Comparation of Titanium Powders for MIM, EURO PM2006, Ghent, Belgium

[33] Froes F.H., Advanced in Titanium Metal Injection Molding, Inovations in Titanium Technology, TMS 2007 Annual Meeting & Exhibition, Orlando, Florida, USA p.157-166

[34] Wagner L., Lujtering G.: Second International Conference on Shot Peening, American Shot Peening Society, USA, (1984) p. 194

[35] L.M. Gammon, R.D. Briggs, J.M. Packard, K.W. Batson, R. Boyer, C.W. Domby, Metallography and Microstructures of Titanium and Its Alloys, *Metallography and Microstructures,* Vol 9, *ASM Handbook*, ASM International, 2004, p. 899–917

[36] Lujtering G., Albrecht J., Ivasishin O. M.: Titanium ’95, Science and Technology, The University Press, Cambridge, UK, (1996) p. 1163

[37] Ivasishin O. M., Lutjering G.: Titanium ’99, Science and Technology, CRISM “Prometey”, St. Petersburg, Russia, (2000) p. 441

[38] Albrecht J., Lütjering G., Nicolai H.P, Liesner C.: *Fatigue 2002*, EMAS, Warley, UK, (2002) p. 2085

[39] J.W. Weeton and R.A. Signorelli, Technical Note 3109, National Advisory Committee for Aeronautics, 1954

[40] Lutterotti L., Matthies S., Wenk H. R., Shultz A. S., Richardson J. W. (1997) J. of Appl. Phys. 81:594-600.

[41] Lonardelli I., Wenk H. R., Lutterotti L., Goodwin M. (2005) Journal of Synchrotron Radiation 12:354-360.

[42] Walker P.S., Blunn G.W., Lilley P.A., Journal of Biomedical Materials Research (Applied Biomaterials) vol. 33, 159-175, 1996

[43] H. Mancha, M. Gómez, M. Castro, M. Méndez, J. Méndez and J. Juárez, "Effect of Heat Treatment on the Mechanical Properties of an As-Cast ASTM F-75 Implant Alloy", *J. Mater. Synth Process*, 1996, vol. 4, no. 4, pp. 217-226

[44] T. Kilner, R. M. Pilliar, G. C. Weatherly, C. Allibert, "Phase Identification and Incipient Melting in a Cast Co-Cr Surgical Implant Alloy", *J. Biomed. Mater. Res.*, 1982, vol. 16, pp. 63-79.

[45] Caudillo M., Herrera-Trejo M., Castro M. R., Ramirez E., Gonzalez C. R., Juarez J. I. (2002) J. Biomed. Mater. Res. 59(2):378-385

[46] Clemow A. J. T. and Daniell B. L. (1979) J. Biomed. Mater. Res. 13:265.

[47] Shortsleeve F. J. and Nicholson M. E. (1951) Transactions, American Society for Metals 43**:**142

[48] Taylor R. N. J. and Waterhouse R. B. (1983) J. Mater. Sci. 18:3265-3280.

[49] Rajan K. (1982) Met. Trans. 13A:1161-1166.

[50] Rajan K. (1984) Met. Trans. 15A:1335-1338.

[51] P. V. Muterlle, M. Zendron, M. Perina, R. Bardini, A. Molinari, "Microstructure and tensile properties of metal injection molding Co-29Cr-6Mo-0,23C alloy", *Journal of Materials Science*, published online 03 December 2009.

[52] P.V. Muterlle, M. Perina, M. Mantovani, A. Molinari, *Metal Powder Report*, 64(2)(2009)30

[53] G. E. Dieter, 'Mechanical Metallurgy', SI Metric ed. (adapted by D. Bacon) (1988) Materials Science & Metallurgy, Singapore

[54] Salinas-Rodriguez A., Rodriguez-Galicia J. L. (1996) J. Biomed. Mater. Res. 31:409-419

[55] Kim Y. G. and Lim C. Y. (1988) Met. Trans. 19A:1625.

[56] Vander Sande J. B., Coke J. R. and Wulff J. (1976) Met. Trans. 7A:389-397.

[57] A. J. Saldivar Garcia, H. F. Lopez, Journal of Biomedical Materials Research 74A(2005)269

[58] Dr. S. Mischler, Tribology and Implants. Cours Biomatériaux, novembre 2006

[59] F.S. Georgette, J.A. Davidson, Journal of Biomedical Materials Research 20(1986)1229.

[60] H.E. Placko, S.A. Brown, J.H. Payer, Journal of Biomedical Materials Research 39(1998)292.

[61] C. Montero-Ocampo and A.S. Rodriguez, Journal of Biomedical Materials Research 29(1995)441

[62] C.V. Vidal and A.I. Muñoz, Electrochimica Acta 54(2009)1798.

[63] I. Milosev, H. Strehblow, Electrochimica Acta 48(2003)2767.

[64] A.W.E. Hodgso et al., Electrochimica Acta 49(2004)2167.

[65] TiJet Medizintechnik GmbH, Innovative Injection Molding of Titanium, 2006

[66] O.M. Ferri, T. Ebel, R. Bormann, Materials Science and Engineering A 504 (2009) 107–113

[67] Shi-bo Guo et al., Trans. Nonferrous Met. Soc. China, 16(2006)s701-s704

[68] J. Telesman, P. Kantzos, T. Gabb, P. Prevey, Proceedings of the Third Joint FAA/DoD/NASA Conference on Aging Aircraft, Albuquerque, New Mexico, USA, September, 1999

[69] R.J. Morrissey, D.L. McDowell, T. Nicholas, Int. J. Fatigue 21 (1999) 679–685

[70] R.K. Nalla, B.L. Boyce, J.P. Campbell, J.O. Peters, R.O. Ritchie, Metall. Mater. Trans. A 33 (2002) 899–918

[71] M.R. Bache, Inter. J. Fatigue 21 (1999) 105–111

Presented at COBEM2009

INFLUENCE OF DELTA FERRITE ON MECHANICAL PROPERTIES OF 316L STAINLESS STEEL PRODUCED BY MIM

P. V. Muterlle, palloma.muterlle@ing.unitn.it
University of Trento, Italy
M. Zendron, marianna.zendron@mimest.com
M. Perina, matteo.perina@mimest.com
MIMEST spa, Pergine Valsugana, Trento, Italy
A. Molinari, alberto.molinari@ing.unitn.it
University of Trento, Italy

Abstract: *Parts produced by Metal Injection Molding of 316L stainless steel powders are sintered at very high temperature, usually above 1300°C, to obtain full density. Under these conditions, a certain amount of delta ferrite is stabilized in the as sintered microstructure. Delta ferrite enhances sintering, since volume diffusion in the bcc lattice is faster than in the fcc austenite lattice. However, when maintained in the as sintered microstructure, it tends to influence the mechanical properties.*
The effect of the amount of delta ferrite on the tensile strength and fatigue strength of an austenitic stainless steel produced by MIM was studied in the present work. The content of delta ferrite was varied by changing the sintering temperature and the results of the mechanical tests were correlated to the microstructural features of the materials.
Keywords: *MIM, 316L stainless steel, delta ferrite, mechanical properties.*

1. INTRODUCTION

Metal Injection Molding (MIM) is a net shape technology which uses powders as raw material to produce parts characterized by a geometrical complexity with close dimensional tolerances (German 1997). It has been intensively developed in the last three-four decades, and finds application in different fields as, for instance, mechanical, automotive, biomedical, hobby and sport equipments industry. The powders are mixed to a binder to obtain a feedstock having the proper rheological properties to be injected in a die cavity and to keep the shape once the injection pressure has been removed. The green parts are then extracted from the die and treated to eliminate the binder. The debinded parts, called brown, are then sintered at high temperature to reach a final density very close to the theoretical one.

MIM is increasingly used to produce parts for biomedical industry. As an example, implantable prosthesis and external devices are produced by stainless steel, in particular the austenitic (Kyogoku *et al.,*

2000 and Loh *et al.,* 1996) and the precipitation hardening (Muterlle *et al.,* 2008 and Wu *et al*., 2002) grades. In the case of austenitic stainless steel, since sintering is carried out at very high temperature (above 1300 °C) the final microstructure may contain delta ferrite (Collins*,* 2002). This constituent is expected to influence the mechanical and corrosion resistance to some extent.

In this work, the effect of delta ferrite on the tensile and fatigue resistance of an AISI 316L stainless steel was investigated. Different amounts of delta ferrite were obtained by changing the sintering temperature and by heat treatment. The results of the mechanical tests were interpreted on the basis of the microstructural characteristics and correlated to the fracture morphology investigated at the Scanning Electron Microscope (SEM).

2. EXPERIMENTAL PROCEDURE

A pre-alloyed gas atomized 316L powder was mixed with a proprietary binder and feedstocks were molded to produce the specimens for tensile tests according to ASTM E 8M-03 – Standard Flat Unmachined Tension Test Specimen for Powder Metallurgy (P/M) Products. The same specimens were produce for fatigue tests, as well. Debinding was carried out in two steps: dissolution in water, to eliminate 80% of the binder, followed by thermal decomposition.

The samples were sintered in TAV (Caravaggio, Italy) vacuum furnaces with 1 hour isothermal holding in 100 mbar Ar backfilling at the temperatures reported in Table 1.

Table 1. Sintering conditions.

Materials	**Sintering Conditions**
316L NF	Sintering at **1360°C** in graphitic furnace
316L F	Sintering at **1380°C** in metallic furnace

Cooling from the sintering temperature was carried out with 1 bar nitrogen flux. A third material was produced carrying out a heat treatment at 1390°C for one hour on 316L F to obtain a material with higher quantity of delta ferrite; it is called **316L HF** in the following.

The carbon analysis was carried out by LECO CS125. Density was measured by the water displacement method.

The microstructure was investigated by Light Optical Microscopy (LOM) after etching with a 25% distilled water, 50% HCl and 25% HNO_3 solution. For the quantitative determination of the amount of delta ferrite, specimens were etched with a 5ml distilled water, 2.5g Potassium hydroxide and 2.5g Potassium ferrocyanide solution, and characterized by Image Analysis.

Microhardness (HV0,02) and hardness (HV10) were measured.

Tensile tests were carried out on an Instron machine with a strain rate of 0.2 s^{-1} and measuring strain with an axial extensometer with a gauge length of 12,5 mm.

High cycle fatigue tests were carried out on a Rumul Mikrotron 20kN machine with a frequency of 150Hz and a load ratio equal 0 (R=0). It was assumed $2x10^6$ cycles as run-out test. The fracture surfaces were investigated by SEM.

3. RESULTS AND DISCUSSION

3.1. Microstructure

Figure 1 show examples of the microstructure of the three materials investigated: NF (1a), F (1b) and HF (1c). The residual porosity is very low, and made of small, spheroidized and homogeneously distributed pores. Austenitic grains show several annealing twins, and the delta ferrite islands are isolated and distributed quite homogeneously, too. Figure 1d shows the effect of the specific etchant used to prepare the specimens for the quantitative determination of the amount of delta ferrite. Etching is localized at the austenite-ferrite interface, and the contrast between the two constituents is very sharp.

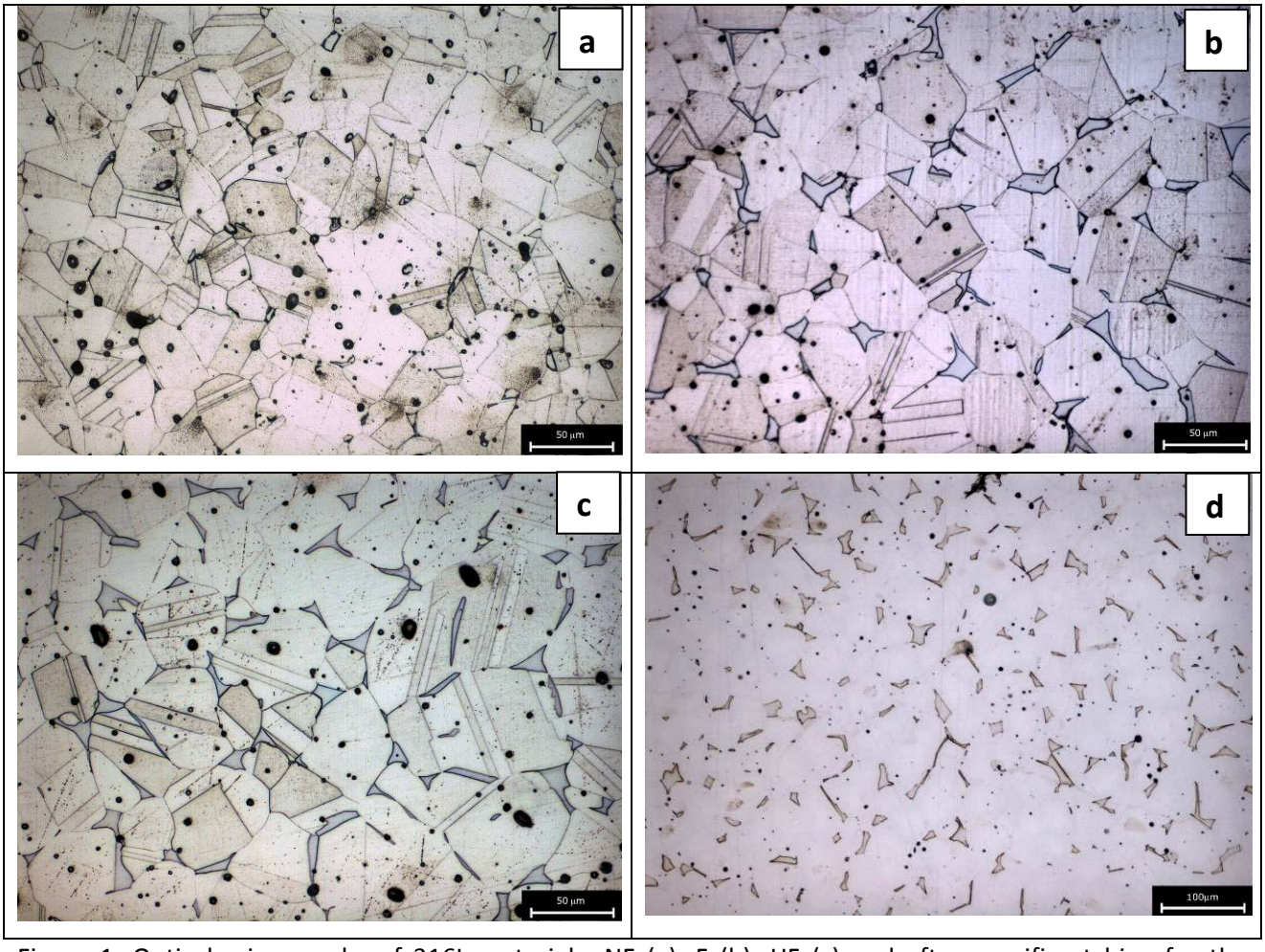

Figure 1. Optical micrographs of 316L materials: NF (a), F (b), HF (c) and after specific etching for the quantitative determination of delta ferrite by Image Analysis (d).

Table 2 reports the volumetric percent of delta ferrite, along with density and carbon content. On increasing the sintering temperature, delta ferrite content increases up to around 4.5%, and heat treatment leads to a further increase up to 8%. Density of the materials increases with the sintering temperature, as expected. At 1380°C, the material is practically full dense. Heat treatment does not change density. The carbon content is higher in the material sintered at the lower temperature, mainly because of the graphite heating bars which tend to reduce decarburization.

Table 2. Chemical analyses and ferrite composition.

Material	delta ferrite, %	Density, (g/cm^3)	C, %
316L NF	< 1	7.83±0.03 (98.5% of theor.)	0.0132
316L F	4.5±0.9	7.94±0.01 (99.8% of theor.)	0.003
316L HF	8±1	7.94±0.01 (99.8% of theor.)	0.003

3.2. Microhardness and hardness

Microhardness and hardness data is reported in table 3. Delta ferrite is harder than austenite, and on increasing its content in the material, hardness increases. Differences are rather low but significant.

Table 3. Microhardness and hardness of the investigated materials.

Samples		Microhardness (HV0.02)	Hardness (HV10)
316L NF	ferrite	Not measurable	111.1±3.1
	austenite	170.3±12.9	
316L F	ferrite	223.5±5.8	120.4±1.7
	austenite	163.5±1.2	
316L HF	ferrite	223.0±29	126.0±3.1
	austenite	167.5±11	

3.3. Mechanical properties

Figure 2 shows the tensile stress-strain curves of NF and F. The materials display a uniform plastic deformation up to the maximum stress, without any appreciable non uniform deformation.

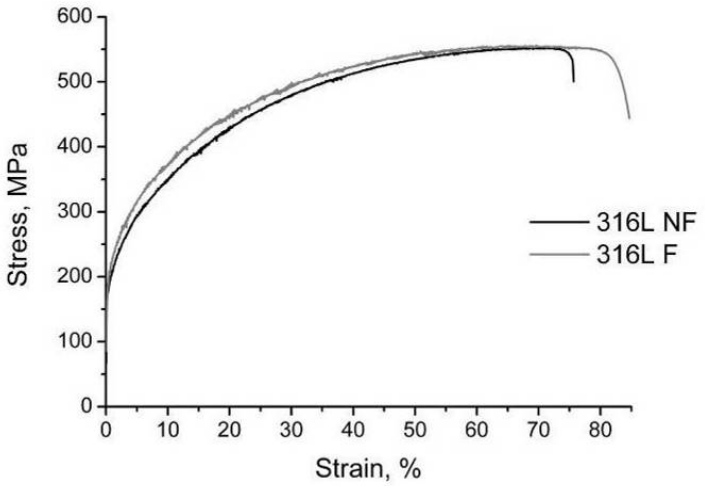

Figure 2. Tensile test curves for 316L materials

Table 4 reports the tensile properties of the three materials investigated. Results are comparable to those reported in the literature (Heaney *et al.,* 2004).

Table 4. Tensile properties of the investigated materials.

Samples	Yield Strength (MPa)	Ultimate Tensile Strength (MPa)	Elongation %
316L NF	186±1.5	549.9±3.9	65.7±9.3
316L F	194.1±5	555.4±0.5	82.7±2.6
316L HF	211.2±2	571.8±7.5	77.7±3

The increase in the sintering temperature from 1360°C to 1380°C causes an increase in both strength and ductility. This is due to the enhanced densification, but even to the increase in the ferrite content. This constituent is expected to increase strength, as actually observed. It also should cause a decrease of ductility, but the increase in density has a prevailing effect. Heat treatment increases strength but decreases ductility. This is only due to the increase in the ferrite content, since density does not change with heat treatment.

The fracture morphology is ductile, characterized by dimples as showed in figure 3, relevant to F and significant of the other materials shows. The fracture morphology does not show any feature attributable to delta ferrite, since this constituent has a typical ductile behavior as well.

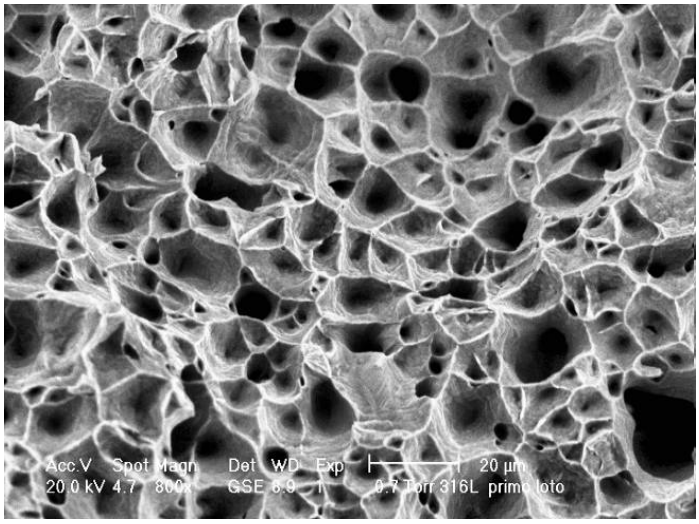

Figure 3. Tensile fracture surface of 316L F material

Table 5 reports the results of fatigue tests. The fatigue strength (FS) at $2x10^6$ cycles is reported, along the ratio between FS and UTS. Results are comparable to those reported in the literature (Kyogoku *et al.,* 2000).

Table 5. Fatigue tests.

Samples	**Fatigue Strength 50% (MPa)**	**FS / UTS**
316L NF	248±15	0.45
316L F	293±1	0.53
316L HF	272±16	0.48

Fatigue strength increases on increasing the sintering temperature (F versus NF), because of the increased density, strength and ductility. Here, the effect of delta ferrite is overshadowed by the enhanced densification provided by the higher sintering temperature. Fatigue strength is around one half of UTS. The effect of delta ferrite is shown by the comparison between HF and F. Here, fatigue strength decreases slightly despite the increased tensile strength, because of the decreased ductility. The FS/UTS ratio decreases, correspondingly.

The analysis of the fracture surface allows the nucleation of the fatigue crack to be individuated. It occurs on the surface, in correspondence of a pore, as figure 4a shows. There is an extensive slow propagation step of the fatigue crack (figure 4b), followed by fast propagation by overloading with the typical ductile morphology (figure 5).

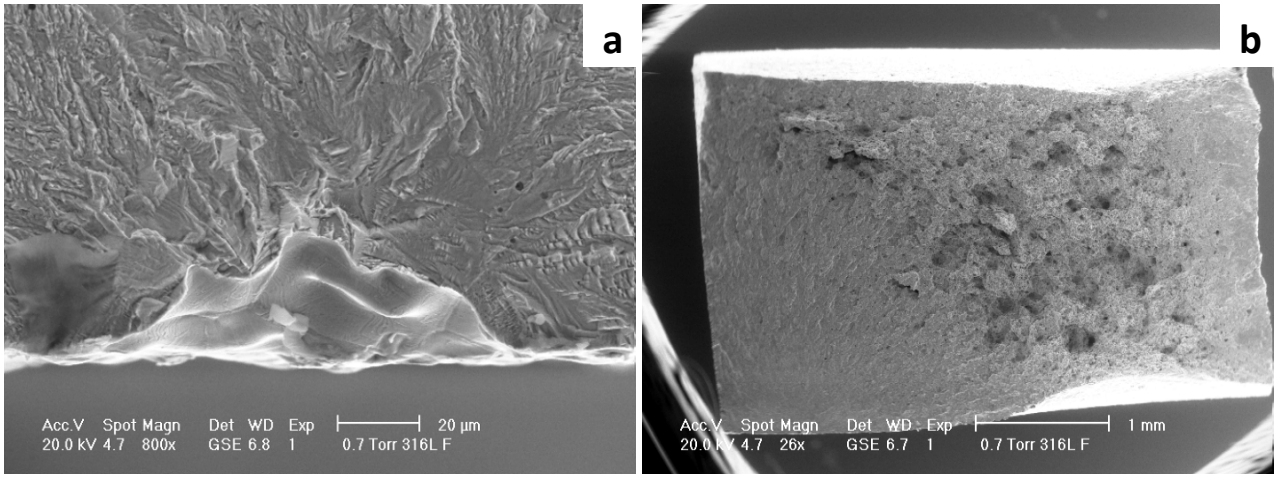

Figure 4. Nucleation site of the fatigue crack (a) and fatigue fracture surface (b) of 316L NF material.

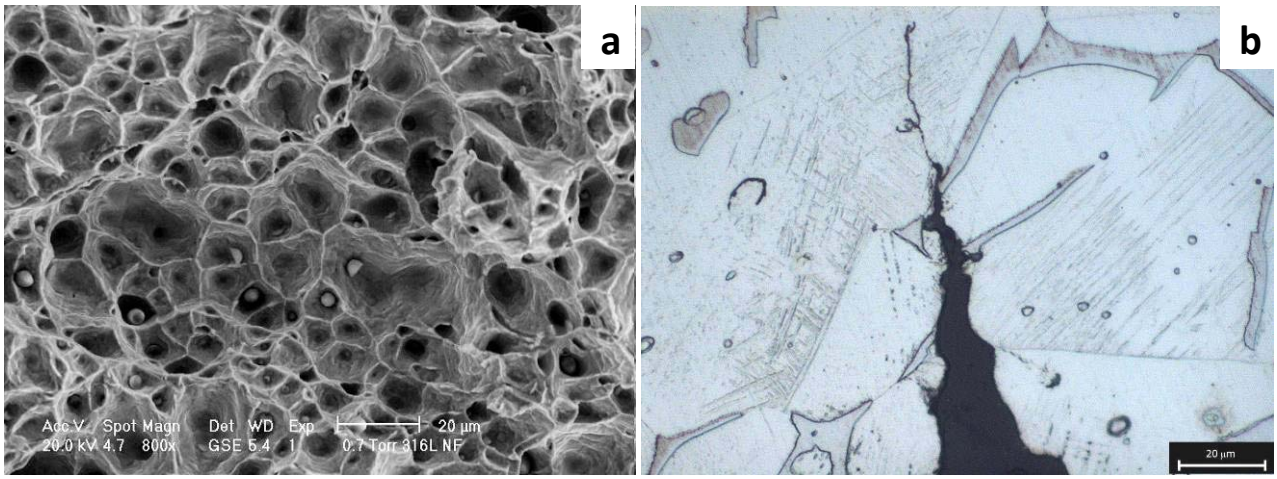

Figure 5. Ductile morphology of the fast fatigue crack propagation (a) and path of crack propagation (b).

As for tensile tests, there isn't any appreciable effect of the presence of ferrite on the fracture surface. The analysis of the propagating crack (figure 5b) confirms the absence of any preferential propagation path. The fatigue crack propagates through austenite grains as well as through delta ferrite grains.

4. CONCLUSIONS

Austenitic stainless steel tensile and fatigue specimens were produced by MIM to study the effect of the content of delta ferrite on mechanical properties. Delta ferrite content increases with the sintering

temperature, and with a post-sintering heat treatment at high temperature. Sintering temperature increases density from 98.5% to 99.8% of the theoretical one.

Delta ferrite increases hardness and both yield strength and Ultimate Tensile Strength, correspondingly. On the other side, ductility decreases. This effect can be overshadowed by density when the increase in delta ferrite is due to an increase in the sintering temperature. In this case, the effect of density on ductility prevails on that of delta ferrite. As far as fatigue strength is concerned, it is correlated to tensile ductility; it decreases with the increase in the delta ferrite content at a constant density. No features attributable to delta ferrite were observed on the fracture surfaces.

5. REFERENCES

German, R.M. and Bose, A., 1997, Injection molding of metals and ceramics, MPIF, Princeton, NJ.

Kyogoku, H., Komatsu, S., Shinzawa, M., Mizuno, D., Matsuoka, T. and Sakaguchi, k., 2000, "Influence of microstructural factors on mechanical properties of stainless steel by powder injection molding", Proceedings of 2000 Powder Metallurgy World Congress, pp. 304-307.

Loh, N. H., Khor, K. A. and Tor, S. B., 1996, "Sintering Characteristics of Metal Injection Moulded Stainless Steel 316L", Advances in Powder Metallurgy & Particulate Materials, Vol. 5, pp. 29-37.

Muterlle, P. V., Zendron, M., Perina, M., Bardini, R. and Molinari, A., 2008, "Influence of carbon content on microstructure and tensile properties of the 17-4 PH stainless steel produced by MIM", Powder Injection Moulding International, Vol. 2, pp. 66-69.

Wu, Y., German, R. M., Blaine, D., Marx, B. and Schlaefer, C., 2002, "Effects of residual carbon content on sintering shrinkage, microstructure and mechanical properties of injection molded 17-4 PH stainless steel", Journal of Materials Science, Vol. 37, pp. 3573-3583.

Collins, S. R., 2002, "Microstructural Characterization of Metal Injection Molded (MIM) AISI 316L", Microscopy Society of America, Vol. 8.

Heaney, D. F., Mueller, T. J. and Davies, P. A., 2004, "Mechanical properties of metal injection moulded 316l stainless steel using both prealloy and master alloy techniques", Powder Metallurgy, Vol. 47, pp. 1-7.

Published at Powder Injection Molding International, 2(2008)56-59.

INFLUENCE OF CARBON CONTENT ON MICROSTRUCTURE AND TENSILE PROPERTIES OF THE 17-4 PH STAINLESS STEEL PRODUCED BY MIM

P. V. Muterlle[1], M. Zendron[2], M. Perina[2], R. Bardini[2], A. Molinari[1]

Abstract

The effect of the carbon content on microstructure and tensile properties of a MIM 17-4PH stainless steels has been investigated. Carbon content influences the formation of delta ferrite at high temperature, which increases sintered density. However, delta ferrite causes a decrease of tensile strength, without a corresponding increase in ductility. In presence of large amounts of delta ferrite, ductility decreases significantly.

Keywords: MIM, stainless steel 17-4PH, carbon content, delta ferrite, tensile properties.

1. INTRODUCTION

The 17-4PH stainless steel has an excellent combination of mechanical properties, provided by the precipitation hardened low carbon martensitic matrix, and corrosion resistance. Mechanical properties are optimized by a precipitation hardening treatment, and depend on the aging temperature. The maximum hardness and strength are obtained by aging between 450°C and 510°C due to the precipitation of coherent copper particles [1,2,3]. The maximum ductility and toughness are instead obtained by aging at higher temperatures (> 540°C), when the copper particles become incoherent with the martensitic matrix [1,2,3].

In the 17-4PH stainless steel produced by Metal Injection Molding (MIM), one of the most important parameter is carbon content, since it has a noticeable effect on density, microstructure and corrosion resistance [4,5].

The sintering temperature varies between 1250°C [6] and 1390°C [7]. At these temperatures, microstructure comprises a certain amount of delta ferrite in the austenitic matrix. It is well known that volume diffusion is faster in the b.c.c. ferrite than in the f.c.c. austenite, then ferrite enhances sintering and densification. Since carbon stabilizes austenite, at a given sintering temperature densification is inversely proportional to its

[1] Dipartimento di Ingegneria dei Materiali e Tecnologia Industriali, Università di Trento, Mesiano 77, 38100, Trento, Italy
E-mail: palloma.muterlle@ing.unitn.it
E-mail: alberto.molinari@ing.unitn.it

[2] NCS Protech Spa, Viale Dante 300, 38057, Pergine Valsugana, Trento, Italy
E-mail: marianna.zendron@ncsprotech.com
E-mail: matteo.perina@ncsprotech.com
E-mail: rudj.bardini@ncsprotech.com

amount. As a consequence, an increase in carbon content requires a corresponding increase in the sintering temperature to get full densification.

In addition, delta ferrite itself decreases mechanical strength. Therefore, the effect of carbon on the mechanical properties results from two opposite trends, both related to the amount of delta ferrite.

In this paper, the results of an experimental study aimed at the optimization of the properties of the 17-4PH stainless steel produced by MIM are presented. Two pre-alloyed powders were used, differing in the carbon content, and sintering was carried out at two temperatures. Density, microstructure and mechanical properties were investigated after aging in the two typical conditions of the industrial practice: H900 (aging at 482°C) and H1100 (aging at 560°C).

2. EXPERIMENTAL PROCEDURE

Two different gas atomized 17-4PH powders were used, containing a different carbon amount: Low Carbon (LC – 0,036%C) and High Carbon (HC – 0,06%C). The powders were mixed with a proprietary binder and feedstocks were molded to produce the specimens for tensile tests according to ASTM E 8M-03 – Standard Flat Unmachined Tension Test Specimen for Powder Metallurgy (P/M) Products. Debinding was carried out in two steps: dissolution in water, to eliminate 80% of the binder, followed by thermal decomposition at 700°C.

Specimens were sintered at 1280°C and 1330°C, one hour isothermal holding, in a graphitic vacuum furnace TAV, with a 100 mbar Ar backfilling at high temperature. Cooling from the sintering temperature was carried out by 1 bar nitrogen flux. Since the cooling rate from the sintering temperature is similar to that of the typical solution annealing treatment, as sintered specimens were aged directly after sintering at two temperatures: 1 hour at 480°C (H900) and 4 hours at 560°C (H1100), in a laboratory furnace under a dry Ar protective atmosphere.

Carbon and oxygen analyses were carried out by LECO CS125 and LECO TC400, respectively.

Density was measured by the water displacement method.

Differential Scanning Calorimetry (DSC) was carried out on both the green and the sintered specimen to investigate the formation of delta ferrite on sintering and the microstructural transformation on aging. Tests were carried out in a pure Ar flux (100ml), with a heating rate of $20 K min^{-1}$.

The quantitative determination of the delta ferrite content was made by Image Analysis at the Light Optical Microscope (LOM) on the metallographic sections etched with Kalling 1.

Microhardness (HV0,1) and hardness (HRC) were measured.

Tensile tests were carried out on an Instron machine with a strain rate of $0.1\ mm.min^{-1}$, and the fracture surfaces were investigated at the Scanning Electron Microscope (SEM)

3. RESULTS AND DISCUSSION

As sintered materials

The C and O content of the brown and the as sintered materials are reported in tab. 1, in comparison to the nominal carbon content of the two powders. Sintered density is reported, as well.

Table 1: carbon and oxygen contents and density of the investigated materials

Material		**%C**	**%O**	**Density [g/cm^3]**	**% of theoretycal density**
Low carbon steel	**Powder**	0,036			
	Brown	0,06	0,12		
	Sint. 1280°C	0,0305	0,0992	7,76	98,9
	Sint. 1330°C	0,0508	0,0832	7,79	99,2
High carbon steel	**Powder**	0,06			
	Brown	0,1	0,06		
	Sint. 1280°C	0,0162	0,0097	7,45	94,9
	Sint. 1330°C	0,0421	0,0028	7,76	98,9

The carbon content of the brown specimens is higher than that of the powder, because of the presence of some residual of the binder. On sintering, a strong decarburization occurs, since carbon reacts with oxygen. Decarburization is stronger in the specimens sintered at the lower temperature since the less densification favors the outward flow of the gaseous product of decarburization.

The LC material has a higher density than HC, in particular on sintering at the lower temperature. This is attributable to the larger amount of delta ferrite, as shown by the microstructural analysis (figures 1 and 2). The quantitative analysis of the content of delta ferrite gives around 20% vol. in LC at both the sintering temperatures, 5% vol. in HC sintered at 1330°C and no ferrite in HC sintered at 1280°C. The effect of ferrite is quite strong, since this last material densifies to around 95% of theoretical density only.

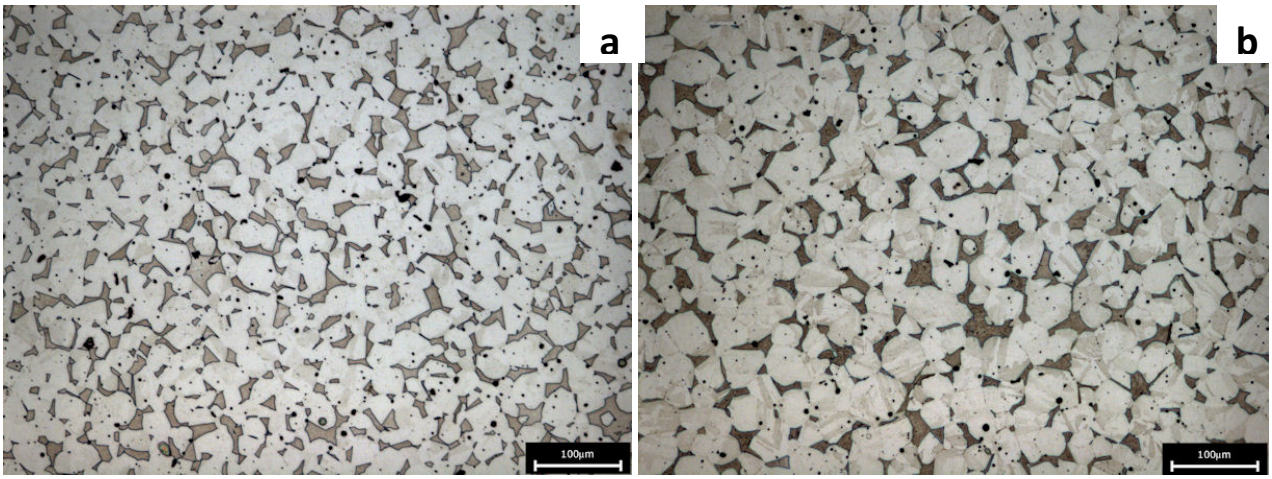

Fig. 1: LC steel sintered at 1280°C (a) and 1330°C (b).

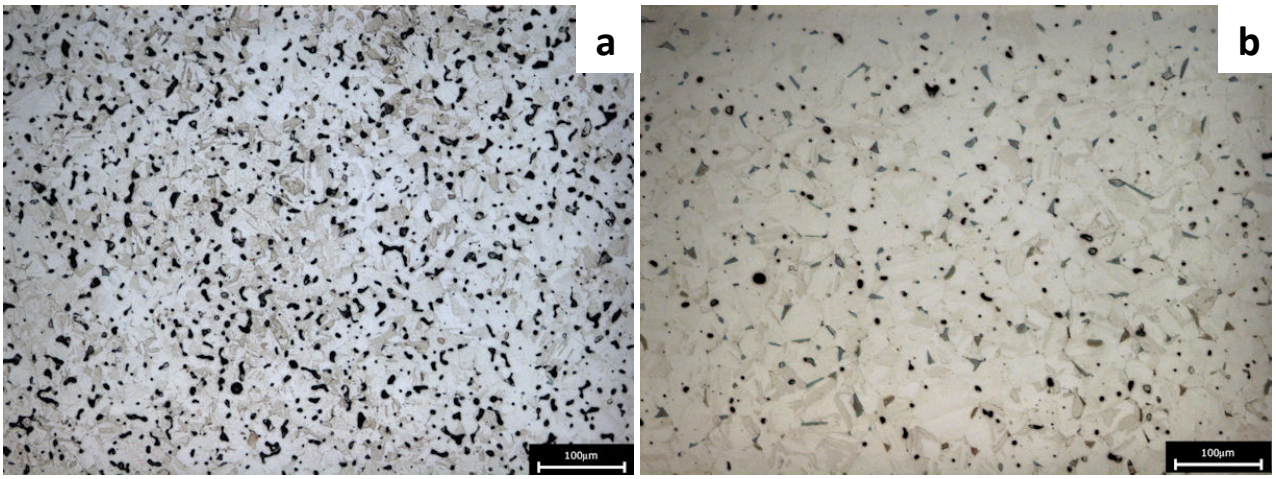

Fig. 2: HC steel sintered at 1280°C (a) and 1330°C (b).

Study of microstructural transformations by DSC

Figures 3 show the high temperature portion of the DSC curves of the two materials in the brown condition. The deviation from linearity of the curve indicates the start of the transformation of austenite in delta ferrite. It occurs at a lower temperature in LC, because of the lower carbon content. The absence of delta ferrite when sintering HC at 1280°C is confirmed, since transformation starts at about 1320°C.

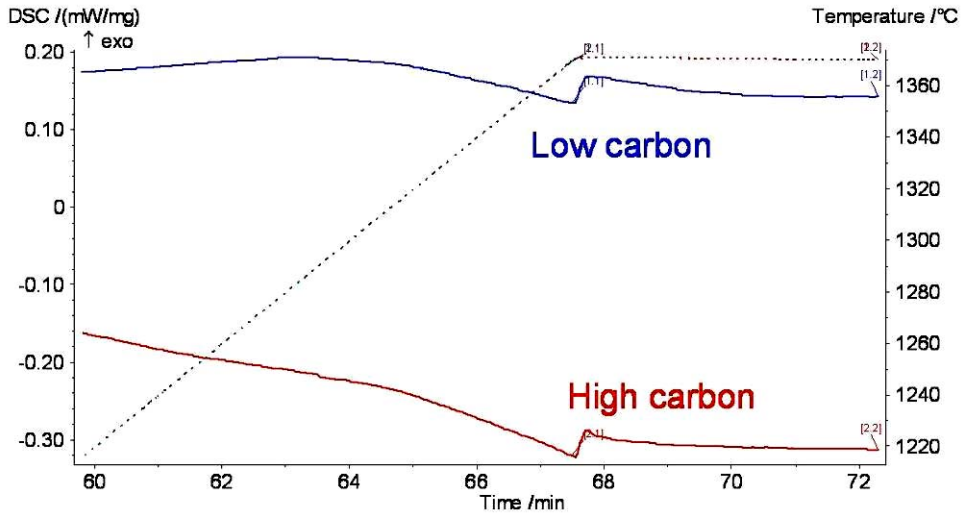

Fig. 3: DSC curves (high temperature) of the two materials investigated

DSC was carried out on the as sintered materials, as well, to study phase transformations occurring in the temperature ranges of aging. Figure 4 shows DSC records of the two sintered materials. The two peaks can be attributed to precipitation phenomena (the exothermic peak at lower temperature) and to the

formation of austenite (the endothermic one at higher temperature). Precipitation is more extensive in HC than in LC, as the heat released shows. Since the copper content is the same in the two materials, this effect can be attributed to the concurrent precipitation of chromium carbides, which has been reported by other authors [8]. The transformation of martensite in austenite occurs at a higher temperature and with a less intensity in HC, since the precipitation of carbides results in a significant carbon depletion of carbon of martensite.

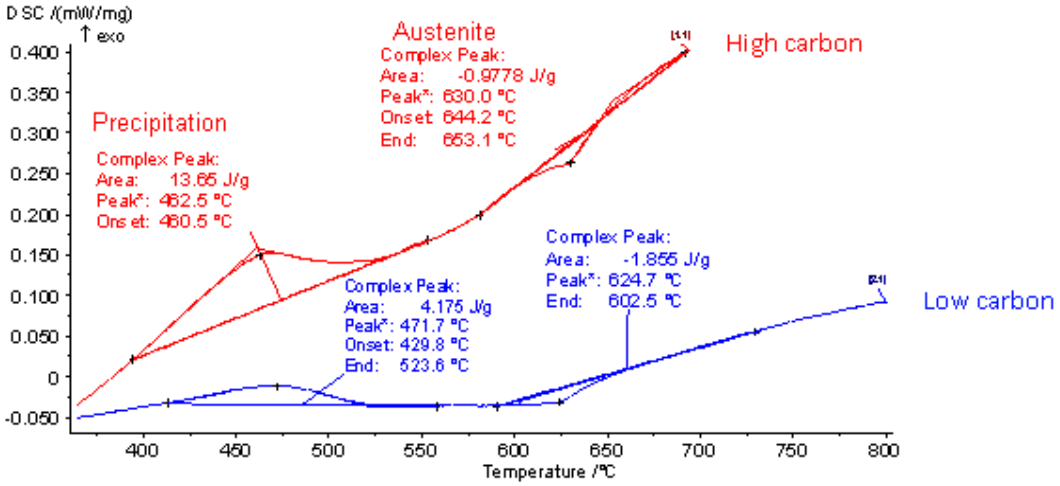

Fig. 4: DSC of the as sintered materials.

Microstructure, microhardness and hardness

The micostructure of the aged materials is shown in figures 5 (H900) and 6 (H1100). Aging at these temperatures does not change the content of ferrite, as indicated by DSC. Precipitation is submicrometric, and then not visible at the LOM.

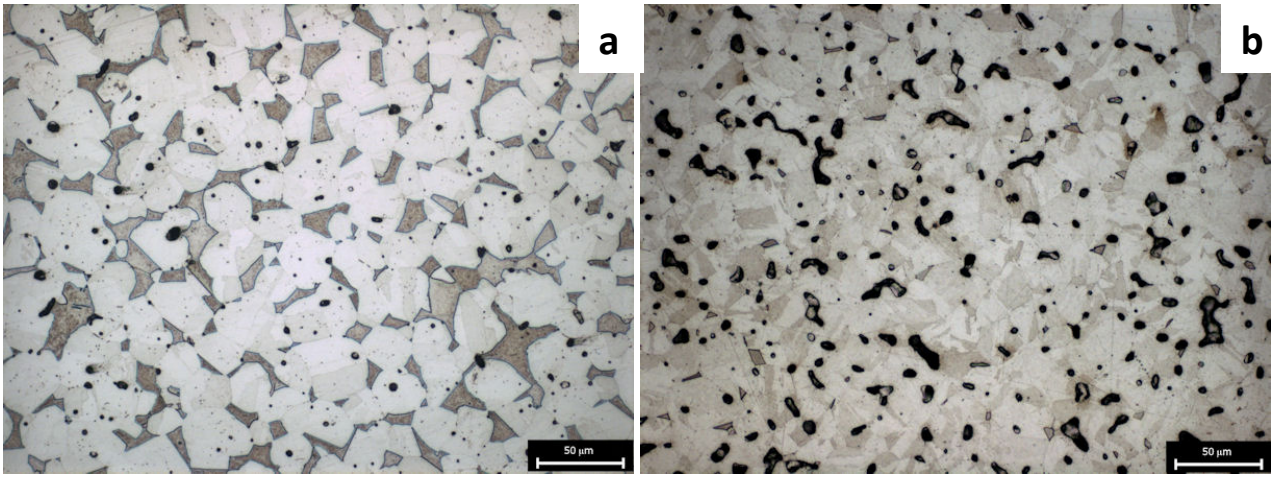

Fig. 5: Microstructure of H900 aged LC (a) and HC (b) sintered at 1280°C

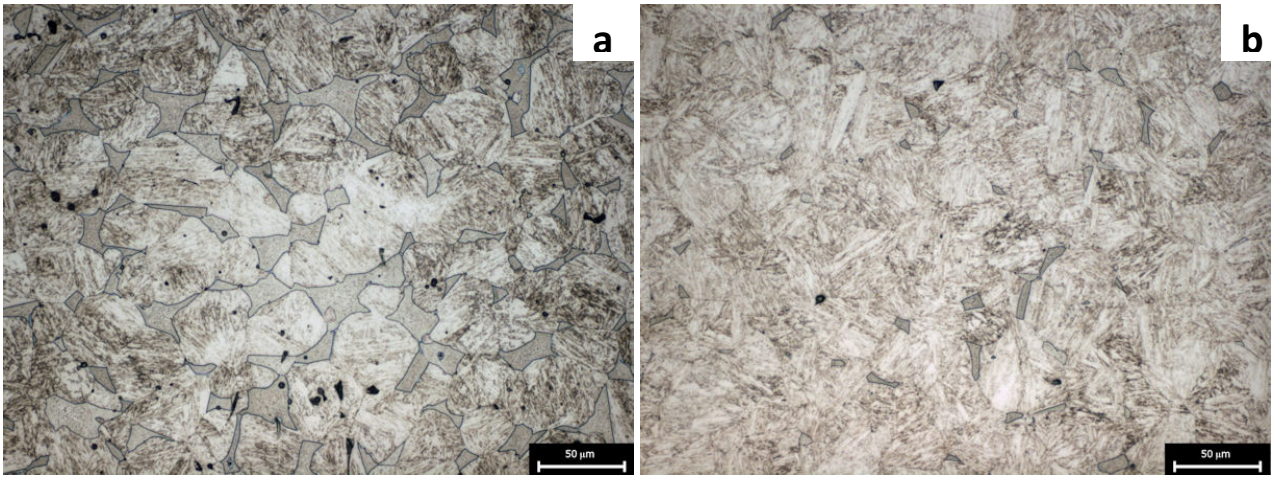

Fig. 6: Microstructure of H1100 aged LC (a) and HC (b) sintered at 1330°C

Tab. 2 reports hardness and microhardness of martensite of the aged materials, in comparison with the as sintered ones. Hardness and microhardness increase with aging, in particular at the lower temperature (H900). Results are in agreement with literature.

Tab. 2: hardness and microhardness

Materials	Treatment	HRC	$HV_{0.1}$ (martensite)
LC - 1280°C	As sintered	30 ± 1	340 ± 6
	H900	38,7 ± 1,4	458 ± 8
	H1100	32,2 ± 0,6	337 ± 9
LC - 1330°C	As sintered	32 ± 0,2	365 ± 12
	H900	42,4 ± 0,4	492 ± 12
	H1100	33 ± 1	372 ± 10
HC - 1280°C	As sintered	21 ± 1	283 ± 30
	H900	30,7 ± 1,2	427 ± 8
	H1100	23,1 ± 1,4	357 ± 29
HC - 1330°C	As sintered	34 ± 0,4	361 ± 20
	H900	42,1 ± 1,4	492 ± 12
	H1100	32,9 ± 0,8	328 ± 22

Tensile resistance

Figures 7, 8, 9 e 10 show the results of tensile tests on the two materials: yield stress (σ_y) Ultimate Tensile Strength (UTS) and percent elongation at fracture (ε) are reported.

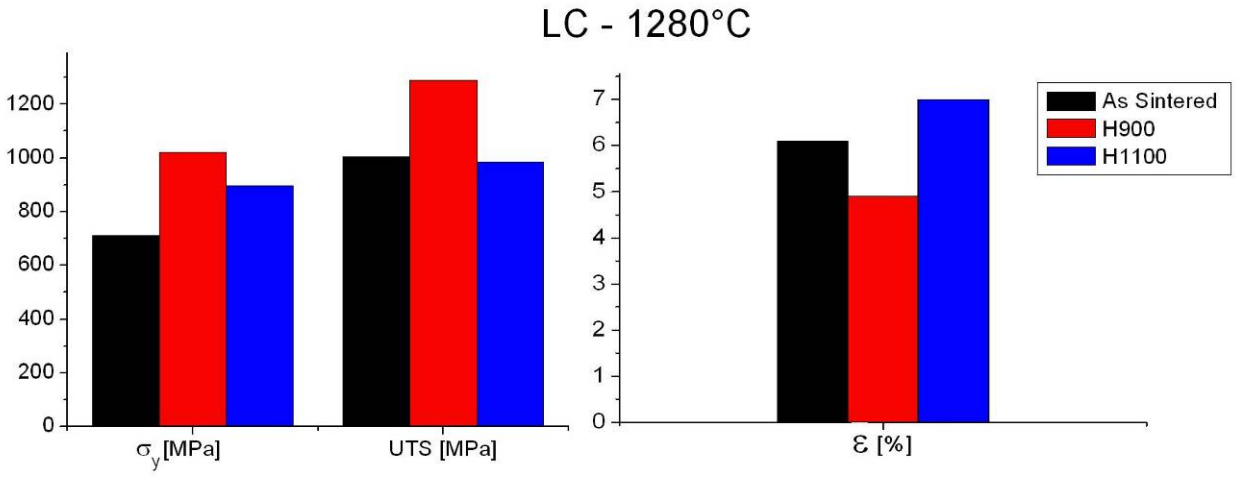

Fig. 7: results of tensile tests on LC sintered at 1280°C

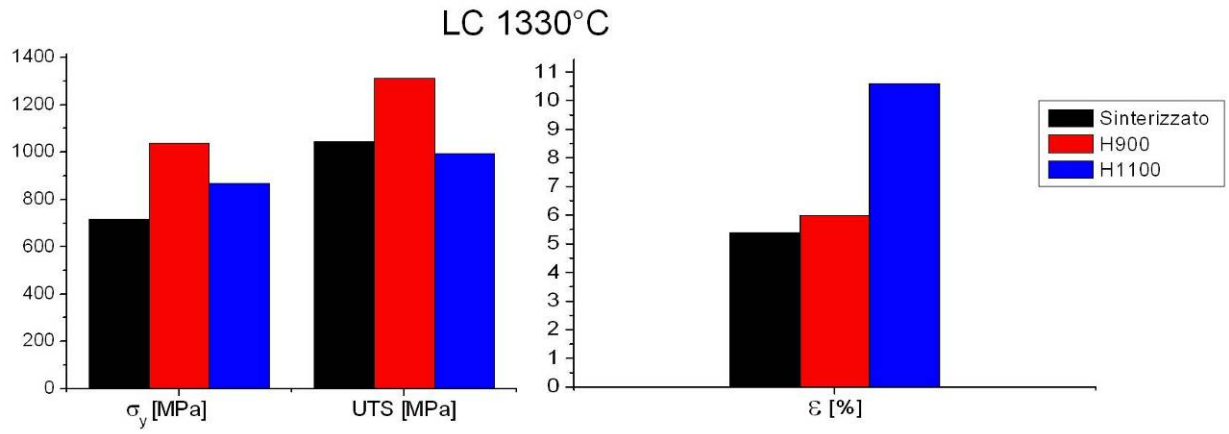

Fig. 8: results of tensile tests on LC sintered at 1330°C

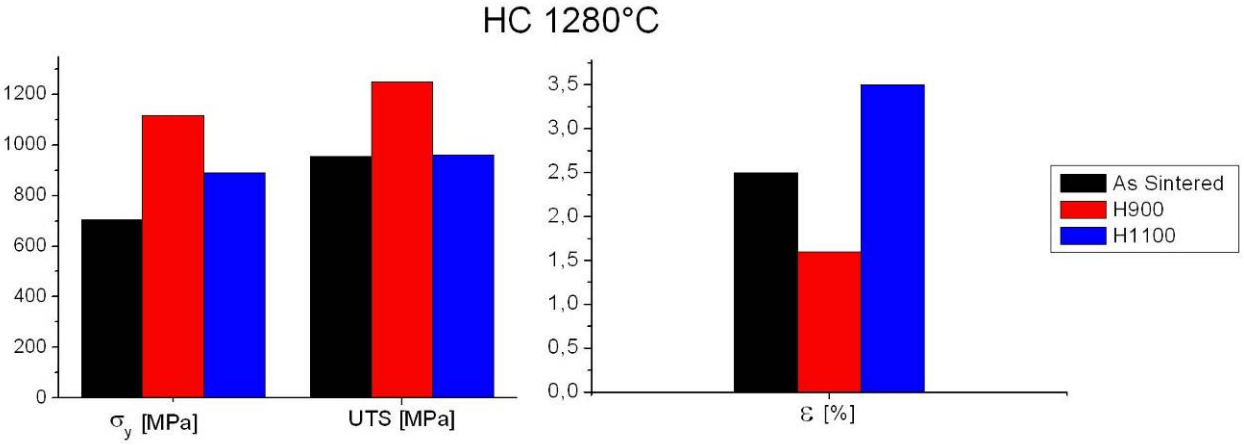

Fig. 9: results of tensile tests on HC sintered at 1280°C

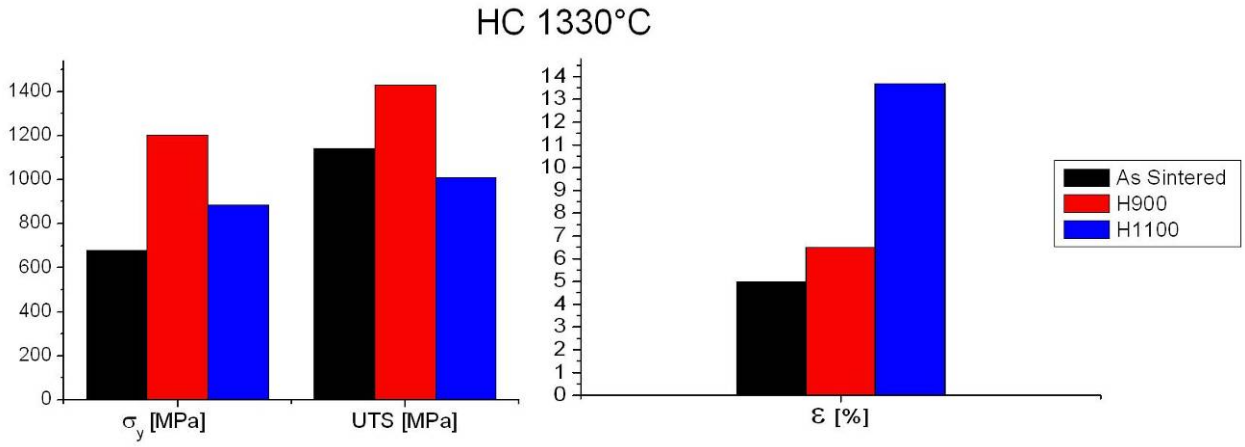

Fig. 10: results of tensile tests on HC sintered at 1330°C

As expected, H900 aging results in the highest strength, whilst H1100 in the highest ductility. The effect of aging on strength (H900) is quite strong in the materials sintered at both the temperatures, whilst that on ductility (H1100) is significant only in the materials sintered at the highest temperature. To compare the four aged materials, results of the tensile tests are reported figures 11 e 12; here, the experimental points are plotted in a "yield stress vs. percent elongation map", to represent the combination of strength and ductility attained. The sintering temperature and the as sintered density are labeled for each experimental point.

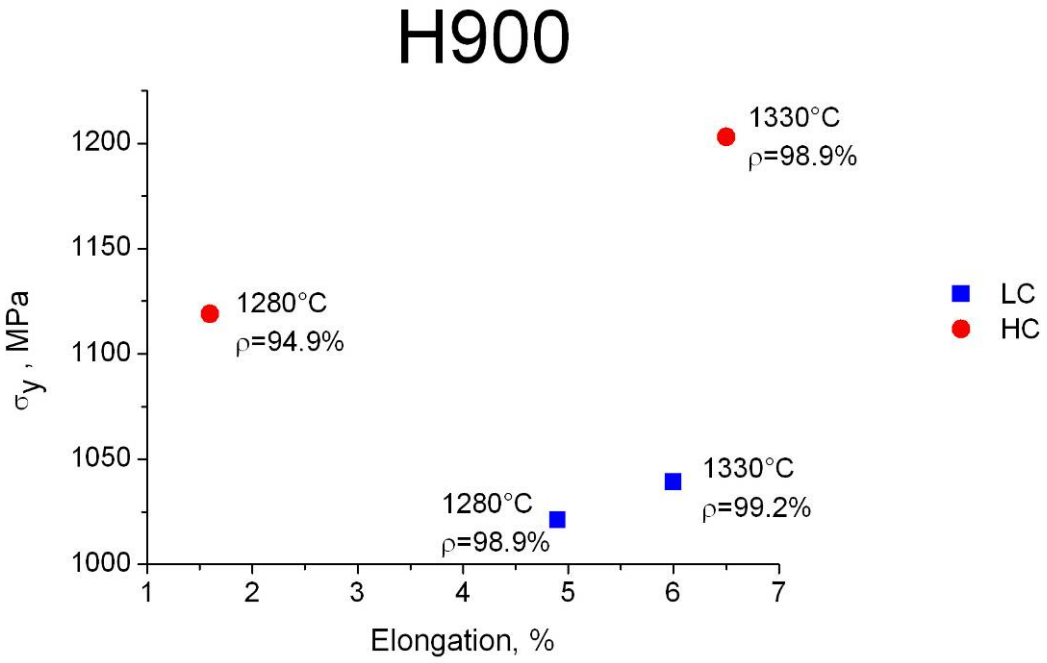

Fig. 11: synthesis of the tensile properties of materials aged H900

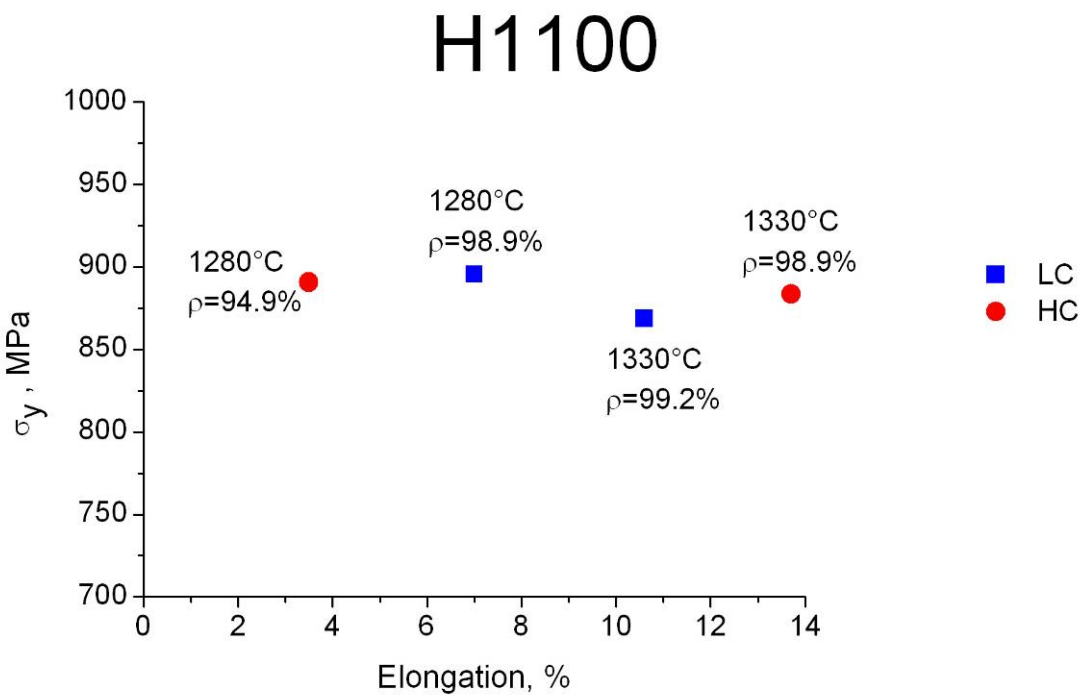

Fig. 12: synthesis of the tensile properties of materials aged H1100

To discuss the figures, it has to be considered that mechanical properties of sintered 17-4PH steel depend on microstructure, which consists of martensite with a minor amount of delta ferrite, and by porosity. Carbon content influences the amount of delta ferrite and the inherent tensile strength of martensite.

In the H900 condition, HC has a higher strength than LC even with a lower density, as in the case of the materials sintered at 1280°C. The higher strength has to be attributed to the lower amount of delta ferrite which, on the other side, does not result in an increase in ductility. The best properties were obtained on materials sintered at 1330°C. Sintering at a lower temperature leaves a residual porosity of about 5%, which reduces both strength and ductility.

In the H1100 condition, all the materials have almost the same yield stress, and a different ductility, which is the highest in HC sintered at 1330°C. Ductility may be correlated to delta ferrite since, a part from HC sintered at 1280°C, the materials have the same density: the lower the ferrite amount, the higher is ductility.

The effect of delta ferrite on ductility has been reported as negative when its content exceeds about 16% [9]. The results of the present study confirm this conclusion, in particular on aging H1100. The materials aged at the lower temperature are less sensitive to delta ferrite, likely because this treatment is specifically aimed at maximizing strength and microstructure is less ductile than that obtained at the higher temperature, because of the presence of the coherent precipitates which oppose more effectively the motion of dislocations.

Figures 13 and 14 show the fracture surface of the four materials aged H900 and H1100, respectively.

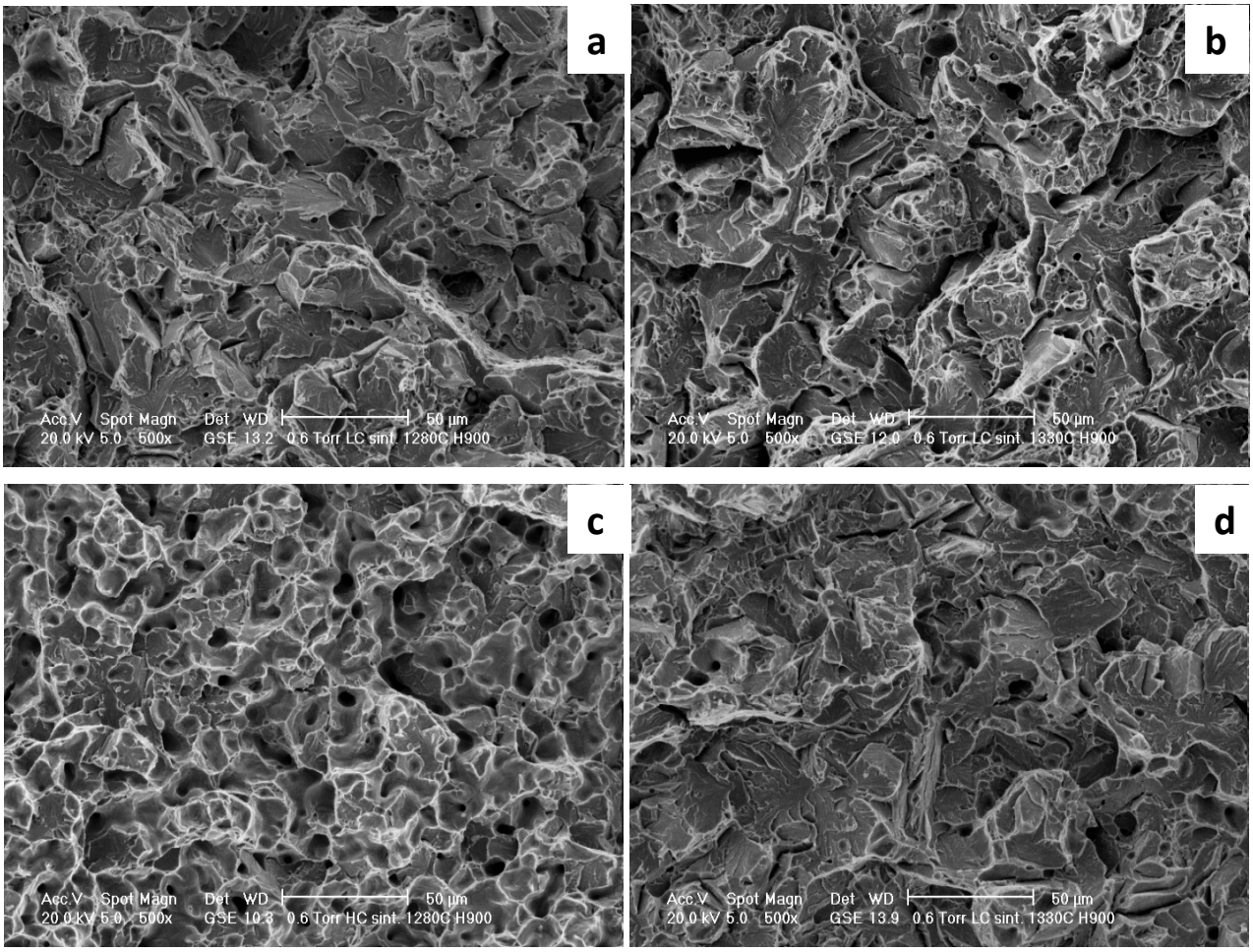

Fig. 13: fracture surfaces of H900 materials: a) LC sintered at 1280°C, b) LC sintered at 1330°C, c) HC sintered at 1280°C and d) HC sintered at 1330°C.

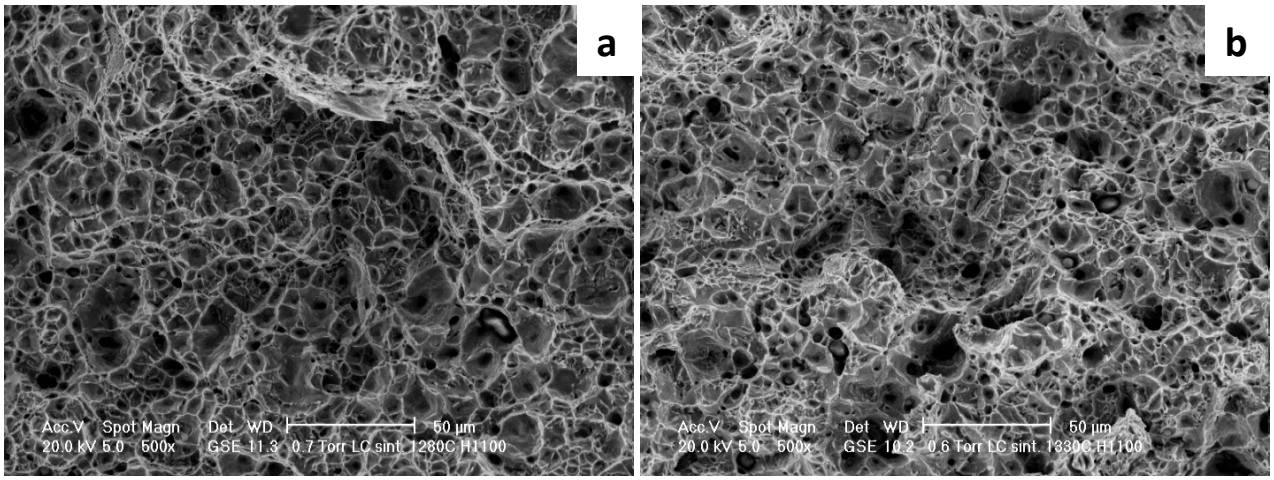

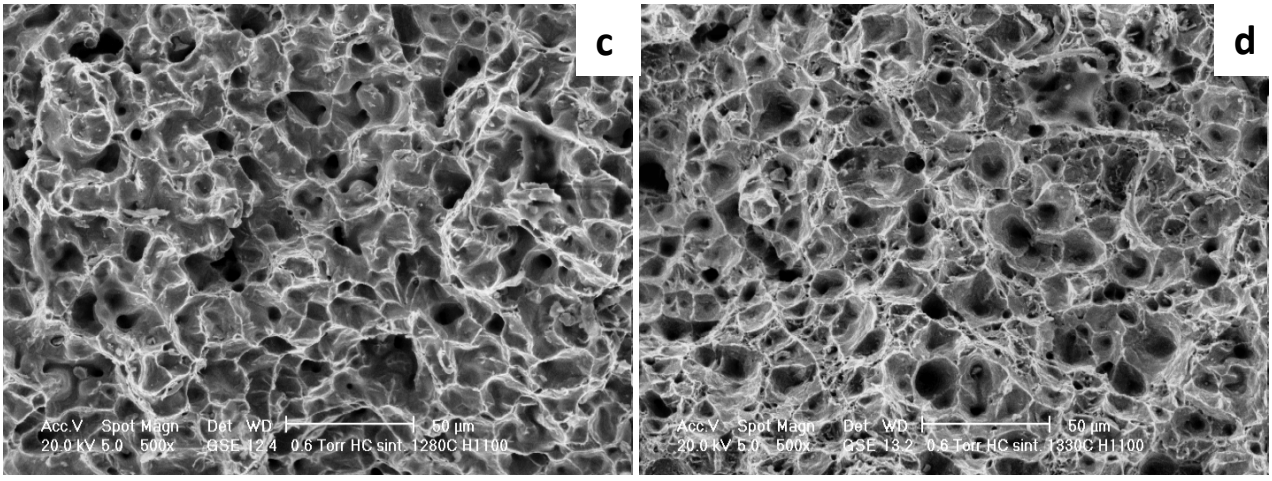

Fig. 14: fracture surface of H1100 materials: a) LC sintered at 1280°C, b) LC sintered at 1330°C, c) HC sintered at 1280°C and d) HC sintered at 1330°C.

On aging H900, HC sintered at 1280°C presents a localized and ductile fracture because of the residual porosity, which tends to concentrate deformation in the neck areas. The other materials, show a generalized deformation with a brittle behaviour. On aging H1100 fracture is ductile in all the materials, thanks to the inherent ductility of the microstructure, and dimples are slightly larger in HC. In both cases there is no evidence of phenomena related to delta ferrite.

4. CONCLUSIONS

The microstructural characteristics and the tensile properties of two 17-4PH stainless steels having different carbon content and produced by MIM has been investigated. By means of a DSC analysis, transformation occurring on the brown and the as sintered compacts were studied, as well.

Density is influenced by the presence of delta ferrite at high temperature; the higher the content of this constituent, the higher as sintered density. The content of delta ferrite depends on the carbon content, since carbon tends to stabilize austenite. On increasing the carbon content, the amount of delta ferrite then decreases.

Delta ferrite causes a decrease of tensile strength, without a corresponding increase in ductility. In presence of large amounts of delta ferrite, ductility tends to decrease significantly.

The 17-4 PH stainless steel may be sintered to a near-full density but delta ferrite, despite its favorable effect on sintering and densification, causes a global worsening of the tensile properties. Then, carbon content has a noticeable influence on the mechanical properties since the delta ferrite content depends mainly in it. Further experiments are in due course to investigate the effect of the microstructural properties on the fatigue resistance and, in particular, on corrosion resistance, since the increase in the carbon content results in the precipitation of chromium carbides on aging.

References

1) W. F. SMITH, Structure and Properties of Engineering Alloys, 2nd ed., McGRAW-HILL, Inc., New York, NY (1993).
2) H. J. RACK and D. KALISH, Metall. Trans. (1974), vol. 5, pp. 1595-1605.
3) C. K. LIN and W.J. TSAI, Fatigue Fract. Eng. Mater. Struct. (2000), vol. 23, pp. 489-97.
4) T. BABA, H. MIURA, T. HONDA, and Y. TOKUYAMA, Advances in Powder Metallurgy and Particulate Materials, M. PHILIPS and J. PORTER, eds., Metal Powder Industries Federation, Princeton, NJ (995) vol. 2, pp. 6271-6278.
5) H. KYOGOKU, S. KOMATSU, H. NAKAYAMA, H. JINUSHI, and K. SHINOHARA, Advances in Powder Metallurgy and Particulate Materials, R. A. McKOTCH and R. WEBB, eds., Metal Powder Industries Federation, Princeton, NJ (1997), vol. 3, pp. 18135-18144.
6) K. A. GREEN, Advances in Powder Metallurgy and Particulate Materials, J. J. OAKES and J. H. REINSHAGEN, eds., Metal Powder Industries Federation, Princeton, NJ (1998), vol. 2, pp. 5119-5130.
7) R. M. GERMAN and D. KUBISH, Int. J. Powder Metall. (1993), vol. 29, pp. 47-62.
8) JUN WANG, HONG ZOU, CONG LI, RULING ZUO, SHAOYU QIU and BAOLUO SHEN: Journal of University of Science and Technology Beijing (2006), vol. 13, n. 3, pp. 235-239.
9) J. J. VALENCIA and J. R. SPIRKO, Advanced Particulate Materials and Processes, (Metal Powder Industries Federation, Princeton, New Jersey (1997), p. 411.